Universidade do Minho
Escola de Ciências

César Rui de Freitas Bernardo

Linear and non-Linear Optical Properties Owing to Interactions of Elementary Excitations in Nanostructures

Linear and non-Linear Optical Properties Owing to Interactions of Elementary Excitations in Nanostructures

César Rui de Freitas Bernardo

UMinho | 2020

junho de 2020
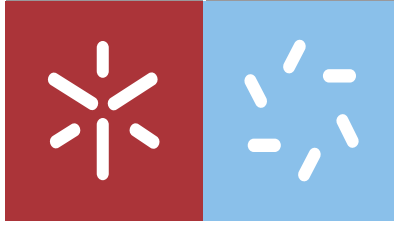
Universidade do Minho
Escola de Ciências

César Rui de Freitas Bernardo

Linear and non-Linear Optical Properties Owing to Interactions of Elementary Excitations in Nanostructures

Tese de Doutoramento
Doutoramento em Física

Trabalho efetuado sob orientação de
Professor Doutor Michael Scott Belsley
e de
Professor Doutor Mikhail Igorevich Vasilevskiy

junho de 2020

ACKNOWLEDGMENTS

STATEMENT OF INTEGRITY

I hereby declare having conducted this academic work with integrity. I confirm that I have not used plagiarism or any form of undue use of information or falsification of results along the process leading to its elaboration.
I further declare that I have fully acknowledged the Code of Ethical Conduct of the University of Minho.

University of Minho, Braga, June, 2020.

César Rui de Freitas Bernardo

RESUMO

Com o objectivo de obter uma multiplicidade de propriedades ópticas e electrónicas específicas, podemos produzir nanoestruturas artificiais controlando o seu material, tamanho e forma. Recentemente temos assistido à exploração de como a combinação de diferentes tipos destas estruturas podem vir a reforçar as suas respectivas caracteristicas. Isto é realizado com o objectivo de uma possivel produção de vários materiais a serem usados na próxima geração de dispositivos optoelectrónicos e nanofotónicos.

Como tal, neste trabalho explorámos como a combinação de materiais bidimensionais, Grafeno e MoS_2, juntamente com Pontos Quânticos ou Nanoplaquetas permitem criar nanoestruturas artificiais e como alteram as suas características.

Sendo que interacção entre a estrutura e excitações elementares em nanoestruturas semicondutoras e orgânicas podem afectar as suas propriedades ópticas lineares e não lineares, explorámos o seu acoplamento através de interacções excitão-plasmão ou excitão-excitão. A investigação deste acoplamento foi realizada utilizando : espectroscopia Raman, contagem de fotões únicos correlacionada com o tempo (TCSPC), espectroscopia de absorção transitória (TA) e geração de segunda harmónico resolvido no tempo (TR2HG) numa tentativa de caracterizar os processos físicos subjacentes e avaliar o possível potencial destas estruturas híbridas.

Além disso, foi realizada uma avaliação de nanofibras biocompatíveis com capacidade de gerar segundo harmónico (2HG). Sendo que os resultados obtidos corroboram a nossa proposta de que estas nanofibras formadas por moléculas não lineares "push-pull" cristalizadas dentro de uma matriz biopolimérica são materiais promissores para aplicações nanofotónicas e possivel recolha de energia.

Por fim foi realizada uma caracterização do índice de refracção não-linear do Grafeno com uso de uma nova abordagem. Através da modulação de fase cruzada através do do efeito óptico Kerr ultra-rápido, caracterizamos a resposta não linear de terceira ordem do grafeno. Verificamos que as alterações não lineares induzidas no grafeno por um campo forte ultra-rápido podem alterar temporariamente o índice de refracção visto por um segundo campo mais fraco, sendo que existe uma forte dependência da frequência analisada. Este efeito é prometedor por exemplo para o desenvolvimento de um interruptor óptico ultra-rápido baseado no grafeno.

Palavras-chave: Nanoestruturas; Propriedades Ópticas; Lineares; não-Lineares; Grafeno; Pontos Quânticos; Nanofibras.

ABSTRACT

Artificial nanostructures can be engineered to obtain a variety of specific optical and electronic properties, depending on their material, size and shape. More recently researchers have begun to explore how combining different types of these structures might reinforce their respective strengths to attain promising materials for the next generation of optoelectronic and nanophotonics devices.

For that, we explored how combining two-dimensional materials, Graphene and MoS_2, with Quantums Dots (QD) or Nanosplatelets (NP) to create artificial nanostructures might reinforce their respective strengths.

Since it's known that the interplay between structure and elementary excitations in semiconductor and organic nanostructures can affect their linear and nonlinear optical properties we explored the effect of coupling them via exciton-plasmon or exciton-exciton interactions. We have probed this coupling using Raman spectroscopy, Time-Correlated Single Photon Counting (TCSPC), Ultrafast Transient Absorption Spectroscopy (TAS) and Time-Resolved Second Harmonic Generation (TR2HG) in an attempt to characterize the underlying physical processes and evaluate the potential technological significance of these hybrids structures.

In addition, an evaluation of biocompatible second harmonic generation (2HG) nanofibers was realized and the produced results support the proposal that electrospun nanofibers formed by nonlinear push-pull molecules crystallized inside a biopolymer matrix are promising hybrid functional materials for nanophotonics and energy harvesting applications.

Furthermore, a characterization of the nonlinear refractive index of graphene was made with the implementation of a new approach. By means of the cross phase modulation via the ultrafast optical Kerr effect method, we characterize the third-order nonlinear response of graphene. We find that in graphene the nonlinear changes induced by a strong pump ultrashort field can temporally alter the refractive index seen by a weaker probe field and observe a strong dependence on frequency. This effect hold promise for developing a high-speed all-optical switch based on graphene.

Keywords: Nanostructures; Optical Properties; Linear; non-Linear; Graphene; Quantum Dots; Second harmonic generation; Nanofibers.

INDEX

PART I

INTRODUCTION

EXPERIMENTAL METHODS

PART II

RAMAN SCATTERING FROM PHONONS IN QUANTUM DOTS AND NANOPLATELETS: INTERACTION WITH GRAPHENE PLASMONS

EFFECTIVE 2HG IN BIOCOMPATIBLE ELECTRO-SPUN FIBERS

PART III

NANOSECOND TO PICOSECOND DYNAMICS OF 0D/2D NANOSTRUCTURES

GAIN OF SECOND-ORDER NONLINEAR-OPTICAL SIGNAL BY OPTICAL STIMULATION

KERR NON-LINEARITY OF GRAPHENE AS SEEN VIA CROSS-PHASE MODULATION

SUMMARY

LIST OF FIGURES AND SCHEMES

light probe were taken to be 120 fs and 2.5ps respectively. Propagation effects were ignored. The modulation depth is linearly proportional to the peak nonlinear phase.

TABLE INDEX

ACRONYMS AND ABBREVIATIONS

0D – Zero-dimensional

2D – Two-dimensional

2HG – Second Harmonic Generation

2PA - Two-photon absorption

3HG- Third harmonic generation

ADC - Analog-to-Digital Converter

ATR - Attenuated total internal reflection

BBO – Beta Barium Borate

CB – Conduction Band

CCD – Charged Coupled Device.

CPA – Chirped Pulse Amplification

CT – Charge transfer

CVD – Chemical Vapour Deposition

DET – Dexter energy transfer

EFISH - Electric Field Induced Second Harmonic Generation

EM – Electro magnetic

ESA - Excited state absorption

FET - Field Effect Transistor

FIR – Far-infrared

FLIM – Fluorescence lifetime imaging microscope

FRET – Forster Resonance Energy Transfer

FROG – Frequency-resolved optical gating

FWHM – Full With Half Maximum

FWM - Four-Wave Mixing

GFET – Graphene Field Effect Transistor

GSB - Ground state bleaching

GUI - Graphical User Interface

IRF –Instrumental Response Function

LBO - Lithium Triborate

LO- Longitudinal Optical

LOS- Local oscillator

MCP- Multi-Channel Plate

ML- Monolayer

MM – Method of moments

Nd:YLF - Neodymium-doped yttrium lithium fluoride

NL – Non-Linear

NLLS – Non-linear least squares

NLO – Non-linear Optical Effects

NP – Nanosplatelets

OHD - Optical heterodyne detection

OKE - Optical-Kerr effect

OPA – Optical parametric amplifier

PCL - Polycaprolactone

PL – Photoluminescence

PL –Photoluminescence

PLLA - Polylactic acid

PMMA - Poly(methyl methacrylate)

QDGR - QDs deposited over graphene

QDMoS- QDs deposited over MoS2

QDs – Quantum Dots

QDTF – Quantum Dots thin film

QWs – Quantum Wells

RET – Radiative Energy Transfer

RET – Radiative energy transfer

RSS - Raman scattering spectroscopy

SE - Stimulated emission

SERS - Surface-enhanced Raman scattering

SPIDER - Spectral phase interferometry for direct electric-field reconstruction

SPM – Self-phase modulation

SPP - Surface plasmon-polariton

SRH - Shockley-Read-Hall

SRS –Spontaneous Raman scattering

TA – Transient absorption

TAC - Time-to-amplitude converter

TAS - Transient Absorption

TCSPC - Time-Correlated Single Photon Counting

Ti:Sapphire - Titanium–sapphire

TM – Transverse magnetic

TMDs - Transition Metal Dichalcogenides

TO - Transverse optical

TR2HG - Time-Resolved Second Harmonic Generation

VB – Valence Band

WLC - White Light Continuum

XPM – Cross Phase Modulation

λ_{abs} – Absorption wavelength

λ_{em} – Emission wavelength

λ_{exc} – Excitation wavelength

PART I

CHAPTER 1

INTRODUCTION

Contents

1.1. **Thesis overview**

This thesis explores several ways in which the interplay between structure and elementary excitations in semiconductors and organic nanostructures can affect their linear and nonlinear optical properties. This work was motivated by the desire to understand and optimize photonic structures of very small dimensions, which can then be integrated or can be the platform for interactions with other systems. This type of hybrid photonic platform is interesting in several contexts, including quantum information, fine control of atomic interactions, and metrology.

There have been several important recent advances in nanotechnologies that broaden our ability to study light-matter interactions. The development of materials science and fabrication techniques opened up the possibility to probe and modify nature on a nanometer scale, revealing a whole new area of science at the interface of biology, chemistry, quantum physics, and optics.

One area of interest is the production of nanomaterials that can be used to manipulate light and, when possible, be biocompatible. This is of utmost importance since, for example, the optical techniques used in medical diagnostics, surgery, and therapy require effective and versatile illumination from light sources to target tissues. Although this need is presently being met by glass and plastic optical fibers, the latest advent of bio-integrated methods, such as optogenetics and implanted devices, requires new waveguides with certain biophysical and biocompatible properties.[1]

Also, the progress in semiconductor materials growth has led to the possibility of studying structures of reduced dimensionality such as quantum wells (QWs), quantum wires, quantum dots (QDs), graphene, and other emerging two dimensional (2D) materials, such as transition metals dichalcogenides (TMDs). Moreover, it opens the way to exploring interactions between them.[2]

Such new man-made and hybrid materials are interesting by themselves but the interest increases when they can be engineered into structures capable of generating or enhancing new light emission capabilities (less explored frequency ranges, e.g. the THz one) or even modulating the local electric field in a controlled way. Therefore, it is critical to evaluate the optical properties of these materials and structures, understand them, and achieve a means to control them, with a view of developing systems for specific applications.

This dissertation describes work exploring the linear and non-linear optical properties of several novel materials that include combinations of QDs with 2D materials (graphene and TMDs) and biocompatible polymeric fibers. The leitmotiv was to study the interplay between elementary

excitations in different semiconductor nanostructures and organic materials, with a focus on their linear and nonlinear optical properties.

The thesis is divided into three parts, with the first one consisting of these introductory notes complemented by a chapter that describes the experimental approaches and materials employed throughout this work.

The second part, also organized in two chapters, is dedicated to the research work that involved steady-state optical methods, namely, Raman scattering (Chapter 3) in Cadmium based nanocrystals/graphene structures and Second Harmonic Generation (2HG) in polymer-based biocompatible materials with enhanced optical properties.

Finally, the third part, comprised of three additional chapters, describes the research performed using time-resolved methods. Chapter 5 describes the energy/charge transfer from the Cadmium based QDs to graphene and MoS_2. In Chapter 6, we demonstrate the enhancement of weak second-order nonlinear optical signals via stimulated sum-frequency generation in a pump and probe experiment. We used this technique to enhance the Second Harmonic Generation by hybrid systems. Chapter 7 presents a versatile method to characterize the signal of the third-order optical nonlinearity of graphene using the Kerr effect, which can be a promising tool for the characterization of the optical nonlinearity of graphene or other 2D materials.

1.2.   Author's contribution

During the course of the work described in this dissertation, several tasks needed to be addressed. The stepping stone was the production of good quality samples and for that several methods were used depending on the material required:

a) Chemical synthesis of QDs and nanoplatelets (NPLs);

b) Exfoliation and identification of the 2D materials from bulk materials;

c) Transfer of CVD (Chemical Vapor Deposition) grown 2D materials from growth substrates to other supports;

d) Spin-coating and drop-casting of QDs;

e) Production of nanofibers.

I carried out all of the above preparation tasks except the synthesis of the NPLs, nanofibers, and their fundamental characterization.

To study the properties of these materials, several setups needed to be designed and implemented: Most are based on techniques reported in the literature and adapted according to our goals and technical capabilities.

The two main setups implemented during the course of this Ph.D. project were:

(i)   A second harmonic generation (2HG) microscope capable of obtaining the second harmonic response as a function of polarization.

(ii) A pump-probe microscope, flexible enough to allow the implementation of several different time-resolved schemes.

During this project, it was possible to achieve a working knowledge of the operation, alignment, and maintenance of the femtosecond laser systems, both a Kerr-lens mode-locked oscillator system and a regenerative amplifier. On a day to day basis, I was responsible for running these systems. I have also acquired practical knowledge in the alignment, calibration, and operation of an optical parametric amplifier with a white light continuum seed, the Topas-C. For several experiments, it was necessary to use diverse electronic equipment including the boxcar-gated integrator, lock-in amplifiers, and a gated photon counter. All of these opportunities combined afforded a hands-on working knowledge of these experimental systems and techniques.

Furthermore, I contributed with the development of the control and pre-analysis software (developed in LabView) for the detection systems and also the automatization of several translation-stages and rotation-stages for use in the presented and future experiments. Each software was developed with a graphical user interface (GUI) to allow for other students/researchers to use it in the future without deep knowledge of the equipment of the underlying computer control interfaces.

Additionally, to analyze the data acquired, I developed several scripts in MatLab to convert the data sets and a respective GUI for the deconvolution and presentation of the signals obtained.

1.3.   Introduction

The focus of this thesis lies in the interaction of light with matter; in this context, we explored several materials. One of the interesting systems that we explored are colloidal QDs, nearly zero-dimensional (0D) objects sometimes called "artificial atoms". They are excellent absorbers and emitters of electromagnetic radiation, however, assemblies of QDs have rather poor carrier-transport properties

in comparison with conventional semiconductors. In contrast, 2D materials such as graphene and the family of transition metal dichalcogenide monolayers have high carrier mobilities. These materials can be coupled to QDs via exciton-plasmon or exciton-exciton interactions. This is the motivation to bring these systems together in hybrid 0D/2D structures and investigate their optical properties.

From a fundamental perspective and also to enable the development of potential applications, it is crucial to understand the energy and charge transfer processes in these systems. As an example, we explored the case of energy/charge transfer from the Cadmium based QDs, to graphene and MoS_2. Usually, the modification of the photoluminescence decay rate is observed for QDs when they are coupled to graphene or TMD, which is attributed to non-radiative energy transfer. However, the question arises if this is limited to incoherent effects through mechanisms such as (irreversible) Förster resonant energy transfer (FRET) or possibly radiative transfer for longer distances. If coherent processes (i.e. reversible energy transfer between the 0D and 2D parts) occur at room temperature, one would expect to be able to manipulate and control such effects on ultrafast time scales, in the picosecond or sub-picosecond domain.

To assess the possibly coherent dynamics in the above-mentioned systems, various optical techniques can be used. Some methods probe the dynamics of charge carriers and the formation of biexcitons, such as the transient absorption, including state-selective and intraband methods, and transient photoluminescence studies. These techniques can determine relaxation dynamics with great accuracy. Typically, ultrafast energy transfer dynamics are experimentally measured using pump-probe techniques providing an insight into the light-matter interaction at the microscopic scale. In the remainder of this introductory chapter, I will briefly describe several key linear and nonlinear optical phenomena, to lay the ground for understanding the experimental efforts described in the following chapters.

1.4. Light-matter interaction

The expression "light-matter interaction" encompasses several physical phenomena ranging from classical to quantum electrodynamics, from black holes and neutron stars to mesoscopic systems, and from nanophotonics to subatomic objects. The linear interaction of light with condensed matter results in a plethora of phenomena that can be grouped into several categories ranging from: (i) reflection by the surface and interfaces of the condensed matter systems; (ii) absorption by the materials, (iii) light scattering, which can be elastic, caused by some heterogeneities that exist in the

materials [3], or inelastic, Raman or Brillouin scattering, which most commonly involves absorption or emission of optical or acoustic phonons, respectively;[4,5] (iv) reemission of part of the energy absorbed in the form of electromagnetic radiation, which generally occurs at frequencies other than those of the incident light, also known as photoluminescence or fluorescence [6]. In addition to these linear effects, there are a vast number of nonlinear optical effects including such processes as sum- and difference-frequency generation, Self- and cross-phase modulation, four-wave mixing, and harmonic generation.
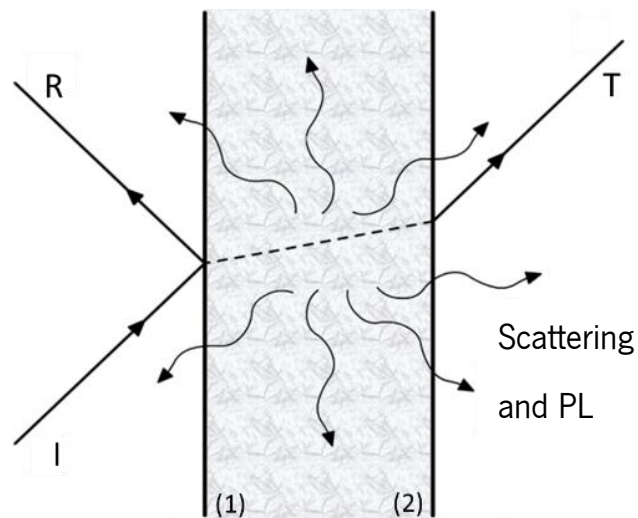
Figure 1.1 The main processes of linear light interaction with solid matter.

1.4.1. Linear phenomena

The most common processes involving light-matter interaction are linear phenomena taking place when the incident light beam has a low intensity. These phenomena give rise to a vast field known as Linear Optics that includes the most common optical effects such as reflection, refraction, and diffraction. They are in the heart of numerous applications in ordinary optical elements like wave-plates, lenses, mirrors, diffraction gratings, etc.[7] A linear optical system has the following properties:

a) It obeys the principle of superposition; for example, if a mirror transforms light input A into output B, and input C into output D, then an input consisting of A and C together gives an output of B plus D;

b) Changing the input light intensity results in a proportional change in the output light;

c) If monochromatic light enters a linear optical system, the output will be at the same frequency. Example: if the input light has a frequency of 500THz in the red part of the spectrum, the frequency of the output light will also be at 500THz.

However, there are a few processes that are often considered to be linear although the last property does not hold. This is the case of spontaneous inelastic scattering, e.g. Raman or Brillouin scattering.[8,9] All these properties can be violated under high-power laser illumination and then one can observe nonlinear optical effects.[10–13]

Usually, the dominant processes are those of reflection and absorption, which are considered as first-order processes, where one can also include the elastic scattering. Those related to the different forms of inelastic scattering may be called second-order processes since they involve certain elementary excitations that are created or eliminated in such processes.

Using the well-known relations of classical optics [3,7], it is possible to relate the characteristics of the first-order processes with the parameters of the material. To simplify, let us consider the case of normal incidence at a planar surface (1), whose normal is taken as the direction of the z-axis. The electromagnetic field within the material, corresponding to a monochromatic incident wave (of frequency ω) can be written as:

$$\vec{E} = \vec{E}_0 e^{i(kz-\omega t)} + \text{c.c.,} \tag{1.1}$$

where the vector $\vec{E}_0$ is the amplitude determined by the incident field amplitude and the boundary conditions at the interface (1) in Figure 1.1 and $\vec{k}$ is the wavevector. In general, there is also a wave reflected at the interface (2) (with the wavevector $-\vec{k}$), but for this description, we will focus only on the forward propagating waves in the medium. The wavevector inside the solid, $\vec{k}$, is related to the frequency through the dispersion relation,

$$k = \frac{\omega}{c}\hat{n}, \tag{1.2}$$

where $\hat{n}$ is the complex refractive index of the material,

$$\hat{n} = \hat{\varepsilon}^{1/2} = \eta + i\kappa, \tag{1.3}$$

with η being the (real) refractive index and κ the extinction coefficient. In Eq. (1.3), $\hat{\varepsilon}$ is the material's dielectric function, a complex function of ω that describes the linear optical properties of the material. The extinction coefficient characterizes the dissipation rate of the luminous energy in the matter, also known as absorption.

In materials with a positive extinction coefficient, the wave intensity will decrease with the distance according to:

$$I \propto \left| E(z) \right|^2 \propto e^{-\alpha z} , \qquad (1.4)$$

where

$$\alpha = 2\kappa\omega/c , \qquad (1.5)$$

is the absorption coefficient, which can also be expressed in terms of the dielectric function since we have:

$$\hat{\varepsilon} = \hat{n}^2 = \underbrace{\eta^2 - \kappa^2}_{Re\,\hat{\varepsilon}} + \underset{Im\,\hat{\varepsilon}}{2\eta\kappa \cdot i} . \qquad (1.6)$$

Combining Eq. (1.5) and (1.6) one finds:

$$\alpha = \frac{\omega\, Im\,\hat{\varepsilon}}{\eta c} . \qquad (1.7)$$

Neglecting the wave reflected brack through the material at the back surface of the sample (and therefore possible interference effects), one can obtain the following relations for the transmittance (T) and reflectance (R) for a slab of absorbing material (of thickness d). For normal incidence, they are:

$$R = \left| \frac{\hat{n}-1}{\hat{n}+1} \right|^2 \quad ; \quad T = \left(1-R\right)^2 e^{-\alpha d} . \qquad (1.8)$$

Notice that $R+T=1$ only if $\alpha = 0$.

1.4.1.1. Raman scattering

Spontaneous Raman scattering was first reported by Raman and Krishnan in 1928 [8] using the predictions stipulated by Smekal in 1923 [14] employing early quantum theory. This eventually led to a new field, Raman spectroscopy. Nowadays there are more than 25 different types of known Raman spectroscopy techniques, such as spontaneous and hyper-Raman scattering, Fourier-transform Raman scattering, Raman-induced Kerr effect spectroscopy and stimulated/coherent Raman scattering.[9]

As this large number of associated techniques indicates, Raman spectroscopy has become a major tool for the characterization of nanomaterials. Properties such as the number of monolayers [15], inter-layer and shear elasticity [16], in-plane anisotropy [17], doping [18], disorder [19], thermal conductivity [20], strain and phonon modes [21], can be probed using Raman spectroscopy. The material's fingerprint assessed by Raman spectroscopy is the difference between the incident and scattered light frequencies, which usually corresponds to the frequency of a vibrational mode characteristic of the specific material under observation. For a single molecular vibration mode, the spectral peak related to the Raman scattering often assumes a Lorentzian line shape, with a width of typically few cm^{-1}.[9]

In solids, the quanta associated with the excitation of vibrational modes are called phonons. As is usual in wave phenomena, the phonon's frequency is determined, in a crystalline solid, by the phonon wave vector, $\vec{q}$. For crystals with more than one atom per unit cell, there are acoustic and optical phonons.[22] Only the latter, with different atoms oscillating in counter-phase, contribute to the Raman scattering, while acoustic phonons may give rise to the so-called Brillouin scattering.[10] This is because the momentum and energy conservation laws dictate that only phonons with very small $\vec{q}$ can participate in the Raman scattering and optical phonons, contrary to the acoustic ones, have finite frequencies as $\vec{q} \rightarrow 0$.
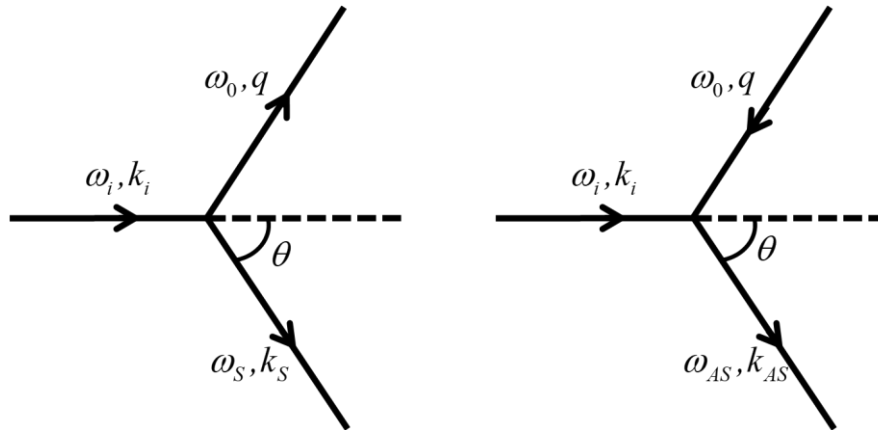
Figure 1.2 Vector diagrams for the conservation of the momentum in: left - Stokes scattering, and right - anti-Stokes scattering.

In Raman scattering, a phonon can be either created or destroyed and these two situations are named Stokes and anti-Stokes processes, respectively. The frequencies of Stokes and anti-Stokes scattered photons are given by $\omega_i \pm \omega_0$, where ω_i and ω_0 are the incident photon and phonon

frequencies. Figure 1.2 represents two vector diagrams for the conservation of the momentum in both of these types of inelastic scattering.[23]

For Stokes scattering, we have:

$$q^2 = k_i^2 + k_S^2 - 2k_i k_S \cos\theta ,\qquad (1.9)$$

where the incident (I) and scattered (S) photon wavevectors are related to their frequencies as follows:

$$k_i c = \eta_i \omega_i , \quad k_S c = \eta_S \omega_S .\qquad (1.10)$$

Here θ is the scattering angle, while η_i and η_s are the refractive indices of the medium for the incident and scattered light. Using Eq. (1.9) and (1.10), we obtain:

$$c^2 q^2 = \eta_i^2 \omega_i^2 + \eta_S^2 \left(\omega_i - \omega_0\right)^2 - 2\eta_i \eta_S \omega_i \left(\omega_i - \omega_0\right)\cos\theta .\quad (1.11)$$

This expression relates the phonon frequency, ω_0, and the magnitude of its wave vector, $\vec{q}$, that scatter the incident light of frequency ω_i through the angle θ. For the most common case where the refractive indices for the incident and scattered photons are nearly equal, $\eta_i = \eta_S = \eta$, we have:

$$\frac{c^2 q^2}{\eta^2} = \omega_0^2 \pm 4\omega_i \omega_S \sin^2\left(\theta/2\right) ,\qquad (1.12)$$

Where the signs + and – correspond to the Stokes and anti-Stokes processes, respectively. From Eq. (1.12) we can estimate that even in the case of Stokes-type backscattering processes ($\theta = \pi$) the phonon wave vector is of the order of 10^7 cm^{-1}, very small compared to the Brillouin zone size.

In a real system, usually several phonon modes, called Raman-active, can contribute to the scattering and the Raman spectra (scattering intensity versus Raman shift, $\omega = \omega_i - \omega_S$) are superposition's of several, sometimes many, peaks of different intensity and different widths.[24] Also, not just optical phonons but also other elementary excitations, such as plasmons and magnons, may contribute to the Raman scattering.[25] Moreover, hybrid excitations, such as polaritons or coupled phonon-plasmon modes may be observed by Raman spectroscopy.[26] In this work, we shall consider Raman scattering on such coupled modes resulting from the interaction of graphene plasmons with optical phonons confined in semiconductor QDs or NPLs attached to graphene.
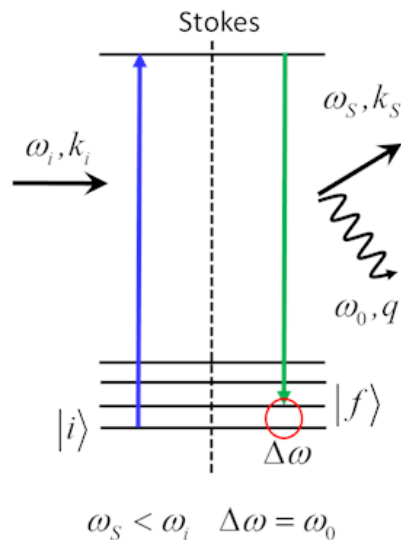
Figure 1.3 Simplified energy diagram for Stokes-type Raman-scattering process. The scatterer´s initial and final states are denoted *i* and *f*. The frequency shift, equal to the difference between the energies of the initial and final states of the scatterer (divided by Planck's constant) is called the Raman shift.

1.4.2. Nonlinear phenomena

Nonlinear Optical Effects (NLO) can be encountered when an intense beam propagates through a material. Even in the linear regime, an electromagnetic wave, which propagates through the material, disturbs the charged particles of the medium making them oscillate around their equilibrium positions. The relative displacement of positively and negatively charged particles creates electric dipoles and the dipole moment per unit volume is the induced polarization, P, of the medium.[11]

When the magnitude of the electromagnetic field is small the relative displacement of positively and negatively charged particles is proportional to the instantaneous magnitude of the electric field[1], behaving linearly. When the magnitude of the electric field is increased sufficiently, the medium will respond by modifying the electromagnetic field in a nonlinear way.

Macroscopically, understanding many nonlinear phenomena starts by considering an electromagnetic wave propagating in a homogeneous non-magnetic, polarizable medium. Like all macroscopic electromagnetic phenomena, Maxwell's equations represent the starting point:

---

[1] Only in the absence of absorption, if there is absorption, then the material will have a finite response function.

$$\nabla \times \vec{E} = -\frac{\partial \vec{B}}{\partial t},$$
(1.13)

$$\nabla \times \vec{H} = \vec{J} + \frac{\partial \vec{D}}{\partial t},$$
(1.14)

$$\nabla \cdot \vec{D} = \rho \,, \, \nabla \cdot \vec{B} = 0 \,.$$
(1.15)

Here $\vec{E}$ and $\vec{H}$ are the electric and magnetic field intensities, $\vec{D}$ and $\vec{B}$ are the corresponding inductions, while ρ and $\vec{J}$ are the densities of the electric charge and current, respectively. In a material, the electric displacement field and the magnetic induction field are related to the electric and magnetic fields by the following constitutive relations:

$$\vec{D} = \varepsilon_0 \vec{E} + \vec{P} \,; \, \vec{D} = \mu_0 \left(\vec{H} + \vec{M} \right).$$
(1.16)

Here ε_0 and μ_0 are the vacuum permittivity and permeability, respectively, $\vec{P}$ is the polarization induced by the electric field and $\vec{M}$ is the magnetization induced by the magnetic field. The induced polarization is related to the applied electric field by the following relationship:

$$\vec{P} = \varepsilon_0 \chi(\omega) \vec{E}.$$
(1.17)

The function $\chi(\omega)$ defined in Eq. (1.17) is called dielectric susceptibility of the medium; in general, it is a tensor. The linear dielectric function introduced in Eq.(1.6) is related to the susceptibility as follows:

$$\hat{\varepsilon}(\omega) = 1 + \chi(\omega).$$
(1.18)

Therefore, the polarization and the electric field are related by the susceptibility χ. If the applied field is weak, the material's response is independent of the electric field amplitude and the polarization is directly proportional to it.

However, if the applied field is sufficiently strong, it can alter the material's response and the susceptibility then becomes a function of the applied electric field strength, causing the polarization to vary non-linearly with the local electric field.[13] Since the nonlinear response usually manifests itself as a small deviation from a linear response, it is conventional practice to make a Taylor expansion of Eq. (1.17), where the expansion terms are associated with successive powers of the electric field:

$$P_i = \varepsilon_0 \left(\sum_j \chi_{ij}^{(1)} E_j + \sum_{jk} \chi_{ijk}^{(2)} E_j E_k + \sum_{jkl} \chi_{ijkl}^{(3)} E_j E_k E_l \right), \quad (1.19)$$

where $\chi^{(n)}$ is the n-th order optical susceptibility tensor and $i,j,k,l = x,y,z$. The first term in Eq. (1.19) accounts for the linear effects such as reflection, refraction, birefringence, and single-photon absorption for low intensities. The other, higher-order terms represent non-linear effects. By convention, the non-linear terms may be written in a symbolic form, e.g. $\chi^{(2)}\vec{E}\vec{E}$ where the tensor form of the nonlinear susceptibility is implicit.

1.4.2.1.   Second-order processes

The second and higher-order terms in Eq. (1.19), are only consequential at high incident intensities. They give rise to processes such as second harmonic generation, self-focusing, parametric amplification, self-phase modulation, and multiphoton absorption, among others.[11–13] In particular, the second-order susceptibility/term is responsible for the second harmonic generation, sum- and difference-frequency generation, and optical parametric amplification. These second-order nonlinear effects are produced by two waves, which interact to produce a third wave. For the process to be efficient, photon momentum and energy need to be conserved. The optical fields of these waves are coupled to one another through the second order susceptibility allowing for the exchange of energy among the interacting fields. In centrosymmetric crystals, this second order susceptibility is identically zero, except at the boundaries, meaning that second-order nonlinear processes are usually only observable in materials that lack inversion symmetry.

The simplest second order processes are sum and difference frequency generation that consists of two waves of frequencies ω_1 and ω_2 interacting nonlinearly to produce a wave with third frequency ω_3. In terms of the nonlinear polarization these processes are written as:

$$\vec{P}(\omega_3) = \varepsilon_0 \chi^{(2)}\left(\omega_3;\omega_1,\omega_2\right)\vec{E}(\omega_1)\vec{E}(\omega_2). \qquad (1.20)$$

In Eq. (1.20) we have $\hbar\omega_3 = \hbar\omega_1 + \hbar\omega_2$ for sum-frequency generation, while for difference-frequency generation $\hbar\omega_3 = \hbar\omega_1 - \hbar\omega_2$ or $\hbar\omega_3 = -\hbar\omega_1 + \hbar\omega_2$.

Another possible second order process is parametric amplification associated with difference-frequency generation. This describes the coupled growth of two waves in the presence of a third strong wave.

If a strong wave with a frequency ω_1 co-propagates in a nonlinear medium with a second weaker wave of frequency ω_2, energy from the stronger can be transferred to the weaker beam as well as to a third beam with frequency ω_3 also known as the idler by using difference frequency generation.

For parametric amplification to take place, a phase-matching condition needs to be satisfied, that relates the propagation vectors of the fields according to:

$$\Delta \vec{k} = \vec{k}_3 - \vec{k}_1 - \vec{k}_2 = 0 \,.$$ (1.21)

Here $\vec{k}_3$, $\vec{k}_2$ and $\vec{k}_1$ are the propagation vectors of the pump, signal, and idler respectively. Since the refractive index inside the nonlinear material depends on the wavelength, the direction of propagation, and the polarization of the waves, it is often possible to use birefringence to compensate dispersion effects by angle tuning the nonlinear medium to fulfill these conditions.
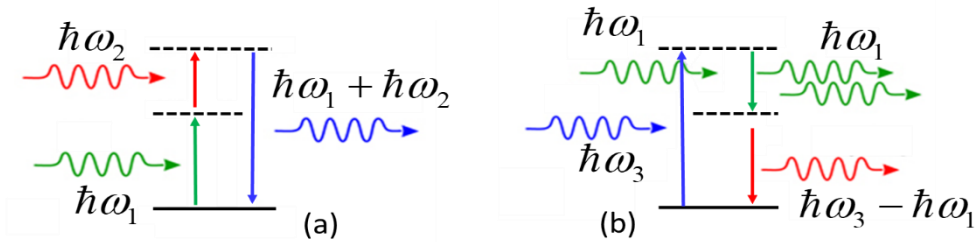
Figure 1.4 Examples of second order nonlinear processes, sum frequency generation (a) and parametric amplification (b).

Another distinct second order process occurs when the sum of two initial waves of the same frequency occur, $\omega_1 = \omega_2 = \omega$, giving rise to a third wave of the frequency $\hbar\omega_3 = \hbar 2\omega = \hbar\omega + \hbar\omega$. This is known as second harmonic generation and was first demonstrated by Franken et al. through the generation of light at twice the frequency of incident Rubi laser by a quartz crystal.[27]

This process can be described as follows:

$$\vec{P}_{\omega_3} = \varepsilon_0 \chi^{(2)}\left(\omega_3; \omega_1, \omega_1\right)\vec{E}^2_{\omega_1} \quad ;$$

$$I_{\omega_3} \propto \left|\vec{P}_{\omega_3}\right|^2 \propto \left|\chi^{(2)}\left(\omega_3; \omega_1, \omega_1\right)\right|^2 I^2_{\omega_1}$$

(1.22)

In chapter 4, I will describe the use of second harmonic generation, to characterize the second order optical response of organic crystals embedded in a polymeric fiber matrix. Second harmonic generation can also be used as a means to probe a variety of second order processes in different materials and systems.

Shortly after the invention of the ruby laser in 1960 [28], the initial results in nonlinear optics concentrated on bulk generation of second harmonic light by inorganic crystals initiated by Franken et al.[27]. However, there quickly followed an immediate interest in the development of several techniques ranging from the electric field induced second harmonic generation (EFISH) [29] to the surface-enhanced 2HG [30]. Because of its high interface [31] or/and surface [32] sensitivity, it is tempting to use 2HG as a technique to probe several ultrafast processes. Currently, 2HG is often used to investigate surface properties, for example, their charge, electronic state density, adsorption, orientation, and symmetry.[33] A prime example is the characterization of excited state dynamics in semiconductor monolayers where the focus lies in the dynamics of the charge transfer.[34]

In this work, a femtosecond laser system has been used to probe the nonlinear optical properties of two completely different material systems, one to improve the characteristics of the material and the other to understand the fundamental interactions between two materials. Using the 2HG as a steady-state spectroscopic probe experiment on electro-spun fibers doped with organic molecules was carried out, characterizing the effective second order nonlinear susceptibilities by measuring the fiber's second harmonic response as a function of the polarization of the incident and generated second-harmonic waves.

The other approach was to use the 2HG in a time-resolved pump-probe experiment to characterize the interaction between the 0D and 2D materials. This has been done using the femtosecond capabilities of the laser setup on several low-dimensional materials and their hybrids, probing the dynamics of the optically induced excitations.

1.4.2.2.   Third-order processes

As seen from Eq. (1.19), if the second order processes are forbidden (or weak), higher-order nonlinearities come into play. When the $\chi^{(3)}$ term is involved, we have third order nonlinear effects. This term is responsible for several novel effects such as the third harmonic generation, optical Kerr effect, four-wave mixing, stimulated Raman scattering and stimulated Brillouin scattering.[11–13] Put simply, the $\chi^{(3)}$ tensor couples together up to four different frequency components, three incident fields interacting to produce a polarization at a fourth possibly different frequency:

$$\vec{P}(\omega_4) = \varepsilon_0 \chi^{(3)} (\omega_4; \omega_1, \omega_2, \omega_3) \vec{E}(\omega_1) \vec{E}(\omega_2) \vec{E}(\omega_3). \quad (1.23)$$

If we have a lossless (transparent) medium, the elements of the susceptibility tensor are all real. In this situation, the primary nonlinear optical effects are the generation of new frequency components, the intensity-dependent refractive index change, the Kerr effect, and a variety of four-wave mixing processes including self-diffraction. If absorption is present, the imaginary part of the tensor can describe both Raman and Brillouin scattering as well as two-photon absorption. The Kerr effect describes an intensity-dependent change in the refractive index. This can be seen by viewing the nonlinear response as an effective modification of the linear response:

$$\vec{P} = \varepsilon_0 \left[\chi^{(1)} \vec{E} + \tfrac{3}{4} \chi^{(3)} |E|^2 \vec{E} \right] = \chi_{eff} \left(|E|^2 \right) E \quad . \quad (1.24)$$

This is essentially a modification of the refractive index by a factor that varies linearly with the incident intensity:

$$n(I) = n_L + n_2 I = n_L + n_2 \frac{W}{A_{eff}}, \quad (1.25)$$

$$n_L^2 = 1 + \chi^{(1)} \qquad ; \qquad n_2 = \frac{3}{4} \frac{\chi^{(3)}}{c \varepsilon_0 n_L^2}, \quad (1.26)$$

where n_L is the linear refractive index of the material, n_2 is the Kerr coefficient, the nonlinear part of the material´s dielectric response, I is the light intensity, W is the power of the signal, and A_{eff} is the effective beam area.[35]

For a continuous wave light or laser pulses of duration of the order of microseconds, the thermal response of the material often dominates, so the heating of the material causes the density change and a negative refractive index change. If we use ultra-short pulses, on the order of picoseconds or shorter, the excitation is too short for thermal effects to play a significant role and we only have the electronic and molecular response of the material, with the electronic response usually dominating. Under these conditions for most materials, the refractive index change is positive.

This change of refractive index induced by the intense optical electric field perturbs the propagation of the pulse itself. The temporally and spatially varying intensity produces a time-varying refractive index profile in the medium. Consequently, different parts of the pulse undergo different phase shifts, with the leading edge suffering a temporally positive phase gradient, and the trailing edge a temporally negative in the case of a positive Kerr index. This phenomenon is known as self-phase modulation.[35,36]

Consequently, the instantaneous frequency of the pulse will vary, that is the pulse develops a frequency chirp. Under the right conditions, this can lead to the appearance of new frequencies. For positive Kerr materials, the rising edge experiences a shift towards the lower frequency and the trailing edge experiences a shift towards the higher frequency, as seen in Figure 1.5. Since this effect depends heavily on the signal intensity, self-phase modulation has a more pronounced effect on high-intensity signal pulses. Depending on the sign this temporal phase chirp can either enhance or counteract the inherent material dispersion. The first case leads to temporally broadened pulses, while the second case, if the effect is strong enough, can lead to pulse compression. [38] Under very specific conditions the self-phase modulation can exactly balance the material dispersion creating conditions for soliton propagation. [37].
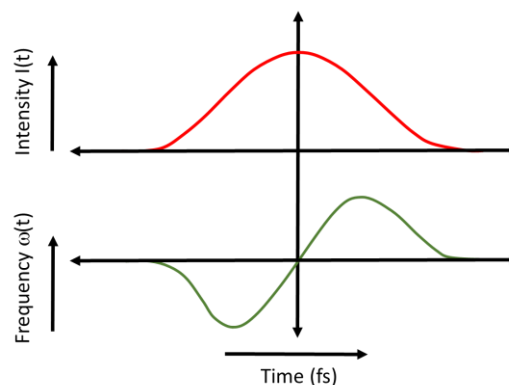
Figure 1.5 Illustration of self-phase modulation in a positive Kerr medium.

Usually, self-phase modulation is considered to lead to a deterioration of the pulses due to the associated frequency chirp and also due to the modulation instability enhancement of the noise. On the positive side, this modulation instability can be used to produce ultrashort pulses at high repetition rates. This can be used for fast optical switching [38] and also for the formation of dispersion managed optical solitons [37]. It also paves ways to other applications such as chirped-pulse amplification [39] or passive mode-locking [40].

The intensity dependence of the refractive index can also lead to another nonlinear phenomenon known as cross-phase modulation when two different incoming electromagnetic fields propagate in the sample, in our case a strong pump pulse and a weak probe pulse. The cross-phase modulation is always accompanied by self-phase modulation and occurs because the nonlinear refractive index seen by an optical beam, A, depends not only on its intensity but also on the intensity of the other co-propagating beam, B,[41]:

$$n_A(I) = n_L + n_2(\left|E_A\right|^2 + 2\left|E_B\right|^2).$$

(1.27)

The factor 2 in the Eq. (1.27) indicates that the cross-phase modulation is twice as effective as the self-phase modulation. This allows the pump to modify not only its spectrum but also the spectrum of the probe. Consequently, cross-phase modulation converts temporal variations in one beam into temporal phase fluctuations in the other co-propagating beam. The result of this may be an asymmetric spectral broadening and distortion of the pulse shape.[41]

If the sample is transparent, regarding both one and two-photon absorption, no net energy is transferred into or out of the sample or either beam. However, cross-phase modulation can be simply detected by spectrally deposing the beam using for example a grating spectrometer with sufficient resolution.

As for self-phase modulation, it is possible to take advantage of the cross-phase modulation effect and use it for nonlinear pulse compression [42], passive mode-locking [43], ultrafast optical switching [44], or pulse characterization [45,46], if one can overcome the amplitude and timing jitter that it produces.

In chapter seven, we describe a potentially novel application of cross-phase modulation to characterize the dispersion of the third-order susceptibility of low dimensional materials such as graphene.

1.5.   Materials and nanostructures of this study

As already mentioned above, the experiments in this work were performed on several kinds of materials, both natural and man-made, ranging from organic molecules and polymers to 0D colloidal nanocrystals (QDs), semiconductor NPLs, graphene, 2D materials of the TMD family and also hybrid systems (0D/2D nanostructures). The essential features of these materials and nanostructures are briefly described in this section.

1.5.1. QDs

Semiconductor QDs, often referred to as "artificial atoms", have discrete energy levels that can be tuned by changing the QD size and shape. Although historically the term "quantum dot" was introduced for small devices obtained by applying the lithography techniques to structures with 2D electron gas to achieve electrostatic confinement of the electrons in the remaining two dimensions [47], nowadays QDs are just nanometer-sized crystalline pieces of semiconductor material and can be divided into two types, (1) epitaxial grown self-assembled dots and (2) colloidal semiconductor nanocrystals coated with a layer of organic or inorganic passivation ligands. The dimensions are small enough to display quantum mechanical confinement properties. The existence of discrete confinement induced states in QDs has been proven by high spectrally and spatially resolved photoluminescence (PL) studies.[48,49] These discrete states can be understood as the result of quantum confinement of "free" electrons and holes that can exist in the conduction (CB) and valence (VB) band, respectively, of a bulk crystalline semiconductor as schematically shown in Figure. 1.6.

Colloidal QDs, which have been used in this study, are nearly spherical in shape, with good crystalline quality and high light-emission efficiency. The number of atoms per nanoparticle can vary from a few hundred to tens of thousands arranged in a crystal lattice. The QDs consist of an inorganic semiconductor core, the photo-active constituent, on which are anchored organic molecules, the surface ligands whose function is to stabilize nanoparticles and prevent their aggregation using special techniques, the size of the NC core can be controlled with good precision (+/- 5-10%).[50,51] The light-emission properties of colloidal semiconductor NCs can be further improved by using a core-shell structure composed of two nearly lattice-matched semiconductor materials where the shell usually has a larger band-gap (e.g. CdSe/ZnS

heterostructure). In this case, the photo-active core is covered with a semiconductor shell, mostly to protect it from degradation and improve its photophysical properties by eliminating electronic traps in the core's surface.[50,52]
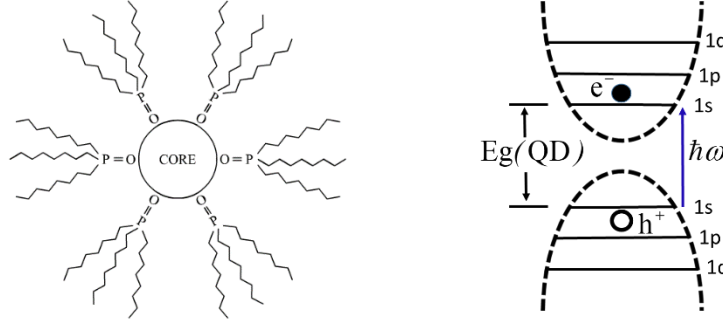
Figure 1. 6 Colloidal semiconductor NC coated with a layer of organic or inorganic passivation ligands and simplified scheme of electron and hole energy levels in such a colloidal QD. These levels are labelled, similar to atomic states, by the "spherical" quantum numbers *n* and *l*, the latter being represented by a letter; for instance, the ground states is 1*s* with *n*=1 and *l*=0.

Colloidal QDs are especially interesting because of their well-controllable size-dependent optical properties. This size dependence is caused by the quantum confinement effect and enables one to tune the wavelength of emission and absorption. The smaller the QD, the larger the energy gap between the lowest CB state and the highest VB state. In the so-called strong confinement regime where the QD radius is smaller than the exciton Bohr radius of the underlying semiconductor crystal, $R < a_{ex}$, the kinetic energy of the electron and hole caused by confinement is larger than the Coulomb energy of their interaction (for instance, $a_{ex} = 5.6\,\text{nm}$ for CdSe). In this situation, assuming infinite barriers and simple parabolic bands, the QD effective band-gap energy, i.e. the separation between the states $1s(\text{CB})$ and $1s(\text{VB})$, can be expressed as:

$$E_g^{QD}(R) = E_g + \frac{\hbar^2 \pi^2}{2R^2}\left(\frac{1}{m_e} + \frac{1}{m_h}\right),$$

(1.28)

where $m_e(m_h)$ is the electron (hole) effective mass and E_g is the bandgap energy of the underlying bulk material.[53] Taking into account the Coulomb interaction, the QD exciton ground state energy is given by:

$$E_{ex}^{QD}(R) = E_g^{QD}(R) - 1.76\frac{e^2}{4\pi\varepsilon_0\varepsilon_s R}, \tag{1.29}$$

where e is the magnitude of the electron's charge and ε_s is the static dielectric constant of the QD material.

A more elaborate calculation that takes into account the VB degeneracy characteristic of the most typical semiconductors (i.e. light hole and heavy hole sub-bands), finite barriers, and the effective masses' discontinuity at the NC's surface leads to a less steep increase of $E_g^{QD}(R)$ as $R \to 0$, as seen in Figure 1.7.[54] The energies of other possible electronic states also depend on R and this gives rise to the size-dependent absorption and emission spectra of QDs.
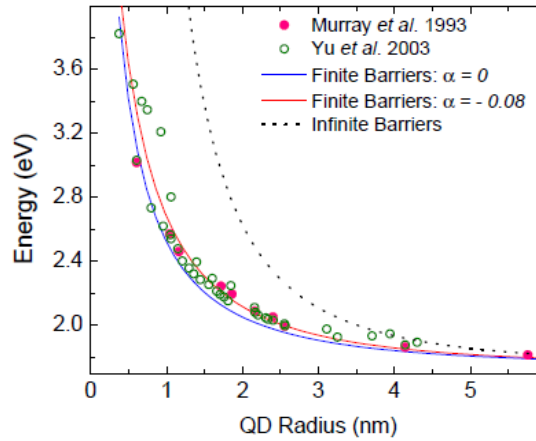
Figure 1.7 Comparison between experimental and theoretical results for CdSe/TOPO QDs relation of QDs radius with its band gap [49].

Upon irradiation with the proper wavelength, the electron is excited to a certain quantized state in the conduction band, leaving a hole in the valence band. Subsequently, the electron relaxes towards the lowest energy state $1s(\text{CB})$ and so does the hole, going up in energy to reach the highest unoccupied (by electron) VB state. Then they recombine by emitting a photon. Relaxation from the excited electron states occurs extremely fast, with characteristic times in the subpicosecond range [51], even though the precise mechanism of this relaxation remains a matter of some controversy [55]. Therefore, PL emission primarily takes place owing to the

recombination of the QD exciton in its ground state, Eq. (1.28), and the emission wavelength is roughly independent of the excitation wavelength.

It is necessary to bear in mind that both emission and absorption spectra are influenced by the size distribution of QDs. As mentioned above, emission line of a single QD is almost as thin as the atomic emission lines [48,49], while emission of a QD ensemble, even with a nominally monodisperse QD size, the width at half maximum of the PL spectra varies usually from about 20 to 40 nm.[50,51] In general, a relatively narrow Gaussian peak is expected in the ensemble emission spectrum.

The absorption spectra of QDs are usually spread over a range of wavelengths from the ultraviolet to visible depending on the size of the nanocrystal because, contrary to emission, many states contribute to the light absorption. Unless the QD ensemble has a broad size dispersion, there is a well-defined absorption band in the spectrum, corresponding to the exciton ground state energy. The emission peak is always red-shifted relative to the maximum of this absorption band and this Stokes shift may be rather large in QD ensembles (see Figure 3.6 in Chapter 3), where it is caused mainly by the size dispersion, with the emission coming mostly from the largest dots in the ensemble. However, even in an individual QD, there is a (smaller) Stokes shift, which is caused by a fine structure of the exciton ground state. It was shown for CdSe QDs that this state is split by a combination of the exchange electron-hole interaction and the crystal field action (CdSe is a hexagonal crystal), into a group of (higher energy) bright states and another group of (lower energy) "dark" states.[56] The latter are not completely dark and the PL emission occurs from these substates and the intrinsic Stokes shift is 20-30 meV.

Due to point defects inside the crystal and dangling bonds on its surface, some additional states (called traps) may be present within the bandgap of a semiconductor. It also happens with nanocrystals. Deep traps may give rise to a secondary peak in the emission spectrum of nanocrystal QDs. Interestingly, apart from these shortcomings, the possibility of a narrow emission band and broad excitation range makes QDs a very attractive tool, for example, for multiplexing imaging using a single excitation source.[57]

One of the most popular methods of synthesis of nanocrystal QDs is the decomposition of organometallic precursors that allows for the synthesis of semiconductor CdSe, CdS, and CdTe nanocrystals in a colloidal solution. With this type of synthesis, a nanocrystal size dispersion of less than 5% can be obtained. It should be noted that the process raises some environmental problems and safety hazards.[52] For avoiding these concerns, one of the popular approaches

is the use of a reverse micellar approach where two immiscible liquids, polar water and a nonpolar long-chain alkane, are mixed and stirred to form an emulsion.[58]   At a high concentration of organic solvent and a small amount of water in the presence of a surfactant, it is possible to observe the development of reverse micellar phases. In this phase, the water is protected by the hydrophobic continuous phase a monolayer of surfactant forming a core that can be used as a nanoreactor. Mixing micellar solutions containing several precursors leads to a continuous exchange of reactants due to dynamic collisions arising from the Brownian motion of the reverse micelles resulting in the desired nanocrystals, the QDs.

1.5.2. Nanoplatelets

Further development of the colloidal chemistry techniques allowed for the fabrication of new objects, called NPLs, which are intermediate between the QDs and 2D materials. With a precisely controlled and small number of atomic layers in one direction, NPLs have lateral dimensions of tens or hundreds of nanometers in the other two directions. They are usually made of II-VI semiconductors (CdSe or CdTe) and there is no quantum confinement in the lateral directions, so sometimes NPLs are called "colloidal quantum wells" (QWs). The advantages of these colloidal QWs include precise control over the number of monolayers in the z-direction, and consequently, narrow optical absorption lines, also a very high emission intensity compared to QDs.[59] Due to the extended lateral dimensions of colloidal NPLs larger than the exciton Bohr radius, these NPLs exhibit quantum confinement effect only along the smaller dimension.
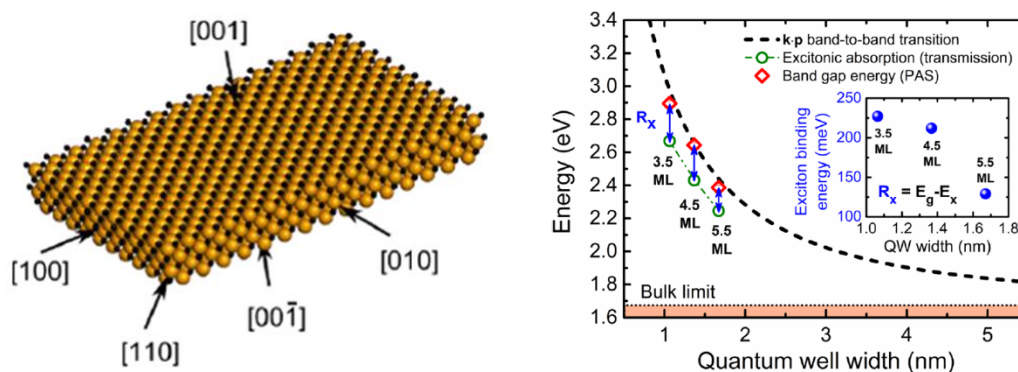
Figure 1.8 Model of a colloidal CdSe quantum well structure or NPL, where quantum confinement takes place in the [001] direction, left. Interband transition energy versus the potential well width.The inset shows the thickness dependence of the exciton binding energy calculated as a difference between the excitonic absorption and the band-to-band transition energies, right.[58]

Therefore, the electronic band structure solely depends on that dimension. With their quasi 2D nanocrystal structure, NPLs show a unique electronic structure and their optical properties are consequently different from the spherical shaped QDs. Sharp excitonic transitions in the absorption spectra corresponding to the electron heavy-hole (lower energy) and light-hole (higher energy) transitions are observed. For example in the case of 4.5 monolayer (ML) thickness CdSe NPLs, the heavy-hole and light-hole transitions are observed at approximately 512 and 480 nm, respectively (Figure 1.9-blue line).

Theoretical calculations and experimental works have already shown that, in the case of CdSe, large shifts, tens of nanometers, are observed in the luminescence spectra when the thickness is changed by just one atomic layer.[60,61]

Since their thickness can be well controlled by the synthesis and purification procedures, it is possible to obtain some well-defined distribution of populations as seen in Figure 1.9. The thickness is 0.9, 1.2, and 1.5 nm, and the lateral extension usually ranges from tens to hundreds of nanometers.

Additionally, these CdSe NPLs exhibit almost zero Stokes shifted emission behavior with the narrowest full width at half maximum (FWHM) value of approximately 30meV when compared to the ~70meV of the QDs.[61] These narrower emission observed in colloidal NPLs can be fitted with a Lorentzian rather than a Gaussian function, as used in the QDs, which indicates the suppression of inhomogeneous broadening.[62]
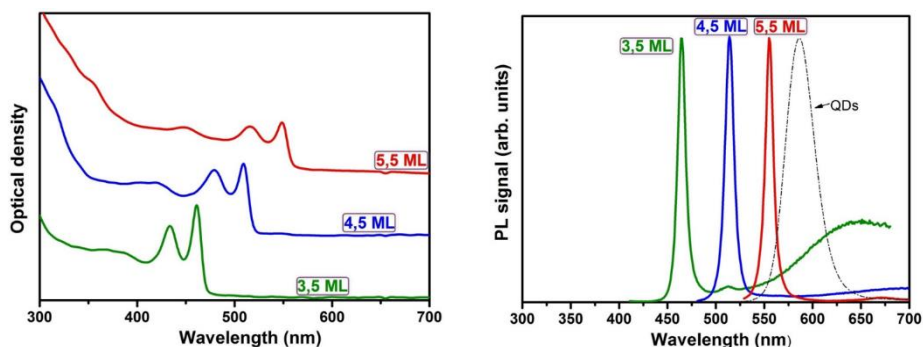
Figure 1.9 Absorption and photoluminescence spectra of 3.5, 4.5 and 5.5 ML thickness CdSe NPLs.

When the thickness of the CdSe NPLs decreases down to the sub-nanometer scale (3.5 MLs for example), surface defects may lead to intensive surface emission with a broad band appearing

at higher wavelengths, which is due to radiative recombination through surface-emission centers.[63,64]

With the strong quantum and dielectric confinement effects, colloidal NPLs have increased oscillator strength, leading to the observation of an enhancement of the absorption cross-section [61,65,66] one order of magnitude larger than the QDs [67] at the same emission wavelengths. For two-photon absorption, the same trend was found.[68,69] Another advantage is that their possible Auger recombination process is suppressed due to strict momentum conservation constraints, becoming more difficult in these higher dimensional systems.[70]

For the production of systems that can rival their analogues, QDs, NPLs can be used in the next generation optoelectronics, especially for low threshold lasing [68,71] and high-performance LEDs [72,73].

1.5.3. Graphene

Graphene is a single atom thick, two-dimensional sheet of carbon atoms, and its 2D nature gives rise to some interesting mechanical, electronic, and chemical properties.[74] These include a high intrinsic charge carrier mobility of $2.5 \cdot 10^5$ cm^{2}V^{-1}s^{-1} at room temperature, a Young's modulus of around 1 TPa yielding second-order and third-order elastic stiffness of 340 N/m and 690 N/m, respectively, a high thermal conductivity of $\approx 4 \cdot 10^3$ W/(m.K), and a high transparency (97.7%) throughout the visible spectrum.[74–76]

Graphene has a honeycomb hexagonal lattice of carbon atoms with their $2s$, $2p_x$, and $2p_y$ orbitals hybridized in a way that each carbon atom is bonded to its three nearest neighbors and are symmetrically distributed in the molecular plane at angles of 120∘ forming three σ-bonds. The remaining $2p_z$ orbital is perpendicular to the lattice and overlaps with other atoms' $2p_z$ orbitals, forming a π bond. These π electrons govern the electronic transport, being delocalized throughout the crystal.[77] Also due to the high carbon-carbon bond energy of 4.9 eV, graphene is chemically stable under a variety of conditions.[78]

The electronic band structure of graphene can be determined using a tight-binding approximation applied to the 2D honeycomb lattice.[79] The conduction band and the valence band touch each other in six points at the border of the 1-st Brillouin zone, which are called K points. The electron dispersion relation near any of the K points is linear, $E = \hbar v_F k$, where v_F is the Fermi velocity

and k is the wavevector relative to the nearest K point. Therefore, electrons and holes in graphene behave as Dirac-type fermions with zero effective mass. The electron (or hole) concentration in graphene can be controlled by so-called "electrostatic doping" or "gating" if the layer is inserted into a field-effect transistor (FET) structure. Thus, both d.c. and high-frequency conductivity and, consequently, the optical transparency of graphene can be controlled via changing its Fermi level by external gating.[80]

Thus, graphene is a very thin and transparent conductor with adjustable conductivity. Owing to this, it supports surface plasmons, more precisely, surface-plasmon-polaritons, which are evanescent electromagnetic waves that accompany electron density oscillations in graphene (known as Drude plasmons).[81]
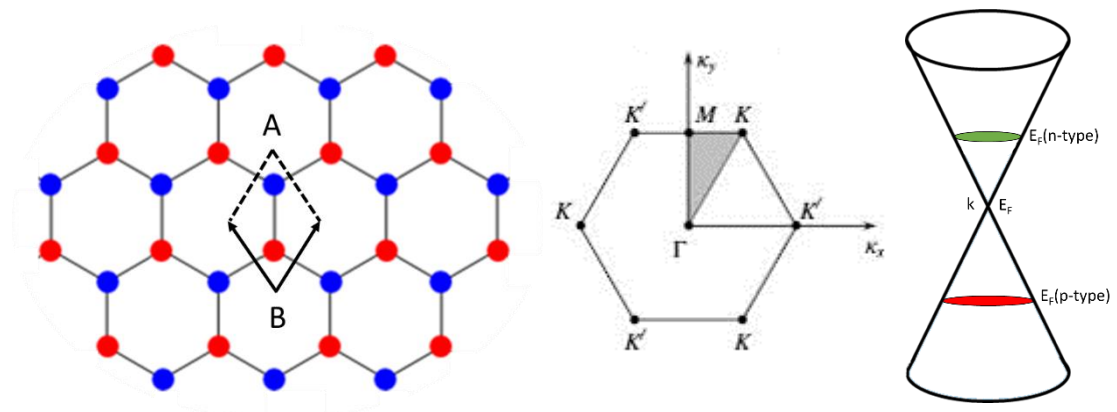
Figure 1.10 Honeycomb lattice structure of graphene, a superposition of two triangular lattices. The sites of each triangular lattice define carbon atoms of type A and B (left). The reciprocal lattice is also a triangular lattice with the 1-st Brillouin zone shown in the middle. The right panel is a schematic representation of low energy band structure exhibiting zero energy gap at the Dirac point. While for neutral graphene the Fermi level is in the Dirac point, 'red' and 'green' Fermi levels correspond to p and n-doped material, respectively.

The interest in these types of waves is due to the fact that they have a wavelength smaller than the incident light, leading to localization of energy in the plasmon modes, with the evanescent field decaying rapidly with the distance from the graphene sheet. This is the cause of the large field enhancements which in turn leads to huge enhancement of interaction strengths with other entities, e.g. adsorbed molecules. Compared to the traditional plasmonic materials, the noble metals, plasmonic losses are low in graphene. These properties promise (and already yield!) application in sensors, surface-enhanced Raman scattering, light absorbers and optoelectronic devices working in the THz spectral range, and even plasmonic circuitry.[82] This is the domain of Graphene Plasmonics, a broad and still growing field of research and technology.[63-66] In

Chapter 3 we shall return to graphene plasmons, in the context of their interaction with QD phonons.

Concerning the nonlinear optical properties of graphene, the 2D honeycomb lattice is centrosymmetric and, therefore, it is expected that $\chi^{(2)} = 0$ for homogeneous graphene.

However, when supported on the surface of a glass substrate, graphene loses its inversion symmetry along the surface normal, so, oblique-incident light may create second-order effects. It has been predicted that monolayer graphene may have a strong Kerr nonlinearity [83], considerably larger than many nonlinear bulk materials, which can be explained by the linear (Dirac-type) dispersion relation of the charge carriers. Several nonlinear optical effects have been predicted for graphene, such as soliton formation [84] and optical bistability [85], in the THz frequency range and physically related to the Drude plasmons in graphene. Interesting nonlinear physics may also take place in the infrared spectral range due to interband transitions that are possible above the twice the Fermi energy, $2E_F$, and $\chi^{(3)}$ of graphene has a resonance at $\hbar\omega \approx 2E_F$ [86] In the range of wavelengths of the order of 1 µm, a strong non-linear response of monolayer and few-layer graphene was observed by four-wave mixing, with $\chi^{(3)} \approx 10^{-15} \mathrm{m}^2/\mathrm{V}^2$ [87], and also by optical third-harmonic generation, with the signal exceeding that from bulk glass by more than two orders of magnitude [88]. The optical Kerr effect in graphene was measured using different experimental techniques but the results of these measurements, presented in terms of the effective nonlinear refractive index n_2 of graphene, are rather contradictory. Not only does the absolute value of the measured n_2 differ by up to 3 orders of magnitude in different papers, but consensus has not yet been reached even regarding the sign of n_2.[86] We shall return to this point in Chapter 7.

Concerning the material's fabrication, there are two major strategies to obtain graphene, top-down and bottom-up.[75,89] In top-down methods, graphene sheets are exfoliated from graphite. The most common method is the micromechanical cleavage technique, also known as the Scotch-tape method.[90] This consists in isolating the carbon sheets of graphite with an adhesive tape. From a fundamental standpoint, the process is exceptionally simple. The starting point is a bulk crystal consisting of millions of layers of 2D crystals stacked on top of each other. This bulk crystal is placed on a piece of tape and by sticking the tape together and peeling it apart repeatedly, the sheets will be cleaved from one another until there are just a few stacked layers. This piece of tape is then set on a substrate and removed, and as there is no bond between the

sheets, a monolayer or few layer will hopefully be deposited on the substrate. The main problems associated with this method are the random positions of the deposited graphene together with the small flake size of the obtained graphene, on the order of around 20 μm. Other top down methods have also been developed that involve sonication [91] or even microwaves [92].

For the "bottom-up" methods surface science provides new strategies to grow graphene using for example epitaxial growth by thermal decomposition of SiC [93] or chemical vapor deposition (CVD) growth [94]. This method of obtaining graphene yields several advantages over the mechanical exfoliation method. The main ones being the possibility to grow graphene on large surface areas and the possibility of controlling the growth process. One of the possible shortcomings of CVD graphene, substantial for certain applications, is the presence of defects.[95]

1.5.4. TMDs

Transition metal dichalcogenides (TMDs) belong to the family of materials of the formula MX_2, where M is a transition metal of group IV (Ti, Zr, Hf...), group V (V, Nb, or Ta) or group VI (Mo, W....), and X is a chalcogen (S, Se or Te). These materials include insulators (HfS_2) semiconductors (MoS_2, WS_2, etc.) and metals (NbS_2).[96,97] The material used in this work, molybdenum disulfide, MoS_2, is a layered crystalline semiconductor with strong light absorption, so it can be applied to photoluminescence, photovoltaic, and photocatalytic research.[97] The optical properties of MoS_2 also show potential for various nonlinear responses, such as optical limiting [98], saturable absorption [99], two-photon absorption [100], multi-photon absorption [101] and second [102] and third harmonic generation [103]. Both linear and nonlinear optical properties of TMDs depend strongly on the number of atomic layers in the material; here we will focus on the "monolayer" form (see Figure 1.11).
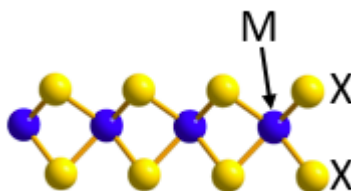
Figure 1.11 MX_2 "monolayer" crystal example, where M is a transition metal atom and X is a chalcogenide atom.

TMD structures consist of two-dimensional X-M-X sheets, stacked along the c axis. An interesting feature of monolayer MoS_2 is that it has two distinct phases, a metallic octahedral 1T and a semiconducting, trigonal prismatic 2H, the latter being of major interest. In such a structure, the metal atom is in a prismatic trigonal position (Figure. 1.11), sandwiched between two chalcogen planes, linked to six chalcogen atoms by covalent bonds. The adjacent planes of two sheets contain only chalcogenes, which leads to the formation of weak Van der Waals bonds, that allow for an easy cleavage.[104]

Unlike graphene, monolayer MoS_2 is non-centrosymmetric material and also has a non-zero direct bandgap, which is attributed to the involvement of d-electron orbitals. Similar to graphene, interesting physics takes place at the K points of the Brillouin zone where the direct bandgap occurs, excitons are formed and the most important optical transitions take place there.

Owing to their 2D nature, excitons are very robust in this material, with the binding energy $E_B \approx$ 0.3 – 0.5 eV.[105] The spin-orbit interaction splits the valence band into two subbands that differ by the spin orientation, which is "up" for A (B) exciton in K (K') point. This alternating order of exciton spins in adjacent K and K' points (see Figure 1.12) is called spin-valley correlation and it enables an efficient valley and spin control by optical helicity.[106] This band structure is responsible for luminescence related to the excitons A and B at 1.85 eV (670 nm) and 1.98 eV (627 nm), respectively, with reasonably good efficiencies.[107]

TMDs can be incorporated into microcavities, where coupled modes called exciton-polaritons are formed [108], with the possibility of achieving the strong coupling regime and polariton lasing.
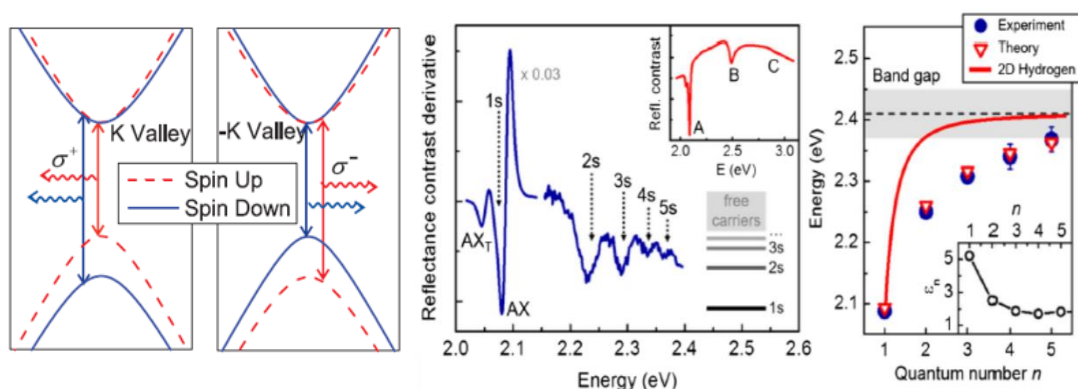
Figure 1.12 Band structure (left) and reflectance spectrum of a MoS_2 monolayer showing various excitonic peaks (middle). The A and B excitons exist because of the spin-orbit splitting of the valence band. The energies of the higher A exciton states do not follow the 2D hydrogen model (right).[104]

The reasonably high mobility of charge carriers in TMD layers also allows for their application in field-effect transistors [85] and photodetectors [109].

Like in the case of graphene, there are similar bottom-up and top-down approaches to obtaining monolayers of MoS_2. Unfortunately, the micromechanical cleavage, the scotch tape method, gives samples smaller than the those typically obtained for graphene, limited to around 10 um, but still usable for some purposes, namely our ultrafast spectroscopic studies. Via chemical processes, it is possible to obtain MoS_2 monolayers crystals of approximately 100 um in size but still far from approaching a continuous layer as is possible for graphene.[110]

1.6. Photo-carrier dynamics in semiconductor nanostructures

The photo-induced carrier dynamics in semiconductors nanostructures taking place in the vicinity of other materials is one of the topics studied in this thesis. Several processes are expected to happen when these nanostructures and materials interact with an electromagnetic field. In most cases, the light-matter interaction involves electronic transitions[2], which, for crystalline solids, can be divided into two categories, (i) intraband and (ii) interband ones. Transitions (i) require the participation of a third particle (usually a phonon) to occur because without which it is impossible to satisfy the requirements of energy and linear momentum conservation. Such transitions underlie, for instance, the Drude plasmons in graphene. In semiconductors, materials with a non-zero bandgap energy (E_g), absorption of a photon with an energy $\hbar\omega \geq E_g$ creates an electron-hole pair, which is an example of an interband transition (ii). If the electron in the conduction band and the hole in the valence band are linked by Coulomb interaction, a photo-induced exciton is generated. Strictly speaking, the term "exciton" applies to a bound electron-hole state and it is common to distinguish Frenkel and Wannier-Mott excitons [111]. The former is a tightly bound exciton, characteristic of molecular systems. The latter is characteristic of conventional (3D) semiconductors and can be rather well described by the Hydrogen atom model, with an effective Bohr radius, a_{ex}, much larger than the lattice constant. The 2D semiconductors of the TMD family are an intermediate case in this sense, with $a_{ex} \approx 1\,\mathrm{nm}$. In QDs, in the strong confinement regime

---

[2] Processes of direct interaction of light with polar optical phonons take place in the far-infrared spectral range and were not studied in this thesis.

discussed in Sec. 1.5.1, an electron-hole pair is confined by the QD "walls" rather than by the Coulomb interaction, so the exciton effect is just a relatively small correction to the carriers' energy, Eq. (1.29). For clarity, we shall often call an exciton any electron-hole pair, even if it is not quite linked by the Coulomb interaction. The processes of photocarrier dynamics range from the generation, dissociation, and recombination of the exciton, transport of the exciton as a whole or just one of its members (charge transfer), and the recombination.[112] In this section, we shall overview the essential features of these processes.

1.6.1. Radiative and non-radiative recombination

When the incoming photon's energy is greater than the bandgap, the energy can be absorbed to excite an electron from the valence band into the conduction band. The excited electron then relaxes to the bottom of the conduction band, usually through interactions with phonons. The same happens to the hole, and usually this process is relatively fast, with the characteristic times of the order of 1 ps, even in QDs. As mentioned above, such an electron-hole pair may be called an exciton, whether or not they are bound by their Coulomb interaction. There are three main exciton recombination mechanisms, schematically shown in Figure. 1.13.

The most universal process taking place in either direct or indirect bandgap semiconductors is the Shockley-Read-Hall [113,114] or trap-assisted recombination where an electron in the conduction band falls into a localized energy state in the forbidden band, created by a lattice defect or an impurity, and becomes "trapped". It "waits" there until a valence band hole approaches it (in real space) and recombines with it. The released energy is dissipated into heat.
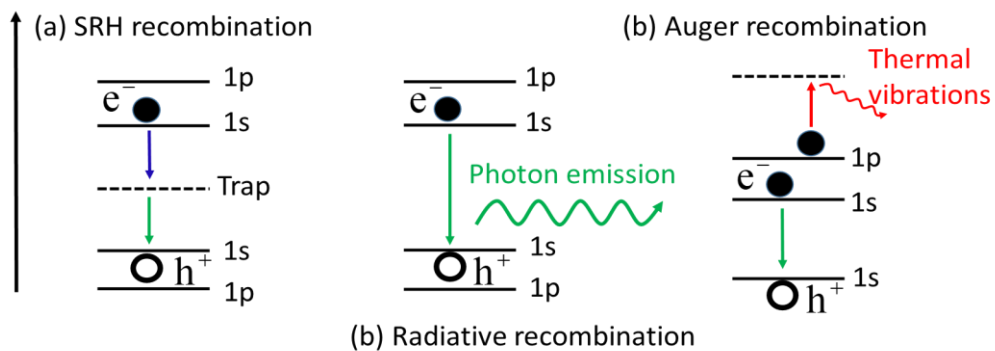
Figure 1.13 Schematic diagram of exciton recombination: (a) Shockley-Read-Hall recombination via traps, (b) radiative recombination, (c) Auger process.

The second process represented in Figure 1.13 is the radiative recombination described first by O.V. Losev [115]. This is a kind of spontaneous emission, with a photon taking the energy released from the exciton recombination. As with atomic systems, when many photons are present around, for instance, if the semiconductor (nanostructure) is placed in a microcavity, the radiative recombination can be stimulated and this can give rise to coupled modes called exciton-polaritons as mention in 1.5.2. However, in the most common situation, the photon is just emitted irreversibly and the exciton ceases to exist. Such a spontaneous emission process is the opposite of the interband absorption and both can be described by the same (linear) susceptibility. Considering, the specific case of a spherical QD of radius R, the susceptibility can be modeled as [116]:

$$\chi(\omega,R) = \frac{4|d_{cv}|^2}{3V} \sum_n \left\{ \frac{|C_n(R)|^2}{E_n(R) - \hbar\omega - i\Gamma_n} + \frac{|C_n(R)|^2}{E_n(R) + \hbar\omega - i\Gamma_n} \right\},$$

(1.30)

where the sum runs over all the confined exciton states with energies E_n ($E_0 = 0$ denotes exciton vacuum), Γ_n is the homogeneous broadening owing to the finite lifetime of the exciton state, d_{cv} is the transition dipole moment matrix element between the valence and conduction bands of the underlying bulk material, V is the QD volume and $C_n = g_n \int \Psi_{ex}^{(n)}(r_e, r_h) dr$ with g_n and $\Psi_{ex}^{(n)}(\mathbf{r}_e, \mathbf{r}_h)$ denoting the degeneracy factor and the wavefunction of the corresponding exciton states with $\mathbf{r}_e$ and $\mathbf{r}_h$ being the electron and hole radius-vectors. In the first approximation, the latter is just a product of the envelope functions of the confined electron and hole. The imaginary part of the two terms in (1.29) describes the absorption and emission, respectively.

In the last process shown in Figure 1.13, Auger recombination [117] occurs when the exciton energy is transfer to a third charge carrier, which is excited to a higher energy state, a process well-known in poly-electronic atoms. In a crystal, the third particle can be a CB electron or a VB hole. Afterward, this third carrier usually dissipates its excess energy into heat by gradually losing its energy to phonons. Auger recombination is important in strong excitation regimes.

1.6.2. Energy and charge transfer processes

So far, we have only considered an isolated exciton state. However, in real systems, for instance, in an ensemble of nanocrystals, an exciton (and also a lone carrier) can jump to another, spatially separated state belonging to the same or a distinct material or nanostructure, for instance, a neighboring QD. Such a transfer can occur by several mechanisms, which are depicted in Figure 1.14: (i) charge transfer (CT) via electron hopping (ii) Dexter energy transfer (DET) [118], (iii) radiative energy transfer (RET); and (iv) non-radiative Förster's resonance energy transfer (FRET) [119].
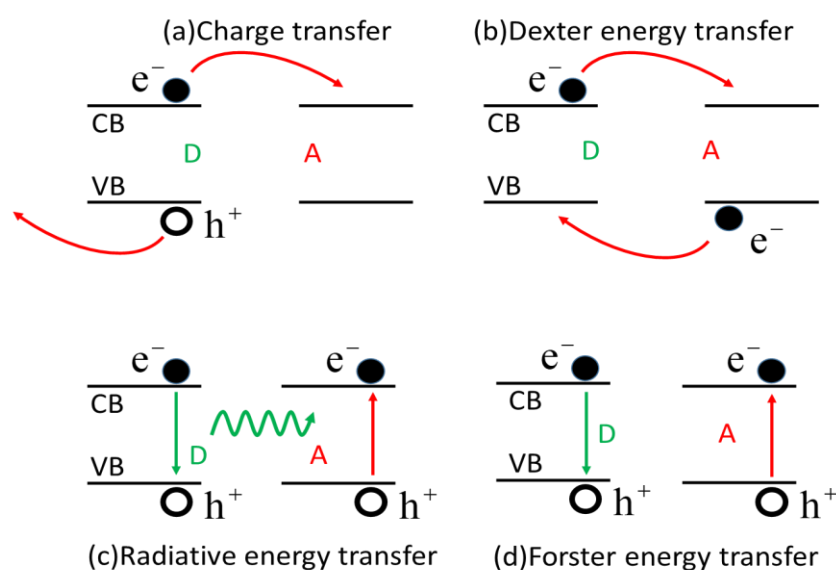
Figure 1.14 Possible energy transfer mechanisms in a system of two QDs. (a) Charge transfer; (b) Dexter energy transfer; (c) Radiative energy transfer; (d) FRET process.

The CT mechanism involves the separation of the exciton into an electron and a hole in the "donor" site and subsequent extraction of at least one of the charge carriers by the other nanostructure, the "acceptor". The transfer occurs via the quantum-mechanical tunneling and the probability decreases exponentially with the donor-acceptor distance.

The DET process occurs as an exchange of two electrons between an excited donor and an acceptor in the ground state, Figure 1.14(b). Effectively, the whole exciton disappears and no net charge is transferred. For this to happen, there must be a suitable wavefunction overlap between the donor and acceptor, as in the case of lone carrier tunneling (CT). Typically, it requires that the separation between the nanostructures be less than 1nm.

The mechanisms (iii) and (iv) are two limiting cases of the same process based on the electromagnetic interaction between two transient dipoles corresponding to the excitonic transitions in the donor and acceptor QDs (or molecules, as originally proposed by Förster [119]). In a simplified way, it can be viewed as exciton recombination in the donor QD by the emission of a photon, with the acceptor subsequently absorbing this photon, Figure 1.14(c). For this, there must be a resonance between the involved states in the donor and acceptor QDs. The difference between RET and FRET is just the distance between the two particles involved, the acceptor is located in either far-field (for RET) or near-field (for FRET) zone of the dipole emission of the donor so that the photon is not actually emitted in the latter case as the donor-acceptor distance is much smaller than the characteristic wavelength of the involved electromagnetic radiation, $\lambda = 2\pi\hbar c / E_{ex}$, where E_{ex} is the exciton energy. A unified theory of RET/FRET, based on the Quantum Electrodynamics of the dipole-dipole interaction, has been developed.[120] In the limiting case of FRET, the transfer rate (i.e. the transition probability per unit time) is given by Fermi's golden rule:

$$W_{D \to A}^{FRET} = \frac{2\pi}{\hbar} \left\langle \sum_f \left| \left\langle f \left| V_{dd} \right| i \right\rangle \right|^2 \rho(E_f, E_i) \right\rangle_i \quad , \qquad (1.31)$$

where

$$V_{dd}(\vec{r}) = \frac{e^2}{4\pi\varepsilon_0 \bar{\varepsilon} r^3} (\vec{d}_D \cdot \vec{d}_A - 3(\vec{d}_D \cdot \vec{e}_r)(\vec{d}_A \cdot \vec{e}_r)) \ , \qquad (1.32)$$

is the interaction potential between the donor and acceptor transition dipoles, $\vec{d}_D$ and $\vec{d}_A$, in a homogeneous medium with the dielectric constant $\bar{\varepsilon}$, the indices i and f indicate the initial and final exciton states (with the sum over the final states and a thermodynamic average over the initial ones), and the Lorentzian function

$$\rho(E_f, E_i) = \frac{\gamma}{\pi \left[(E_f - E_i)^2 + \gamma^2 \right]} \quad , \qquad (1.33)$$

describes the resonance between the initial and final states, broadened due to a variety of natural reasons. As can be seen from (1.30), the transition rate is inversely proportional to the sixth power of the donor-acceptor distance, so it is commonly written in the form

$$W_{D \to A}^{FRET} = W_0 \left(\frac{R_0}{r} \right)^6 ,$$
(1.34)

where W_0=const and R_0 is a parameter with the dimension of length, called the Förster radius, which depends on the superposition of the absorption and emission spectra of the donor and acceptor. Typically, it is of the order of a few nanometers. The FRET mechanism is effective only if the acceptor is located within a distance of the order of R_0 from the donor.

FRET, as a mechanism of dipole-dipole near field interaction between two exciton states, one occupied and the other empty, can be generalized to other systems, for instance, a QD located in the vicinity of a 2D material. It depends on the dimensions of the two components, which affects the rates scaling with distance, and the electronic properties of the acceptor system. We shall return to this point in Chapter 5.

1.7. References

[1]   S. Shabahang, S. Kim, and S.-H. Yun, "Light-Guiding Biomaterials for Biomedical Applications," *Adv Funct Mater*, vol. 28, no. 24, Jun. 2018, doi: 10.1002/adfm.201706635.

[2]   M. Bernardi, C. Ataca, M. Palummo, and J. C. Grossman, "Optical and Electronic Properties of Two-Dimensional Layered Materials," *Nanophotonics*, vol. 6, no. 2, Jan. 2017, doi: 10.1515/nanoph-2015-0030.

[3]   L. D. Landau, E. M. Lifšic, J. B. Sykes, and J. S. Bell, *Electrodynamics of continuous media*. Oxford : Pergamon, 1960.

[4]   William. Hayes and Rodney. Loudon, *Scattering of light by crystals*. New York: John Wiley and Sons, 1978.

[5]   P. Yu and M. Cardona, *Fundamentals of Semiconductors: Physics and Materials Properties*, 4th ed. Berlin Heidelberg: Springer-Verlag, 2010.

[6]   C. F. Klingshirn, *Semiconductor optics*. Berlin: Springer, 1995.

[7]   M. Born and E. Wolf, *Principles of optics : electromagnetic theory of propagation, interference, and diffraction of light*. London ; Pergamon Press, 1959.

[8]   C. V. Raman, "A new radiation [Reproduced from Indian J. Phys., 1928, 2, 387–398]," *Current Science*, vol. 74, no. 4, pp. 382–386, 1998.

[9]   D. A. Long, *Raman spectroscopy*. New York (N.Y.) : McGraw-Hill, 1977.

[10]   G. P. Agrawal, *Nonlinear fiber optics*, Fifth edition. Amsterdam: Elsevier/Academic Press, 2013.

[11]   R. W. Boyd, *Nonlinear Optics, Third Edition*, 3rd ed. Orlando, FL, USA: Academic Press, Inc., 2008.

[12]   P. N. Butcher and D. Cotter, *The Elements of Nonlinear Optics*. Cambridge: Cambridge University Press, 1990.

[13]   R. W. Munn and C. N. Ironside, *Principles & applications of nonlinear optical materials*. London; Glasgow; New York: Blackie, 1993.

[14]   A. Smekal, "Zur Quantentheorie der Dispersion," *Naturwissenschaften*, vol. 11, no. 43, pp. 873–875, Oct. 1923, doi: 10.1007/BF01576902.

[15] Y. Y. Wang *et al.*, "Raman Studies of Monolayer Graphene: The Substrate Effect," *J. Phys. Chem. C*, vol. 112, no. 29, pp. 10637–10640, Jul. 2008, doi: 10.1021/jp8008404.

[16] Y. Zhao *et al.*, "Interlayer Breathing and Shear Modes in Few-Trilayer MoS2 and WSe2," *Nano Lett.*, vol. 13, no. 3, pp. 1007–1015, Mar. 2013, doi: 10.1021/nl304169w.

[17] D. A. Chenet *et al.*, "In-Plane Anisotropy in Mono- and Few-Layer ReS2 Probed by Raman Spectroscopy and Scanning Transmission Electron Microscopy," *Nano Lett.*, vol. 15, no. 9, pp. 5667–5672, Sep. 2015, doi: 10.1021/acs.nanolett.5b00910.

[18] A. Das *et al.*, "Monitoring dopants by Raman scattering in an electrochemically top-gated graphene transistor," *Nature Nanotechnology*, vol. 3, no. 4, pp. 210–215, Apr. 2008, doi: 10.1038/nnano.2008.67.

[19] A. C. Ferrari, "Raman spectroscopy of graphene and graphite: Disorder, electron–phonon coupling, doping and nonadiabatic effects," *Solid State Communications*, vol. 143, no. 1, pp. 47–57, Jul. 2007, doi: 10.1016/j.ssc.2007.03.052.

[20] J.-U. Lee, D. Yoon, H. Kim, S. W. Lee, and H. Cheong, "Thermal conductivity of suspended pristine graphene measured by Raman spectroscopy," *Phys. Rev. B*, vol. 83, no. 8, p. 081419, Feb. 2011, doi: 10.1103/PhysRevB.83.081419.

[21] C. Rice *et al.*, "Raman-scattering measurements and first-principles calculations of strain-induced phonon shifts in monolayer MoS2," *Phys. Rev. B*, vol. 87, no. 8, p. 081307, Feb. 2013, doi: 10.1103/PhysRevB.87.081307.

[22] Karlheinz. Seeger, *Semiconductor physics : an introduction*. Berlin; London: Springer, 2011.

[23] William. Hayes and Rodney. Loudon, *Scattering of light by crystals*. New York: John Wiley and Sons, 1978.

[24] A. G. Rolo and M. I. Vasilevskiy, "Raman spectroscopy of optical phonons confined in semiconductor quantum dots and nanocrystals," *Journal of Raman Spectroscopy*, vol. 38, no. 6, pp. 618–633, Jun. 2007, doi: 10.1002/jrs.1746.

[25] H. Farhat *et al.*, "Observation of Electronic Raman Scattering in Metallic Carbon Nanotubes," *Phys. Rev. Lett.*, vol. 107, no. 15, p. 157401, Oct. 2011, doi: 10.1103/PhysRevLett.107.157401.

[26] T. Kozawa *et al.*, "Raman scattering from LO phonon-plasmon coupled modes in gallium nitride," *Journal of Applied Physics*, vol. 75, no. 2, pp. 1098–1101, Jan. 1994, doi: 10.1063/1.356492.

[27] P. A. Franken, A. E. Hill, C. W. Peters, and G. Weinreich, "Generation of Optical Harmonics," *Phys. Rev. Lett.*, vol. 7, no. 4, pp. 118–119, Aug. 1961, doi: 10.1103/PhysRevLett.7.118.

[28] T. H. Maiman, "Stimulated Optical Radiation in Ruby," *Nature*, vol. 187, no. 4736, pp. 493–494, Aug. 1960, doi: 10.1038/187493a0.

[29] C. H. Lee, R. K. Chang, and N. Bloembergen, "Nonlinear Electroreflectance in Silicon and Silver," *Phys. Rev. Lett.*, vol. 18, no. 5, pp. 167–170, Jan. 1967, doi: 10.1103/PhysRevLett.18.167.

[30] F. Brown, R. E. Parks, and A. M. Sleeper, "Nonlinear Optical Reflection from a Metallic Boundary," *Phys. Rev. Lett.*, vol. 14, no. 25, pp. 1029–1031, Jun. 1965, doi: 10.1103/PhysRevLett.14.1029.

[31] G. Lüpke, "Characterization of semiconductor interfaces by second-harmonic generation," *Surface Science Reports*, vol. 35, no. 3, pp. 75–161, Nov. 1999, doi: 10.1016/S0167-5729(99)00007-2.

[32] Y. R. Shen, "Surface properties probed by second-harmonic and sum-frequency generation," *Nature*, vol. 337, no. 6207, pp. 519–525, Feb. 1989, doi: 10.1038/337519a0.

[33] R. M. Corn and D. A. Higgins, "Optical second harmonic generation as a probe of surface chemistry," *Chem. Rev.*, vol. 94, no. 1, pp. 107–125, Jan. 1994, doi: 10.1021/cr00025a004.

[34] J. E. Zimmermann, G. Mette, and U. Höfer, "Second-harmonic imaging microscopy for time-resolved investigations on transition metal dichalcogenides," *arXiv:1608.03434 [cond-mat]*, Sep. 2016, Accessed: Nov. 13, 2019. [Online]. Available: http://arxiv.org/abs/1608.03434.

[35] T. Schneider, "Self- and Cross-Phase Modulation," in *Nonlinear Optics in Telecommunications*, Berlin, Heidelberg: Springer Berlin Heidelberg, 2004, pp. 143–165.

[36] K. S. Mathur, *Fundamentals of fiber optics communications -.* ZORBA Books, 2018.

[37] R. Gangwar, S. P. Singh, and N. Singh, "Soliton Based Optical Communication," *Progress In Electromagnetics Research*, vol. 74, pp. 157–166, 2007, doi: 10.2528/PIER07050401.

[38] Ö. Boyraz, P. Koonath, V. Raghunathan, and B. Jalali, "All optical switching and continuum generation in silicon waveguides," *Opt. Express, OE*, vol. 12, no. 17, pp. 4094–4102, Aug. 2004, doi: 10.1364/OPEX.12.004094.

[39] M. D. Perry, T. Ditmire, and B. C. Stuart, "Self-phase modulation in chirped-pulse amplification," *Opt. Lett., OL*, vol. 19, no. 24, pp. 2149–2151, Dec. 1994, doi: 10.1364/OL.19.002149.

[40] R. G. M. P. Koumans and R. Van Roijen, "Theory for passive mode-locking in semiconductor laser structures including the effects of self-phase modulation, dispersion, and pulse collisions," *IEEE Journal of Quantum Electronics*, vol. 32, no. 3, pp. 478–492, Mar. 1996, doi: 10.1109/3.485400.

[41] K. Okamoto, *Fundamentals of Optical Waveguides.* 2011.

[42] G. P. Agrawal, P. L. Baldeck, and R. R. Alfano, "Optical wave breaking and pulse compression due to cross-phase modulation in optical fibers," *Opt. Lett., OL*, vol. 14, no. 2, pp. 137–139, Jan. 1989, doi: 10.1364/OL.14.000137.

[43] M. Hofer, M. E. Fermann, F. Haberl, M. H. Ober, and A. J. Schmidt, "Mode locking with cross-phase and self-phase modulation," *Opt. Lett., OL*, vol. 16, no. 7, pp. 502–504, Apr. 1991, doi: 10.1364/OL.16.000502.

[44] S. Larochelle, Y. Hibino, V. Mizrahi, and G. I. Stegeman, "All-optical switching of grating transmission using cross-phase modulation in optical fibres," *Electronics Letters*, vol. 26, no. 18, pp. 1459–1460, Aug. 1990, doi: 10.1049/el:19900936.

[45] M. A. Franco, H. R. Lange, J.-F. Ripoche, B. S. Prade, and A. Mysyrowicz, "Characterization of ultra-short pulses by cross-phase modulation," *Optics Communications*, vol. 140, no. 4, pp. 331–340, Aug. 1997, doi: 10.1016/S0030-4018(97)00201-0.

[46] M. D. Thomson, J. M. Dudley, L. P. Barry, and J. D. Harvey, "Complete pulse characterization at 1.5 µm by cross-phase modulation in optical fibers," *Opt. Lett., OL*, vol. 23, no. 20, pp. 1582–1584, Oct. 1998, doi: 10.1364/OL.23.001582.

[47] M. A. Reed *et al.*, "Spatial quantization in GaAs–AlGaAs multiple quantum dots," *Journal of Vacuum Science & Technology B: Microelectronics Processing and Phenomena*, vol. 4, no. 1, pp. 358–360, Jan. 1986, doi: 10.1116/1.583331.

[48] S. A. Empedocles, D. J. Norris, and M. G. Bawendi, "Photoluminescence Spectroscopy of Single CdSe Nanocrystallite Quantum Dots," *Phys. Rev. Lett.*, vol. 77, no. 18, pp. 3873–3876, Oct. 1996, doi: 10.1103/PhysRevLett.77.3873.

[49] M. Grundmann *et al.*, "Ultranarrow Luminescence Lines from Single Quantum Dots," *Phys. Rev. Lett.*, vol. 74, no. 20, pp. 4043–4046, May 1995, doi: 10.1103/PhysRevLett.74.4043.

[50] A. Rogach, Ed., *Semiconductor Nanocrystal Quantum Dots: Synthesis, Assembly, Spectroscopy and Applications*. Wien: Springer-Verlag, 2008.

[51] V. I. Klimov, *Nanocrystal quantum dots*. Boca Raton: CRC Press, 2010.

[52] M. Green, "Semiconductor quantum dots : organometallic and inorganic synthesis," 2014. http://site.ebrary.com/id/10928422.

[53] L. E. Brus, "Electron–electron and electron-hole interactions in small semiconductor crystallites: The size dependence of the lowest excited electronic state," *J. Chem. Phys.*, vol. 80, no. 9, pp. 4403–4409, May 1984, doi: 10.1063/1.447218.

[54] Yuriel Núñez Fernández, "Exciton States in Free-Standing and Embedded Semiconductor Nanocrystals," in *Fingerprints in the Optical and Transport Properties of Quantum Dots*, Mikhail I. Vasilevskiy, Ed. Rijeka: IntechOpen, 2012, p. Ch. 8.

[55] T. Stauber and M. I. Vasilevskiy, "Polaron relaxation in a quantum dot due to anharmonic coupling within a mean-field approach," *Phys. Rev. B*, vol. 79, no. 11, p. 113301, Mar. 2009, doi: 10.1103/PhysRevB.79.113301.

[56] Al. L. Efros, M. Rosen, M. Kuno, M. Nirmal, D. J. Norris, and M. Bawendi, "Band-edge exciton in quantum dots of semiconductors with a degenerate valence band: Dark and bright exciton states," *Phys. Rev. B*, vol. 54, no. 7, pp. 4843–4856, Aug. 1996, doi: 10.1103/PhysRevB.54.4843.

[57] "Quantum Dots in Bioanalysis: A Review of Applications across Various Platforms for Fluorescence Spectroscopy and Imaging - Eleonora Petryayeva, W. Russ Algar, Igor L. Medintz, 2013." https://journals.sagepub.com/doi/10.1366/12-06948 (accessed May 03, 2020).

[58] A. M. Fontes Garcia, M. S. Fernandes, and P. J. Coutinho, "CdSe/TiO2 core-shell nanoparticles produced in AOT reverse micelles: applications in pollutant photodegradation using visible light," *Nanoscale Res Lett*, vol. 6, no. 1, p. 426, 2011, doi: 10.1186/1556-276X-6-426.

[59] A. V. Antanovich *et al.*, "Colloidal synthesis and optical properties of type-II CdSe–CdTe and inverted CdTe–CdSe core–wing heteronanoplatelets," *Nanoscale*, vol. 7, no. 17, pp. 8084–8092, Apr. 2015, doi: 10.1039/C4NR07134D.

[60] S. J. Zelewski, K. C. Nawrot, A. Zak, M. Gladysiewicz, M. Nyk, and R. Kudrawiec, "Exciton Binding Energy of Two-Dimensional Highly Luminescent Colloidal Nanostructures Determined from Combined Optical and Photoacoustic Spectroscopies," *J. Phys. Chem. Lett.*, vol. 10, no. 12, pp. 3459–3464, Jun. 2019, doi: 10.1021/acs.jpclett.9b00591.

[61] S. Ithurria, M. D. Tessier, B. Mahler, R. P. S. M. Lobo, B. Dubertret, and A. L. Efros, "Colloidal nanoplatelets with two-dimensional electronic structure," *Nat Mater*, vol. 10, no. 12, pp. 936–941, Oct. 2011, doi: 10.1038/nmat3145.

[62] S. Ithurria, G. Bousquet, and B. Dubertret, "Continuous Transition from 3D to 1D Confinement Observed during the Formation of CdSe Nanoplatelets," *J. Am. Chem. Soc.*, vol. 133, no. 9, pp. 3070–3077, Mar. 2011, doi: 10.1021/ja110046d.

[63] M. Sharma *et al.*, "Near-Unity Emitting Copper-Doped Colloidal Semiconductor Quantum Wells for Luminescent Solar Concentrators," *Adv. Mater. Weinheim*, vol. 29, no. 30, Aug. 2017, doi: 10.1002/adma.201700821.

[64] S. Ithurria and B. Dubertret, "Quasi 2D Colloidal CdSe Platelets with Thicknesses Controlled at the Atomic Level," *J. Am. Chem. Soc.*, vol. 130, no. 49, pp. 16504–16505, Dec. 2008, doi: 10.1021/ja807724e.

[65] A. Yeltik, S. Delikanli, M. Olutas, Y. Kelestemur, B. Guzelturk, and H. V. Demir, "Experimental Determination of the Absorption Cross-Section and Molar Extinction Coefficient of Colloidal CdSe Nanoplatelets," *J. Phys. Chem. C*, vol. 119, no. 47, pp. 26768–26775, Nov. 2015, doi: 10.1021/acs.jpcc.5b09275.

[66] M. D. Tessier, C. Javaux, I. Maksimovic, V. Loriette, and B. Dubertret, "Spectroscopy of Single CdSe Nanoplatelets," *ACS Nano*, vol. 6, no. 8, pp. 6751–6758, Aug. 2012, doi: 10.1021/nn3014855.

[67] C. A. Leatherdale, W.-K. Woo, F. V. Mikulec, and M. G. Bawendi, "On the Absorption Cross Section of CdSe Nanocrystal Quantum Dots," *J. Phys. Chem. B*, vol. 106, no. 31, pp. 7619–7622, Aug. 2002, doi: 10.1021/jp025698c.

[68] M. Li *et al.*, "Ultralow-threshold multiphoton-pumped lasing from colloidal nanoplatelets in solution," *Nature Communications*, vol. 6, no. 1, p. 8513, Sep. 2015, doi: 10.1038/ncomms9513.

[69] B. Guzelturk *et al.*, "Stable and Low-Threshold Optical Gain in CdSe/CdS Quantum Dots: An All-Colloidal Frequency Up-Converted Laser," *Advanced Materials*, vol. 27, no. 17, pp. 2741–2746, 2015, doi: 10.1002/adma.201500418.

[70] L. T. Kunneman *et al.*, "Bimolecular Auger Recombination of Electron–Hole Pairs in Two-Dimensional CdSe and CdSe/CdZnS Core/Shell Nanoplatelets," *J. Phys. Chem. Lett.*, vol. 4, no. 21, pp. 3574–3578, Nov. 2013, doi: 10.1021/jz401970p.

[71] Z. Yang, M. Pelton, I. Fedin, D. V. Talapin, and E. Waks, "A room temperature continuous-wave nanolaser using colloidal quantum wells," *Nature Communications*, vol. 8, no. 1, p. 143, Jul. 2017, doi: 10.1038/s41467-017-00198-z.

[72] U. Giovanella *et al.*, "Efficient Solution-Processed Nanoplatelet-Based Light-Emitting Diodes with High Operational Stability in Air," *Nano Lett.*, vol. 18, no. 6, pp. 3441–3448, Jun. 2018, doi: 10.1021/acs.nanolett.8b00456.

[73] Z. Chen, B. Nadal, B. Mahler, H. Aubin, and B. Dubertret, "Quasi-2D Colloidal Semiconductor Nanoplatelets for Narrow Electroluminescence," *Advanced Functional Materials*, vol. 24, no. 3, pp. 295–302, 2014, doi: 10.1002/adfm.201301711.

[74] A. K. Geim and K. S. Novoselov, "The rise of graphene," *Nature Mater*, vol. 6, no. 3, pp. 183–191, Mar. 2007, doi: 10.1038/nmat1849.

[75] K. S. Novoselov, V. I. Fal'ko, L. Colombo, P. R. Gellert, M. G. Schwab, and K. Kim, "A roadmap for graphene," *Nature*, vol. 490, no. 7419, pp. 192–200, Oct. 2012, doi: 10.1038/nature11458.

[76] M. Aliofkhazraei, N. Ali, W. I. Milne, C. S. Ozkan, S. Mitura, and J. L. Gervasoni, *Graphene Science Handbook Electrical and Optical Properties*. 2016.

[77] N. M. R. Peres, "Graphene, new physics in two dimensions," *Europhysics News*, vol. 40, no. 3, pp. 17–20, May 2009, doi: 10.1051/epn/2009501.

[78] D. W. Brenner, O. A. Shenderova, J. A. Harrison, S. J. Stuart, B. Ni, and S. B. Sinnott, "A second-generation reactive empirical bond order (REBO) potential energy expression for hydrocarbons," *J. Phys.: Condens. Matter*, vol. 14, no. 4, pp. 783–802, Jan. 2002, doi: 10.1088/0953-8984/14/4/312.

[79] S. Reich, J. Maultzsch, C. Thomsen, and P. Ordejón, "Tight-binding description of graphene," *Phys. Rev. B*, vol. 66, no. 3, p. 035412, Jul. 2002, doi: 10.1103/PhysRevB.66.035412.

[80] Z. Q. Li *et al.*, "Dirac charge dynamics in graphene by infrared spectroscopy," *Nature Phys*, vol. 4, no. 7, pp. 532–535, Jul. 2008, doi: 10.1038/nphys989.

[81] Yu. V. Bludov, A. Ferreira, N. M. R. Peres, and M. I. Vasilevskiy, "A primer on surface plasmon-polaritons in graphene," *Int. J. Mod. Phys. B*, vol. 27, no. 10, p. 1341001, Apr. 2013, doi: 10.1142/S0217979213410014.

[82] P. A. D. Gonçalves and N. M. R. Peres, "An introduction to graphene plasmonics," 2016. http://public.ebookcentral.proquest.com/choice/publicfullrecord.aspx?p=4528867.

[83] S. A. Mikhailov and K. Ziegler, "Nonlinear electromagnetic response of graphene: frequency multiplication and the self-consistent-field effects," *J. Phys.: Condens. Matter*, vol. 20, no. 38, p. 384204, Aug. 2008, doi: 10.1088/0953-8984/20/38/384204.

[84] M. L. Nesterov, J. Bravo-Abad, A. Y. Nikitin, F. J. García-Vidal, and L. Martin-Moreno, "Graphene supports the propagation of subwavelength optical solitons," *Laser & Photonics Reviews*, vol. 7, no. 2, pp. L7–L11, 2013, doi: 10.1002/lpor.201200079.

[85] N. M. R. Peres, Yu. V. Bludov, J. E. Santos, A.-P. Jauho, and M. I. Vasilevskiy, "Optical bistability of graphene in the terahertz range," *Phys. Rev. B*, vol. 90, no. 12, p. 125425, Sep. 2014, doi: 10.1103/PhysRevB.90.125425.

[86] N. A. Savostianova and S. A. Mikhailov, "Optical Kerr effect in graphene: Theoretical analysis of the optical heterodyne detection technique," *Phys. Rev. B*, vol. 97, no. 16, p. 165424, Apr. 2018, doi: 10.1103/PhysRevB.97.165424.

[87]   E. Hendry, P. J. Hale, J. Moger, A. Savchenko, and S. A. Mikhailov, "Coherent nonlinear optical response of graphene.," *Physical review letters*, vol. 105, no. 9, p. 097401, 2010, doi: 10.1103/PhysRevLett.105.097401.

[88]   S.-Y. Hong, J. I. Dadap, N. Petrone, P.-C. Yeh, J. Hone, and R. M. Osgood, "Optical Third-Harmonic Generation in Graphene," *Phys. Rev. X*, vol. 3, no. 2, p. 021014, Jun. 2013, doi: 10.1103/PhysRevX.3.021014.

[89]   W. Choi, I. Lahiri, R. Seelaboyina, and Y. S. Kang, "Synthesis of Graphene and Its Applications: A Review," *Critical Reviews in Solid State and Materials Sciences*, vol. 35, no. 1, pp. 52–71, Feb. 2010, doi: 10.1080/10408430903505036.

[90]   K. S. Novoselov, "Nobel Lecture: Graphene: Materials in the Flatland," *Rev. Mod. Phys.*, vol. 83, no. 3, pp. 837–849, Aug. 2011, doi: 10.1103/RevModPhys.83.837.

[91]   A. Ciesielski and P. Samorì, "Graphene via sonication assisted liquid-phase exfoliation," *Chemical Society Reviews*, vol. 43, no. 1, pp. 381–398, 2014, doi: 10.1039/C3CS60217F.

[92]   M. Matsumoto, Y. Saito, C. Park, T. Fukushima, and T. Aida, "Ultrahigh-throughput exfoliation of graphite into pristine 'single-layer' graphene using microwaves and molecularly engineered ionic liquids," *Nature Chem*, vol. 7, no. 9, pp. 730–736, Sep. 2015, doi: 10.1038/nchem.2315.

[93]   H. Huang, S. Chen, A. T. S. Wee, and W. Chen, "1 - Epitaxial growth of graphene on silicon carbide (SiC)," in *Graphene*, V. Skákalová and A. B. Kaiser, Eds. Woodhead Publishing, 2014, pp. 3–26.

[94]   O. Frank and M. Kalbac, "2 - Chemical vapor deposition (CVD) growth of graphene films," in *Graphene*, V. Skákalová and A. B. Kaiser, Eds. Woodhead Publishing, 2014, pp. 27–49.

[95]   H. Terrones, R. Lv, M. Terrones, and M. S. Dresselhaus, "The role of defects and doping in 2D graphene sheets and 1D nanoribbons," *Rep. Prog. Phys.*, vol. 75, no. 6, p. 062501, May 2012, doi: 10.1088/0034-4885/75/6/062501.

[96]   S. Manzeli, D. Ovchinnikov, D. Pasquier, O. V. Yazyev, and A. Kis, "2D transition metal dichalcogenides," *Nature Reviews Materials*, vol. 2, no. 8, p. 17033, Jun. 2017, doi: 10.1038/natrevmats.2017.33.

[97]   Q. H. Wang, K. Kalantar-Zadeh, A. Kis, J. N. Coleman, and M. S. Strano, "Electronics and optoelectronics of two-dimensional transition metal dichalcogenides," *Nature Nanotech*, vol. 7, no. 11, pp. 699–712, Nov. 2012, doi: 10.1038/nnano.2012.193.

[98]   K. P. Loh, H. Zhang, W. Z. Chen, and W. Ji, "Templated Deposition of MoS2 Nanotubules Using Single Source Precursor and Studies of Their Optical Limiting Properties," *J. Phys. Chem. B*, vol. 110, no. 3, pp. 1235–1239, Jan. 2006, doi: 10.1021/jp055959t.

[99]   "Ultrafast Saturable Absorption of Two-Dimensional MoS2 Nanosheets | ACS Nano." https://pubs.acs.org/doi/abs/10.1021/nn403886t (accessed May 04, 2020).

[100]   "Giant two-photon absorption in monolayer MoS2 - Li - 2015 - Laser & Photonics Reviews - Wiley Online Library." https://onlinelibrary.wiley.com/doi/abs/10.1002/lpor.201500052 (accessed May 04, 2020).

[101]   S. Zhang *et al.*, "Direct Observation of Degenerate Two-Photon Absorption and Its Saturation in WS2 and MoS2 Monolayer and Few-Layer Films," *ACS Nano*, vol. 9, no. 7, pp. 7142–7150, Jul. 2015, doi: 10.1021/acsnano.5b03480.

[102]   N. Kumar *et al.*, "Second harmonic microscopy of monolayer MoS$\{\}_{2}\$," *Phys. Rev. B*, vol. 87, no. 16, p. 161403, Apr. 2013, doi: 10.1103/PhysRevB.87.161403.

[103]   R. Wang, H.-C. Chien, J. Kumar, N. Kumar, H.-Y. Chiu, and H. Zhao, "Third-Harmonic Generation in Ultrathin Films of MoS2," *ACS Appl. Mater. Interfaces*, vol. 6, no. 1, pp. 314–318, Jan. 2014, doi: 10.1021/am4042542.

[104]   A. V. T. Kolobov Junji., *Two-dimensional transition-metal dichalcogenides.* [Place of publication not identified]: SPRINGER, 2018.

[105] G. Wang *et al.*, "Colloquium: Excitons in atomically thin transition metal dichalcogenides," *Rev. Mod. Phys.*, vol. 90, no. 2, p. 021001, Apr. 2018, doi: 10.1103/RevModPhys.90.021001.

[106] K. F. Mak, K. He, J. Shan, and T. F. Heinz, "Control of valley polarization in monolayer MoS 2 by optical helicity," *Nature Nanotech*, vol. 7, no. 8, pp. 494–498, Aug. 2012, doi: 10.1038/nnano.2012.96.

[107] M. Amani *et al.*, "Near-unity photoluminescence quantum yield in MoS2," *Science*, vol. 350, no. 6264, pp. 1065–1068, Nov. 2015, doi: 10.1126/science.aad2114.

[108] J. N. S. Gomes, C. Trallero-Giner, N. M. R. Peres, and M. I. Vasilevskiy, "Exciton–polaritons of a 2D semiconductor layer in a cylindrical microcavity," *Journal of Applied Physics*, vol. 127, no. 13, p. 133101, Apr. 2020, doi: 10.1063/1.5143244.

[109] N. Huo and G. Konstantatos, "Ultrasensitive all-2D MoS 2 phototransistors enabled by an out-of-plane MoS 2 PN homojunction," *Nature Communications*, vol. 8, no. 1, p. 572, Sep. 2017, doi: 10.1038/s41467-017-00722-1.

[110] Y.-H. Lee *et al.*, "Synthesis of Large-Area MoS2 Atomic Layers with Chemical Vapor Deposition," *Advanced Materials*, vol. 24, no. 17, pp. 2320–2325, 2012, doi: 10.1002/adma.201104798.

[111] P. Kumar. Basu, *Theory of optical processes in semiconductors : bulk and microstructures*. Oxford: Clarendon Press, 2005.

[112] C. F. Klingshirn, *Semiconductor Optics*, 3rd ed. Berlin Heidelberg: Springer-Verlag, 2007.

[113] W. Shockley and W. T. Read, "Statistics of the Recombinations of Holes and Electrons," *Phys. Rev.*, vol. 87, no. 5, pp. 835–842, Sep. 1952, doi: 10.1103/PhysRev.87.835.

[114] R. N. Hall, "Electron-Hole Recombination in Germanium," *Phys. Rev.*, vol. 87, no. 2, pp. 387–387, Jul. 1952, doi: 10.1103/PhysRev.87.387.

[115] V. S. Vavilov, "Effects of Radiation on Semiconductors.," 2013. https://public.ebookcentral.proquest.com/choice/publicfullrecord.aspx?p=5587468.

[116] John. Donegan and Yury. Rakovich, *Cadmium Telluride Quantum Dots Advances and Applications*. Singapore: Pan Stanford Publishing, 2016.

[117] A. Haug, "Band-to-band Auger recombination in semiconductors," *Journal of Physics and Chemistry of Solids*, vol. 49, no. 6, pp. 599–605, Jan. 1988, doi: 10.1016/0022-3697(88)90190-4.

[118] D. L. Dexter, "A Theory of Sensitized Luminescence in Solids," *J. Chem. Phys.*, vol. 21, no. 5, pp. 836–850, May 1953, doi: 10.1063/1.1699044.

[119] Th. Förster, "Transfer Mechanisms of Electronic Excitation Energy," *Radiation Research Supplement*, vol. 2, pp. 326–339, 1960, doi: 10.2307/3583604.

[120] G. D. Scholes and D. L. Andrews, "Resonance energy transfer and quantum dots," *Phys. Rev. B*, vol. 72, no. 12, p. 125331, Sep. 2005, doi: 10.1103/PhysRevB.72.125331.

PART I

CHAPTER 2

EXPERIMENTAL METHODS

Contents

2.1. Introduction

The physical sciences are essentially experimental and to explore any given problem, a good experimental design is needed with a set of techniques that can support the underlying objectives. The use of the absorption and emission of electromagnetic radiation by matter has long been used as a stepping stone for several approaches to probe the internal structure and properties of matter.[1–3] A key experimental tool for these spectroscopic studies has been the development of short pulse, tunable lasers [4,5] which has led to the development of a powerful set of techniques [6] for probing and characterizing electronic and structural properties of materials. By using flexible and tunable light sources we can have a wide spectral selectivity as well as cover a wide range of temporal scales. This ability allows researchers to characterize in detail dynamic photo physical material processes from the microsecond to the femtosecond scale.

An overview of the systems and experimental methods used in this thesis work are presented in this chapter, together with a general description of the accompanying instrument control software that was developed.

However, having a shiny laser and a full set of experimental methods without anything to explore is not very productive. So to avoid this situation, several systems were produced. In the last part of this chapter, the procedures employed to obtain the samples used in this work are described in detail.

2.2.   Light Sources

2.2.1.   Laser System Oscillator

A laser amplifies light through the process of stimulated emission. Usually, laser systems have an oscillator constituted by a pair of mirrors enclosing the desired gain medium pumped to obtain a high population inversion for the stimulated emission, creating a laser cavity. One of the mirrors, the output coupler, will have a finite transmission to allow for the extraction of the light circulating in the laser cavity. Energy is needed for the process and is injected into the gain medium using a pump. In the first step, there's a production of spontaneous emission photons in the system, which then will be reflected back into the gain medium by the laser cavity mirrors. These photons will then lead to stimulated emission, which produces more coherent photons,

and then the process will repeat going around the cavity and the gain medium resulting in a powerful and stable coherent beam. In a continuous wave laser, a small fraction of this beam is allowed to exit through the output coupler and, in the steady-state, the overall laser cavity losses are balanced by the gain due to stimulated emission.[7]

The base laser system used in our laboratory is a femtosecond Ti:Sapphire, Coherent Mira 900-f, laser oscillator pumped by a frequency-doubled CW Neodymium-laser, Coherent Verdi 5W, which generated femtosecond pulses from 700 nm to 1000 nm as needed. This femtosecond oscillator in normal operating conditions produces 10nJ pulses with a duration of approximately 100fs and a bandwidth of 12nm at a constant repetition rate of 76 MHz.

These short pulses were generated by a process called Kerr lens mode-locking [8], to force the different cavity modes to oscillate in phase with each other. This causes the modes to interfere constructively to form a single and intense short pulse at a repetition rate equal to the round trip time of the oscillator laser cavity. The greater the number of modes oscillating together at a fixed phase, the shorter the pulse duration.[9]

While the cavity can in principle support an extremely large number of modes, the modes that can be amplified will depend on the spectral profile of the gain medium used and the ability to control the dispersion of the cavity modes that oscillate at slightly different frequencies. This number can range from only 2 to 3 modes for a He:Ne laser, up to tens of thousands for a titanium doped sapphire ($Ti_3{}^+:Al_2O_3$) laser system with pulse durations of order 10 fs.

To synchronize the phase of the circulating laser modes some sort of modulation is introduced into the cavity. Active mode-locking based on periodic losses introduced via an active electro-optic device such as a Pockels cell or an acousto-optic modulator can be used to produce pulses with durations in the range of nanoseconds down to tens of picoseconds, but not shorter due to the finite electronic responses of the driving circuity. Passive mode-locking techniques rely on an intrinsic modulation of the optical properties of a component of the laser cavity. Two main techniques are used, that of saturable absorption where the transmission of an element quickly switches from low to high when intense incident light saturates the transition and Kerr lens mode-locking in which intense light alters the local refractive index. The Mira oscillator as seen in Figure 2.1 [10] uses Kerr lens mode-locking in the gain medium. Basically, when a sufficiently intense light beam passes through the gain medium, the third-order susceptibility provokes a temporary increase in the medium's refractive index proportional to the incident light's intensity. Since the beam has a higher intensity on-axis this provokes a positive lens that focuses the beam

downstream. By placing a narrow aperture at the point where the Kerr lens makes the beam the smallest, intense pulses will experience lower losses and be favored over the lower intensity continuous wave oscillation. This leads to an intense pulse train with a repetition rate of c/2L, 2L being the round trip cavity length.[11]

To initiate this process an initial perturbation is required which is usually achieved by vibrating one of the cavity optics. This perturbation will provoke a random increase in the light circulating in the cavity initiating the Kerr lens self-focusing mechanism. An intra-cavity Brewster prism pair is used to compensate for the positive dispersion induced by the gain medium and the birefringent tuner. In the end, we obtain pulses with a full-width half-maximum (FWHM) duration of approximately 100fs coupled out at a high repetition rate of 76 MHz
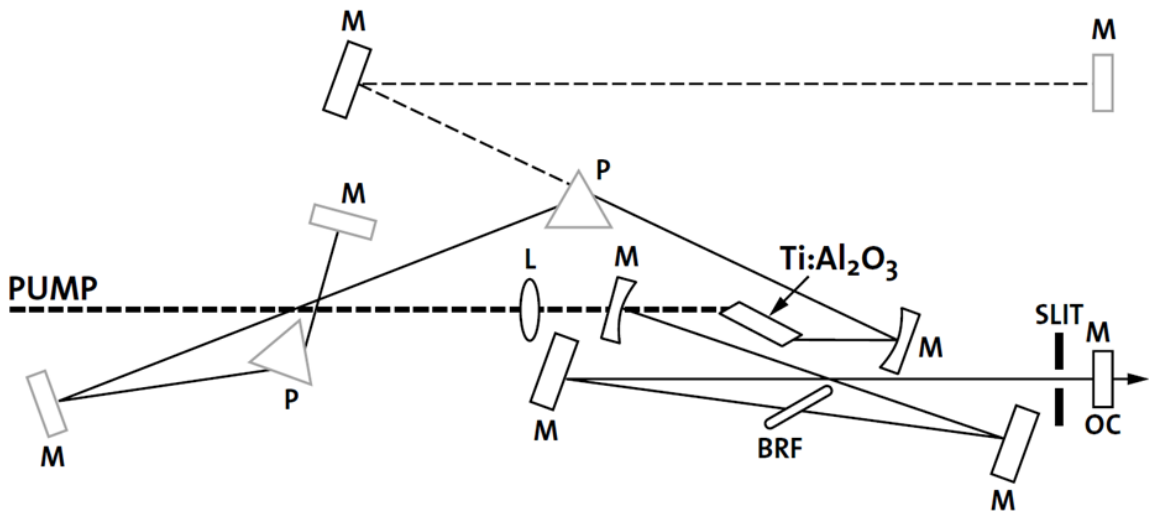
Figure 2.1 Schematic of the Oscillator Laser. L-Focusing lens; M- Mirror; P- Brewster prism; Ti:Al$_2$O$_3$- Ti:Sapphire Crystal; OC- Output coupler; BRF- Birefringent plate.[10]

2.2.2. Second and third harmonic generation

Second (2HG) and third harmonic generation (3HG) are two of the most straightforward and frequently used nonlinear optical processes to obtain laser pulses at shorter wavelengths.

Our oscillator laser being a Ti:Sapphire system is tunable, from 700 nm to around 1000 nm which also gives a small degree of tunability in 2HG pulses or even in 3HG pulses if needed using nonlinear crystals. The second harmonic pulses of the Mira beam were generated in a Type I

lithium triborate (LBO) crystal with 2.5mm of thickness cut so the optical axis makes an angle of θ =31.2 to the normal. Typically only a part of the oscillator pulse is selected to be doubled, either by using a beam splitter or a pulse picker to reduce the repetition rate. LBO was selected because of its high damage threshold and a 20% conversion efficiency.[12]

For generating the third harmonic, a collinear geometry setup is used. The 2HG pulse is mixed with the remaining fundamental pulse beam in a third harmonic beta barium borate (BBO) crystal also Type I with 2.5mm of thickness and θ =44°.

$$\omega + \omega = 2\omega \ , \ \ \omega + 2\omega = 3\omega \ . \tag{2.1}$$

The produced 2HG pulse has a small delay in time and is orthogonally polarized to the fundamental beam pulse. Since we use a type I crystal to obtain the production of the nonlinear effect we use a dual wave plate to rotate only the polarization of the 2HG beam pulse by 90 degrees, so the fundamental beam and second harmonic beams have the same polarization. Before rotating the polarization, a calcite crystal time-plate is used to compensate for the different group velocities of the two beams. This is possible due to the calcite crystal being a negative uniaxial material. This produces a delay to the ordinary beam relative to the extraordinary beam, with the delay being adjustable by tilting the crystal angle. The total conversion efficiency of the third harmonic generation is around 8% of the incident fundamental beam's power.

2.2.3. The Regenerative Amplifier

Amplification of ultrafast pulses without damage to the optics generally requires a significant reduction in peak pulse intensities to prevent optical damage and nonlinear effects during the process. This is accomplished by temporally broadening ultrafast pulses, stretching them, to the hundreds of picoseconds range before the amplification process and subsequently narrowing the pulses, compressing them, back to the ultrafast timescale after amplification. To amplify the pulses emitted by the Mira oscillator we used a Legend system that employs a grating based stretcher and compressor. The amplification occurred in a Ti:Sapphire laser cavity which is pumped by a nanosecond Q-switched Nd:YLF laser Evo Model laser running at a 1 kHz repetition rate.

The amplification of a laser pulse is performed similarly to the way they are initially generated in the oscillator. The seed pulse, at 794 nm, is propagated through the gain medium with a high

population inversion and the stimulated emission will provoke an increase in the energy of the pulse. But there's a problem since very intense pulses will undergo self-focusing, and as we increase the energy of the pulse through the amplification, this focusing effect will increase, eventually to the point where we exceed the damage threshold of the amplifying crystal or other materials in the system, mirrors, etc.

To avoid this problem we use the method of chirped pulse amplification (CPA) which was first demonstrated by Strickland et al.[13] and is the key technology that has allowed researchers to push these systems towards ultra-high-energy fields. This method is based on the controllable dispersion that can be generated using a complementary set of grating pairs. The initial part uses this controllable dispersion to cause a strong frequency chirp. In a typical stretcher configuration, two gratings and a telescope are used to stretch the pulse from roughly 100fs to several hundreds of picoseconds with a proportionally lower peak intensity, Figure 2.2.
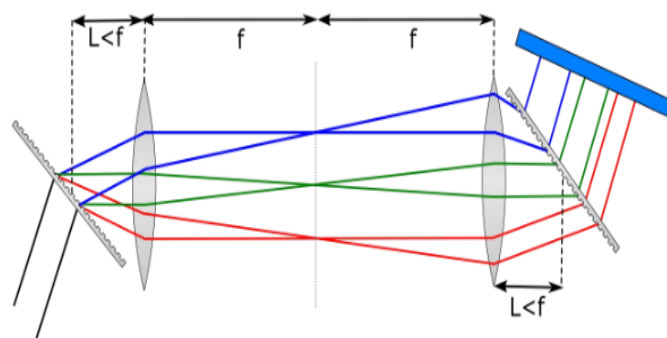
Figure 2.2 Schematic representation of a stretcher.

This stretched pulse is then sent to a Pockels cell, which selects one of the oscillator pulses to arrive close to the moment the gain is highest in the Ti:Sapphire amplifier. This chosen stretched pulse is then coupled into the regenerative cavity containing the amplifying medium and since it is stretched in time it can be significantly amplified in energy without reaching intensity levels at which nonlinear effects or damage become a problem. Typically 18 to 20 passes are needed to extract the maximum energy from the amplifier leading to pulses with an energy of roughly 4 mJ (having started with pule energies of approximately 5 nJ from the oscillator). A regenerative cavity is used instead of a multipass scheme where the passes through the amplifying medium are separated geometrically. This results in a better spatial profile and pointing stability of the beam, but does introduce extra dispersion due to the passage of the beam through the intra-cavity Pockels cells and quarter waveplate multiple times.

After the desired number of passes, the output pulse is switched out of the cavity using a second Pockels cell. This scheme allows one to adjust the number of passes as desired to ensure that the maximum gain is extracted. After the amplification, we obtain pulses with roughly 4mJ energy several hundreds of picoseconds in duration. In the final step, the pulse is sent to a compressor, Figure 2.3. This uses a reversed stretcher geometry to allow the compression of the pulse close to its original timescale. The main difference between the compressor and the stretcher is the existence of telescope added between the gratings in the stretcher to invert the sign of the dispersion from negative to positive. Typically we obtain pulses with a FWHM duration of around 110 fs.
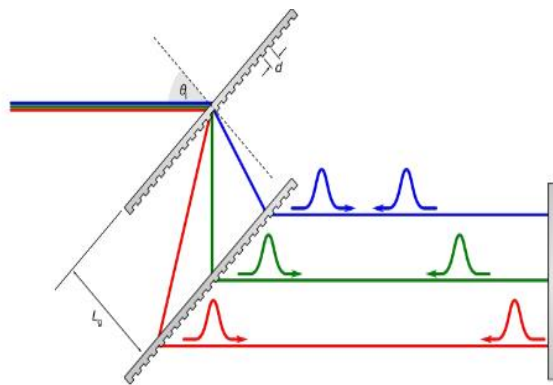
Figure 2.3 Schematic representation of a compressor.

2.2.4. Topas

An optical parametric amplifier (OPA) more exactly the Light Conversion TOPAS-C, was the option used to generate different wavelengths required for several experiments when we worked at a low repetition rate of 1 kHz. The 794 nm output from the regenerative amplifier laser system, was divided into two parts using a beam splitter, and one of them was used to pump the OPA. In the OPA, this high-intensity laser pulse is converted via a series of nonlinear interactions into a high-intensity optical field whose frequency and bandwidth can be controlled with phase matching and temporal delay schemes.

In the OPA the input beam is separated again in two separate beams in a ˜9:1 ratio using a beam sampler. The beam with 10% of energy is then divided again at a second beam splitter and part is used as a pre-pump and other to seed a super-continuum in a sapphire plate. This super-continuum is used to provide, a broadband seed, a range of frequencies that can be mixed with

the pre-pump pulse to produce a third pulse through parametric down-conversion. The seed, a super-continuum pulse is temporally stretched by chirping with a ZnSe crystal and spatially delayed relative to the remaining fundamental so the red wavelengths are preceded by the blue wavelengths and the duration of the pulse is several times that of the pre-pump duration. This temporal dispersion means that the pre-pump will only overlap with a small portion of the super-continuum seed, the "signal" when they are superposed in a nonlinear crystal. The consequence is that only specific frequency components will interact, allowing for tunable difference-frequency generation to create an "idler" and amplify the signal via parametric amplification. An LBO crystal, type II is used for the nonlinear medium angle tuned so the light waves of different frequencies undergo a nonlinear interaction in the nonlinear crystal,   generating a third wave to conserve energy and momentum, the so-called phase-matching condition.

$$\omega_{pump} = \omega_{signal} + \omega_{idler} \quad , \quad \vec{k}_{pump} = \vec{k}_{signal} + \vec{k}_{idler} \; . \qquad (2.2)$$

This allows one to amplify the "signal" exponentially as the beams pass through the crystal. By convention, the higher frequency light is called the signal and the lower frequency is called the idler, Figure 2.4.

A delay stage between the pre-pump and super-continuum controls the temporal overlap between the wavelengths and can be adjusted to select the wavelength of amplification. The phase-matching condition will vary depending on which portion of the bandwidth of the continuum is being amplified. As the crystal is birefringent, phase matching and optimization of the bandwidth can be achieved by rotating the nonlinear crystal. Since the nonlinear crystal is cut for a type II interaction, pre-pump and super-continuum must be orthogonally polarized and the nonlinear crystal's strong birefringence allows one to angle tune the respective refractive indices to achieve phase matching.
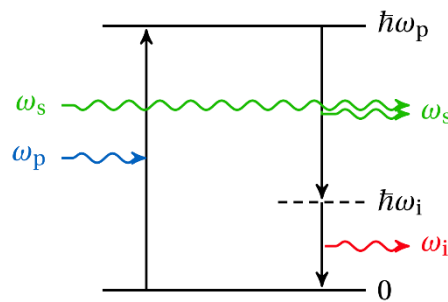
Figure 2.4 Stimulated emission of signal photons from a virtual level excited by the pump photons and creation of the idler.

Due to differences in the group index of refraction of the pre-pump and super-continuum wavelengths, the two pulses will experience temporal walk off as they go through the nonlinear crystal. This has the effect of limiting the effective length of the nonlinear crystal and consequently the amount of gain that can be attained in this first stage. To further amplify the signal beam or idler beam, a second stage of amplification is used, where again the optical parametric generation method is employed in a second nonlinear crystal, using the 90% of energy remaining in the original pump beam. The pulses again must be overlapped in space and time but here a collinear arrangement is used to reduce spatial chirp across the beam. This provides a better spatial profile for later stages in the system. To further expand the tunability of this system, external frequency mixers allow one to generate sum, difference, and harmonics of the pump and signal or idler beams to obtain a continuous coverage of the spectra from the ultraviolet to the near-infrared.

The idler can also be used to perform intra-pulse difference-frequency generation, to generate light in the Terahertz region of the spectrum. Theoretically, we can produce any wavelength between 230 nm and 20,000 nm, but practically we stop at 3000 nm. The experimentally obtained tuning curves are shown in Figure 2.5. The pulses generated bu the Topas-C have a minimal additional temporal broadening, around 5 % even when optimally compressed.
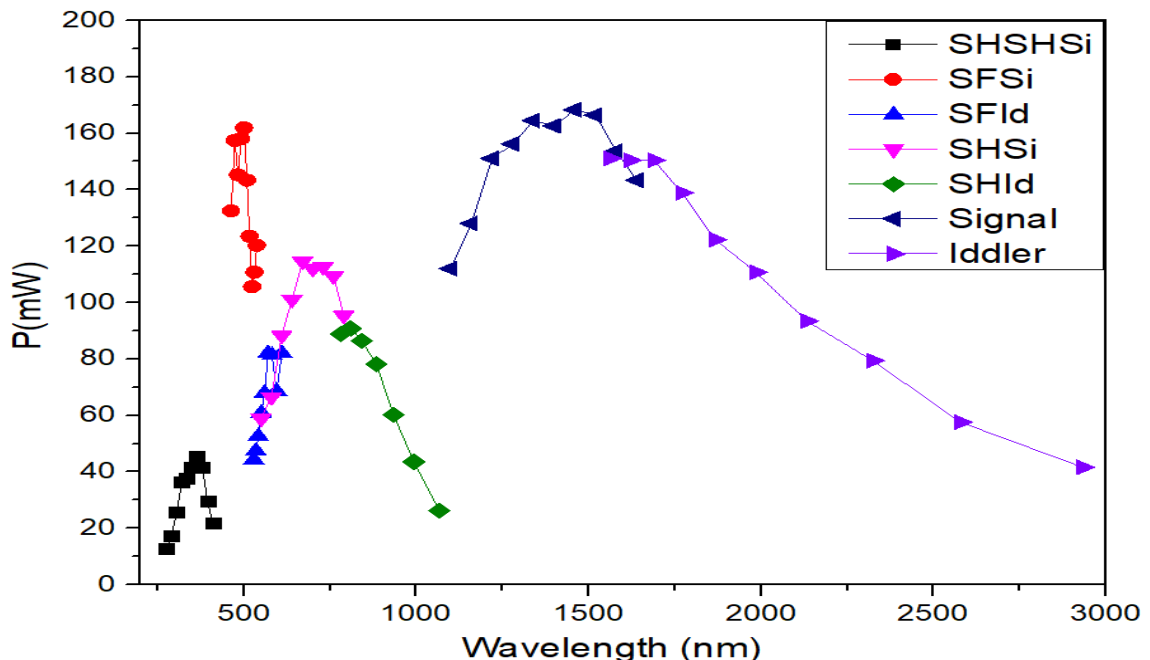
Figure 2.5 Obtained tuning curves for TOPAS-C pumped at 794nm.SHId- Frequency doubling Idler; SHSi- Frequency doubling Signal; SFId-Sum frequency generation when mixing pump and idler; SFId- Sum frequency generation when mixing pump and signal; SHSHSi- Frequency doubling of the SHSi.

2.2.5. White Light Continuum Generation -WLC

The generation of white-light continuum (WLC) pulses that are stable in both spatial and spectral domains was necessary for the transient absorption experiments. This light was used for probing, or to excite samples at a specific wavelength.

Depending on the experiment undertaken, we used WLC generated from the laser oscillator coupled to a photonic fiber at 76 MHz or some of the output of the regenerative amplifier at 1 kHz focused onto a sapphire plate. Typically, the most stable single-filament WLC pulses were generated when the spatial profile of the seed beam pulse was smoother and the temporal duration of the pulses was as short as possible.

For the high repetition rate system the pulses from the oscillator laser, with 12 nm FHWM around 794 nm, and a temporal duration of 100 femtoseconds were used at a repetition rate of 76 MHz. An average power of 60 mW (roughly 800pJ/pulse) of this beam was launched into a photonic crystal fiber (Thorlabs NL-PM-750, 1.6 μm mode diameter, with a zero-dispersion wavelength at 750 nm) through a 20 times microscope objective with a numerical aperture of 0.35.

These fibers are comprised of a solid glass high index core embedded in an air-filled cladding structure where several air holes are arranged in a hexagonal pattern that runs along the length of the fiber creating a hybrid air-silica material with a refractive index lower than the core. By controlling the ratio of the hole size and space between them, the dispersion properties of the fiber can be tailored. While the lowest possible zero-dispersion wavelength in conventional fused silica fibers is around 1300 nm and limited by the material dispersion, photonic crystal fibers can have zero-dispersion wavelength as low ~650 nm. This allows for pumping in the anomalous dispersion regime using light sources in the ~800 nm range such as our mode-locked Ti:Sapphire laser.

The fiber length used was of 90 cm for practical reasons, since this was found to be more than enough to obtain a wide spectrum stretching below 500nm. A three-dimensional fiber positioning stage is used to simplify this alignment procedure. Under these conditions, it was possible to obtain WLC generation ranging from 450 nm to almost 800nm, see Figure 2.6.
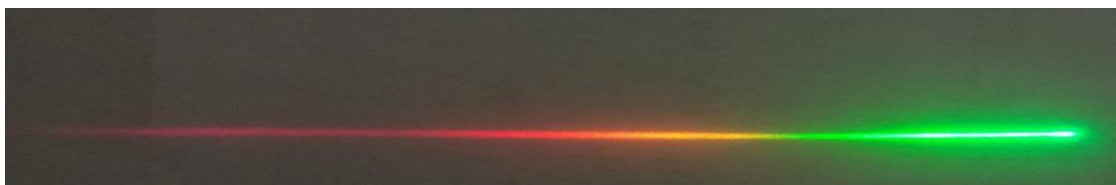
Figure 2.6 Dispersed white light continuum generated by the photonic crystal fiber.

For the low repetition rate system we have higher pulse energies and several transparent materials like sapphire, Al_2O_3, and calcium fluoride, CaF_2, show sufficient self-phase modulation as a third-order response to an intense light field allowing for WLC generation. The refractive index of the medium is changed by the high intensity of the beam pulse, the optical Kerr effect, and then, the instantaneous frequency is altered by self-phase modulation, leading to a spectrally broadened output pulse.

As the induced frequency change depends upon the nonlinear refractive index temporal variation, it is also dependent upon the pulse intensity variation in time. Accordingly, the frequency at the front of the pulse is red-shifted, stokes shifted, while the blue-shifted or anti-stokes shifted, travels at the back of the pulse. So, different wavelength components in the pulse arrive at different times at the sample. The effect of this chirp is that the relative delay between the pump pulses and the different wavelength components of the white light spectrum will vary depending on the amount of chirp induced.

Sapphire is well suited for producing a super-continuum since it has a high laser-induced damage threshold, is optically transparent from the UV to the near IR, and produces a continuum from around 400 nm to 1000 nm.

For obtaining the supercontinuum we used a 100 mm focal length lens to focus the beam into the sapphire plate to increase the power density and therefore going over the threshold for critical self-focusing to allow the super-continuum generation, Figure 2.7. The white light is then collected by a microscope objective, 10x, in a variable z-axis stage to collimate the beam and modify its coupling into the sample microscope if necessary.

The spatial profile and the power density of the WLC beam were controlled with an adjustable iris. The beam clipping provides a simple but effective spatially filtering which smoothed the WLC beam profile while also providing an additional adjustment of the beam power density and avoiding multiple filamentation.
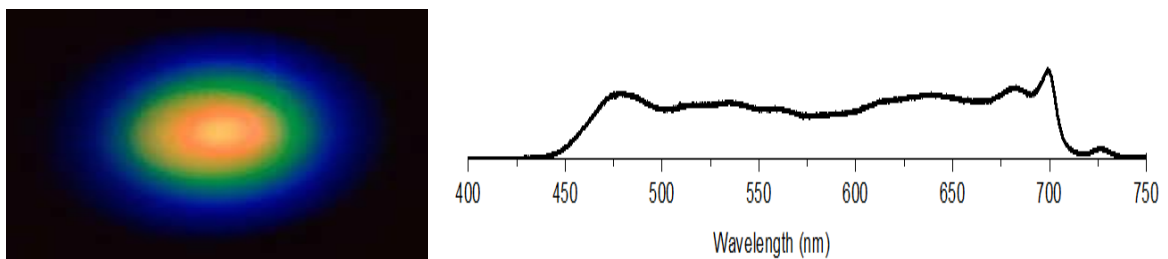
Figure 2.7 White light continuum generated by the sapphire plate, CCD image (left) and spectral data of our window of observation (right).

2.3.   Laser Beam characterization

Perhaps one of the simplest characterizations of a laser beam is to specify its average power. This can be determined using a power meter and knowing the repetition rate of the laser it is then trivial to calculate the average energy per pulse. For further evaluation, it is possible to obtain spatial beam profile measurements by simply focusing the beam onto a charge-coupled device to obtain both intensity profile information from the pixel value and the size of the focus from the number of CCD pixels illuminated while knowing the pixel dimensions. Before exposing the CCD camera, the laser beam will need to be attenuated by several orders of magnitude using for example a neutral density filter to avoid damaging the detector and care must be taken to avoid thermal effect provoked by excessive absorption in the filters. "Wincam" is one of the commercial solutions which include software that will automatically calculate parameters such as FWHM and $1/e^2$ profile sizes for the beam. The spectrum can be easily measured using a commercial spectrometer. So we can routinely obtain the average power, the transverse spatial profile, and the spatial FWHM.

Things start to get complicated when we want to characterize temporal characteristics on a picosecond or shorter scale since conventional detectors and electronics are typically limited to a bandwidth of at most 100s of GHz. The solution to this problem is to use the pulse itself to resolve its temporal behaviour. There are several approaches, but the most regularly used methods are the intensity and interferometric autocorrelation, frequency-resolved optical gating (FROG), and the spectral phase interferometry for direct electric-field reconstruction, (SPIDER). The intensity autocorrelation and FROG are the ones routinely used in our lab.

Intensity autocorrelation is the simplest way of measuring a laser pulse. It is obtained by splitting the pulse into two noncollinear beams using a beamsplitter and then overlapping them both spatially and temporally in a nonlinear crystal, in our case one that generates SHG. In essence, we gate the pulse with itself. Then we measure the average power of the second harmonic generated as a function of the path length difference between the two beams using a motorized delay stage placed in one arm to obtain the autocorrelation signal:

$$I_{ac}(\tau) = \int I(t) \times I(t+\tau)dt \qquad (2.3)$$

Where I(t) is the intensity of a pulse at time t and I(t +τ) is this pulse shifted by a time delay, τ between the two beams. The pulse duration is then found by multiplying the autocorrelation signal

width by a deconvolution factor that depends on the pulse shape that is assumed. For a Gaussian shape, which is roughly valid for output of the regenerative amplifier, this factor is $1/sqrt(2)$ $\approx$ 0.71 and for a sech^2 (more appropriate for the oscillator) pulse it is ≈0.65.

Another option is using the same geometry but with the addition of a spectrometer to spectrally resolve the obtained nonlinear signal, the FROG scheme. So with this concept, we obtain measurements discriminated in both time and frequency simultaneously. The FROG scheme was first demonstrated by Trebino et al. and since that time a large number of derivative techniques have been developed, like the cross/correlation FROG, the third harmonic generation, the polarization gating, etc. Using the SHG nonlinear crystal in the FROG scheme causes an ambiguity in the trace due to the symmetry of the SHG process, but this can be resolved by simply introducing a known dispersion onto the beam. The main advantage of second harmonic based FROG is that we can work with weaker signals than if we use a higher-order nonlinear process.

The FROG device concept is described using the Eq. (2.4) , where E is the electric field.

$$\sum S_{2HG}(\omega,\tau) \equiv \left| \int E(t)E(t-\tau)e^{-i\omega t}dt \right|^2. \qquad (2.4)$$

After obtaining the so-called FROG trace as shown in Figure. 2.8. (a), next page, we need to extract the complex-valued electric field from it. This is a 2-D case of the phase-retrieval problem so we use one of several algorithms functions to retrieve the complex electric field. The retrieval algorithm functions by first guessing an electric field E for the pulse, and calculating theoretical FROG trace for that field. This trace is then compared to the experimental trace, producing a matrix of the error function between the two traces. This error function is then used to adjust the initial guess of the electric field. By going through multiple iterations of this algorithm the two FROG traces should finally converge to the true electric field. One of the big advantages of this scheme is that it has an intrinsic error checking, as the algorithm can easily check to see if the pulse shape is physically possible.

Finally, by constructing a Mach-Zehnder interferometer in which one of the beams suffers one addition reflection in comparison with the other beam upon superposition at the output so that the spatial profiles of the two beams are flipped along an axis perpendicular to the plane of the extra reflection. By placing a second harmonic crystal in the superposed beam one can ascertain

the amount of wavefront-tilt in the ultrafast pulse along the direction in which the two spatial profiles were flipped.
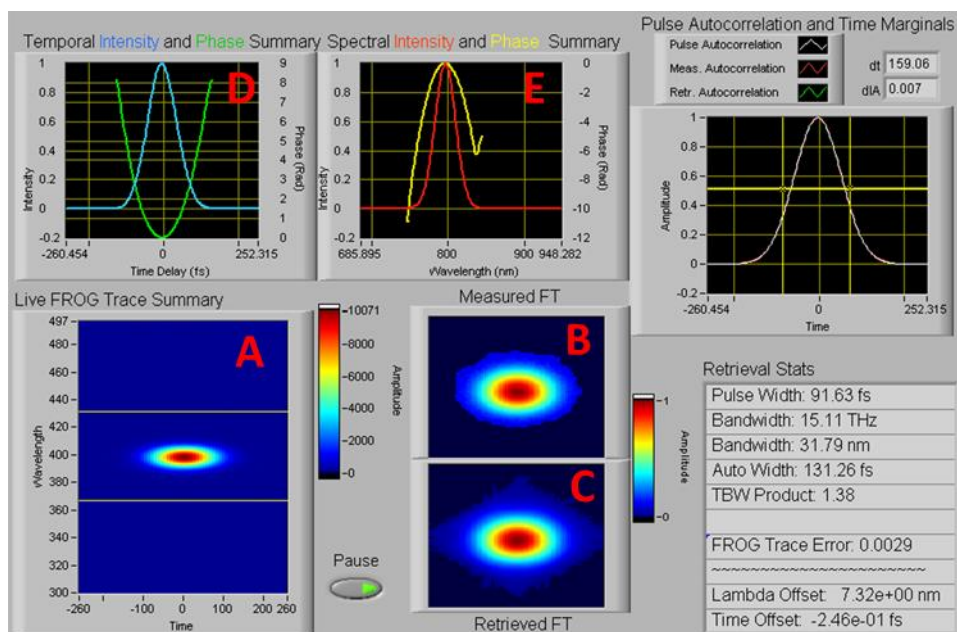
Figure 2.8 FROG trace of the 794 nm pulses (A). The measured (B) and retrieved trace (C). The electric field intensity and phase as a function of time (D) and of wavelength (E).

2.4.   Time domain

2.4.1. Time-Correlated Single Photon Counting - TCSPC

Time-resolved emission decay measurements are important for characterizing materials as they provide information on the dynamics of the probed system. For example, the measured lifetime decays can be related to how carriers relax or to characterize radiative and non-radiative processes. To obtain the photoluminescence decay times we used the Time-Correlated Single Photon Counting (TCSPC) [14] technique. The use of femtosecond lasers alongside fast multichannel plate detectors (MCP) and constant fraction amplifiers and discriminators (CFDs) allows the measurement of lifetimes down to a few picoseconds.

TCSPC is a digital counting technique that relies upon the detection of single photons which are time-correlated to a reference signal produced by the excitation beam pulse.

Usually, the excitation light pulse is divided such that a photodiode is triggered at the same time as the sample is excited. It is as if a stopwatch is started at this moment. When the first photon on our window of observation is detected by a multichannel plate photomultiplier, MCP, the

stopwatch is stopped. Basically, the TCSPC technique represents a start-stop technique. So the time delay τ between the excitation pulse and single detected fluorescent photon from the emitter, for example, is converted by a time-to-amplitude converter, TAC, to an output voltage signal. Then the Analog-to-Digital Converter, ADC, is used to resolve the signal from TAC into thousands of time channels and write into the corresponding address of memory. Then it just records the photons and their arrival time relative to the initial signal and builds a histogram of photon arrival times, as seen in Figure 2.9.
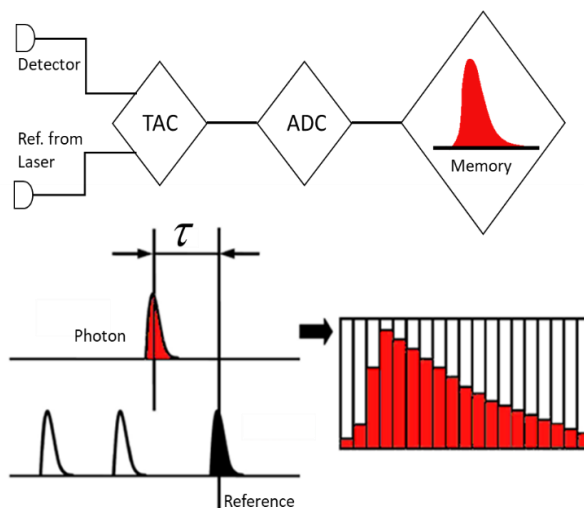
Figure 2.9 Principle of TCSPC. Here TAC represents a time-to-amplitude converter and the ADC is an analog to digital converter.

This experiment is replicated several times and a histogram of occurrence of each time delay is constructed and due to the probability of detecting a photon at a particular time is proportional to the fluorescence intensity our measurement yields the decay of the PL intensity versus time. The experimental curves obtained are the result of a convolution between the fluorescence decay and the instrument response function (IRF). The IRF is obtained at the excitation wavelength via a scattering sample which has an instantaneous time response. It indicates the shape of the excitation pulse seen by the detector and therefore provides a clean signal of its electronic characteristics, as well as the influence of the optical components located in the path of the pulse/beam. Additionally, for short lifetime decays, the IRF plays a major role, in the treatment of the data deconvolution, and, to estimate the lifetimes. The drawback of this technique is that it cannot resolve extremely fast processes, below several picoseconds, since its time resolution is limited by the electronic response of the detector and associated electronics.[14,15]

The setup used was first implemented during the course of my Master's thesis and is depicted in Cesar Bernardo et al.[16], Figure 2.10.
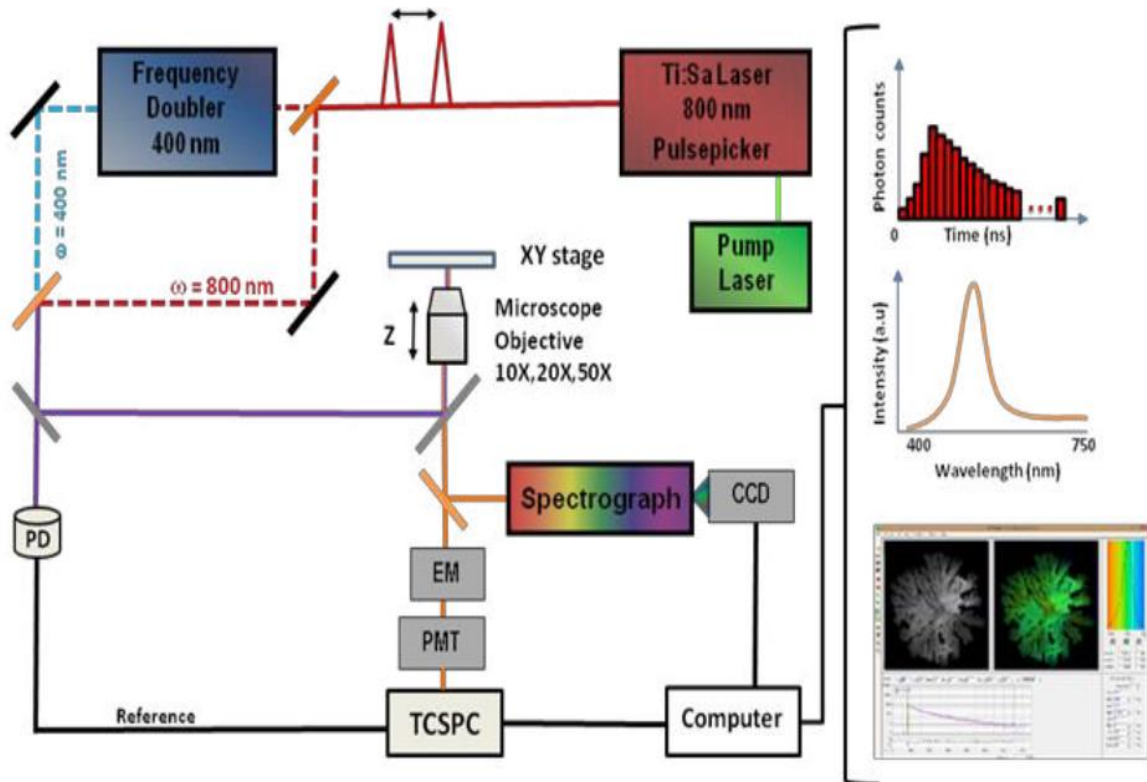
Figure 2.10 The Fluorescence Lifetime Imaging Microscope consisting of a Ti:Sapphire mode-locked laser tunable between λ=700–1000 nm and a pulse-picker and a second harmonic generator as excitation source. Fluorescence intensity images can be taken by using a CCD camera and the fluorescence spectra are collected by a 0.3 m monochromator with a CCD detector. [16]

For excitation, we used several light sources originating from the laser oscillator, for example by doubling the frequency of the oscillator beam or using a narrow band selected from the white light continuum generated in the photonic fiber. Depending on the desired spatial resolution, the laser beam was focused by a lens or a long working length microscope objective to a fixed position while the sample is moved through the focused laser beam by an x-y stage. This allows for measurements of large areas without spatial or temporal distortion. For the highest resolution imaging a 100X Mitutoyo Plan Infinity- Corrected Long WD Objective was mounted to a P.I Instrumente P-721 PIFOC® Piezo Flexure Objective Scanner that allows one to obtain focused spots sizes on the order of 1 micrometer.

A single-photon detection Micro-channel plate photomultiplier (MCP), model Hamamatsu R3809U-51 with a temporal resolution of 20 ps was used for detecting the incoming photons. The wavelength selection was achieved by a computer-controlled double monochromator (Spectral Products CM-110) or by appropriate filters. The signals were collected by a Time-Correlated Single Photon Counting board (Becker&Hickl SPC-150) with a pulse jitter of a few picoseconds.

The overall time resolution is determined by using a scattering sample and taking the IRF. When the system is optimized, the overall time-resolution is around 22 ps. For single-point measurements or solution measurements, the decay signal is deconvoluted by this IRF. For evaluating images, an approximate IRF is provided for each individual point by calculating the first derivative of the rising part of the experimental kinetics and used for deconvolution.

The sample is mounted on an x-y stage which moves it through the laser beam. This stage is operated by two micro translation DC motors (PI instruments M112.1DG) with a minimum step size of 50 nm and a scanning range of 25x25 mm.

To produce the lifetime image, the card uses three TTL input channels, which indicate the start of a new measurement, a new line, and a new frame, respectively. This was originally designed to be employed with a commercial Laser Scanning Microscope which emits the corresponding TTL signals to communicate the position of the laser beam. We took advantage of this scheme and the TTL for line return and the frame are generated by software through the motor control card. However, to provide the necessary precision for individual points within a line, the respective TTL is generated by a timer card (National Instruments NI PCI-6221).

2.4.2. Pump and Probe

To improve the time resolution of transient decay measurements, it is possible to take another approach where we measure light with light.[17] One common means is the implementation of pump & probe experiments [18] like the ones described within this work that utilize the ultrafast pulses to overcome the limitations. In a simple example, it is possible to pump a system into an excited state and subsequently probe the system with another ultrafast pulse at a delayed time. The time resolution of this ultrafast pump & probe experiments depends on the duration of both of the ultrafast pulses used to pump & probe as well as the resolution of the time delay generated between the pump and probe pulses.

In the simplest case, the pump & probe experiments are one color experiments, where we pump and probe at the same wavelength, and the intensity changes of the probe are measured due to transient absorption changes induced by the pump pulse. The fundamental laser beam, or its second or third harmonics, are split on a dichroic mirror into two parts, the pump and the probe. The pump beam goes through a fixed optical path and the other one, the probe beam, passes through an optical delay line consisting of two perpendicular flat mirrors mounted on a computer-controlled motorized translation stage. They are both then focused inside the sample cell or the surface of the structure/thin film and the data obtained. The total time window of the experiment is defined by the total difference in the optical length between the pump and probe pulse.[18,19] Another option is the use of a broadband probe that can be generated by using self-phase modulation in a sapphire or a calcium fluoride plate. For this, a portion of the initial beam goes through a neutral density filter and a diaphragm with a variable aperture to find the appropriate energy threshold and power density, and then it is focused on the plate to form a single filament via self-focusing leading to white light continuum generation.[20] This can then be used as the probe beam.

This section describes the implemented pump & probe system that was used as the base for several of the experiments developed, the modifications for each experiment are communicated in the corresponding chapters.

The pump pulse travels to the sample via a fixed path with the possibility of controlling its intensity by a half-wave plate and a polarizer arrangement. An optical chopper is inserted to modulate the pump pulses, by repetitively switching light beam on and off. The light beam is directed with the help of mirrors and inserted in the path of the probe to have a collinear geometry via a beam splitter. With this arrangement, only part of the pump is used the rest transmits through the beamsplitter.

The probe pulse after being generated was sent through a dichroic mirror to eliminate the contribution of the fundamental wavelength from the white light spectrum.

To ensure that the energy of the probe pulse is sufficiently low so as not to induce any significant pumping of the sample into the excited state, a second (broadband) half-wave plate and a polarizer combination was used.

The pump and probe beams are finally focused on the sample and aligned to have good spatial overlap between them at the sample surface.

Spatial overlap of the pump and probe beams at the sample was an important consideration in the developed experiments. Since some of the materials were produced by exfoliation, and their sizes were less than tens of microns and others originated from chemical vapor deposition having large surfaces it was decided to use a collinear geometry of the beams to allow the use of interchangeable microscope objectives as necessary.

This geometry allowed us to change the dimension of the probe beam to be coupled in the objective. Adjustments were made so that the focused probe fit well within the transverse area of the focused pump beam. Additionally, making the weak pulse smaller and the strong pulse larger allows us to avoid unwanted WLC generation from the sample/substrate and self-focusing of the pump in the sample. When for some reason these two nonlinear effects were present they generate unstable signals as they distorted the pump beam profile and generated increased scattered pump light. The output beam is then collected and directed to the spectrometer which is used as the detector. When the signal and pump beam are close spectrally we often used orthogonal polarization for the pump and probe beams and then filtered out the pump beam using a high-quality calcite polarizer. Due to the pulse to pulse instability, we found that a sufficient signal-to-noise ratio could only be obtained if we implemented a shot-to-shot normalization procedure. The intensity of the probe beam was measured with a reference photodiode (ThorLabs, DET100) and the resultant signal was integrated in time with a gated boxcar integrator (Stanford Research Systems, Model SR250). The integrated signal was monitored on an oscilloscope (Tektronix, Model DPO7254) and then acquired with a Multifunction I/O Device NI-USB6211 card and used for the normalization for the shot by shot acquisition. The final spectra and its behavior can be viewed in software designed for the pump-probe setup, Figure 2.11.
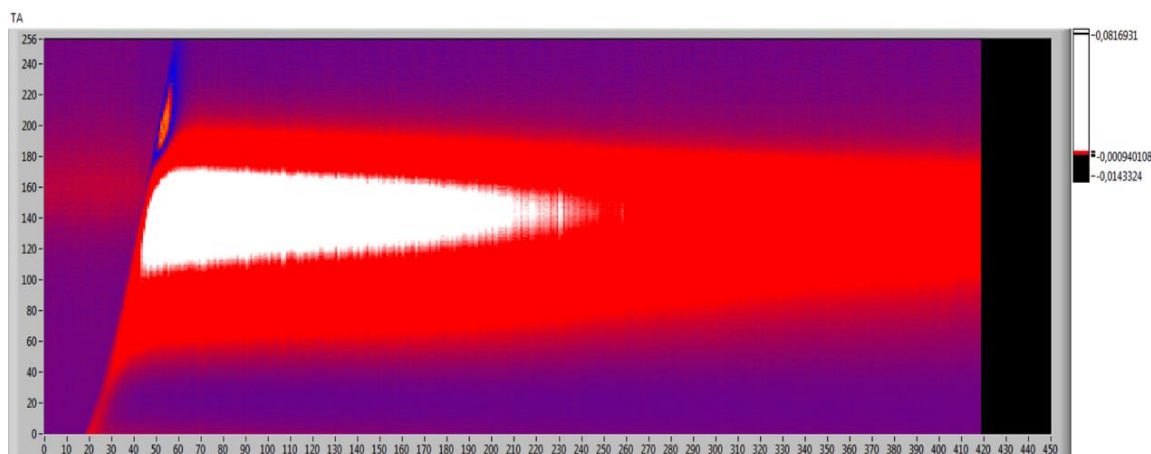
Figure 2.11 Transient map data constituted by ~420 averaged spectra as acquired.

When using the WLC as a probe we have to account for its temporal behavior and chirp which are related to the temporal duration of the seed pulse and the amount of material that the WLC goes through before reaching the sample. The first parameter was addressed by minimizing the seed pulse duration pulse through optimizing the compressor, preforming a pre-compression to compensate for the downstream optics. Additionally, the amount of material that the WLC pulse goes through was minimized by reducing the intervening optics to only those which were essential and using reflective optics when possible. This setup allowed us to produce WLC pulses stable enough to measure absorption changes as low as approximately 0.001 absorbance units with sub-picosecond resolution.

The relative delay between the pump and probe pulses was controlled by adjusting the probe pulse arrival time at the sample with an optical delay line consisting of a stepper motor driven translation stage purchased from Physik Instrumente Model PI M 413 and a retro-reflection mirror mount. The PI stage had a total travel distance of 30 cm with which corresponds to over 2 nanoseconds of time delay and a minimum step size of 0.25 μm giving a resolution of 1.66 fs. The retro-reflector consists of two mirrors that were oriented 90 degrees relative to each other and at 45 degrees relative to the incoming and exiting beams.

The PI stage stepping was controlled through a serial port connection (RS-232) with the data control/collection computer. Custom programs in LabVIEW were developed to sequentially step the stage position (delay time) and control the other parts of the experiment while collecting data. A second delay line was used when needed and following the same general scheme. Specifically, a Newport micro manual linear stage, coupled to a piezo z stage mount with nm resolution also from Physik Instrumente allowed us to fine-tune the distance. This allowed us to control the delay to sub-wavelength resolution, essential for the interferometric experiments involving amplified second harmonic light.

2.5.   Control

2.5.1. Data collection and analysis

For the pump and probe design, the experiments start with the collection of the ambient light and electronic noise by the spectrometer in the absence of both pump and probe beams. This is denoted as $T_{background}$. After that a loop starts, with the acquisition of the probe pulse before the excitation of the sample. Then the pump pulse excites the sample, followed by a second probe

pulse at a variable delay time. The transmission changes in the probe beam caused by the interaction of the pump pulse with the sample are recorded. The acquisition rate from the spectrograph, 1000 Hz, is the same as the pulse rate of the regenerative amplifier and the probe beam allowing shot by shot acquisition. The pump was chopped at half of the base rate, 500 Hz. The spectrometer sends the recorded spectra in the absence of the pump pulse as T and with the pump present as T_{pumped} . The computer first corrects both of these signals with the $T_{background}$ previously acquired and then normalizes the spectra using the reference signal from the photodiode through the boxcar integrator at also 1kHz. And then the loop restarts.

For each delay time, the sample is repeatedly excited by a succession of laser pulses, and the array of the signal collected by the detection system is then averaged. Averaging over a large number of acquisitions, 10000, allowed us to improve the signal to noise ratio and enhances the stability and accuracy of the collected spectral data.

The change in the transient spectra corrected for all the undesired noise and fluctuations due to the white light instability was calculated as:

$$\Delta T_{\Delta t} = \frac{T_{pumped} - T}{T} .$$

(2.5)

The obtained transient spectra contain an artifact originating from the chirped probe due to self-phase modulation and group velocity dispersion. So, different spectral wavelengths of the probe arrived at the sample at different times for any particular time delay. For example, this effect can seen be easily when looking at the cross-phase modulation data shown in Figure 2.12.

The shorter wavelengths, towards the blue, arrive at the sample later than the longer wavelengths, towards the red. If the delay between pump and probe beams is changed, the shape of the recorded spectrum will also change. For example, imagine that the pump beam arrives at the sample after the whole of the probe beam has passed. Then the probe beam will not be perturbed. If this delay is changed the longer wavelengths would still arrive before the pump beam and still not be perturbed, but the blue wavelengths would begin to become superposed with the pump beam and this part of the probe spectrum would be perturbed. Only the blue part of the spectrum would reflect the perturbation. Increasing the delay shifts the perturbation more and more into the red part of the spectrum as seen in Figure 2.12.

To have a good time resolution, the measured data must be compensated for this chirp, requiring the dispersion of the WLC to be characterized. Changing the delay time between the pump and

probe makes it possible to obtain the time at which the pump and probe pulses are overlapped for a given wavelength. The recorded spectra are analyzed in the software and are fit with a univariate quadratic polynomial function, to correct the measured data determining the real zero time delay for each wavelength.
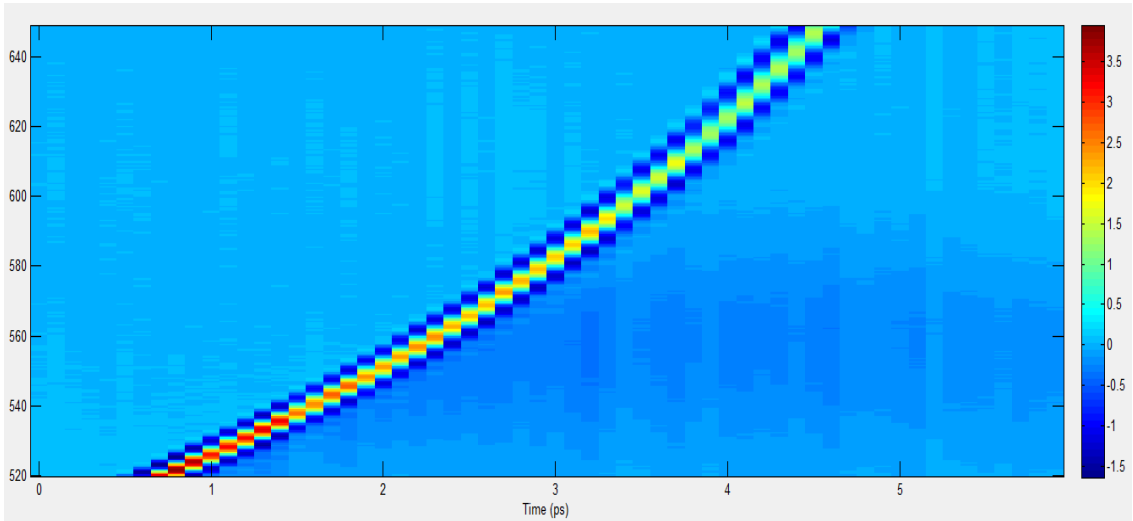
Figure 2.12 Transient spectra obtained for the glass substrate when pumped at 800 nm, the signal is due to the cross phase modulation from the pump on the probe spectra.

Left scale-Wavelength (nm); Color-bar (right) scale -$\Delta T*10^3$.

2.5.2. Software

The software for controlling all the experiments was developed in LabVIEW.

These programs also provided a first assessment of the acquired data via a real-time analysis.

The real-time analysis was sufficient in some experiments as was the case for 2HG in nanofibers, but in various other experiments, MatLab scripts were developed for further evaluation of the data.

These programs address data collection, instrument control, and data analysis.

The following flowcharts outline the basic principles of the more important aspects of the implemented software.
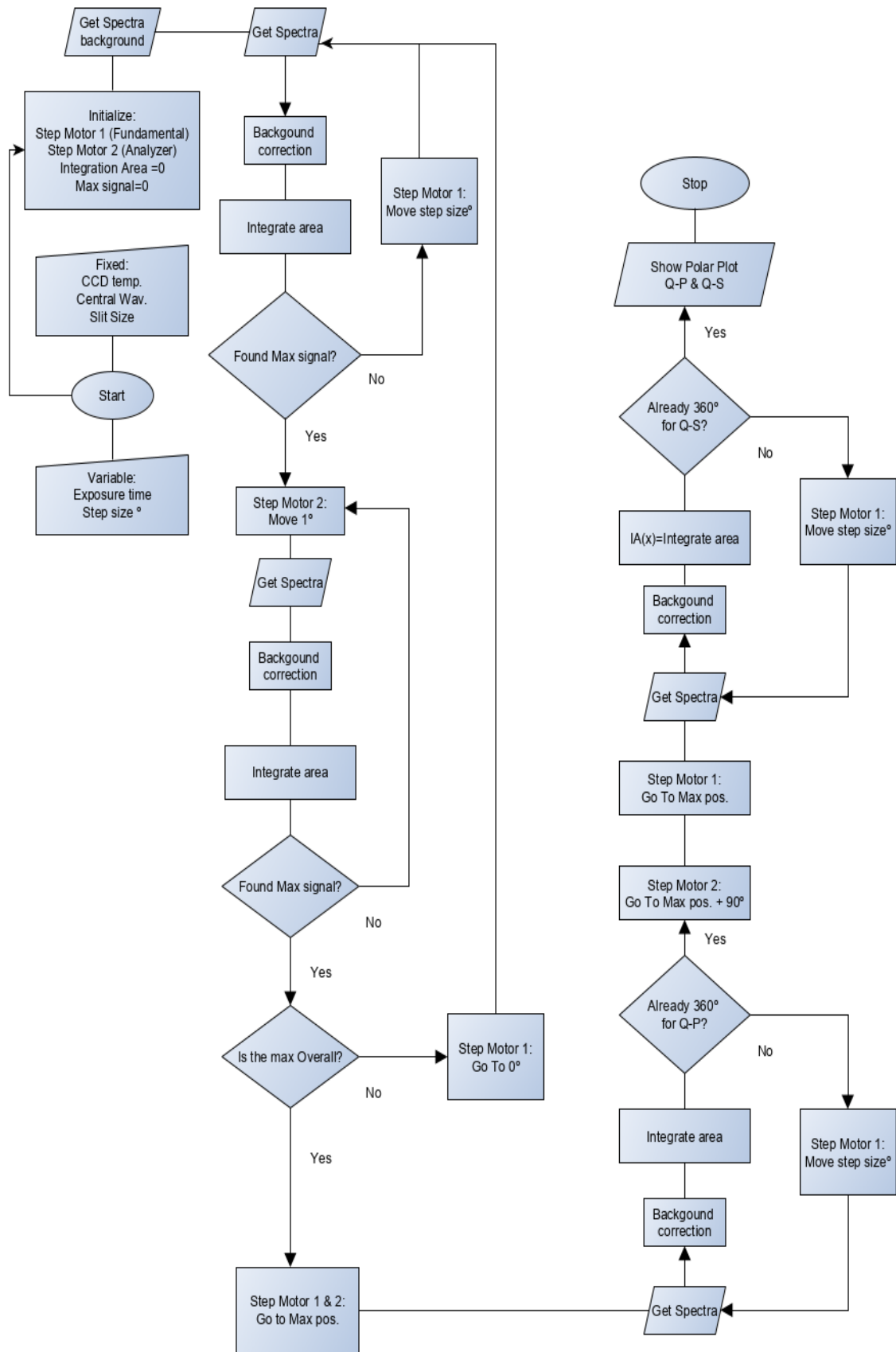
Figure 2.13 Programming flowchart of the "2HGPAnalyser" program.
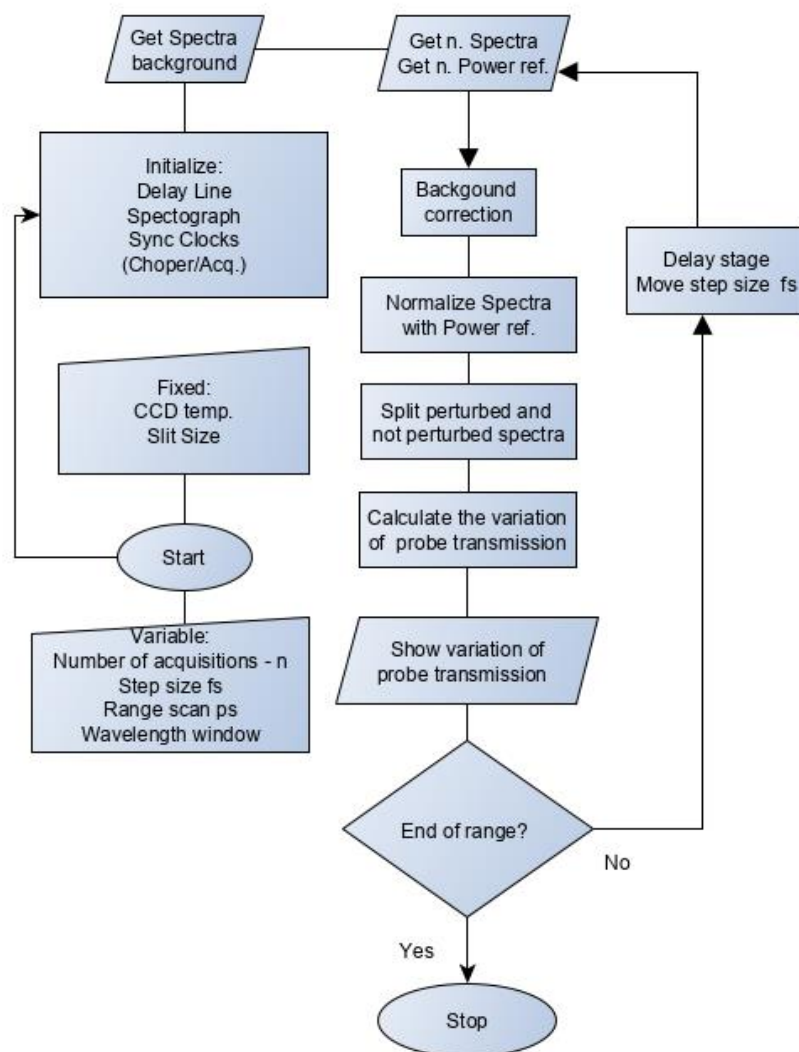
Figure 2.14 Programming flowchart of the "PPSystem" program.

The program, "PPSystem", Figure 2.14, was developed in LabVIEW for interfacing with the pump & probe setup. Due to the different experiments using a pump & probe geometry but with different components for the acquisition of data and its analysis and presentation, this program underwent several iterations. The structure depicted below represents the baseline program.

This program interfaced with the delay stages, with the imaging spectrograph Andor Shamrock SR-303i, and with the Multifunction I/O Device NI-USB6211 card. This card was used for interfacing with the SR530 Lock-In Amplifier and with the SR250 gated boxcar integrator both from the Stanford Research Systems. The NI card had its internal clock synchronized with the laser that was pumping the system, and triggered the choppers and the data acquisition.

The program, "2HGPAnalyser", Figure 2.13, was also developed in LabVIEW for measuring the second harmonic response as a function of polarization. This program interfaced with two rotational stages for control of the incoming polarization and analyzers and with the imaging spectrograph Andor Shamrock SR-303i.

2.6.   Synthesis and Sample preparation

In this work, the experiments were focused on investigating materials from several classes ranging from, organic molecules to 0D, 2D materials, and hybrid systems arising from their conjugation. This was done to explore how it might be possible to improve the performance strengths of each material. This part of the thesis details the preparation of the samples used in the experiments.

2.6.1. Reagents and compounds

All reagents were used as received without further purification.

Selenium powder (99.5%) was obtained from ACROS. Cadmium nitrate tetrahydrate (98%), sodium sulfide (98%), sodium bis(2-ethylhexyl) sulfosuccinate (AOT, 99%), hydrazine, 25% (w/w) sodium methoxide solution in methanol, $FeCl_3$, HCl, PMMA (Poly(methyl methacrylate)) were all acquired from Sigma-Aldrich. Aluminum telluride was purchased from Cerac Inc. Analytical-grade hexane, technical-grade oleylamine (OlAm), 1-octadecene (ODE), tetrachloroethylene (TCE $\geq$ 99.9%, anhydrous), myristic acid (HMyr, 99%), cadmium oxide (CdO, 99.5%), water-free cadmium acetate ($Cd(OAc)_2$, 99.995%), selenium dioxide (SeO_2, 99.8%), cadmium chloride ($CdCl_2$, 99%) were purchased from Sigma-Aldrich. Ethanol (99.9%) was purchased from VWR. Analytical-grade toluene and cadmium acetate dihydrate($Cd(OAc)_2 \cdot 2H_2O$, 99%) were purchased from Merck. Cadmium fluoride (CdF_2, 99%) was purchased from abcr. Selenium powder (mesh 160, 99.99%) was purchased from Chempur. Technical-grade oleic acid (OlAc) was purchased from Fisher. Dimethyl formamide (DMF) and Dichloromethane (DCM) were purchased from Sigma-Aldrich.

2-Methyl-4-nitroaniline, 2-Amino-4-nitroaniline, 3-Nitroaniline, and 2-Methyl-benzyl-4-nitroaniline were purchased from Sigma Chemical Co. Deionized water was used in all experiments.

2.6.2. Quantum Dots

The synthesis of CdSe Quantum Dots (QDs) was adapted from an original approach based on reverse AOT/cyclohexane micelles by Arlindo et al.[21]

Briefly, two water-in-oil microemulsions were prepared by injecting a given amount of precursor solutions to 2.5 mL of AOT in cyclohexane (0.15 M). In one of the two microemulsions, 16 μL of 0.2 M cadmium nitrate tetrahydrate aqueous solution was injected into the AOT solution followed by 8 μL of 1 M aqueous solution of sodium sulfide and 43.5 μL of water to obtain Wo=10 (Wo-H2O: AOT ratio). The Wo was adjusted to control the QDs size; as Wo decreases, the confinement increased. Subsequently, the solution was stirred in a vortex mixer at maximum speed.

A solution of polyselenide in DMSO was used as a precursor for the other microemulsions. This solution was obtained by adding hydrazine as a reduction agent to 1.579 mg of selenium (Se) powder dispersed in DMSO. To control the pH sodium hydroxide (1M) was added dropwise.

For the preparation of the second microemulsion, to obtain the same Wo, 59.5 μL water was supplemented to the AOT solution. 8 μL of a 1 M aqueous solution of sodium sulfide was also added. Finally, 16 μL from the polyselenide in a DMSO solution were injected avoiding exposition to the air. The microemulsion obtained presented a rose color, which disappears after strong vortexing.

Then, this microemulsion was added slowly to the first one, drop by drop, under stirring and avoiding over-exposition to the air. The resulting solution is almost colorless. The final solution was vortexed for 5 minutes and then heated in a sealed vial during one hour at 80°C and an orange color appears, depending on the size, evidencing the formation of CdSe QDs.

For the surface modification of QDs to become hydrosoluble, the AOT was exchanged with a Thiol Ligand. For that, the AOT protected particles in cyclohexane (2.5 mL) were reacted with a 2.5 mL solution of thioglycolic acid in methanol (0.6 M) overnight, assuring protection from light with aluminum foil.

Then the QDs were precipitated by centrifugation at 10000 rpm, washed several times with methanol to ensure removal of the AOT and possible non reacted thiol, dried under nitrogen, and dissolved again by adding dropwise a NaOH (1 M) aqueous solution followed by sonication.

The sample was centrifuged and precipitated again at the same rotational speed, followed by the re-dissolution of the particles in a phosphate buffer solution with pH 7.4 (10 mM) for storage.

The evaluation of the synthesized QDs was made by SEM, absorption, photoluminescence spectroscopy, and TCSPC.

2.6.3. Nanoplatelets

Synthesis of the anisotropic 2D CdSe Nanoplatelets (NPLs) is based on the reaction between Cd and Se precursors in a non-coordinating solvent and subsequent triggering of the platelet growth via the addition of cadmium acetate.[22] For convenience, Cd(Myr)2 was synthesized in situ. Additional selenium precursor was injected during the growth period to increase the lateral size of the NPLs.to 4 ML CdSe NPLs. In a 50 mL three-neck flask, a mixture of CdO (0.5mmol) and HMyr (1.5 mmol) in 25mL of ODE was degassed at 100°C for 30 min under vacuum. After filling the flask with nitrogen, the temperature was raised to 285°C and the mixture was kept stirring until the solution turned colorless. Afterward, the flask was cooled down to 100°C and degassed again to remove water from the reaction mixture. In the next step, Se powder (0.3 mmol) was dispersed in 3 mL of ODE and treated by ultra-sonication for 30 min. This dispersion was added to the flask with Cd precursor at 100°C followed by an additional degassing step. Then the flask was filled with nitrogen, and the temperature was raised to 240°C. Upon heating, Cd(OAc)2·2H2O (0.6 mmol) was swiftly added at 195°C. Upon reaching 240°C a solution of SeO2(0.4 mmol) in 5 mL of ODE, prepared by heating the mixture to 200°C until a clear orange solution formed, was injected at a rate of 25 mL/h (10 min). The NPLs were left to grow for 10 min, and thereafter the flask was cooled down. At 165°C 1.5 mL of OlAc was added. The solution was then precipitated by adding a hexane/ethanol mixture (3:1 vol.) with subsequent centrifugation. The precipitated NPLs were dispersed in hexane.

200 μl of the as-synthesized NPLs were further diluted in 400 μl of hexane, followed by the addition of 150 μl of formamide, 5 μl of oleyl amine, and 10 ul of ammonium sulfide solution (20% in water). The obtained solution was stirred for 90 minutes. Afterward, the hexane phase was washed with the addition of 150 μl of formamide for each washing, repeating the process 3 times. Then the hexane-phase solution was extracted with the final 4 ML NPLs. The evaluation of the synthesized NPls was made by SEM, absorption, and photoluminescence spectroscopy.

2.6.4. Graphene

The graphene was produced by chemical vapor deposition, CVD [23], and was provided as grown on the cooper growth substrate by the group of Professor Pedro Alpuím at INL, Braga.

Briefly, after loading the Cu foil into the CVD furnace, the temperature in the furnace was gradually ramped up with Ar and H2 gas flow. Then, the Cu foil was annealed for 1 h under the same gas conditions allowing an initial surface treatment of the Cu foil. After the annealing process, monolayer graphene was grown with an average grain size of several micrometers. After the growth step, the sample was allowed to naturally cool to room temperature. The grain size of as-grown CVD-graphene was evaluated to be of the order of several micrometers.

I then transferred the CVD-grown monolayer graphene onto glass slide substrates by the conventional PMMA-transfer method. The first step is the removal of the graphene obtained in deposition on the underside of the substrate by an attack with a plasma of O2 at 250W for 2 minutes.

After removal of the graphene from the unwanted side, a temporary sacrificial layer of PMMA is deposited on the graphene to support the graphene after the removal of the copper. The PMMA is spin-coated at 1000 rpm for 60 seconds and then annealed for 8 minutes at 80 °C. The thickness of the fully dried PMMA layer was estimated to be around 200 nm using optical profilometry.

The copper foil is then floated over an iron chloride solution, 0.5M, with the graphene/PMMA face up for 2 hours to dissolve the cooper. After the dissolution of the cooper, the sample goes to an after-treatment, where the graphene film is floated on an acid solution (2 % HCl) for 30 minutes to remove residues of metals originating from iron chloride or catalyst. It is then placed in deionized water for 5 minutes. The acid and water solution steps are repeated 10 times.

The graphene transfer procedure follows with the scooping of the graphene from the deionized water to the final substrate of which the surface was treated by the usual RCA cleaning.

Then the transferred stack is dried, with the help of a nitrogen flow, to remove the residual water molecules between the graphene and the final substrate. After this, the samples were baked at 120 °C in air for 60 minutes to improve the adhesion between the transferred graphene and the substrate. Before removing the PMMA sacrificial layer, we coated a second PMMA layer onto the previous one to avoid the cracking of graphene and allow more efficient removal of the sacrificial layer. The removal of the temporary sacrificial layer of the PMMA substrate is carried out in an

acetone bath for 10 hours. Lastly, the samples were rinsed with deionized water and IPA and dried by nitrogen blowing followed by a final heat treatment for cleaning the graphene surface at 120°C for 4 hours. The quality of the monolayer graphene layer was evaluated by a Raman spectroscope with a 532 nm laser (WITec Alpha 300 R) before and after transfer.

There was a second type of graphene used, obtained from bulk graphite sample trough the mechanical exfoliation process. This was obtained in the same way as the MoS_2 sample that is described in the following paragraph.

2.6.5. MoS$_2$

The MoS_2 flakes used were obtained from a bulk sample through the mechanical exfoliation process.[24] Concisely, a small bulk portion of MoS2 was attached to the adhesive side of Scotch adhesive tape and pressed to another adhesive tape to cleave the material. The process is repeated several times until a final adhesion is made with the final substrate followed by a final cleavage of the expected final layers, in hope that a monolayer is present.

The identification of the few and monolayer MoS_2 flakes was performed by a laborious search to identify the possible areas with a monolayer using optical microscopy and then confirmed by Raman spectroscopy.

2.6.6. Coupling the nanomaterials to the monolayers.

A clear mixture of the photoluminescent nanomaterial and PMMA was obtained dispersing 10 μl of the obtained nanomaterials in a stock solution of PMMA dissolved in chloroform. After the QDS and polymer were completely mixed with a vigorous vortex mixing, the solution was filtered using 0.5 and 0.22 mm millipore filters successively (Millipore). The thin films were prepared by the spin-coating method on the microscope glass substrates already containing the monolayer 2D films. The spin-coating process was carried out under normal laboratory conditions and the film thickness was confirmed to be roughly 10 nm by ellipsometry. The procedure used to obtain a thin film of PMMA with a specific thickness via spin-coated followed a method reported by Walsh and Franses [25] and already used by our group, which gives reproducible high-quality PMMA layers of well-defined thickness. This thickness was controlled by the rotational speed of the substrate and the concentration of PMMA in chloroform and confirmed by ellipsometry.

Note that the process for making spacers is identical but without the presence of the nanomaterial.

2.6.7. Organic fibers

For the precursor solutions, a 10% polymer solution formed by 0.5 g of the chosen organic molecule (a) and 0.5g of the base polymer was dissolved in 1ml of DMF and 4ml of DCM respectively. The relative weight ratio of the organic compound to the polymer in the final precursor solution was 1:1, and the obtained solutions stirred for several hours under ambient conditions before being used in the electrospinning equipment.

The precursor was loaded into a syringe with its needle connected to the anode of a high voltage power supply (Spellmann CZE2000). To obtain properly aligned fiber arrays, a dedicated syringe pump regulated the precursor solution flow rate (0.15 mL/h) and a 16 kV was applied between the needle and the grounded drum collector which rotated at 100 rpm. The needle diameter was 0.5 mm, while the distance between anode and collector was 12 cm.

To achieve ideal morphological characteristics, the electrospinning experimental conditions such as solution feeding rate to the needle, distance from the needle to the collector, and the voltage applied during the electrospinning process were carefully tuned depending on the precursor solutions and the morphology of the initially obtained fibers.[26]

(a) The different organic molecules employed were one of the following: 2-Methyl-4-nitroaniline; 2-Amino-4-nitroaniline; 3-Nitroaniline and 2-Methyl-benzyl-4-nitroaniline.

2.7. References

[1]   N. Tkachenko, *Optical Spectroscopy -Methods and Instrumentations*, 1st ed. Elsevier, 2006.
[2]   E. Roduner, T. Krüger, P. Forbes, and K. Kress, *Optical Spectroscopy*. World Scientific, 2018.
[3]   W. W. Parson, *Modern Optical Spectroscopy: With Exercises and Examples from Biophysics and Biochemistry*. Berlin, Heidelberg: Springer, 2015.
[4]   F. Krausz *et al.*, "Femtosecond solid-state lasers," *IEEE Journal of Quantum Electronics*, vol. 28, no. 10, pp. 2097–2122, Oct. 1992, doi: 10.1109/3.159520.
[5]   O. Svelto, *Ultrafast Processes in Spectroscopy*. Springer US, 1996.
[6]   E. N. Glezer, "Techniques of Ultrafast Spectroscopy," in *Spectroscopy and Dynamics of Collective Excitations in Solids*, B. Di Bartolo and S. Kyrkos, Eds. Boston, MA: Springer US, 1997, pp. 375–416.
[7]   A. E. Siegman, *Lasers*. Mill Valley, Calif.: University Science Books, 1986.
[8]   T. Brabec, C. Spielmann, P. F. Curley, and F. Krausz, "Kerr lens mode locking," *Opt. Lett., OL*, vol. 17, no. 18, pp. 1292–1294, Sep. 1992, doi: 10.1364/OL.17.001292.

[9]   W. Koechner, "Mode Locking," in *Solid-State Laser Engineering*, W. Koechner, Ed. New York, NY: Springer, 2006, pp. 534–586.

[10] P. H. Drive and S. Clara, *Coherent Mira - Operator Manual*.

[11] H. A. Haus, "Mode-locking of lasers," *IEEE Journal of Selected Topics in Quantum Electronics*, vol. 6, no. 6, pp. 1173–1185, Nov. 2000, doi: 10.1109/2944.902165.

[12] "Borate Nonlinear Optical Crystals for Frequency Conversion," in *Nonlinear Optical Borate Crystals*, John Wiley & Sons, Ltd, 2012, pp. 117–260.

[13] D. Strickland and G. Mourou, "Compression of amplified chirped optical pulses," *Optics Communications*, vol. 56, no. 3, pp. 219–221, Dec. 1985, doi: 10.1016/0030-4018(85)90120-8.

[14] W. Becker, *The bh TCSPC Handbook*. Berlin: Becker & Hickl, 2014.

[15] M. Sauer, J. Hofkens, and J. Enderlein, *Handbook of Fluorescence Spectroscopy and Imaging: From Single Molecules to Ensembles*. Weinheim, Germany: Wiley-VCH Verlag GmbH & Co. KGaA, 2011.

[16] C. Bernardo *et al.*, "A versatile fluorescence lifetime imaging system for scanning large areas with high time and spatial resolution," presented at the Second International Conference on Applications of Optics and Photonics, Aveiro, Portugal, Aug. 2014, p. 928637, doi: 10.1117/12.2063940.

[17] G. Porter and M. R. Topp, "Nanosecond Flash Photolysis and the Absorption Spectra of Excited Singlet States," *Nature*, vol. 220, no. 5173, pp. 1228–1229, Dec. 1968, doi: 10.1038/2201228a0.

[18] Andrew. Weiner, *Ultrafast Optics*. New York, NY: John Wiley & Sons, Inc., 2008.

[19] A. Beeby, "Pump-Probe Laser Spectroscopy," in *An Introduction to Laser Spectroscopy: Second Edition*, D. L. Andrews and A. A. Demidov, Eds. Boston, MA: Springer US, 2002, pp. 105–137.

[20] A. Brodeur and S. L. Chin, "Ultrafast white-light continuum generation and self-focusing in transparent condensed media," *J. Opt. Soc. Am. B, JOSAB*, vol. 16, no. 4, pp. 637–650, Apr. 1999, doi: 10.1364/JOSAB.16.000637.

[21] A. M. Fontes Garcia, M. S. Fernandes, and P. J. Coutinho, "CdSe/TiO2 core-shell nanoparticles produced in AOT reverse micelles: applications in pollutant photodegradation using visible light," *Nanoscale Res Lett*, vol. 6, no. 1, p. 426, 2011, doi: 10.1186/1556-276X-6-426.

[22] C. Meerbach *et al.*, "Brightly Luminescent Core/Shell Nanoplatelets with Continuously Tunable Optical Properties," *Advanced Optical Materials*, vol. 7, no. 7, p. 1801478, 2019, doi: 10.1002/adom.201801478.

[23] O. Frank and M. Kalbac, "2 - Chemical vapor deposition (CVD) growth of graphene films," in *Graphene*, V. Skákalová and A. B. Kaiser, Eds. Woodhead Publishing, 2014, pp. 27–49.

[24] K. S. Novoselov, "Nobel Lecture: Graphene: Materials in the Flatland," *Rev. Mod. Phys.*, vol. 83, no. 3, pp. 837–849, Aug. 2011, doi: 10.1103/RevModPhys.83.837.

[25] C. B. Walsh and E. I. Franses, "Ultrathin PMMA films spin-coated from toluene solutions," *Thin Solid Films*, vol. 429, no. 1, pp. 71–76, Apr. 2003, doi: 10.1016/S0040-6090(03)00031-2.

[26] H. Gonçalves, M. Lúcio, P. E. Lopes, C. Bernardo, and M. Belsley, "Self-assembled para-Nitroaniline polymeric thin films as highly efficient generators of second harmonic light," *Optical Materials*, vol. 88, pp. 15–23, Feb. 2019, doi: 10.1016/j.optmat.2018.11.010.

PART II

CHAPTER 3

RAMAN SCATTERING FROM PHONONS IN QUANTUM DOTS
AND NANOPLATELETS: INTERACTION WITH GRAPHENE
PLASMONS

Contents

3.1.   Introduction

As briefly discussed in Section 1.4.1.1, the Raman component of scattered light, usually resulting from scattering by molecular vibrations or, in the case of solids, by optical phonons, is characterized by the Raman shift of the light frequency, $\Delta\omega = \omega_I - \omega_S$, where ω_I and ω_S are, respectively, the incident and scattered photon frequencies.[1] The Raman shift is positive for the (more intense) Stokes component, which corresponds to the creation of an elementary excitation, such as a quantum of molecular vibration or an optical phonon. In solids, even in their nanocrystalline form, the lattice vibrations can couple to other types of elementary excitations provided that energy and

momentum are conserved (energy and momentum matching). The most common example is the coupling between polar longitudinal optical (LO) phonons and bulk plasmons in doped semiconductors, which leads to the formation of phonon-plasmon coupled modes, which have been studied through Raman spectroscopy.[2,3]

Surface plasmons (SPs) can occur at the interface between a dielectric and a conductor, such as a metal or a doped semiconductor. They are coherent oscillations of conduction electrons that, in contrast with the bulk plasmons, occur only near the surface, in the sense that the amplitude of these oscillations decreases exponentially with the distance from the surface (or interface). Charge density oscillations that propagate along an extended surface are usually referred to as surface plasmon-polaritons (SPPs), to distinguish them from localized SPs.[4] The accompanying oscillating electromagnetic (EM) field has a wavevector component along the surface, k_x, such that

$$k_x > \sqrt{\varepsilon}\,\frac{\omega}{c}\ ,$$ (3.1)

where ε is the dielectric constant of the medium in contact with the conductor and ω is the SPP frequency. Because of this, the wavevector component perpendicular to the surface is imaginary, which means that the EM field amplitude decreases exponentially with distance on both sides of the interface. Therefore, SPPs are essentially evanescent waves of coupled EM fields (which are transverse magnetic, TM) and charge density oscillations as depicted in Figure. 3.1. For a planar dielectric conductor interface, polaritons can propagate for length scales of tens to hundreds of micrometers along the surface.[4]
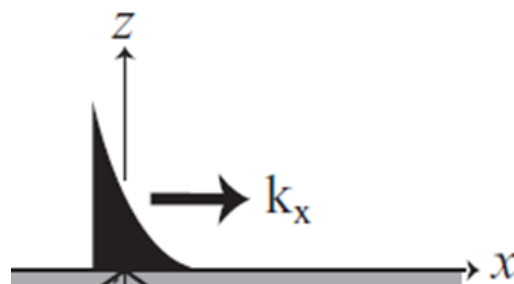
Figure 3.1 Schematic illustration of a surface plasmon-polariton.

Graphene, a two-dimensional conductor with an electrically tunable electron density, can also support propagating SPPs, which typically oscillate in the THz or far-infrared (FIR) frequency range.[5] In this case, charge oscillations occur within the atomically thin layer, the graphene sheet, while the evanescent EM field is confined in the z-direction to a few micrometers. Their excitation and propagation were demonstrated, for the first time, in two works published in the same issue of

Nature.[6,7] The advantage of graphene is the possibility of relatively easy control of the electron density. In addition to the "traditional" doping, electron density can also be controlled by assembling a Field Effect Transistor (FET) structure with graphene on a substrate and a top gate electrode through which a gate voltage is applied.[8] In this way, the SPP properties can be also effectively tuned.[6,7] The simple Drude model for a two-dimensional electron gas, predicts the following expression for the frequency-dependent optical conductivity of graphene [5]:

$$\sigma_g(\omega) = \sigma_0 \frac{E_F}{\hbar(\omega - i\gamma_D)},$$
(3.2)

where E_F is the graphene Fermi energy, $\sigma_0 = e^2/\pi\hbar$ is the quantum of conductivity and γ_D is a damping parameter. The validity of Eq. (3.2) was verified experimentally in the work of L. Ju et al [8]. The dispersion relation for SPPs (i.e. the $\omega(k_x)$ dependence) is determined implicitly by the following equation [5]:

$$\frac{\varepsilon_1}{\sqrt{k_x^2 - \varepsilon_1(\omega/c)^2}} + \frac{\varepsilon_2}{\sqrt{k_x^2 - \varepsilon_2(\omega/c)^2}} = \frac{\sigma_g(\omega)}{i\omega\varepsilon_0},$$
(3.3)

where ε_0 is the vacuum permittivity and $\varepsilon_{1,2}$ are the dielectric constants of two media cladding the graphene sheet. Note that the dispersion relation depends on the Fermi level through $\sigma_g(\omega)$.
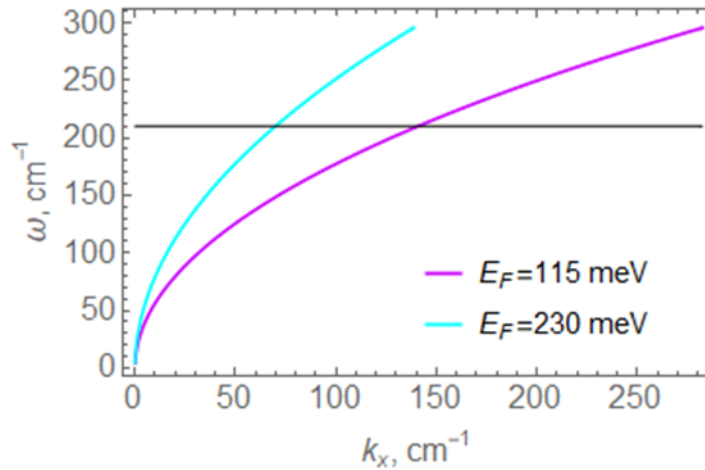
Figure 3.2 Calculated SPP dispersion curves for graphene cladded by two thick glass slabs, for two values of the Fermi energy as indicated. The horizontal black line indicates the bulk CdSe LO phonon

SPPs are the eigenmodes of the dielectric-conductor graphene interface. Due to the restriction stated in Eq. (3.1), they cannot be directly excited by an external light source. However, there are several

ways to bypass the restriction imposed by the in-plane momentum conservation necessary for coupling between two waves propagating along the interface, such as using a prism to create an attenuated total internal reflection (ATR) geometry or a grating, which modulates the in-plane component of the incident propagating light and enables the coupling to SPPs.[4] The field intensity in the near-surface region can be amplified by 2 or 3 orders of magnitude relative to the incident field intensity. This means that the light-matter interactions with adsorbed molecules on the surface are also enhanced. This near-field effect is in the base of several schemes for enhanced molecular sensing relying on the detection of characteristic molecular vibration modes through either enhanced FIR absorption [9] or surface-enhanced Raman scattering (SERS).[4,10] The evanescent EM field associated with SPPs also enables coupling to the propagating polar optical phonons in a substrate, such as SiO_2,[11] or a thin hexagonal boron nitride (h-BN) layer commonly used for graphene encapsulation [12] and this coupling can be quite strong. For instance, coupling energies of the order of 20 meV between graphene plasmons and SiO_2 phonons were reported by X. Zhu et al [11]. For comparison, the SiO_2 optical phonon energy is about 136 meV.

In this chapter, we shall present and discuss Raman scattering spectroscopy (RSS) results obtained for colloidal fabricated CdSe quantum dots (QDs) [13], and nanoplatelets (NPLs) [14], deposited onto graphene. The graphene sheet was incorporated into a field-effect transistor device to permit the tuning of its Fermi level and, consequently, the electron density and the SPPs' dispersion curve steepness. This gives one some control over the coupling between the (Raman-active) semiconductors LO phonon modes and the graphene plasmons, thus influencing Raman scattering by QDs or NPLs. Before describing the theoretical background of Raman scattering on coupled modes and presenting experimental results, let us say a few words about phonons in semiconductor nanostructures.

Besides electrons, quantized lattice vibrations, i.e. phonons, are present in the nanostructures and they also influence its optoelectronic properties, mainly through the electron-phonon interaction. This is because the material underlying a nanostructure such as QDs or NPLs is a crystalline semiconductor.

A phonon can be seen as an elementary excitation of a crystal. It represents an excited state of a quantized collective oscillation mode of the interacting lattice atoms, a normal mode of the crystal.[15] In contrast with photons, phonons can be also longitudinal, not just transverse, with the atomic displacement oscillating along or perpendicularly to the direction of propagation.

For a 3D crystal with s atoms per unit cell, there are $3s$ branches with dispersion curves $\omega(\vec{q})$. Three of them are acoustic phonons with $\omega(\vec{q} \to 0) = 0$, while the remaining curves correspond to optical phonons. The optical phonon branches are only present in crystal lattices with more than one atom per unit cell. For instance, the diamond and zin-blend structures have two atoms per unit cell ($s = 2$) and, consequently, 3 acoustic branches and 3 optical branches exist. In the long-wavelength limit ($\vec{q} \to 0$) of the acoustic modes, two atoms of the unit cell have exactly the same displacement, equal to the displacement of the center of mass of the unit cell. They correspond to sound waves in the continuous limit, with a linear dispersion relation and two distinct sound velocities; the higher one corresponding to the longitudinal waves. Acoustic phonons can be confined in a small crystal if it has a large acoustic impedance contrast with the environment. In QDs, the frequencies of confined acoustic phonons are inversely proportional to the radius of the dot.[16]

In the optical phonon modes of a diatomic crystal, the displacements two atoms of the same unit cell occur in counter-phase, in the $\vec{q} \to 0$ limit. The term "optical" in this case does not necessarily signify an associated optical activity, it rather indicates that the oscillation frequencies fall in the infrared spectral range. Yet, if the crystal is (at least, partially) ionic (as is the case of CdSe), the transverse optical (TO) phonons can interact with photons directly. This process leads to resonant absorption of EM radiation in the far-infrared. In such materials, the TO and LO phonon frequencies are unequal in the Brillouin-zone center, with $\omega_{LO} > \omega_{TO}$, and this splitting is a measure of the degree of iconicity of the crystal. LO phonons create a (longitudinal) long-range quasistatic electric field, which gives rise to the strongest interaction with electrons, holes and excitons, the Fröhlich mechanism.[17]

The dispersion curves of optical phonons in many crystals are rather flat and, in the first approximation, can be described by the dispersionless "Einstein model", which means just two parameters, ω_{LO} and ω_{TO}, in the case of diatomic crystals with cubic symmetry.

In the case of the hexagonal würtzite structure (characteristic of CdSe), there are four atoms per unit cell ($s = 4$), corresponding to 3 acoustic branches and 9 optical branches.

However, the anisotropy has a rather small impact on the polar optical phonons in this case and can be ignored, at least, in the first approximation.[13]

Optical phonon modes in small semiconductor particles are spatially confined and, therefore, quantized, similar to electrons and holes. A detailed discussion of these modes in the framework of a continuum theory can be found, for instance, in the work of R. Ruppin and R. Englman, [18] for a

very thin semiconductor layer, such as NPL, and in Chapter 8 of the book edited by A. L. Rogach [13] for spherical QDs. Without entering into details, the lowest-order confined optical phonon mode (which has the highest frequency, due to the downward dispersion curve of the LO phonon with respect to the Brillouin zone center), is Raman-active and the most prominent in the spectra.

In nearly-spherical colloidal QDs, this mode is spherically-symmetric and sometimes is labeled a "breathing" mode, although optical phonons, whose excitation consists of a relative displacement between two sublattices do not result in QD volume changes. The optical phonon confinement effect is even stronger in NPLs, for instance, LO-type phonon frequencies of 199.5, 202.8, and 204.5 cm^{-1} were observed for CdSe NPLs of 4, 5, and 6 monolayers, respectively.[19]

3.2.   Theoretical background

In Raman scattering, the intensity of the Stokes scattering component, caused by a localized vibration mode (e.g. molecular or QD) can be written as [1]:

$$I_S\left(\omega_S,\omega_I;\omega\right) \propto \left|\left(\frac{\partial\alpha_e}{\partial u}\right)_{u=0}\right|^2 \left\langle u^2\right\rangle_\omega \omega_S^4 \delta\left(\omega_S-\omega_I-\omega\right), \quad (3.4)$$

where α_e is the electronic polarizability of the scatterer, which depends on the atomic displacement (more precisely, the normal coordinate), u, and $\left\langle u^2\right\rangle_\omega$ is the spectral component of the square of the normal coordinate, averaged over time and also an appropriate thermodynamically ensemble, with a specified lattice temperature. The latter represents fluctuation displacements in the absence of an external force and often is called the fluctuation power spectrum. The δ-function in Eq. (3.4) guarantees the energy conservation and requires that the Raman shift is equal to the spectral frequency of the atomic displacement.

In Quantum Mechanics, the displacement can be described in terms of the expectation value of the normal coordinate operator [20],

$$\hat{u} = C\sqrt{\frac{\hbar}{2\omega_0}}\left(\hat{b}+\hat{b}^+\right), \quad (3.5)$$

where C is a normalization constant that depends on the system's details, ω_0 is the mode's frequency and $\hat{b}\left(\hat{b}^+\right)$ is the bosonic destruction (creation) operator.

Using this formalism, the required power spectrum is determined as follows:

$$\left\langle \hat{u}^2 \right\rangle_\omega = C^2 \frac{\hbar}{2\omega_0} \left\langle \hat{b}\hat{b}^+ + \hat{b}^+\hat{b} \right\rangle_\omega .$$

(3.6)

The first and the second terms in the brackets in Eq. (3.6) represent the Stokes and anti-Stokes processes respectively. In particular, the Stokes term is:

$$\left\langle \hat{b}\hat{b}^+ \right\rangle_\omega = \left[N(\omega) + 1 \right] \delta(\omega - \omega_0),$$

(3.7)

where $N(\omega)$ denotes the Bose-Einstein function. Omitting constants, we can write:

$$I_S(\omega_I;\omega) \propto \left| \left(\frac{\partial \alpha_e}{\partial u} \right)_{u=0} \right|^2 \frac{\left[N(\omega) + 1 \right]}{\omega} \delta(\omega - \omega_0),$$

(3.8)

where the dependence on the incident frequency is through the electronic susceptibility derivative. In practice, the δ-function in Eq. (3.8) is replaced by a Lorentzian,

$$\delta(\omega - \omega_0) \Rightarrow \frac{1}{\pi} \frac{\gamma}{\left(\omega - \omega_0\right)^2 + \gamma^2},$$

(3.9)

where γ is the width of the vibrational line mode due to broadening. Thus, an idealized Raman scattering spectrum for a single vibration mode (of a QD, for instance) is a single Lorentzian peak of a certain magnitude.

If the QD is placed in the vicinity of a plasmonic surface and its vibration mode is polar, the latter can interact with the evanescent EM field of the surface plasmon. This interaction decreases exponentially with the QDs distance from the surface.

The interacting system can be described by the following Hamiltonian:

$$\hat{H} = \hbar\omega_0 \left(\hat{b}^+\hat{b} + 1/2 \right) + \hbar\omega_{SP} \left(\hat{a}^+\hat{a} + 1/2 \right) + g \left(\hat{a}^+\hat{b} + \hat{b}^+\hat{a} \right),$$

(3.10)

where ω_{SP} is the surface plasmon frequency, $\hat{a}$ and $\hat{a}^+$ are destruction and creation operators of the plasmons, and g is the interaction constant. The Hamiltonian (3.10) describes two interacting boson modes and was first considered by Hopfield.[21] The coupled plasmon-phonon modes can be obtained by introducing new bosonic operators for two new modes denoted L (lower) and U (upper):

$$\hat{c}_L = A\hat{a} - B\hat{b}; \quad \hat{c}_U = A\hat{b} + B\hat{a}; \quad |A|^2 + |B|^2 = 1.$$

(3.11)

The parameters A and B are called Hopfield coefficients. By expressing $\hat{a}$ and $\hat{b}$ operators in terms of $\hat{c}_L$ and $\hat{c}_U$, and choosing the Hopfield coefficients in such a way that the resulting Hamiltonian is diagonal, the energies of the coupled modes can be shown to be given by:

$$E_{U,L} = \frac{1}{2}\left(\hbar\omega_0 + \hbar\omega_{SP}\right) \pm \sqrt{\frac{1}{4}\left(\hbar\omega_0 - \hbar\omega_{SP}\right)^2 + g^2} \ . \qquad (3.12)$$

The plasmon frequency (for a fixed k_x) depends on the graphene Fermi energy, E_F as $\omega_{SP} \propto \sqrt{E_F}$ (as follows from Eq. (3.3)) and so do the energies in Eq. (3.12) as qualitatively shown in Figure. 3.3. They demonstrate the typical avoided crossing behavior of two interacting modes, the Landau-Zener effect.
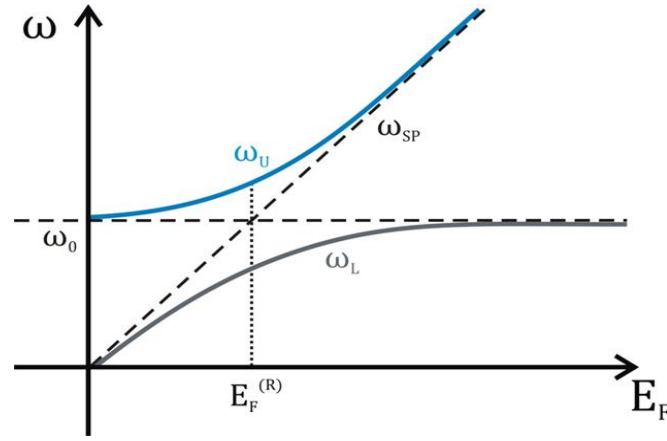
Figure 3.3 Coupled plasmon-phonon modes, upper (blue) and lower black) *vs* graphene Fermi energy. Dashed lines show uncoupled surface plasmon and QD phonon modes.

Figure 3.4 shows, also qualitatively, the variation of the Hopfield coefficients. There squared moduli, $|A|^2$ and $|B|^2$, measure the "fraction" of the plasmon and the phonon present in the mixed modes. At resonance, the avoided crossing point, the coupled modes are half phonons, half plasmons $\left(|A|^2 = |B|^2 = 1/2\right)$. The upper mode is mostly phononic and the lower one is mostly plasmonic below the avoided crossing point with the character switched above the crossing point.

The intensity of Raman scattering by the coupled plasmon-phonon modes is obtained by writing the phonon amplitude in terms of the coupled modes' amplitudes:

$$\left\langle \hat{b}\hat{b}^+ \right\rangle_\omega = |A|^2 \left\langle \hat{c}_L \hat{c}_L^+ \right\rangle_\omega + |B|^2 \left\langle \hat{c}_U \hat{c}_U^+ \right\rangle_\omega \ . \qquad (3.13)$$
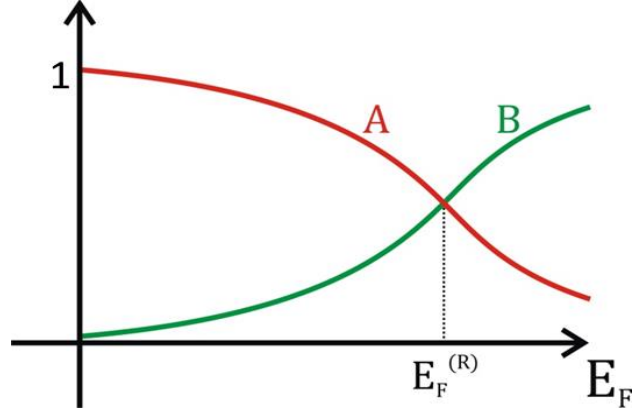
Figure 3.4 Variation of the Hopfield coefficients as a function of the graphene Fermi energy.

Therefore, from Eq. (3.4), (3.6) and (3.13) we have for the Stokes component:

$$I_S(\omega) \propto \frac{N(\omega)+1}{\omega} \left[|A|^2 \, \delta(\omega-\omega_U) + |B|^2 \, \delta(\omega-\omega_L) \right]. \quad (3.14)$$

It follows from Eq. (3.14) that, in general, one can expect to observe two Raman modes for a single optical phonon mode, as depicted in Figure. 3.5. However, the frequency of the plasmon-like, lower, branch decreases quickly as the Fermi level becomes lower than the resonant value, $E_F^{(R)}$, and also its contribution to the scattering, proportional to $|B|^2$ decreases, in Figure. 3.4. Thus, the two-mode behaviour may be expected only in a limited range of Fermi energies. For lower E_F, one may expect just a blue shift of the phonon-like, Raman mode.
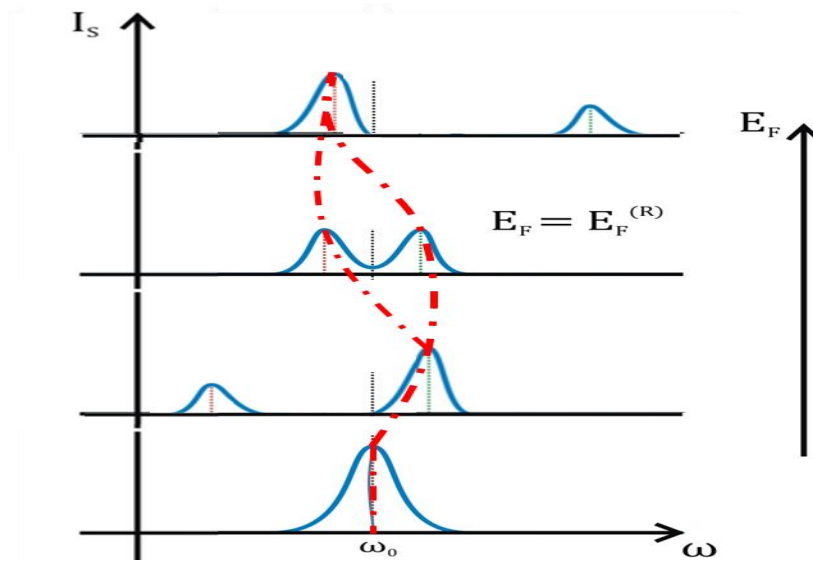
Figure 3.5 Qualitative sketch of the expected dependence of Raman spectrum for scattering from coupled plasmon-phonon modes, upon the graphene Fermi energy. Dashed red lines indicate the expected spectra's evolution as the Fermi energy is increased.

The feasibility of observing the expected effect depends, of course, on the strength of the coupling constant, g. It can be evaluated by calculating the interaction energy between the electric field created by surface plasmons and the polarisation associated with an optical phonon mode,

$$E = -\int \left(\vec{p} \cdot \vec{E} \right) d\boldsymbol{r} .$$

(3.15)

Where the integral is calculated over the volume of the semiconductor nanoparticle, i.e. the QD or NPL. If the electric field in Eq. (3.15) corresponds to a single surface plasmon, an excitation of energy $\hbar \omega_{SP} = \hbar \omega(k_x)$, and the polarisation is:

$$\vec{p} = \alpha \vec{w},$$

(3.16)

with $\vec{w}$ representing the relative displacement of two ions in the same unit cell, corresponding to a single optical phonon. Eq. (3.15) then yields the required coupling constant, g. In Eq. (3.17),

$$\alpha = \sqrt{\frac{\varepsilon_{\infty} \left(\omega_{LO}^2 - \omega_{TO}^2 \right)}{4\pi}} \rho ,$$

(3.17)

where ε_{∞} is the background dielectric constant of the semiconductor $\omega_{LO} (\omega_{TO})$ is the longitudinal (transverse) optical phonon frequency, and ρ is the reduced atomic mass density, according to Chapter 8 of the book edited by A. L. Rogach [13] and in A.G.Rolo et al.[22].

A calculation for a spherical QD of radius R, considering the lowest order optical phonon mode (the so-called "breathing mode", which is purely longitudinal with a frequency just slightly below ω_{LO} [22]) yields the following result [23]:

$$g \approx \hbar \sqrt{\left(\omega_{LO}^2 - \omega_{TO}^2 \right) \frac{\varepsilon_{\infty}}{\bar{\varepsilon}} \frac{\pi k_x R^3}{S}} ,$$

(3.18)

where S is the area of coherence of graphene SPPs (of the order of the square of their propagation length), $\bar{\varepsilon}$ is the average of the dielectric constants of the cladding materials and k_x is the wavevector of "resonant" SPPs with $\omega(k_x) = \omega_{LO}$. Taking as typical values $R = 5\,\mathrm{nm}$, $k_x = 0.1\,\mathrm{nm}^{-1}$, $S = 1\,\mu\mathrm{m}^2 = 10^6\,\mathrm{nm}^2$, $\bar{\varepsilon} = 1.6$ and phonon parameters of CdSe from the work of E.S.Freitas Neto et al [24], we obtain $g \approx 0.01\,\hbar\omega_{TO} \approx 0.2\,\mathrm{meV}$. Although this is rather small, according to this estimate, one should expect a bigger effect for larger semiconductor nanoparticles such as the NPLS.

3.3. Experimental Methods

3.3.1. Sample preparation

For the work reported in this chapter, CVD graphene was used with QDs and NPLs both made of CdSe. These nanostructures were produced as explained in Chapter 2.

The produced CdSe QDs were characterized through absorption and photoluminescence spectroscopy, see Figure 3.6. The maximum of the absorption band lies at λabs=530 nm and the emission peak is located at λem=590nm. From the former, we estimate the radius of the representative QDs as <R> = 4 nm using the effective mass approximation formula (Chapter 8 of Ref. [13]). The CdSe NPLs used consisted of an estimated 4-5 layers and the thickness of the deposited film was approximately 7 nm, as measured by ellipsometry.

Hybrid structures
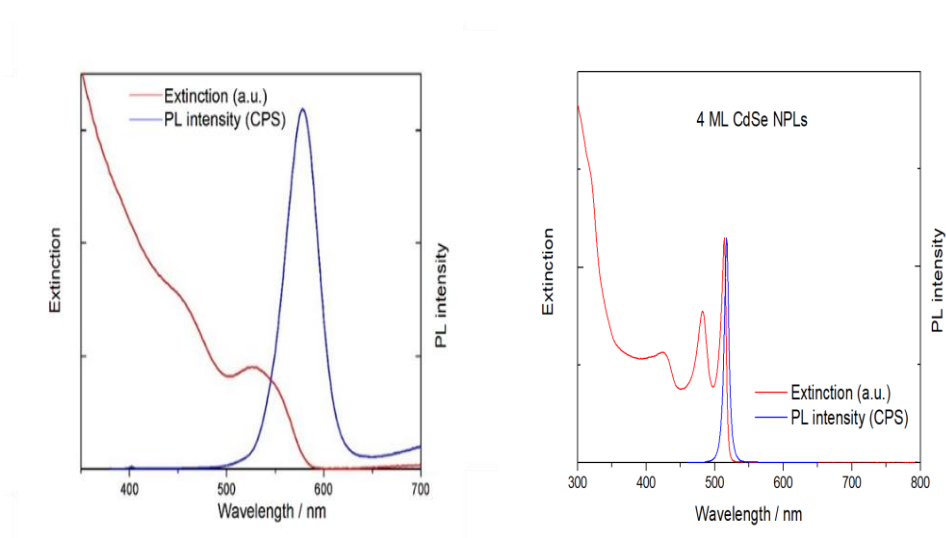
Figure 3.6 Absorption and PL spectra of CdSe QDs (left) and NPLs (right) used in this study.

The NPLs and QDs were deposited on several types of substrates on which graphene was already deposited to carry out the Raman studies. They ranged from mass-produced devices, graphene field-effect transistors (GFET) either liquid gated or back gated, to simpler devices fabricated from a microscope slide upon which a back gate was deposited, while the source and drain were constructed using conductive silver glue.
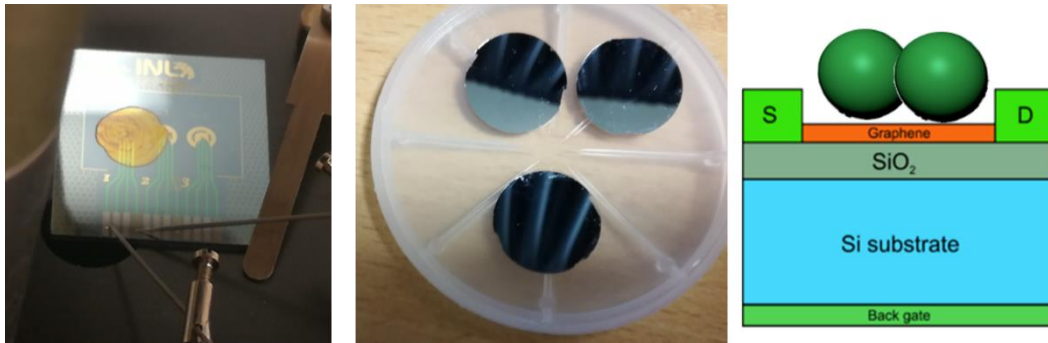
Figure 3.7 Mass produced GFET, left. Microscope slide back gated, center. Schematic of the back gated transistor, right.

Note that for the GFET and the other devices that were produced with CVD graphene, the transference method introduces roughness and some contamination by impurities, which limits the carrier mobility and can also introduce some doping, in this case, p-doping. Also, the dimensions between contacts were on the order of several hundred µm, which is far above the characteristic length associated with the ballistic effect. Under these conditions, the mobility can be well described by the Drude model (Eq. (3.2) for zero frequency).

Fabrication of NPLs or QDs/PMMA thin films

A clear mixture of the photoluminescent nanomaterial and Poly(methyl methacrylate) (PMMA) was obtained using 10 µl of the nanomaterials and dispersing them in a stock solution of PMMA in chloroform. After the nanomaterial and polymer were mixed completely, the solution was filtered using 0.5 and 0.22 mm millipore filters successively (Millipore). The thin films were then prepared by the drop-casting and the spin-coating method on the substrates already covered with the graphene. The spin-coating process was carried out under normal laboratory conditions and the obtained film thickness was under 10 nm as confirmed by ellipsometry. This thickness was controlled by the concentration of PMMA in chloroform and the rotational speed of the substrate, according to the work of Christopher B. Walsha and Elias I. Franses [25].

Chemical doping of graphene

In addition to an electrostatic control of the Fermi level, a chemical method using hydrazine to inject charge into the graphene was also employed.

Hydrazine (N_2H_4) solutions of several concentrations (1, 10, 25, and 50 wt. %) were prepared by diluting concentrated N_2H_4 monohydrate solution (from Aldrich, 98%) with de-ionized (DI) water. The chemical doping of graphene was obtained by submerging the entire surface of graphene with several droplets of the N_2H_4 diluted solutions and then drying with N_2 gas after a 2-minute interval. To characterize the electrical properties of the obtained doped graphene dependence on the N_2H_4 concentration, several graphene transistors (GFET) were treated by the aforementioned N_2H_4 solutions and then the respective EV curve as obtained. This evaluation was carried out during several hours and the graphene gradually recovered some of its original properties, probably due to the desorption of the N_2H_4 molecules from the surface.

3.3.2. Data collection

Several resonant Raman scattering, RRS, studies were made while adjusting the electron density in the GFET and the other devices. Then several chemically doped and un-doped graphene and hybrid systems were also studied with a commercial Raman spectroscopy equipment, the WITec Alpha 300 R Raman confocal imaging setup. This system was used in the form of a micro-Raman back-scattering spectroscope. The system works with a single monochromator together with a CCD array detector for spectral measurements and a filter to block the reflected and excitation radiation. A filter is used for the absorption of the signal below 100 cm^{-1} of the laser line and the grating used had 1800 grooves/mm.

To analyze the Raman signal of the sample, a coherent light source with sufficiently high intensity is needed. This is used to gain a high signal to noise ratio and to distinguish the elastically scattered light from the inelastically-scattered light. A frequency-doubled diode laser with a 532 nm emission line was used. The incident power was adjusted to between 500 uW and 4 mW and coupled to the sample with a 50 x objective: The resulting spot size of the excitation on the sample was approximately 1 μm^2.

3.4. Results and discussion

3.4.1. Bare graphene

First-order Raman spectra of carbon-based materials usually show two main features known as G and D peaks, which lie at ~1580 cm^{-1} and 1360 cm^{-1}, respectively. The G peak corresponds

to E_{2g} symmetry phonons at the Brillouin zone center. The D peak is due to the stretching mode of sp^2 – bonded carbon atoms and requires a defect for its activation.[26] The absence of the D mode in graphene spectra indicates a low amount of structural defects (present mainly at the edges).[27,28]

The most prominent Raman spectrum feature of graphene is the second order of the D peak: the 2D peak [27], which lies at ~2700 cm^{-1}. The 2D mode is seen, even when no D peak is present since no defects are required for the activation of the second-order process.

Before performing RRS measurements for the hybrid structures, some Raman studies of the graphene samples were performed, to serve as a baseline for monitoring the graphene quality before and after doping with hydrazine. Raman spectra were acquired as described in 3.3.2, in the range of 80 - 3200 cm^{-1}. The spectra obtained before the hydrazine treatment clearly shows the G and 2D peaks at the expected positions. Figure 3.8 presents a portion of the spectra in the vicinity of the G and 2D modes, before (orange lines) and after (blue lines) the doping respectively.
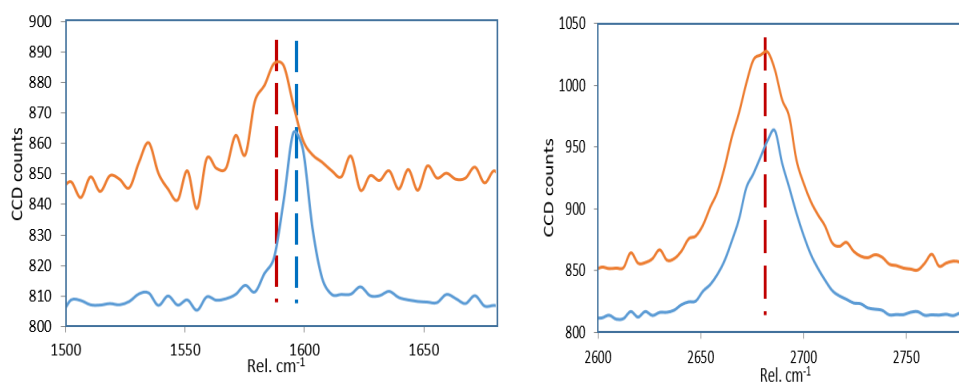
Figure 3.8 Raman spectra of bare graphene showing that G band (left) and 2D band (right) peak positions change due to hydrazine doping: Orange curves show the spectra taken before doping and blue lines after doping.

Comparing the Raman spectra before and after doping, it is seen that the 2D mode essentially remains in the same position, while the G mode shifts upwards and narrows. One needs to be careful in attributing this change to the doping as it is known that disorder, doping, and stress can strongly affect the properties, and peak positions of the G and 2D modes of graphene.[29] However, the Raman spectra of our samples do not show the characteristic disorder mode (D-mode). Therefore, the change in the G peak position should not be associated with the disorder.

From this, we can conclude that the observed changes in the Raman spectra are likely to be related to charged impurities, i.e. doping affecting the Fermi level. It is known that the G mode position shifts to higher wavenumbers for increasing electron and hole doping and the 2D mode upshifts for p-type doping and down-shifts for n-type doping.[30] However, the latter is considerably smaller than the G mode shift.[29] For n-doping and charged impurity concentrations that lead to G-mode frequencies in the range of 1585 cm^{-1} < ω_G< 1595 cm^{-1}, the 2D peak position (ω_{2D}) is almost the same, while for p-doping and similar impurity concentrations, ω_{2D} shifts considerably upwards. In our case, the observed blue shift of the G mode and almost no shift of the 2D mode indicates n-doping of the graphene, in agreement with other works performed in graphene doped using various chemical and electrochemical techniques.[30] Therefore, the presented Raman spectra of bare graphene show some sensitivity to hydrazine doping, and the observed changes are related to the electrons in graphene, i.e. they take place together with changes in the Fermi level. This is confirmed by the measurements of characteristic current-voltage curves of graphene, Figures 3.12 and 3.13.

3.4.2. Graphene/QDs structures

This RRS study initially was carried with a liquid gate GFET where the nanomaterials were produced with a hydrophilic behavior to be dispersed in water. This dispersion was then drop-cast on the GFET with the added value that the water could be used for gating the transistor.
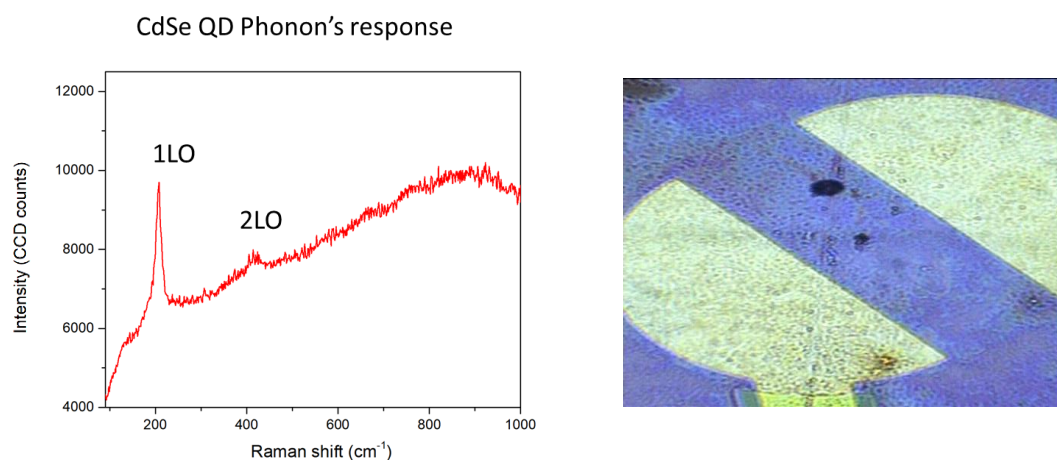
Figure 3.9 RRS spectra of CdSe QDs with a 5nm diameter (left). Active area of the liquid gate GFET, note the black area where the QDs agrgregated (right).

This procedure seemed to be a simple and good idea to achieve our objectives when the initially obtained RRS signal was clearly resolved as seen in Figure 3.9 (left). The Raman spectrum shows the well-documented first-order optical phonon peak, appearing here at 206 cm^{-1}, shifted downwards relative to the bulk CdSe value (210 cm^{-1}) as expected because of the phonon confinement effect. It is mostly due to the spherically symmetric LO-type phonon mode.[22]

Unfortunately, the approach using the liquid-gate FET structure led to unstable Raman signals, probably due to the Brownian movement of the QDs or NPLs in the solution. Thus, there was no guarantee that the nanomaterial was in the vicinity of the graphene due to the 3D nature of the water droplet. Furthermore, the nanomaterials tended to aggregate at the spot probed during the experiment, as seen in Figure 3.8.(right), adding even more entropy to the measurements. This effect might have been the result of the laser acting like an optical tweezer.

Therefore, instead of the liquid-gate GFET, the use of a back-gated GFET was attempted. The nanomaterials were deposited in the form of a few nanometers thin film placed in the vicinity of the graphene. This thin film allows for better control of whether the nanomaterials were deposited close to the graphene since its thickness only allowed for a minimal number of layers of nanomaterial and these were fixed within the polymeric matrix.

After the deposition of the nanomaterial, the RSS spectra were recorded, firstly, for a spot that was not covered with graphene and then a spot within the graphene. The RSS spectrum associated with the graphene displayed a LO-phonon peak slightly shifted upwards (by 4 cm^{-1}) compared to the spot where the QDs were deposited directly on the bare substrate, Figure 3.10. The upward shift is also clearly observed if we examine the second-order mode of the QD phonons.

Interestingly, the first-order LO peak for QDs located on top of graphene took the position of the LO-phonon mode of bulk CdSe, 210 cm^{-1}. It is as if only the largest QDs were Raman active when placed on top of the graphene.
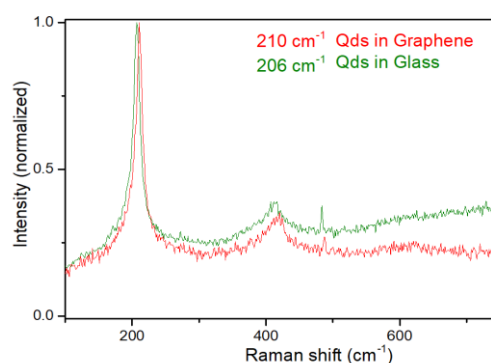
Figure 3.10 RRS spectra of CdSe QDs deposited directly on graphene and on a glass substrate.

The experiment was then carried out with the operational back-gated GFET. The system was swept through several gate voltages in an attempt to change the electrostatic doping. Unfortunately for both the QDs and NPLs the change in the LO signal Raman shift of the nanomaterials was not visible as the voltage was swept through various voltages as seen for example in Figure 3.11 (left) for the QDs.
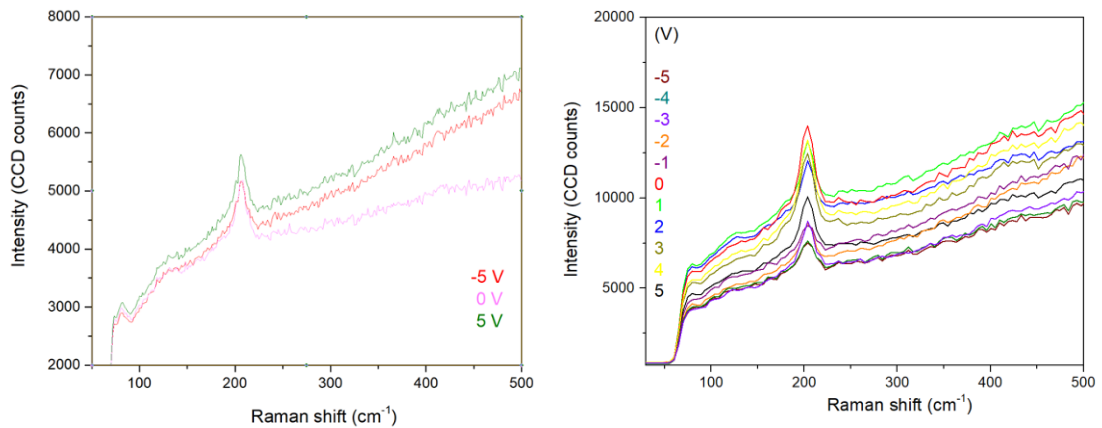
Figure 3.11 RRS spectra of CdSe QDS on graphene recorded for 3 representative values of the gate voltage for QDs incorporated in the back-gate GFET structure (left) and swept through several voltages (right).

However, although the frequency of the Raman peak remains roughly constant when the gate voltage is varied, the intensity of the Raman signal does vary, Figure 3.11 (right). Probably this is not the effect one should expect from the physics discussed in Sections 3.1 and 3.2. If it were possible to exclude some possible secondary effects (such as a possible mechanical motion of the dots into and out of the illuminated spot), it would imply a kind of SERS effect, although probably not related to a near-field enhancement but rather to an electron transfer between the dots and graphene that could be enabled by an alignment of the Fermi level of graphene with the QD energy levels. [31] These potentially interesting effects are out of the scope of this thesis chapter and will be investigated further in the future. As for the expected effects of phonon-plasmon coupling that should be revealed by mode shift and/or splitting, these were not observed for the QD-graphene system.

3.4.3. Graphene/NPLs structures

Firstly, the same experimental approach (using a back-gate GFET structure) was undertaken for the NPLs and the results were similar. Since the electrostatic doping apparently did not affect the

system as expected, we turned to the chemical doping, for which hydrazine was used, following the literature. To evaluate the effect of the hydrazine doping on the Fermi level of graphene, a field-effect transistor structure with graphene and a liquid gate was used to obtain the work function. The work function of any material can be defined as the energy required to remove an electron from the highest filled level in the Fermi distribution of a solid to the vacuum at absolute zero and is a fundamental electronic property of any material since it indicates the relative position of the Fermi level. It was possible to demonstrate that the adsorption of hydrazine on graphene results in a negative shift of the Dirac point (relative to vacuum) as already reported in the literature. This is illustrated in Figure 3.12, where the transfer (or characteristic) curve (drain-source current versus gate-source voltage) after the hydrazine exposure exhibits a shift of the neutrality point to lower gate voltages under the experimental conditions used.

The as-produced GFET shows a p-type transport behavior with a positive-shifted Dirac point, which is altered when exposed to a solution concentration of 25 wt % hydrazine. The air stability of the hydrazine doped GFET was monitored by measuring its behavior as a function of time, in which graphene was doped with a solution concentration of 25 wt % hydrazine and followed for 76 hours, as shown in Figure. 3.12.
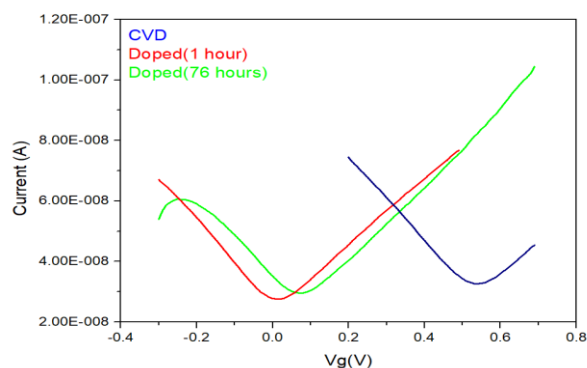
Figure 3.12 Characteristic current-voltage curves of graphene: (a) as grown, (b) after doping with hydrazine 25% and (c) after 76 hours.

After the initial shift, we can see a recovery of 15% towards the initial behavior, which is probably due to the desorption of the molecules, and it is more pronounced because of the use of the GFET with a liquid gate. Each time that one needs to make a run it is necessary to use the liquid gate, and this leads to a dilution out the molecules of the dopant adsorbed in the GFET. There is also the recovery due to the surface-air desorption present but its influence is secondary compared to the effect of cleaning that happens with the liquid gate.
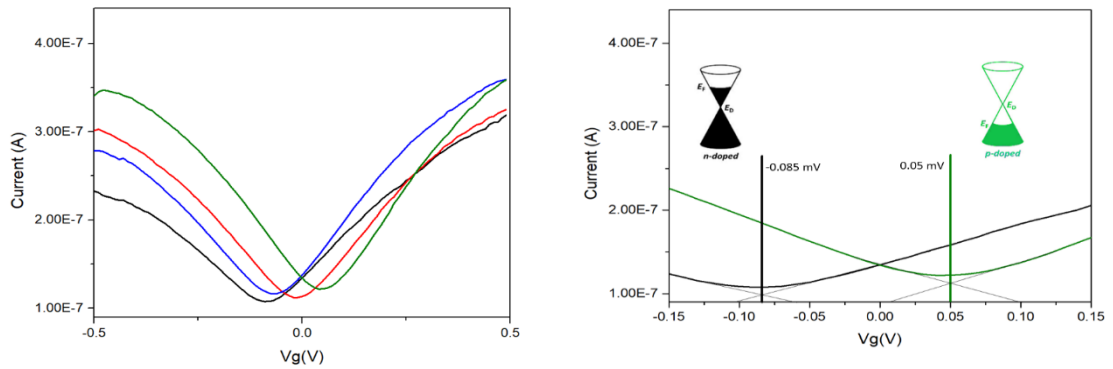
Figure 3.13 Transfer curve obtained after doping with hydrazine with different concentrations (left). Fermi level positions, with respect to the Dirac points, extracted from the current-voltage characteristics for p-doped (green) and n-doped (black) graphene GFET (right).

The intrinsic Fermi level of graphene is shifted into the conduction band when graphene is exposed to hydrazine at higher concentrations and it is possible to tune it using different levels of doping, as depicted in Figure. 3.13.

Using the NPLs hybrid systems with the hydrazine doped graphene, the Raman spectra recorded in the vicinity of the CdSe LO phonon mode do show some changes with the graphene doping, Figure 3.14.
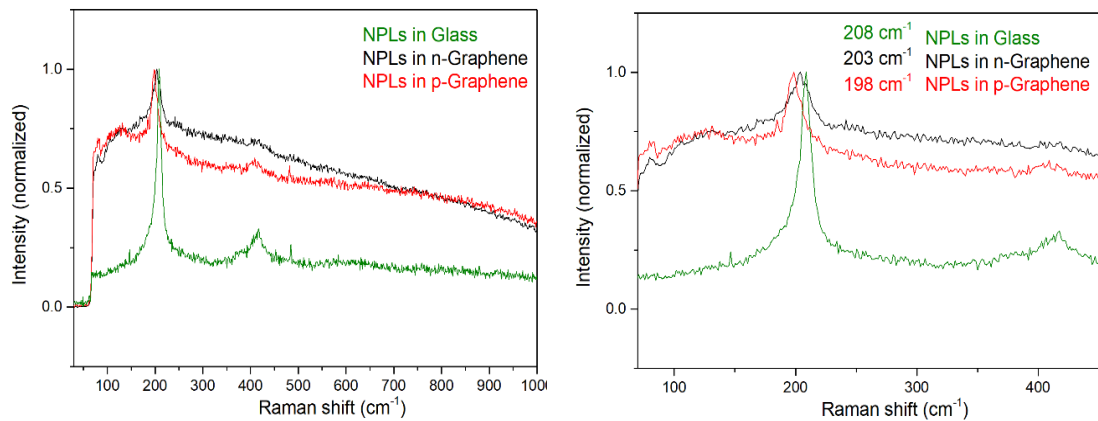
Figure 3.14 RRS spectra of CdSe NPLs on graphene. The right panel shows the region near the CdSe LO phonon frequency. The spectra were excited by a 532-nm line of a diode laser. Black curves are for n-doped graphene and green curves are for p-doped graphene.

As for the case of QDs, the main peak corresponds to the LO phonon shifted from the bulk LO frequency by the confinement effect.

Since NPLs are 5 monolayers thick, the frequency shift relative to the bulk CdSe value (210 cm^{-1}) is similar to that for the QDs (for instance, $R = 3\ \mathrm{nm}$ corresponds to approximately 5 unit cells). Also seen is the first overtone of the main mode, appearing close to 400 cm^{-1}.

Considerable changes are seen as the Fermi level varies, namely, the 8 cm^{-1} shift of the main Raman mode observed in Figure. 3.14 (right). Unfortunately, for technical reasons, it was not possible to measure Raman spectra with a more gradual and continuous tuning of E_F. Even though, we see that the effect of graphene on the Raman of NPLs is completely different from that observed for QDs. Indeed, a downwards shift of the LO-phonon peak is observed when NPLs are placed on graphene. The value of the shift changes considerably with graphene's doping. The downward shift could be attributed to either a stronger phonon confinement effect (remember the LO-phonon dispersion curves bend downward) or a tensile strain.[24] However, none of these factors is likely to be induced by the graphene environment. The remaining explanation is that the Raman scattering in these nanostructures is due to some coupled modes. However, with the limited experimental data available, it is difficult to assert or exclude the plasmon-phonon coupling as a possible reason. Indeed, this coupling can take place with either n- or p-type graphene and both these situations may correspond to the lower coupled mode of Figure. 3.4 for $E_F = E_F^{(R)}$ and, by chance, no other situation occurred in our hydrazine-doped graphene, that would expectedly yield an upward-shifted coupled Raman mode.

3.5. Summary

To summarize, it has not been possible to experimentally verify the theoretical idea of RSS detection of coupled plasmon-phonon modes in hybrid systems consisting of graphene and semiconductor nanoparticles (QDs or NPLs). With dots, it is possibly due to the too low coupling constant that may be achieved because of their small size, as suggested by the numerical estimates made at the end of Section 3.2. With NPLs, which are much larger than dots in two spatial dimensions (although smaller in the third one) and thus may provide the stronger coupling, experimental results, in principle, are compatible with the theoretical predictions. Yet, further experiments are required to fully prove the theoretical concept analyzed in this Chapter.

Nevertheless, we obtained a rather clear indication that the graphene environment does indeed influence the RRS signal coming from either QDs or NPLs. With the former, there are two effects observed: (i) QDs deposited on graphene show a much smaller shift of the LO-phonon peak relative

to the bulk CdSe value than dots deposited on glass (Figure. 3.8), and (ii) the magnitude of the Raman peak varies considerably with the gate voltage applied to graphene (Figure. 3.9). Both effects may be related to electron transfer between graphene and QDs of certain sizes, which can suppress (or enhance) Raman scattering for that QD population. This explanation, however, would not work for NPLs because, in contrast to the QDs, they have a very limited thickness dispersion. Therefore, the hybrid nature of the NPLs' Raman mode, with the frequency varying as seen in Figure. 3.13, remains a plausible explanation.

3.6. References

[1] W. Hayes and R. Loudon, *Scattering of light by crystals*. Wiley, 1978.

[2] R. Cuscó, L. Artús, S. Hernández, J. Ibáñez, and M. Hopkinson, "Raman scattering by LO phonon-plasmon coupled modes in n-type InGaAs," *Phys. Rev. B*, vol. 65, no. 3, p. 035210, Dec. 2001, doi: 10.1103/PhysRevB.65.035210.

[3] W. Limmer *et al.*, "Coupled plasmon–LO-phonon modes in Ga(1−x)Mn(x)As," *Phys. Rev. B*, vol. 66, no. 20, p. 205209, Nov. 2002, doi: 10.1103/PhysRevB.66.205209.

[4] L. Novotny and B. Hecht, *Principles of nano-optics*. Cambridge: Cambridge University Press, 2006.

[5] Yu. V. Bludov, A. Ferreira, N. M. R. Peres, and M. I. Vasilevskiy, "A primer on surface plasmon-polaritons in graphene," *Int. J. Mod. Phys. B*, vol. 27, no. 10, p. 1341001, Apr. 2013, doi: 10.1142/S0217979213410014.

[6] Z. Fei *et al.*, "Gate-tuning of graphene plasmons revealed by infrared nano-imaging," *Nature*, vol. 487, no. 7405, pp. 82–85, Jul. 2012, doi: 10.1038/nature11253.

[7] J. Chen *et al.*, "Optical nano-imaging of gate-tunable graphene plasmons," *Nature*, vol. 487, no. 7405, pp. 77–81, Jul. 2012, doi: 10.1038/nature11254.

[8] L. Ju *et al.*, "Graphene plasmonics for tunable terahertz metamaterials," *Nat. Nanotechnol.*, vol. 6, no. 10, pp. 630–634, Oct. 2011, doi: 10.1038/nnano.2011.146.

[9] D. Rodrigo *et al.*, "Mid-infrared plasmonic biosensing with graphene," *Science*, vol. 349, no. 6244, pp. 165–168, Jul. 2015, doi: 10.1126/science.aab2051.

[10] L. M. Almehmadi, S. M. Curley, N. A. Tokranova, S. A. Tenenbaum, and I. K. Lednev, "Surface Enhanced Raman Spectroscopy for Single Molecule Protein Detection," *Sci. Rep.*, vol. 9, no. 1, pp. 1–9, Aug. 2019, doi: 10.1038/s41598-019-48650-y.

[11] X. Zhu *et al.*, "Plasmon–Phonon Coupling in Large-Area Graphene Dot and Antidot Arrays Fabricated by Nanosphere Lithography," *Nano Lett.*, vol. 14, no. 5, pp. 2907–2913, May 2014, doi: 10.1021/nl500948p.

[12] V. W. Brar *et al.*, "Hybrid Surface-Phonon-Plasmon Polariton Modes in Graphene/Monolayer h-BN Heterostructures," *Nano Lett.*, vol. 14, no. 7, pp. 3876–3880, Jul. 2014, doi: 10.1021/nl501096s.

[13] A. Rogach, Ed., *Semiconductor Nanocrystal Quantum Dots: Synthesis, Assembly, Spectroscopy and Applications*. Wien: Springer-Verlag, 2008.

[14] S. Ithurria and B. Dubertret, "Quasi 2D Colloidal CdSe Platelets with Thicknesses Controlled at the Atomic Level," *J. Am. Chem. Soc.*, vol. 130, no. 49, pp. 16504–16505, Dec. 2008, doi: 10.1021/ja807724e.

[15] C. Kittel, *Introduction to solid state physics*. New York: Wiley, 2005.

[16] L. Saviot, B. Champagnon, E. Duval, I. A. Kudriavtsev, and A. I. Ekimov, "Size dependence of acoustic and optical vibrational modes of CdSe nanocrystals in glasses," *J. Non-Cryst. Solids*, vol. 197, no. 2, pp. 238–246, May 1996, doi: 10.1016/0022-3093(96)00164-0.

[17] Ulrike. Woggon, "Optical Properties of Semiconductor Quantum Dots." Springer-Verlag Berlin-Heidelberg : Springer e-books, Berlin, Heidelberg, 2008.

[18] R. Ruppin and R. Englman, "Optical phonons of small crystals," *Rep. Prog. Phys.*, vol. 33, no. 1, pp. 149–196, Jan. 1970, doi: 10.1088/0034-4885/33/1/304.

[19] S. A. Cherevkov, A. V. Fedorov, M. V. Artemyev, A. V. Prudnikau, and A. V. Baranov, "Anisotropy of electron-phonon interaction in nanoscale CdSe platelets as seen via off-resonant and resonant Raman spectroscopy," *Phys. Rev. B*, vol. 88, no. 4, p. 041303, Jul. 2013, doi: 10.1103/PhysRevB.88.041303.

[20] L. D. Landau, E. M. Lifshits, J. B. Sykes, and J. S. Bell, "Quantum mechanics : non-relativistic theory," 1977. http://site.ebrary.com/id/10685767.

[21] J. J. Hopfield, "Theory of the Contribution of Excitons to the Complex Dielectric Constant of Crystals," *Phys. Rev.*, vol. 112, no. 5, pp. 1555–1567, Dec. 1958, doi: 10.1103/PhysRev.112.1555.

[22] A. G. Rolo and M. I. Vasilevskiy, "Raman spectroscopy of optical phonons confined in semiconductor quantum dots and nanocrystals," *J. Raman Spectrosc.*, vol. 38, no. 6, pp. 618–633, Jun. 2007, doi: 10.1002/jrs.1746.

[23] M. I. Vasilevskiy, private communication.

[24] E. S. F. Neto, S. W. da Silva, P. C. Morais, M. I. Vasilevskiy, M. A. Pereira-da-Silva, and N. O. Dantas, "Resonant Raman scattering in CdSxSe1−x nanocrystals: effects of phonon confinement, composition, and elastic strain," *J. Raman Spectrosc.*, vol. 42, no. 8, pp. 1660–1669, 2011, doi: 10.1002/jrs.2918.

[25] C. B. Walsh and E. I. Franses, "Ultrathin PMMA films spin-coated from toluene solutions," *Thin Solid Films*, vol. 429, no. 1, pp. 71–76, Apr. 2003, doi: 10.1016/S0040-6090(03)00031-2.

[26] C. Thomsen and S. Reich, "Double Resonant Raman Scattering in Graphite," *Phys. Rev. Lett.*, vol. 85, no. 24, pp. 5214–5217, Dec. 2000, doi: 10.1103/PhysRevLett.85.5214.

[27] A. C. Ferrari *et al.*, "Raman Spectrum of Graphene and Graphene Layers," *Phys. Rev. Lett.*, vol. 97, no. 18, p. 187401, Oct. 2006, doi: 10.1103/PhysRevLett.97.187401.

[28] C. Casiraghi *et al.*, "Raman Spectroscopy of Graphene Edges," *Nano Lett.*, vol. 9, no. 4, pp. 1433–1441, Apr. 2009, doi: 10.1021/nl8032697.

[29] C. Casiraghi, "Probing disorder and charged impurities in graphene by Raman spectroscopy," *Phys. Status Solidi RRL – Rapid Res. Lett.*, vol. 3, no. 6, pp. 175–177, 2009, doi: 10.1002/pssr.200903135.

[30] A. Das *et al.*, "Monitoring dopants by Raman scattering in an electrochemically top-gated graphene transistor," *Nat. Nanotechnol.*, vol. 3, no. 4, pp. 210–215, Apr. 2008, doi: 10.1038/nnano.2008.67.

[31] D. J. Late, A. Ghosh, B. Chakraborty, A. K. Sood, U. V. Waghmare, and C. N. R. Rao, "Molecular charge-transfer interaction with single-layer graphene," *J. Exp. Nanosci.*, vol. 6, no. 6, pp. 641–651, Dec. 2011, doi: 10.1080/17458080.2010.529174.

PART II

CHAPTER 4

EFFECTIVE 2HG IN BIOCOMPATIBLE ELECTRO-SPUN FIBERS

Contents

4.1 Introduction

Intensive efforts have been recently focused on nanoscale engineering and the design of materials with enhanced optical properties. Organic compounds with strong optical responses [1] and easy conjugation with biomaterials [2] are an attractive choice [3] since they can offer a broad range of potential applications ranging from fluorescence probes [4], light waveguides [5,6] and also frequency-doubled sources for local probes that can interact with biological systems.

These biomaterials are one of the platforms necessary for the proper development of emerging technologies ranging from sensing to treatment, including the possibility of restoring damaged biological systems.[7] Synthetic polymers, which represent the largest and most flexible class of biomaterials, are extensively used in several applications.[8,9] Their widespread use can be

attributed to their easily modified chemical composition, relatively simple synthesis, and high adaptability, since their physical and chemical properties can be tailored to the specific needs of their applications.[10] In addition to the above-mentioned advantages, another important factor in favor of employing polymer-based biomaterials is their cost, which is low compared to inorganic materials.[9] One way to obtain these biomaterials is to conjugate the polymer with a class of organic molecules, known as push-pull compounds.[1] These organic materials often have stronger nonlinear optical properties than inorganic materials due to their molecular units having highly delocalized electrons in the π orbitals in conjugation with additional electron donor and/or electron acceptor groups on

opposite sides of the molecules, making a push-pull system. It is also interesting that their properties can sometimes change dramatically when processed.[11]

One of the advantages of using organic materials over inorganic materials as nonlinear optical materials is the capacity to alter the organic molecular structure to improve the nonlinear optical properties. Since organic crystals often have weak intermolecular bonding interactions, the molecules in organic crystals often function independently of each other. How they are oriented relative to one another within the crystal lattice significantly influences the macroscopic optical properties of the organic crystal. In inorganic nonlinear optical materials, lattice vibrations play a dominant role in enhancing the nonlinear optical properties but in organic crystals, the nonlinear optical properties are determined largely by the electron polarizability in the π- bonding orbitals.

The selection of usable materials is based on factors such as ease of synthesis with low production cost, large second-order nonlinear susceptibility, thermal and chemical stability, wide optical transparency, availability of large single crystals, architectural flexibility for molecular design, ability to tune the surface morphology, high second harmonic generation (2HG) efficiency, adequate mechanical strength and some tolerance against optical damage by intense irradiation.[3] These requirements are difficult to all be fulfilled by a single crystal, so optimizing systems to fulfill the most advantageous combination of these characteristics is an on-going area of active research.

Good optical quality molecular organic crystals are more difficult to grow than inorganic crystals but their performance as excellent quadratic nonlinear crystals largely exceeds that of inorganic ones. Organic derivative nanocrystals growth under the form of thin films or nanofibers has been recently explored with a view of developing them for applications in ultrafast optics.[12–14]

However, it has proven difficult to incorporate these molecules at high density into non-centrosymmetric structures capable of providing a second-order nonlinear response since most of

them crystallize in a centrosymmetric space group, which impedes the observation of a significant macroscopic second-order nonlinear effect.

To overcome the problem of crystallizing in a centrosymmetric structure way, it's possible to use electric field poling, electrospinning. This is possible since the centro-symmetry can be broken by applying a strong electric field to align the molecular dipole moments along a single direction. To maintain this electric field-induced alignment, the molecules are typically incorporated inside polymeric hosts to prevent the relaxation into their natural, lower energy centrosymmetric state.[15–17]

Also, it is convenient that the electrospinning process allows also a facile processing of biomaterials offering the means to form systems based on nanofibers with high surface to volume ratios.[16]

Using a wide range of polymers, including the biopolymers, this process generally results in the formation of a colored mat composed of small fibers.

Two of the more widely used biopolymers are Polylactic acid (PLLA) used for nerve [18,19] and smooth muscle regeneration [20], and Polycaprolactone (PCL) used in artificial organs [21].

In this chapter we present the production and characterization of nanofibers exhibiting a strong quadratic non-linear optical response. These sub-micron fibers consisting of optically nonlinear organic molecules embedded in PLLA and PCL as a biopolymer host were produced by the electrospinning technique.

We have characterized the effective second-order nonlinear susceptibilities of these fibers by measuring their second harmonic response as a function of polarization using a femtosecond mode-locked Ti:Sapphire laser system with a fundamental wavelength centered at 800nm.

4.2 Experimental Methods

4.2.1.   Sample preparation

For this work, we used the preparation depicted in chapter 2.6.7 using Polylactic acid (PLLA) and Polycaprolactone (PCL) as the biocompatible polymer hosts for incorporating four different optically nonlinear organic molecules, namely 2-Methyl-4-nitroaniline, 2-Amino-4-nitroaniline, 3-Nitroaniline and 2-Methyl-benzyl-4-nitroaniline, Figure 4.1.
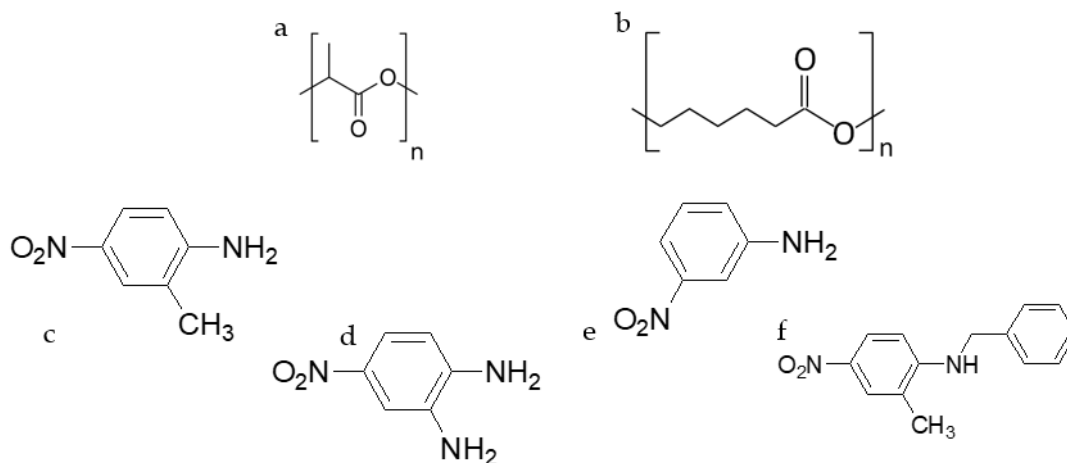
Figure 4.1 The hosts : Polylactic acid (PLLA) (a) and Polycaprolactone (PCL) (b) monomers.   The organic nonlinear molecules used:2-Methyl-4-nitroaniline(c); 2-Amino-4-nitroaniline (d); 3-Nitroaniline (e); 2-Methyl-benzyl-4-nitroaniline (f).

4.2.2.   Setup

A schematic diagram of the experimental setup for measuring the second harmonic response as a function of polarization is shown in Figure 4.2.
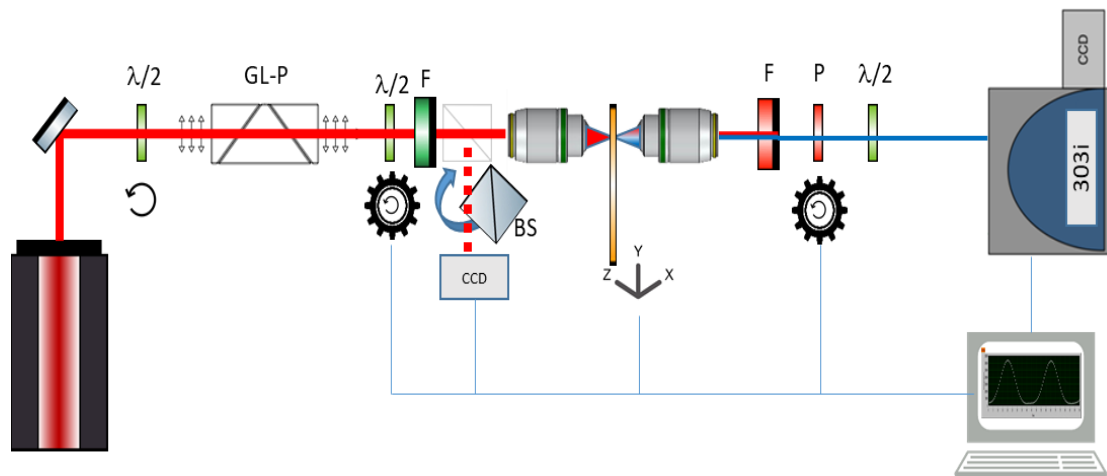
Figure 4.2 Diagram for optical SHG experiments implemented in our laboratory. The experiment is controlled through a LabVIEW program. $\lambda/2$-half wave-plate; GL-P- Glan-Laser Calcite polarizer; F-Filter; P-Polarizer; BS Beam splitter.

Briefly, a femtosecond Ti:Sapphire (Coherent Mira) laser oscillator pumped by a frequency-doubled CW Neodymium-laser (Coherent Verdi 5W) was used as the excitation light source. The source pulses had a center wavelength of 800 nm, a full-width at half-maximum (FWHM) spectral width of 13 nm, a duration of around 90 fs (FWHM), an average power ˜730 mW and were

generated at a repetition rate of 76 MHz. This experiment illuminated the electrospun nanofibers with linearly polarized fundamental light and then analyzing the polarization of the transmitted SHG light. The samples were mounted on an XYZ stage to facilitate the choice of the probed area. The average powers of the laser beam on the sample surface were controlled using a half wave-plate ($\lambda/2$) and a Calcite Glan-Laser polarizer combination. The polarizer also ensures that the incident polarization was linear. After attenuation, the polarized light passed through a computer motorized precision rotation mount with an achromatic half-wave plate ($\lambda/2$), this was used to rotate the polarization angle, ϕ of the incident light on the sample. After the half-wave plate, the fundamental light wave passed through a long-pass filter that blocks optical wavelengths below 780 nm. This ensures that no parasitic second harmonic signals from upstream optical components are detected.

The polarized beam of diameter 5 mm was then focused onto the sample using an objective microscope lens (10X, 0.3 N.A., Olympus Corp., Japan) to achieve a high enough power density to produce a measurable nonlinear response. Then the generated SHG light from the sample's surface, interface, or bulk, was collected by an identical objective lens in a trans-illumination configuration. A set of filters was used to eliminate the transmitted fundamental beam intensity and select the SHG light generated with a central frequency twice that of the source. A second computer motorized precision rotation mount with a polarizer was used as the analyzer of the generated SHG light.

This analyzer was rotated to be either parallel, q-p configuration, or perpendicular, q-s configuration, to the nanofiber's longitudinal axis. The analyzed SHG light was then coupled to the entrance slit of a 0.3 mm imaging spectrograph Andor Shamrock SR-303i, using a grating with a resolution of 0.20nm. Since the efficiency of the grating varies slightly with the polarization of the incoming light, the analyzed SHG light was also passed through a half-wave plate ($\lambda/2$) before entering the spectrograph. This half-wave plate ($\lambda/2$) was adjusted to maximize the efficiency of the grating used. The combination of the second wave plate and fixed analyzer orientation allows us to acquire the q-p and q-s curves with the same overall normalization. To visually observe how the incident fundamental beam illuminated the sample, a beam sampler was used to direct a fraction of the back-reflected light at a CCD camera. This allowed us to select the individual fibers that were probed.

4.2.3.   Data Collection & Analysis

A single integrated program, "2HGPAnalyser" was developed in LabView (flowchart in chapter 2.5.2) to control the setup (rotational stages and spectrograph), collect the data, and analyze it. The program continuously displayed the spectra collected from the spectrograph in real-time and then generated the corresponding polar plot.

This program automatized the experiment avoiding the tedious work of manually finding the longitudinal axis, rotating the incident light, and then analyzing the obtained spectra. For every spectrum obtained, the background is subtracted and then the integral of the spectrum is calculated. This integrated signal is the quantity represented in the polar plot. Before the measurement, the spectrometer, motors, and the data acquisition are configured in the "2HGPAnalyser" software, Figure 4.3.
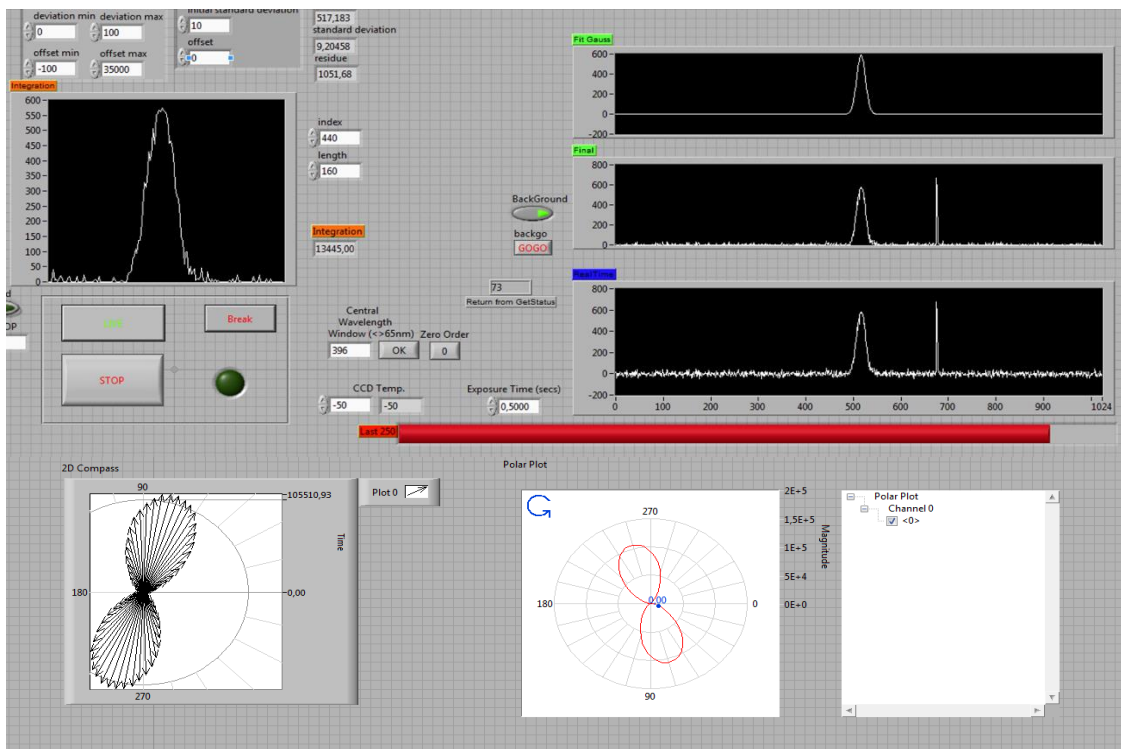
Figure 4.3 Layout of "2HGPAnalyser" software.

The spectral acquisition procedure begins with the initialization of the instruments. The application then scans the polarization angle of the incident fundamental beam by rotating step-by-step the polarizer in the analyzer interactively with the also step-by-step rotation of the half-wave plate ($\lambda/2$) to search for the maximum signal that can be correlated to the nanofiber's longitudinal axis.

After obtaining these positions, the motorized half-wave plate (λ/2) is rotated stepwise, between 0 and 360° for the acquisition in the q-p configuration first, as shown in Figure 4.4. Then the transmission axis of the motorized analyzer is rotated 90° and again the motorized half-wave plate (λ/2) is rotated stepwise to obtain the q-s configuration.
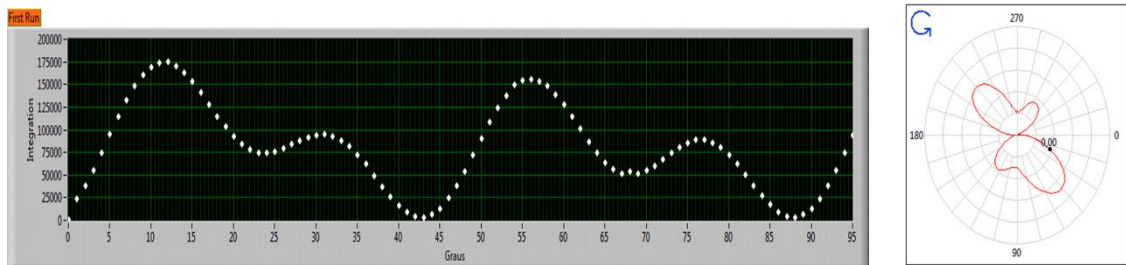
Figure 4.4 Example of the data obtained for one configuration. Respective real-time polar plot.

4.3 Results

The obtained electrospun nanofibers had several morphologies, as depicted in the SEM measurements in Figure 4.5.
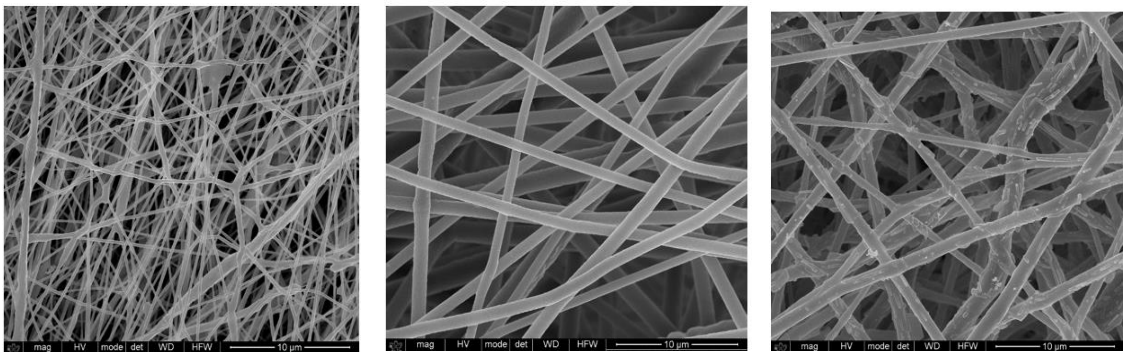
Figure 4.5 SEM micrographs from produced nanofibers. From left to right: 3NA-PCL, 2A4NA-PLLA, 2M4NA-PLLA hosted nanofibers.

The average fiber diameter ranged from slightly below 1 micrometer for the 2MBNA-PCL fibers to 200 nanometers for the case of 3NA-PCL hosted fibers, Figure 4.6. Every sample consisted of an array of continuous nanofibers, which were denser in the case of the 3NA-PCL system, Figure 4.5. The presence of beads or crystals grown on the external surfaces was detected in some of the nanofibers produced, specifically in the 2A4NA-PCL hosted system, Figure 4.6, and in both of the 2M4NA fiber systems.
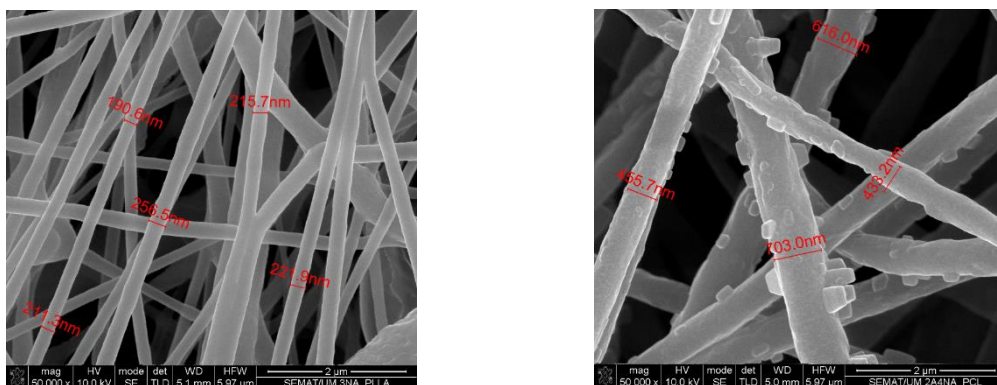
Figure 4.6 SEM micrographs of the produced nanofibers. 3NA-PCL (left) and 2A4NA-PCL (right) hosted nanofibers.

For all of the other nanofibers produced, the crystals were all embedded within the fiber interior. These were the best specimens obtained after tuning the spin coating parameters to optimize the nanofiber morphologies.

The SHG efficiency of the fiber arrays was measured using the polarimetry setup. A thin (2mm) BBO crystal was employed as a reference to calibrate the detection efficiency of our set-up.

Figure 4.7 shows the polarization variation of the SHG generated by the BBO single crystal used as a reference and 3NA-PLLA hosted nanofibers. Both curves present a similar trend, a stronger second harmonic intensity in the p-polarization than s-polarization output, but with a different ratio. However, the s polarization SHG of the 3NA-PLLA hosted nanofibers is relatively stronger displaying a different symmetry than that generated by the BBO crystal.

Using the signal of the BBO crystal, Figure 4.7, as a reference it was possible to estimate the relative efficiency of second harmonic generation for the several nonlinear molecules in both hosts. The relative signals taking into account only the excitation intensity, acquisition duration, and intensity of the acquired signal are listed in table 4.1.
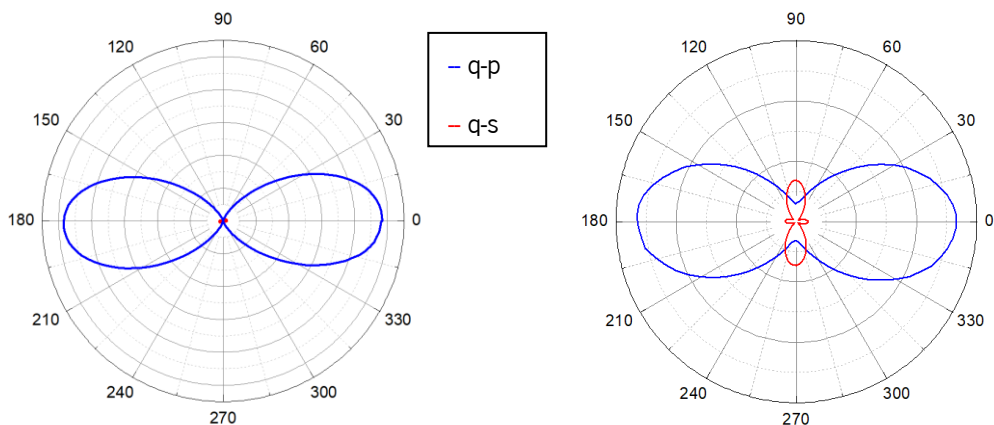
Figure 4.7 Polar plot of the SHG data generated by a 2mm thick BBO single crystal (left) and electro-spun 3NA-PLLA hosted nanofibers (right).

	PLLA	PCL
3-Nitroaniline	0.11	0.18
2-Amino-4-nitroaniline	0.08	0.06
2-Methyl-4-nitroaniline	0.06	0.04
2-Methyl-benzyl-4-nitroaniline		0.05

Table 4.1 Relative efficiency of 2HG for the several nonlinear molecules in both hosts.

In this preliminary evaluation, the 3NA had the best performance in both hosts compared to the other nonlinear molecules used. Also, the PCL host led to higher signals than PLLA.

For 3NA, an almost planar molecule consisting of an aromatic benzene ring with the acceptor nitro N_2O group in the para-position while the donor NH_2 group occupies the ortho-position, a strong molecular dipole moment points from donor to acceptor groups.

The crystallographic c-axis is a polar axis and summation of components of the molecular dipole moment projected on the c-axis results in a static polarization $P_s = 6.5 \times 10^{-2}\ Cm^{-2}$ [22,23] indicating the high electric accentricity of the crystal unit cell and a predominately electronic polarizability. The three-dimensional structure of 3NA can be described as an array of all-parallel polar layers perpendicular to [100] and interconnected by weak C–H⋯O bonds [24]. The most striking structural feature is a polar supermolecular charge-transfer network along $[00\bar{1}]$.

Analyzing the X-ray diffraction, Figure 4.7, powder patterns measured on a 3NA-PCL fiber array and the data for bulk 3NA and PCL published crystallographic information file we have that for 3NA bulk crystals, the most intense Bragg reflection is (211) closely followed by (400), while (311) and (110) have much smaller intensities, as shown in Figure 4.7, inset 3NA. For bulk crystalline PCL there are mainly three intense Bragg reflections with (110) one order of magnitude more intense than the other two, as shown in Figure 4.7, inset PCL.

However, the X-ray pattern of electrospun nanofibers shows that (400) Bragg reflection is the most intense reflection followed by (200) and now with the (211) reflection at least five times less intense than (400). This result indicates that for 3NA_PCL electrospun nanofibers there is a strong preferential crystalline orientation such that 3NA crystallizes inside the fibers with its crystallographic (400) plane coincident with the fiber array plane. The 3NA molecules lying on (400) plane are arranged so that as a net molecular dipole moment is displayed along the unit cell polar axis, which is in turn aligned with the fiber´s longitudinal axis. We may, therefore,

envision composite 3NA-PCL electrospun fiber arrays as two-dimensional nanohybrid structures where each fiber is formed at a microscopic level by highly oriented 3NA molecules inside the crystal unit cell. There is no expected molecular interaction through bonding between PCL and 3NA molecules.
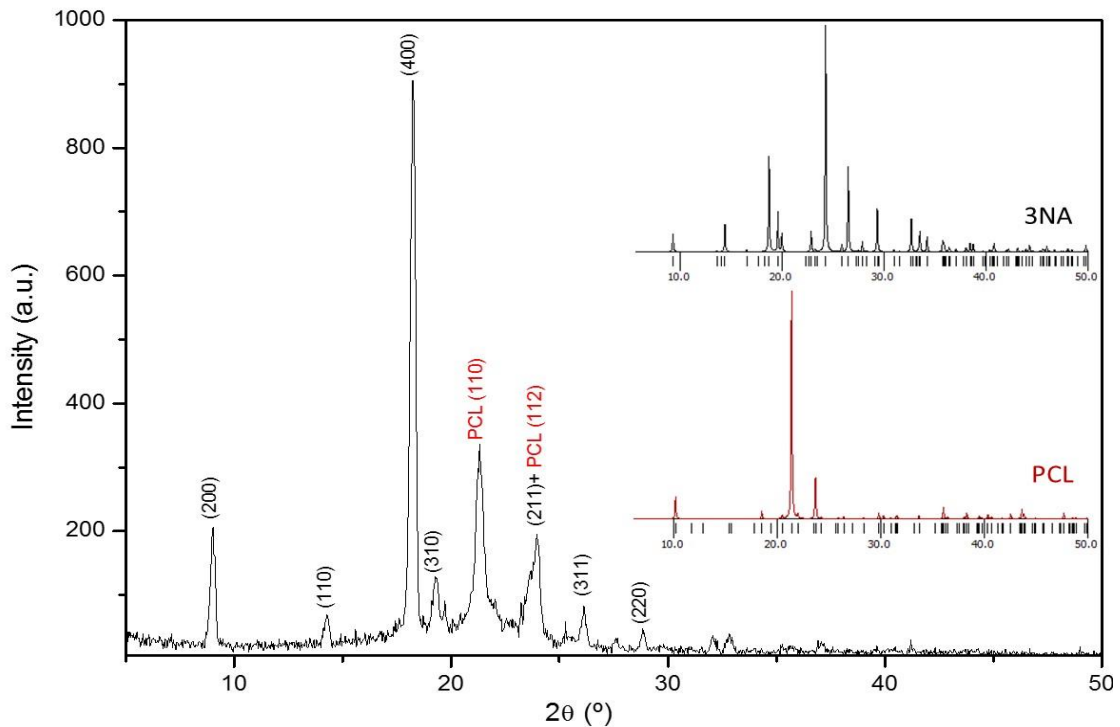
Figure 4.8 The X-ray diffraction powder patterns measured on a 3NA-PCL fiber array and for bulk 3NA and PCL, inset.

4.4 Discussion

According to the x-ray diffraction patterns, the 3NA crystals inside the fibers are mainly oriented with their crystallographic $\vec{c}$ polar axis along the longitudinal fiber axis having the crystallographic (400) plane in the fiber array plane. This highly oriented 3NA crystalline arrangement inside the fibers should lead to a very anisotropic nonlinear optical response for light traveling with its wave vector perpendicular to the polar axis. For crystals belonging to point group mm2 and taking into account Kleinman's symmetry conditions [25], the second-order optical polarizability coefficients are represented by the matrix in Eq. (4.1) [26] written in the conventional contracted notation.

$$\vec{d} = \begin{bmatrix} 0 & 0 & 0 & 0 & d_{31} & 0 \\ 0 & 0 & 0 & d_{32} & 0 & 0 \\ d_{31} & d_{32} & d_{33} & 0 & 0 & 0 \end{bmatrix}, \qquad (4.1)$$

and the polarizability components of the generated doubled frequency optical field are expressed by the relations,

$$P_x^{2\omega} = 2d_{31}E_x^{\omega}E_z^{\omega}$$
$$P_y^{2\omega} = 2d_{32}E_y^{\omega}E_z^{\omega} \qquad . \qquad (4.2)$$
$$P_z^{2\omega} = d_{31}E_x^{\omega}E_x^{\omega} + d_{32}E_y^{\omega}E_y^{\omega} + d_{33}E_z^{\omega}E_z^{\omega}$$

Here d_{ij} are the elements of the second-order polarizability tensor and E_x^{ω}, E_y^{ω} and E_z^{ω} are the electric field vector components of the incident fundamental optical field applied along x, y, and z optical crystal axis, respectively. Assuming the fundamental light is incident along the optical x-axis, then the detected signal will vary with the incident field polarization angle, θ, according to the following relations:

$$I_{q-p}^{2\omega} \propto \left[d_{32} \sin^2(\theta) + d_{33} \cos^2(\theta) \right]^2$$
$$I_{q-s}^{2\omega} = d_{32}^2 \sin^2(2\theta) \qquad . \qquad (4.3)$$

The observed polar plots are shown in Figure 4.9 were acquired by integrating the signal over 0.25 seconds with an average incident energy of 6.5 pJ. The "q-p" polarimetry curve closely approximates a single $\cos^4 \theta$ pattern, confirming the strong preferential crystallographic orientation of 3NA crystals embedded into the PCL polymer matrix. However, the "q-s" configuration does not display the expected four-lobed "cloverleaf" pattern of a $\sin^2 2\theta$ dependence. Furthermore, the ratio of the maximum signals for the "q-p" to "q-s" configurations is 9.3 nearly a factor of twenty smaller than the expected ratio based on the values for the second-order polarizability tensors elements of 3NA, $d_{33} = 21 \ pm/V$ and $d_{32} = 1.6 \ pm/V$ [27]. This suggests that the incident light illuminated several 3NA nanocrystals, some of which were not completely oriented along the preferential direction indicated by the x-ray diffraction data.
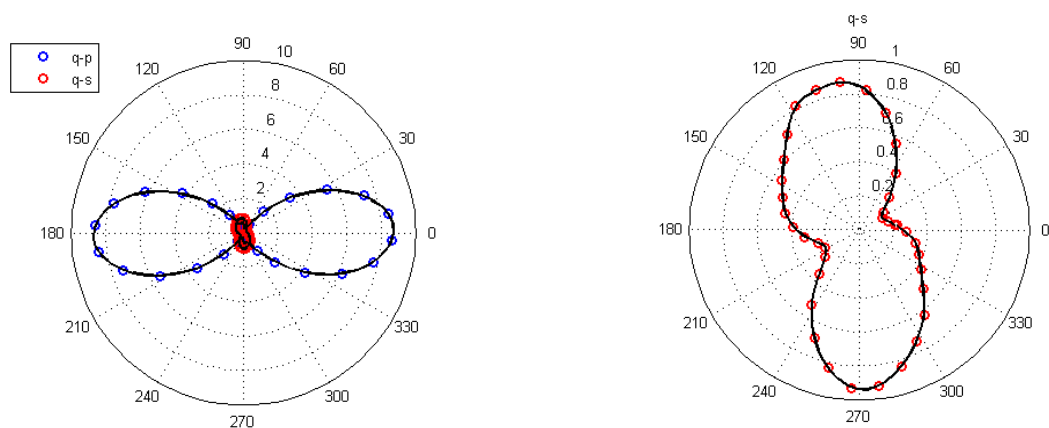
Figure 4.9 Polar plot of the SHG polarimetry data collected on a single 3NA electrospun nanofiber. These measurements correspond to the signal integrated over 0.25 seconds of a 76 MHz repetition incident fundamental beam with an average energy of 6.5 pJ per pulse. The radial axis values are expressed in millions of counts. (left) "q-p" and "q-s" polarimetry curve (right) a detailed look at the "q-s" polarimetry curve.

For comparison, we present the obtained polarimetry curves from a 3NA single crystal (100) platelet with dimensions $1.5 \, x \, 5 \, x \, 0.44 \, mm^3$ under the same excitation conditions with the fundamental incident beam normally incident. A detail of the q-s configuration shown in Figure 4.10 (right) more closely approximates the expected four-lobed "cloverleaf" pattern of a $\sin^2 2\theta$ dependence. We believe the pattern is asymmetric due to a difference in phase matching efficiency of SHG for light with a polarization orientated at an angle of $\pm 45°$ relative to the direction of the maximum q-p signal.
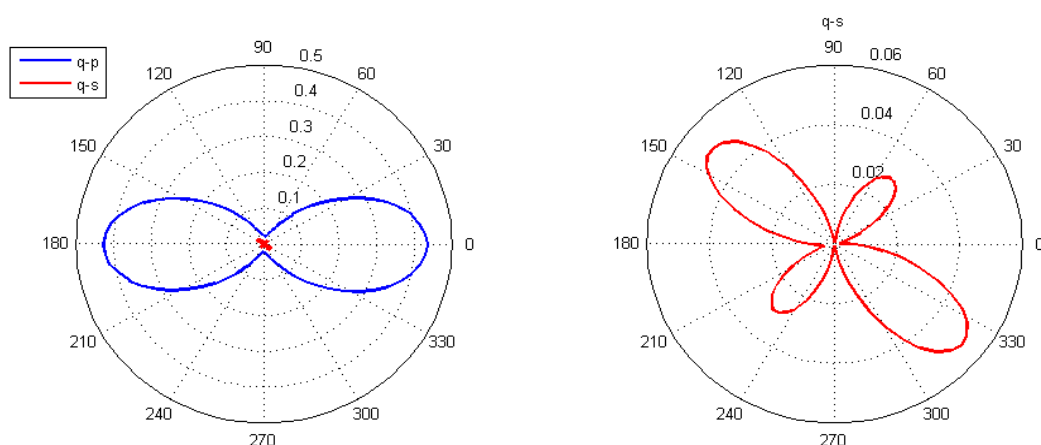
Figure 4.10 Polar plot of the SHG polarimetry data collected on single 3NA crystal (010) platelet with dimensions of $1.5 \, x \, 5 \, x \, 0.44 \, mm^3$. The radial axis values are expressed in million counts. (left) "q-p" and "q-s" polarimetry curves (right) a detailed look at the "q-s" polarimetry curve.

Note that this platelet is 440 μm thick, and that 3NA being orthorhombic is optically a biaxial crystal. Remarkably, the measured SHG output intensity for the q-p configuration of this platelet is lower than that of the submicron nanofiber. We attribute this lower output to phase mismatch in the SHG generated by the platelet.

To determine the effective nonlinear susceptibility coefficient, d_{eff}^{3NA}, the SHG response of the electrospun fibers was measured against an oriented BBO crystal of $1\,mm$ thickness. To calibrate the collection efficiency of the set-up, Type I phase matching occurs for an incident field at 800nm that propagates at 29.2 degrees relative to the optic axis with an effective second-order nonlinear coefficient of $d_{eff} = 2.0 \times 10^{-12}\,mV^{-1}$ [28]. Using the 10X objective, the effective length over which the fundamental and second harmonic beams remain superimposed with the BBO crystal is limited by the 69 *mradian* walk-off angle of the extraordinarily polarized second harmonic wave to a distance l_S^{BBO} of approximately 25 μm. By comparison, temporal walk-off between the fundamental and second harmonic beams is negligible under our conditions. Haifeng and Weiner [29]have developed a theoretical expression to estimate the efficiency of second-harmonic generation by ultrashort pulses. Given the tight focus produced by the microscope objective their expression reduces to the form:

$$\eta_{2\omega}^{BBO} = \frac{U_{2\omega}^{BBO}}{U_{\omega}^{BBO}} = \frac{\left[2\omega d_{eff}^{BBO}\right]^2}{n_{\omega}n_{2\omega}\lambda_0 c^3 \varepsilon_0} \sqrt{\frac{\pi^2 \ln(2)}{2}} \frac{U_{\omega}^{BBO} l_S^{BBO}}{t_p}. \tag{4.4}$$

Here U_{ω} and $U_{2\omega}$ are the energies of the incident fundamental and generated second harmonic pulses while t_p is the FWHM pulse duration of the fundamental beam, roughly 100 *femtoseconds*. At phase matching the respective refractive indices n_{ω} and $n_{2\omega}$ are both equal to 1.660. In contrast, the submicron thickness of electrospun nanofibres allows one to use the standard phase-matched plane wave result for second-harmonic generation:

$$\eta_{2\omega}^{3NA} = \frac{\left[2\omega d_{eff}^{3NA}\right]^2}{n_{\omega}n_{2\omega}\lambda_0 c^3 \varepsilon_0} \sqrt{\frac{2\ln 2}{\pi}} \frac{U_{\omega}^{3NA} L_{3NA}^2}{b t_p}, \tag{4.5}$$

where *b* is the confocal length of the focused incident beam (36 μm) and L_{3NA} is the thickness of an individual fiber.

Taking the ratio between the two above expressions allows one to estimate the effective second-order susceptibility coefficient of the electrospun fibers:

$$d_{eff}^{3NA} \approx d_{eff}^{BBO} \frac{\pi^{3/4}}{\sqrt{2}} \left(\frac{U_{\omega}^{BBO}}{U_{\omega}^{3NA}} \right) \sqrt{\frac{U_{2\omega}^{3NA}}{U_{2\omega}^{BBO}}} \frac{\sqrt{bl_{S}^{BBO}}}{L_{3NA}} , \qquad (4.6)$$

where we have neglected small corrections due to differences in the refractive indices. In our measurements, the ratio of detected energies in the "q-p" was $U_{2\omega}^{3NA} / U_{2\omega}^{BBO} = 0.032$ while the ratio of incident fundamental energies was $U_{\omega}^{3NA} / U_{\omega}^{BBO} = 10$. However, this latter factor should be corrected to take into account that an individual fiber with a diameter of 225 nm is significantly smaller than the estimated focused fundamental beam $1/e^2$ diameter of 3.3 μm, effectively reducing the ratio of incident energies. The estimated effective second-order susceptibility coefficient for the "q-p" configuration is approximately 80 pm/V. This is almost a factor of 4 greater than the largest tensor element $d_{33} = 21 \, pm/V$ for bulk crystalline 3NA [27].

4.5 Summary

The results show that polymer nanofibers embedded with optically nonlinear organic compounds give rise to a strong anisotropic response of the second-harmonic generation as a function of the polarization direction of the incident light. The macroscopic orientation of small nonlinear active molecules in conjugation with an appropriate biopolymer host can improve the optical properties of the materials, exceeding the properties of the bulk crystals. The values obtained for the 3NA-PCL hosted nanofibers encourage us to look forward to developing promising and low cost bioorganic optical devices, with several potential applications.

4.6 References

[1]   M. B. Ros, "Organic Materials for Nonlinear Optics," in *Engineering of Crystalline Materials Properties*, Dordrecht, 2008, pp. 375–390, doi: 10.1007/978-1-4020-6823-2_18.

[2]   D. Shan *et al.*, "Polymeric biomaterials for biophotonic applications," *Bioactive Materials*, vol. 3, no. 4, pp. 434–445, Dec. 2018, doi: 10.1016/j.bioactmat.2018.07.001.

[3]   S. R. Marder, "Organic nonlinear optical materials: where we have been and where we are going," *Chem. Commun.*, no. 2, pp. 131–134, Dec. 2006, doi: 10.1039/B512646K.

[4]   Y. Zhang and J. Yang, "Design strategies for fluorescent biodegradable polymeric biomaterials," *J. Mater. Chem. B*, vol. 1, no. 2, pp. 132–148, Dec. 2012, doi: 10.1039/C2TB00071G.

[5] S. Shabahang, S. Kim, and S.-H. Yun, "Light-Guiding Biomaterials for Biomedical Applications," *Adv Funct Mater*, vol. 28, no. 24, Jun. 2018, doi: 10.1002/adfm.201706635.

[6] M. Humar, S. J. J. Kwok, M. Choi, A. K. Yetisen, S. Cho, and S.-H. Yun, "Toward biomaterial-based implantable photonic devices," *Nanophotonics*, vol. 6, no. 2, pp. 414–434, 2016, doi: 10.1515/nanoph-2016-0003.

[7] J. Yin and S. Luan, "Opportunities and challenges for the development of polymer-based biomaterials and medical devices," *Regen Biomater*, vol. 3, no. 2, pp. 129–135, Jun. 2016, doi: 10.1093/rb/rbw008.

[8] M. F. Maitz, "Applications of synthetic polymers in clinical medicine," *Biosurface and Biotribology*, vol. 1, no. 3, pp. 161–176, Sep. 2015, doi: 10.1016/j.bsbt.2015.08.002.

[9] W. Scheler, "Synthetic polymers in biology and medicine," *Makromolekulare Chemie. Macromolecular Symposia*, vol. 12, no. 1, pp. 1–34, 1987, doi: 10.1002/masy.19870120103.

[10] H. F. Brinson and L. C. Brinson, Eds., "Characteristics, Applications and Properties of Polymers," in *Polymer Engineering Science and Viscoelasticity: An Introduction*, Boston, MA: Springer US, 2008, pp. 55–97.

[11] D. V. Isakov, M. S. Belsley, E. de Matos Gomes, H. Gonçalves, P. Schellenberg, and B. G. Almeida, "Intense optical second harmonic generation from centrosymmetric nanocrystalline para-nitroaniline," *Appl. Phys. Lett.*, vol. 104, no. 18, p. 181903, May 2014, doi: 10.1063/1.4875908.

[12] B. Hajj, S. Melanson, J. Desforges, S. Gauvin, D. Chauvat, and J. Zyss, "Performance and Quality Characterization of the Reference MNA Nonlinear Optical Molecular Crystal by Pockels Electrooptic Confocal Microscopy," *Advanced Optical Materials*, vol. 3, no. 8, pp. 1088–1095, 2015, doi: 10.1002/adom.201500059.

[13] Sophie Brasselet and Joseph Zyss, *Nano-Crystals for Quadratic Nonlinear Imaging : Characterization and Applications*. INTECH Open Access Publisher, 2010.

[14] H. Gonçalves, I. Saavedra, R. A. Ferreira, P. E. Lopes, E. de M. Gomes, and M. Belsley, "Efficient second harmonic generation by para-nitroaniline embedded in electro-spun polymeric nanofibres," *J. Phys. D: Appl. Phys.*, vol. 51, no. 10, p. 105106, Feb. 2018, doi: 10.1088/1361-6463/aaa9da.

[15] D. Isakov *et al.*, "High nonlinear optical anisotropy of urea nanofibers," *EPL*, vol. 91, no. 2, p. 28007, Jul. 2010, doi: 10.1209/0295-5075/91/28007.

[16] D. Li and Y. Xia, "Electrospinning of Nanofibers: Reinventing the Wheel?," *Advanced Materials*, vol. 16, no. 14, pp. 1151–1170, 2004, doi: 10.1002/adma.200400719.

[17] B. Ding and J. Yu, *Electrospun nanofibers for energy and environmental applications*. SPRINGER, 2016.

[18] R. Li, L. Chen, J. Fu, Z. Liu, S. Wang, and Y. Pan, "Promoting peripheral nerve regeneration with biodegradable poly (DL-lactic acid) films," *Int J Clin Exp Pathol*, vol. 8, no. 7, pp. 8057–8065, Jul. 2015.

[19] T. Haddad, S. Noel, B. Liberelle, R. E. Ayoubi, A. Ajji, and G. D. Crescenzo, "Fabrication and surface modification of polylactic acid (PLA) scaffolds with epidermal growth factor for neural tissue engineering," *Biomatter*, vol. 6, no. 1, p. e1231276, Jan. 2016, doi: 10.1080/21592535.2016.1231276.

[20] M. Santoro, S. R. Shah, J. L. Walker, and A. G. Mikos, "Poly(lactic acid) nanofibrous scaffolds for tissue engineering," *Adv Drug Deliv Rev*, vol. 107, pp. 206–212, Dec. 2016, doi: 10.1016/j.addr.2016.04.019.

[21] D. Mondal, M. Griffith, and S. S. Venkatraman, "Polycaprolactone-based biomaterials for tissue engineering and drug delivery: Current scenario and challenges," *International Journal of Polymeric Materials and Polymeric Biomaterials*, vol. 65, no. 5, pp. 255–265, Mar. 2016, doi: 10.1080/00914037.2015.1103241.

[22] A. C. Skapski and J. L. Stevenson, "X-ray crystal structure of the electro-optic material meta-nitroaniline," *J. Chem. Soc., Perkin Trans. 2*, no. 8, pp. 1197–1200, Jan. 1973, doi: 10.1039/P29730001197.

[23] G. Wójcik and J. Holband, "Variable-temperature crystal structure studies of m–nitroaniline," *Acta Cryst B*, vol. 57, no. 3, pp. 346–352, Jun. 2001, doi: 10.1107/S010876810100489X.

[24] A. E. Goeta, C. C. Wilson, J. C. Autino, J. Ellena, and G. Punte, "Hydrogen Bonding in Nitroanilines: Neutron Diffraction Study of m-Nitroaniline at 100 K," *Chem. Mater.*, vol. 12, no. 11, pp. 3342–3346, Nov. 2000, doi: 10.1021/cm001092u.

[25] D. A. Kleinman, "Nonlinear Dielectric Polarization in Optical Media," *Phys. Rev.*, vol. 126, no. 6, pp. 1977–1979, Jun. 1962, doi: 10.1103/PhysRev.126.1977.

[26] J. F. Nye and P. P. L. J. F. Nye, *Physical Properties of Crystals: Their Representation by Tensors and Matrices*. Clarendon Press, 1985.

[27] A. Carenco, J. Jerphagnon, and A. Perigaud, "Nonlinear optical properties of some m-disubstituted benzene derivatives," *J. Chem. Phys.*, vol. 66, no. 8, pp. 3806–3813, Apr. 1977, doi: 10.1063/1.434373.

[28] D. Eimerl, L. Davis, S. Velsko, E. K. Graham, and A. Zalkin, "Optical, mechanical, and thermal properties of barium borate," *Journal of Applied Physics*, vol. 62, no. 5, pp. 1968–1983, Sep. 1987, doi: 10.1063/1.339536.

[29] Haifeng Wang and A. M. Weiner, "Efficiency of short-pulse type-I second-harmonic generation with simultaneous spatial walk-off, temporal walk-off, and pump depletion," *IEEE Journal of Quantum Electronics*, vol. 39, no. 12, pp. 1600–1618, Dec. 2003, doi: 10.1109/JQE.2003.819531.

PART III

NANOSECOND TO PICOSECOND DYNAMICS OF 0D/2D NANOSTRUCTURES

Contents

5.1.   Introduction

Quantum dots (QDs), nearly 0D objects with the electronic energy spectra containing discrete levels, as briefly discussed in chapter 1.5.1, are excellent absorbers and emitters of electromagnetic radiation.[1] However, their assemblies (such as polymer thin fils with embedded colloidal QDs or matrix-free films composed of loosely liked nanocrystals) have relatively poor carrier transport properties as compared to conventional semiconductors.[2] In contrast, graphene and the family of transition metal dichalcogenide monolayers (TMDs) have high carrier mobilities.[3] These materials can be coupled to QDs via exciton-plasmon[4] or exciton-exciton

coupling[5]. This is a strong motivation to bring these systems together in hybrid structures and then investigate their interaction.

From a fundamental perspective and also to provide a foundation upon which to develop potential applications, it is crucial to understand the energy and charge transfer process in these systems. In particular, we wish to examine the case of energy/charge transfer from the Cadmium based QDs, to graphene and MoS_2.

Usually, the modification of the QDs photoluminescence decay rate when coupled to graphene or MoS_2, is attributed to non-radiative energy transfer[6–9] but the question arises if this is limited to incoherent effects through mechanisms such as Förster resonant energy transfer (or possibly radiative transfer for longer distances). If coherent processes contribute, one would expect such effects to occur on ultrafast timescales, picosecond or sub-picosecond timescales, at ambient temperatures

The emission dynamics of these systems were studied in this chapter using Time-Correlated Single Photon Counting (TCSPC) and a pump-probe technique, the transient absorption (TA) experiments.

5.2. Experimental methods

5.2.1. Samples

For the studies described in this chapter, systems of CdSe QDs, exfoliated samples of graphene and MoS_2, and CVD graphene were prepared and transferred to the same substrate as described in chapter 2.6. Thin Poly(methyl methacrylate) (PMMA) films and spacers were also produced as described in the same chapter. Details of the graphene-QDs structures have been provided in chapter 3. Examples of microscope images and Raman spectra used to characterize the MoS_2 flakes are shown in Figure 5.1.

To investigate the emission dynamics of these systems, three areas of the samples' surface were probed: (i) the thin-film containing only QDs (QDTF), (ii) a section with the QDs deposited over graphene (QDGR), and (iii) an area with the QDs on top of the MoS_2 (QDMoS).

It was possible to visualize the area of the MoS_2 flake using an optical microscope where one can see several bulk MoS_2 pieces and a small zone with the expected monolayer, Figure 5.1.

The measured Raman spectra confirmed that the latter exhibits the characteristic signatures of a few-layer MoS_2. Moreover, the frequency difference between the two Raman modes is 18.63

cm^{-1}, close to the value of the 18.40 cm^{-1} that is the principal fingerprint of the presence of a monolayer of MoS_2.[10,11]
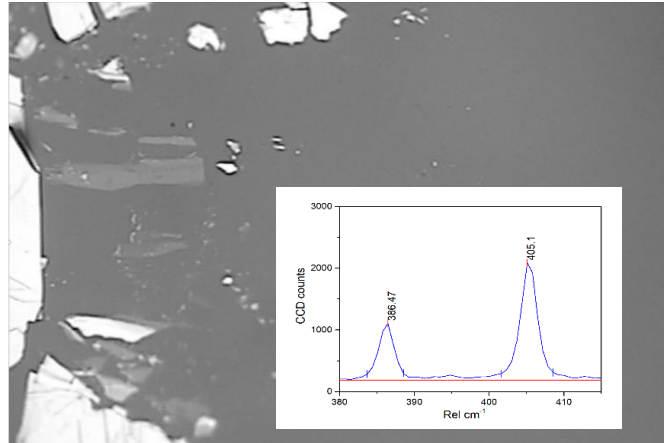
Figure 5.1 Microscope image with the presence of MoS_2 bulk and monolayer. Inset: Raman spectrum showing the out-of-plane A_{1g} phonon mode at $\approx$ 405 cm^{-1} and the in-plane E_{2g1} mode at $\approx$ 386 cm^{-1}.

For the graphene, the verification of the area where the scooped graphene was deposited was made first by an enhancement of graphene visibility on the transparent substrate by using the microdroplet [12] and the refractive index principle [13]; looking through the microscope glass increases the graphene contrast making it much easier to identify. This was only to pinpoint the area since the confirmation was also made by Raman spectroscopy where we see the Stokes phonon energy shift caused by laser excitation that creates two main peaks in the Raman spectrum. It is possible to see in Figure 5.2 (upper panel, left) the primary in-plane vibrational mode of the sp^2–bonded carbon atoms, the G peak at 1580 cm^{-1}, and the 2D mode at 2690 cm^{-1} which is an overtone of the D band. This D band and the overtone appear due to the breathing modes of sp^2–bonded atoms and is caused by disordered carbon atoms in the lattice. Also, we can use the ratio of the 2D/G peaks intensities to confirm the presence of a monolayer.[14,15] The QDs' presence was manifested by their Raman spectra and the characteristic PL emission. Using the FLIM setup we could see the effective coupling of the QDs to the monolayers as seen in Figure 5.8. Looking at the microscope image as already noted, it's almost impossible to identify a monolayer, but when we take a FLIM map the contrast in the lifetimes from the quenching of the QDs by the monolayer is quite noticeable (Figure 5.8, center). Data from integrating these FLIM maps over an area of 100 μm^2 to obtain the mean fluorescence intensities from the three systems was also acquired, Figure 5.2 (upper panel, right).
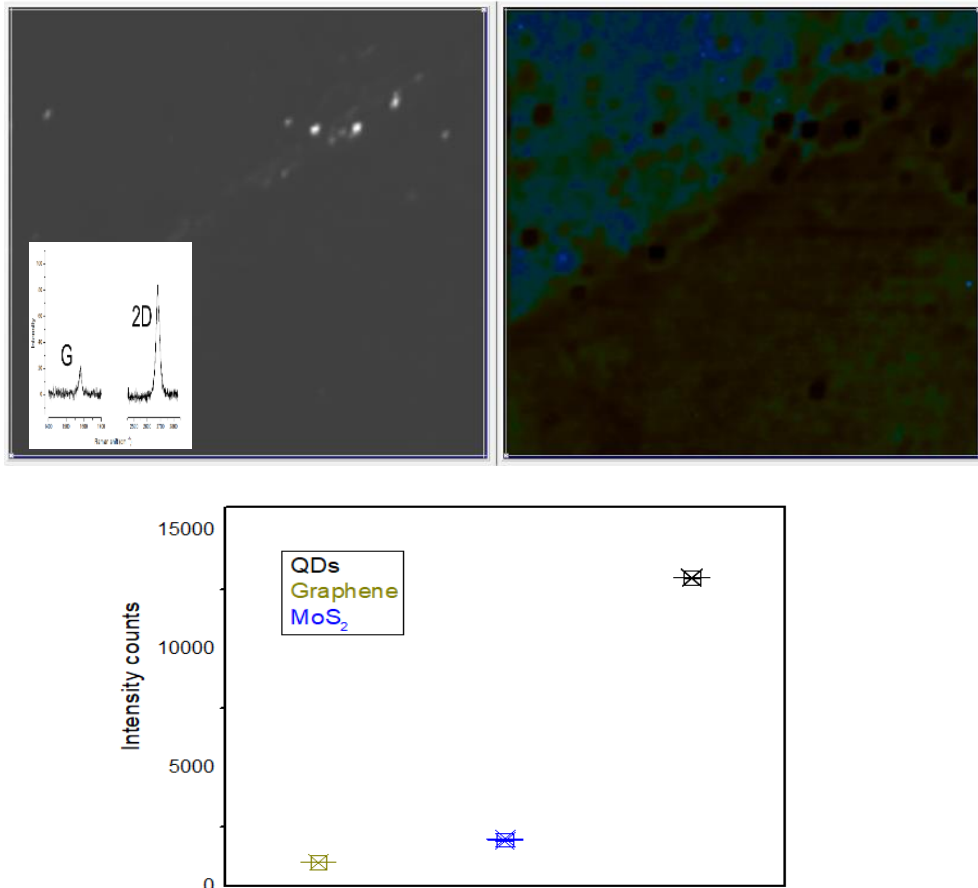
Figure 5.2 Upper panel: Microscope image showing the presence of a CVD graphene monolayer and QDs (left) with a Raman spectrogram of the lower right area shown in the inset. FLIM image of the same area where we can see the quenching of the QDs via its lifetimes (right). Lower panel: Integrated intensities for different areas.

5.2.2. Optical setup

The details of the laser system, the Time-Correlated Single Photon Counting (TCSPC) system, and the broadband ultrafast transient absorption setup with associated software are explained in Chapter 2. In this section, several modifications applied to that base description for the broadband TA are described.

Briefly, for the TCSPC experiment, the data was obtained using a mode-locked femtosecond Ti:Sapphire Laser (Titanium:Sapphire -Coherent Mira) and a frequency doubler/tripler for excitation. The detection system consists of a Multi-Channel Plate (MCP) photomultiplier and a Becker & Hickl detection card (SPC-150). The instrument response function of the system has a

temporal full-width half maximum of 20 ps. The excitation light was coupled into the microscope objective (20X, 0.8 NA, Zeiss, finite conjugate), which was used to focus the laser on the sample. The emission was collected by a lens in an L configuration and with magic angle arrangement (Fluorescence polarization detected an angle of 54.7° relative to the polarization of excitation laser) for solutions. For the solid-state samples, an epi-luminescence geometry was employed using the FLIM setup. It should be noted that during the measurements the excitation flux was kept very low (1 uJ/cm^2) to avoid the Auger recombination due to multi-photon excitations.

For the TA experiment, Figure 5.3, a portion (500 μJ/pulse) of the chirped output pulse from the regenerative amplifier (100 fs FWHM pulses at 800 nm, at 1 kHz repetition rate) was used to pump the parametric amplifier which generates the final pump pulses with energies of around 10 μJ per pulse, for the wavelengths studied in this the experiment. Before reaching the sample, the pump beam is optically chopped to provide a reference signal. The chopper was synchronized with the regenerative amplifier and worked at half of its repetition rate.

The remaining part of the fundamental beam of the chirped pulse regenerative amplifier was sent down a variable delay line that determines the relative delay between the pump and probe pulses. After the delay line, a single filament white-light continuum is generated in a sapphire plate used for the probe pulses. An iris was inserted in front of the focusing lens to adjust the beam diameter for optimal white light generation.
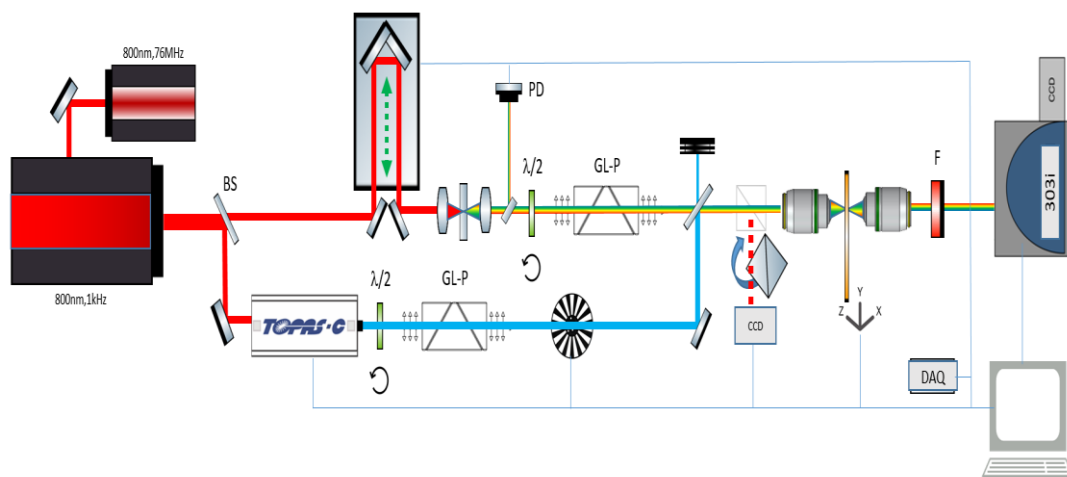
Figure 5.3 Diagram for optical differential transmission experiments implemented in our laboratory. The experiment is controlled through a LabVIEW program. λ/2-half wave-plate; GL-P- Glan-Laser Calcite polarizer; F-Filter; P-Polarizer; BS Beam splitter, PD-Photodiode.

The pump and probe beams are focused onto the sample in a collinear geometry using a microscope objective. To avoid any multi-photon excitation intensity effects, the experiments were made at low fluency, between 2.5 µJ cm^{-2} and 5 µJ cm^{-2} at the entrance pupil of the microscope objective. The probe intensity was always less than the pump intensity, and the probe spot size was chosen to be approximately 10 times smaller than the pump spot size to ensure homogeneous excitation over the probed area. The light was then collected by an identical objective lens in a trans-illumination configuration and subjected to a long-pass dichroic filter or a notch filter to diminish the spectral intensity of the pump and avoid saturating the spectrometer's detector.

The differential transmission signals were collected using an Andor Shamrock SR-303i spectrograph which is synchronously triggered externally, at 1kHz, at twice the frequency of the pump beam modulation. For normalization, the intensity of a small portion of the probe beam was registered by a fast photodiode and integrated by a Stanford Research boxcar integrator (SRS SR250) whose output was subsequently sampled via a NI-Daqmx.

The temporal resolution depends on the pulse duration of the pump pulse ($\sim$120 fs), the chirp of the white-light continuum, and the step size of the delay line. The temporal resolution was approximately 150 fs, and was experimentally determined by analyzing the data from the cross-phase modulation measured on a glass microscope slide to extract the chirp and the IRF.

5.2.3. Data Collection and Analysis

5.2.2.1 Time-correlated single-photon counting – TCSPC

The TCSPC data were acquired using the software SPCM64 from Becker & Hickl and was analyzed through the software SPCImage also from Becker & Hickl and FluoFit from PicoQuant GmbH. To fit the decay parameters to the fluorescence decay trace measured by the system, a deconvolution with the instrumental response function (IRF) was carried out.

Several methods can be applied to extract the lifetime from the collected data, $D(t)$, using the instrumental response function, $IRF(t)$:

$$D(t) = \int_{0}^{t} IRF(t`)F(t-t`)dt.$$

(5.1)

The most common ones are the nonlinear least squares (NLLS) [16] the method of moments (MM) [17], and the maximum entropy method [18]. In this work, we used the first two methods. The NLLS was employed since it is the method routinely used in decays with one or multi-exponential behavior. The MM was also used since it yields the lifetime distributions without assumptions about the temporal shape of the underlying kinetics.

For a correct evaluation of the decay parameters, the fit window was chosen so that the fitting range contained a portion of the time-independent background signal both to the right of the tail and before the IRF initial rise. The offset value was then fixed as a constant parameter in each fit and was assessed from the background count, present before the rising edge of the IRF.

The results of the NLLS fit are a set of calculated values, which describe the experimental data. These calculated values are optimized by minimizing the weighted sum of the squares, χ^2, of deviations of the calculated points, $Y(t)$, from the experimental ones, $X(t)$, according to equation 19, for all channels (numbered by i) of data in the fitting window.

$$\chi^2 = \sum_{i=1}^{n} W_i \left[X(t_i) - Y(t_i) \right]^2 = \sum_{i=1}^{n} \frac{\left[X(t_i) - Y(t_i) \right]^2}{X(t_i)} \qquad (5.2)$$

Here W_i is the weighting factor of the data in the i-th channel (out of a total of n channels sampled).

This approach assumes that the noise associated with each channel has zero mean and is independent of the other channel. To satisfy these conditions, a minimal number of counts, 10^2 -10^5,[16] must be collected to support the assumption of Gaussian statistics. In the case of MM analysis, the minimum is less demanding; usually 100 counts are sufficient.[17]

The χ^2 value was minimized by varying the decay parameter either by itself or together with the pre-exponential factor C_i,

$$F(t) = \sum_i C_i e^{\left(-\frac{t}{\tau_i} \right)} . \qquad (5.3)$$

Individual decay curves were initially fitted with a single exponential, followed by inspection of the goodness of the fit in the form of the weighted residuals, Figure. 5.4, and the magnitude of the reduced χ^2 criterion, which is expected to be near unity. If these objectives were not attained, additional exponential components were introduced.
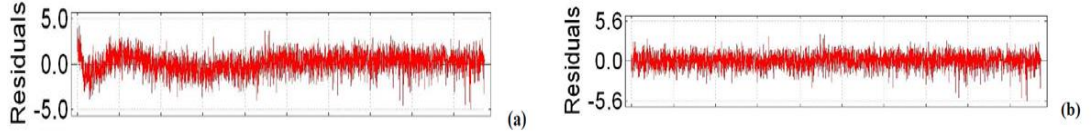
Figure 5.4 Weighted residuals, visualization of a non-ideal fit (a) and a smoother one (b). Notice that in the second case the residuals are uniformly distributed.

For fitting with the MM, the first moment was defined as:

$$M_1 = \sum_i t_i N_i \, .$$

(5.4)

where N_i is the number of counts in time channel i and t_i is the time for the i-th time channel, which results in the following mean lifetime estimation:

$$\tau_{1m} = M_1 \bigg/ \sum_i N_i \, .$$

(5.5)

Once the 1-st moment lifetime is found, one can correct for the instrument response function contribution using the simple prescription:

$$\tau = \tau_{1m_{(k_r)}} - \tau_{1m_{(IRF)}} \, .$$

(5.6)

where $\tau_{1m_{(IRF)}}$ is the first moment of the instrument response function.

5.2.2.2 Transient absorption – TA

The differential transmission data were collected as a function of the delay between the pump and probe pulses, $\Delta T_{\Delta t}$, using the "TASpectra" program that controlled the setup and sequentially measured the white light continuum transmitted through the sample with the pump on (the disturbed signal), T_{pumped}, and with the pump blocked (the reference signal), T at each Δt .

The spectra were acquired at 1024 wavelength values over a 120 nm range and collected over delays ranging from $\approx$ 250 fs to 2 ns with an adjusted linear time-delay step depending on the desired resolution. For each acquisition, the spectrum was normalized using the synchronized information from the generated white light continuum intensity.

The differential transmission spectra were then calculated as:

$$\Delta T_{\Delta t} = \frac{T_{pumped} - T}{T}.$$

(5.7)

At each delay time step, the acquired spectral region indicates the state of the system at that instant of time. The differential transmission spectra were averaged at each delay until the desired signal-to-noise ratio was achieved.

The differential transmittance of Eq. 5.7 used in this work follows the convention of plotting the excited state absorption, ESA, as a negative signal. Consequently, the stimulated emission, SE, and ground-state bleaching, GSB, correspond to positive signals.

The chirp due to the spectral components of the white light continuum, that is the fact that the lower frequency components (red part of the spectrum) arrived at the sample earlier than the higher frequency components (blue end of the spectrum), was corrected for by importing the obtained data and using a MATLAB script.

In the analysis procedure, due to the complexity of the TA dynamics, it is challenging to formulate a kinetic model that describes all these dynamics, so no specific model was applied. After the deconvolution with a Gaussian instrument response function, the data were analyzed using a sum of exponential functions to estimate the time scales on which the main processes are occurring.

5.3. Results and Discussion

5.3.1. PL decay kinetics

The first approach to gain insight into the processes occurring in these systems was an extension of previous work in our group where the quenching of an excited dye molecule by energy transfer to a graphene surface was evaluated together with its possible use as an accurate molecular ruler.[19] This time QDs were used instead of a dye molecule to investigate the effect of nearby graphene on the light emission kinetics of the QDs. The procedure included the fabrication of structures where the separation between the excited QDs and the graphene could be well controlled as it is crucial for performing such measurements. For this purpose hybrid structures were created consisting of a monolayer graphene flake, a PMMA layer acting as spacer and insulator, and a second thin layer of the same polymer doped with the QDs. For this experiment, QDs with emission at λ_{em} =520nm were used together with two different graphene samples. One of them was a monolayer of an exfoliated crystal and the other was produced by CVD. Both were

transferred onto the same substrate in adjacent areas so that we could guarantee that the conditions of the PMMA spacer and the QDs were the same for both. The distance was then controlled by PMMA spacers that were estimated to be roughly 35, 30, 25, 20, 15, 10, 5 and 2 nm thick. To assess the influence of graphene and the distance, TCSPC data were obtained from the QDs immobilized in the PMMA, with their emission band centered at 520 nm.

The emission of QDs has a fluorescence rate, k_r, characteristic of the QD. The emission quenching often observed in the presence of other materials implies that the QD was de-excited through other processes due to the presence of these materials. Possible de-excitation processes include charge transfer (CT) from the light-emitting entity to the environment and energy transfer (ET), already briefly discussed in the Introduction, and also internal conversion (IC). The total effect of these processes can be combined into a non-radiative decay rate, k_{nr}, as:

$$k_{nr} = k_{CT} + k_{ET} + k_{other}.$$

(5.8)

In general, a sum of radiative and non-radiative decay rates describes how fast the excited entities return to the ground state, accordingly, its inverse can be called an effective excited state lifetime.

$$\tau = \frac{1}{k_r + k_{nr}}.$$

(5.9)

This lifetime can be used as a measure of how much the QDs' emission is influenced by the local environment. Parameters affecting the lifetime, beyond the emission wavelength, include temperature, the state of the other material (e.g. the Fermi energy of graphene in our case), and the distance to this other material.

With this mind, TCSPC data for both graphene-QD systems were recorded, which are shown in Figures 5.5 and 5.6 on the next page. The reproducibility of measurement results was checked by carrying out at least five different acquisitions under the same experimental conditions.
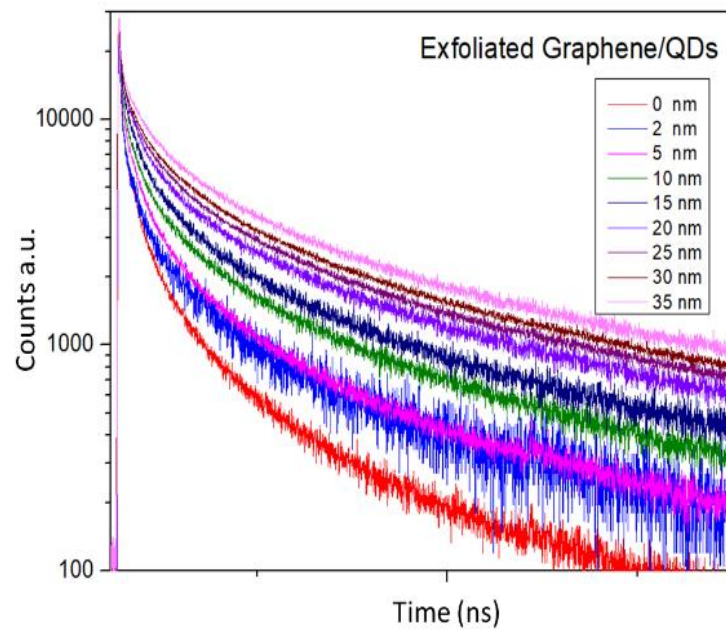
Figure 5.5 TCSPC decays obtained for the exfoliated graphene.
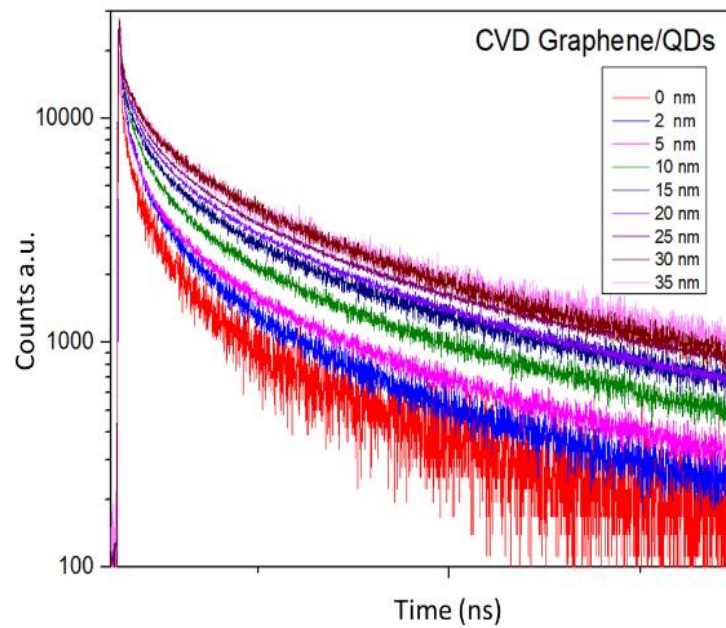
Figure 5.6 TCSPC decays obtained for the CVD graphene.

Both methods, i.e. multiexponential fitting and direct model-free evaluation of the first moment of the decay kinetics, explained in 5.2.2 were used to evaluate the effective lifetime. The results are presented in Figure 5.7. The variation in the effective lifetime at each distance was typically less than 2 % over the five acquisitions for each method.
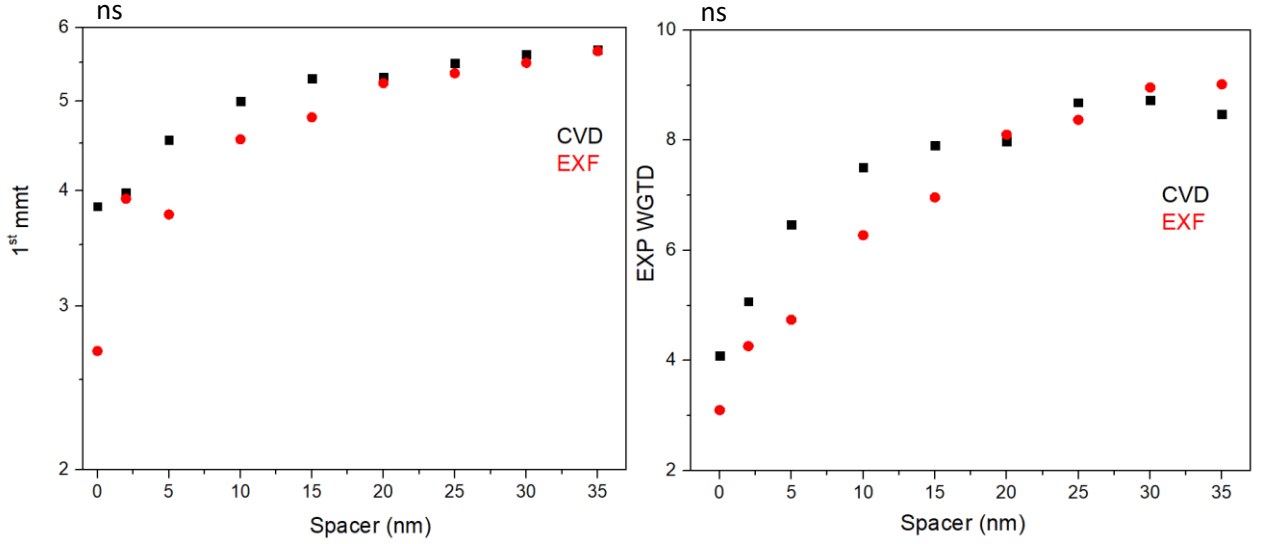
Figure 5.7 Extracted first moments of kinetics (left) and the weighted exponentials (right) for CVD (black points) and exfoliated (red points) graphene

As seen in Figure 5.7, similar trends are observed for the two evaluation methods. As expected, the graphene, either exfoliated or CVD-grown, provokes emission quenching and the effect is stronger the smaller the spacer between the QDs and the graphene surface. Interestingly, the distances over which the energy quenching is observed in this hybrid system reaches out to spacer thickness on the order of $\lambda_{em}/15$. This is lower than $\lambda_{em}/10$, the value previously found for the organic dye perylene [19] but it still considerably exceeds those found usually in molecular systems [20].

Let us discuss the dependence of the quenching effect upon the QD-graphene distance, i.e. the spacer thickness. First, it is convenient to write the non-radiative decay rate in the QD-graphene system with spacer thickness d as

$$k_{nr}(d) = k_{nr}^{(0)} + k_{nr}^{(1)}(d),$$ (5.10)

where $k_{nr}^{(0)} = \lim_{d \to \infty} k_{nr}(d)$ is unrelated to graphene. We may define an effective lifetime of QD emission in the absence of graphene as

$$\tau_0 1 = \left(k_r + k_{nr}^{(0)} \right)^{-1}. \tag{5.11}$$

Therefore, we have:

$$k_{nr}^{(1)}(d) = \frac{1}{\tau(d)} - \frac{1}{\tau_0}. \tag{5.12}$$

Also, it is convenient to define the following dimensionless quantity:

$$\Phi(d) = k_{nr}^{(1)}(d)\tau(d) = 1 - \frac{\tau(d)}{\tau_0}. \tag{5.13}$$

This quantity, which measures the efficiency of graphene as an emission quencher is plotted in Figure 5.8. It can be seen from the figure that $\Phi \approx 0$ for $d = 35$ nm, while it reaches the values of $0.6 - 0.7$ for the smallest d. We can see that the graphene-induced quenching is more efficient for the exfoliated sample, but in neither case is it as high as has been reported in some previous publications, over 90% in the work of Raja et al.[8] or even nearly 100% as found by Gaudreau et al.[21].
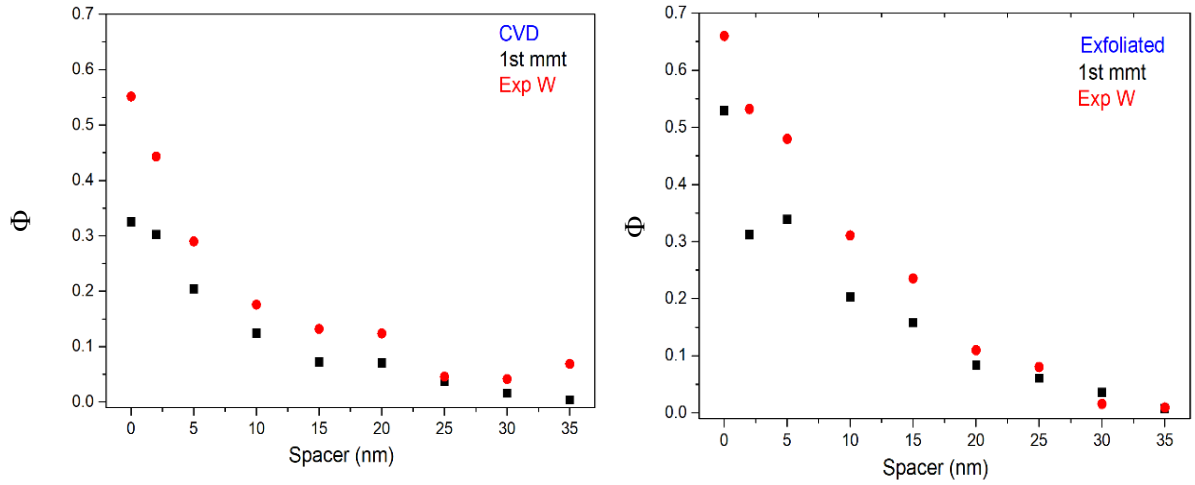
Figure 5.8 Dimensionless rate of graphene-induced quenching of the QD emission for the CVD (left) and exfoliated (right) graphene samples.

The simplest model that can be assumed is that graphene-induced quenching is entirely due to non-radiative (near-field) energy transfer from excited QDs to graphene. Indeed, $\Phi(d)$ is non-negligible for the distances that exclude any charge transfer process via electron tunneling (say, $d \approx 10$ nm); at the same time, it tends to zero still within the near-field zone ($d \ll \lambda$). Moreover,

we may assume further that the surrounding dielectric (PMMA) does not contribute to the non-radiative transfer processes as it is a transparent dielectric.

We may apply here the dipole-dipole (Förster) resonant energy transfer (FRET) theory briefly discussed in section 1.6.2. For a donor and an acceptor, both idealized as point dipoles and separated by a distance R, the FRET rate is given by (1.34) where the constant W_0 can be identified with the spontaneous emission rate of a dipole emitter located in an infinite homogeneous medium with the refractive index η (see e.g. [22]):

$$W_0 = \frac{\left|\vec{p}\right|^2 \omega^3 \eta}{3\pi\varepsilon_0 \hbar c^3}.$$

(5.14)

Here ω is the emission frequency and $\vec{p}$ is the transition dipole moment. The Förster [23] radius can be expressed as follows:

$$R_0^6 = \frac{3\hbar^4 c^4}{4\pi\eta^4} Q_A \int F_D(E) F_A(E) E^{-4} dE,$$

(5.15)

where Q_A is the integrated absorption cross-section of the acceptor and $F_D(E)$ and $F_A(E)$ are the emission and absorption lineshapes of the donor and acceptor, respectively, both normalized to unity. If the acceptor dipoles are distributed within a plane (representing the graphene sheet), the FRET rate can be obtained by integrating over this plane and written as follows:

$$\frac{k_{ET}}{W_0} = \rho_A \int_0^{2\pi} d\varphi \int_0^{\infty} r\,dr \left[\frac{R_0^6}{\left[r^2 + d^2 \right]^3} \right],$$

(5.16)

where ρ_A is the surface density of acceptor dipoles. The emitter $F_D(E)$ lineshape may be taken as a δ-function. Since $\rho_A Q_A F_A(E) = \beta(\omega)$ is the absorbance of the graphene sheet at photon frequency $\omega = E/\hbar$, the integration in Eq. (5.16) yields:

$$\frac{k_{ET}}{W_0} = \frac{3c^4}{8\eta^4 \omega^4 d^4} \beta(\omega).$$

(5.17)

This scaling law of the FRET rate from a point dipole emitter to graphene in the near-field zone, $k_{ET} \propto d^{-4}$, may be obtained more rigorously. [24] The graphene absorbance, for $\hbar\omega > 2E_F$ (i.e. in the visible region) is almost independent of the frequency and equal to $\approx 2.3\%$. [25] Therefore, Eq. (5.17) may be rewritten as:

$$\frac{k_{ET}}{W_0} = \frac{k_{ET}}{k_r} = const\left(\frac{\lambda}{d}\right)^4 .$$

(5.18)

To compare the above theoretical prediction with our experimental results, the data presented in Figure 5.7 was replotted in terms of $k_{nr}^{(1)}(d) = \Phi(d)/\tau(d)$, using a double logarithmic scale, Figure 5.9 right. No straight line was obtained and the experimental dependence $k_{nr}^{(1)}(d)$ is considerably weaker than the expected $k_{ET} \propto d^{-4}$ one.

The above theory does not take into account the finite size of the QDs. As a first approximation one can assume the dipole is located at the center fo the QD. In this case, the distance of the dipole from the graphene sheet can be approximated as $d^* = d + R_{QD} + s$, where R_{QD} is the radius of the nanocrystal core of the QD (which can be estimated as 1.5 nm from Figure 1.7 in the Introduction) and s is the size of the organic capping agent, AOT. The latter has a chain length of 12.57 Å, a head group diameter equal to 6 Å, which increases the effective QD radius by approximately 1.9 nm.[26,27] So, roughly $d^* = d + 3.4\,\mathrm{nm}$. Taking $\tau_0 = W_0^{-1}$, combining Eq. (5.13) with Eq. (5.18) and substituting d^* in place of d, the following formula for the parameter Φ is obtained:

$$\Phi(d^*) = 1 - \left[1 + const\left(\frac{\lambda}{d^*}\right)^4\right]^{-1} .$$

(5.19)

Using Eq. (5.19) and excluding to first three points with the smallest spacer thickness results in a fit that comes close to the expected d^{-4} dependence, as seen in Figure 5.9.

However, it fails to adequately explain the observed dependence for spacer thicknesses below 10nm. Extrapolating the fit for the exfoliated graphene to the limit of no spacer, one would predict a value for Φ of 0.99, much higher than the observed value of 0.66. This suggests that there is something missing in the above theory that is particularly important for small spacer thicknesses.
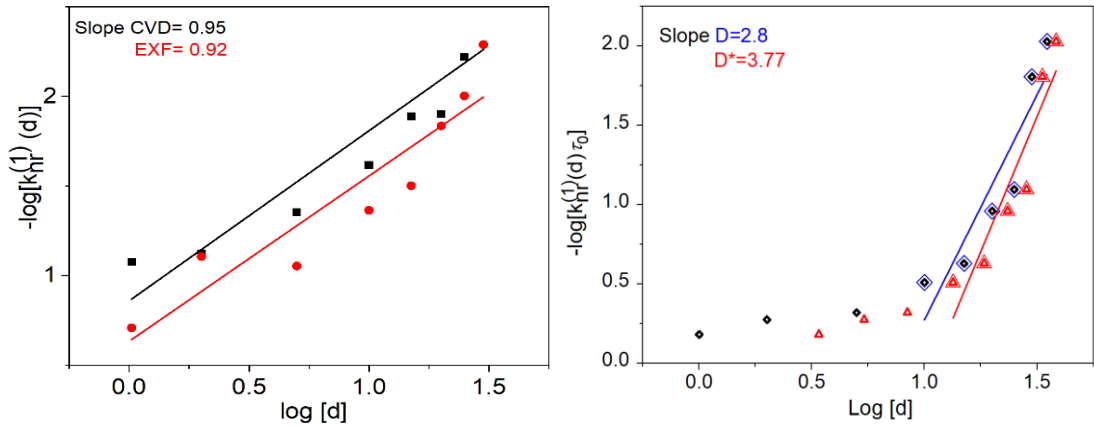
Figure 5.9 Double logarithm plot of k_{nr} in function of distance (left). Fit of the experimental values of the quenching rate for exfoliated graphene using equation (5.19) excluding the three nearest values, (right).

The theory does not take into account the effects of the substrate and the spacer layer on the radiative decay rate, which may take place due to the scattering of the light emitted by the QD at the interfaces back to the emitter.[22] However, since the energy transfer efficiency estimate was carried out using the ratio of the decays with and without the presence of graphene and the same dielectric spacer thickness, this influence, in principle, should cancel.[28] Some additional processes could potentially be significant. One of these might be graphene-mediated FRET between QDs, a mechanism that might oppose the graphene-induced quenching, may cause the too slow variation of the decay rate with the decreasing distance to graphene. Another possibility is the presence of trapped states in a small fraction of the QDs. If these trapped states are less susceptible to quenching by graphene, they could serve as a reservoir for the QD excitation.

An additional investigation of the near-field effects on QD emission was performed by placing a MoS_2 layer side by side with a graphene sheet. The sample was prepared with an exfoliated MoS_2 flake, which was transferred together with the CVD graphene to the same substrate to have exactly the same conditions, concentration, and thickness of the film of the spin-coated QDs, with no spacer in this case ($d = 0$).
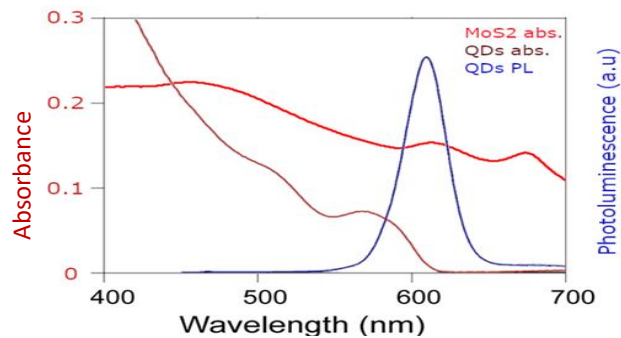
Figure 5.10 Absorption spectra of the MoS_2 monolayer and the QDs used in the decay kinetics measurements (red); photoluminescence spectra of the QDs (blue).

Notice that the QDs immobilized in the PMMA for this investigation for experimental purposes had their emission band centered at 610 nm, Figure 5.10.To compare the influence of graphene and MoS_2 on these QDs' emission, TCSPC data were collected, as shown in Figure 5.11. They are from the QDs immobilized in the PMMA thin film at several probing spots, both on top of the graphene, MoS_2, and in the area far away from either of the monolayers, at the same emission band at 610 nm.

These decays were fitted using the same approach as before. The values of the corresponding parameters and the quenching efficiency are given in Table 5.1
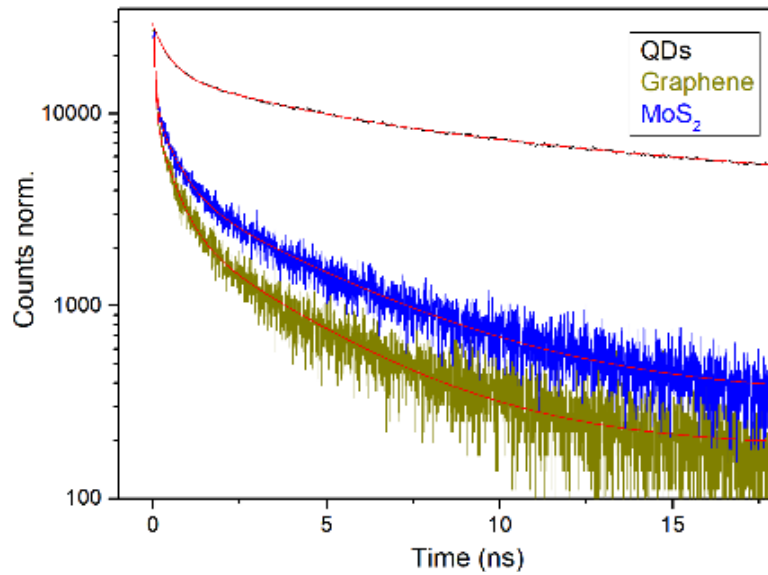
Figure 5.11 Decays and corresponding fits (red) obtained for three different areas of the same sample with TCSPC QDs deposited over graphene, MoS2 and away from both of them.

Multiexp. (ns)						System		First moment	
1st	2st	3rd	W.average	Φ				(ns)	Φ
0.53	3.42	0.04	1.4	0.91		QDGR		1.52	0.90
0.58	4.22	0.05	2.76	0.84		QDMoS		3.31	0.79
0.43	3.75	21.1	18.05			QDTF		16.45	

Table 5.1 Parameters obtained from both fit procedures of the measured photoluminescence decay kinetics.

It can be seen from Figure 5.10 that the QD emission band overlaps with the higher-energy absorption band of the TMD layer, which probably originates from B-excitons of MoS_2 (see section 1.5.4). The quenching rate was found to be lower for QDs on top of MoS_2, in comparison with the dots deposited on graphene. The first-moment lifetime value obtained for the QDs/graphene

system was ≈ 1.5 ns, while for the QDs/MoS2 system it was ≈ 3.3 ns. This is surprising given Eq. (5.17) since graphene's absorption is much lower than that of MoS$_2$, at the relevant wavelengths. One possible explanation is that the energy transfer between the QDs and the semiconductor layer is much stronger and reversible, i.e. the excitation can go back and forth, in contrast with the situation assumed by the Förster (perturbation) theory. If the dipole-dipole interaction energy is sufficiently large (in comparison with environment effects), the FRET theory and, consequently, Eq. (5.18) is not valid. Such regimes are known for molecular chains involved in energy transport in photosynthesis systems.[29]

5.3.2. Transient absorption

To better understand the 0D-2D hybrid systems, we carried out a pump and probe experiment and measured the differential transmission at a higher temporal resolution, hoping to gain some insight into the QD excited state evolution. Applying pump pulses with a central wavelength of 480 nm, we performed time-resolved measurements of the differential transmission of the QDs at wavelengths ranging from 520 nm to 650 nm, with an overall delay of up to 800 ps.

The spectra are characterized by a reduced absorption, i.e. photo-bleaching, at the QD exciton resonance around 580 nm. Photo-bleaching appears as a positive signal due to the convention adopted for the differential transmission, see Figure 5.12. This signal indicates that a significant portion of the population leaves the ground state and is transferred to the excited state, i.e. ground state bleaching, GSB.
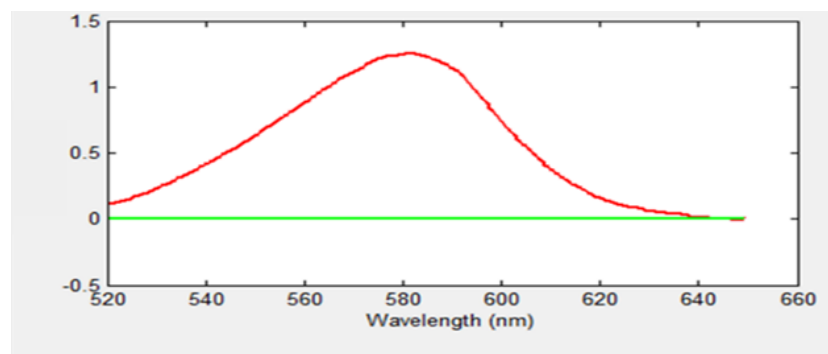
Figure 5.12 Differential transmission spectrum of the QDs around the bleaching wavelengths with scale -ΔT*10^3 (left). The red curve correspond to the differential transmission at a time delay of 1 ps between the pump and probe pulses.

One can readily find both large and small differences in these differential transmission spectra, presented in Figures 5.13 and 5.14. on the following page.
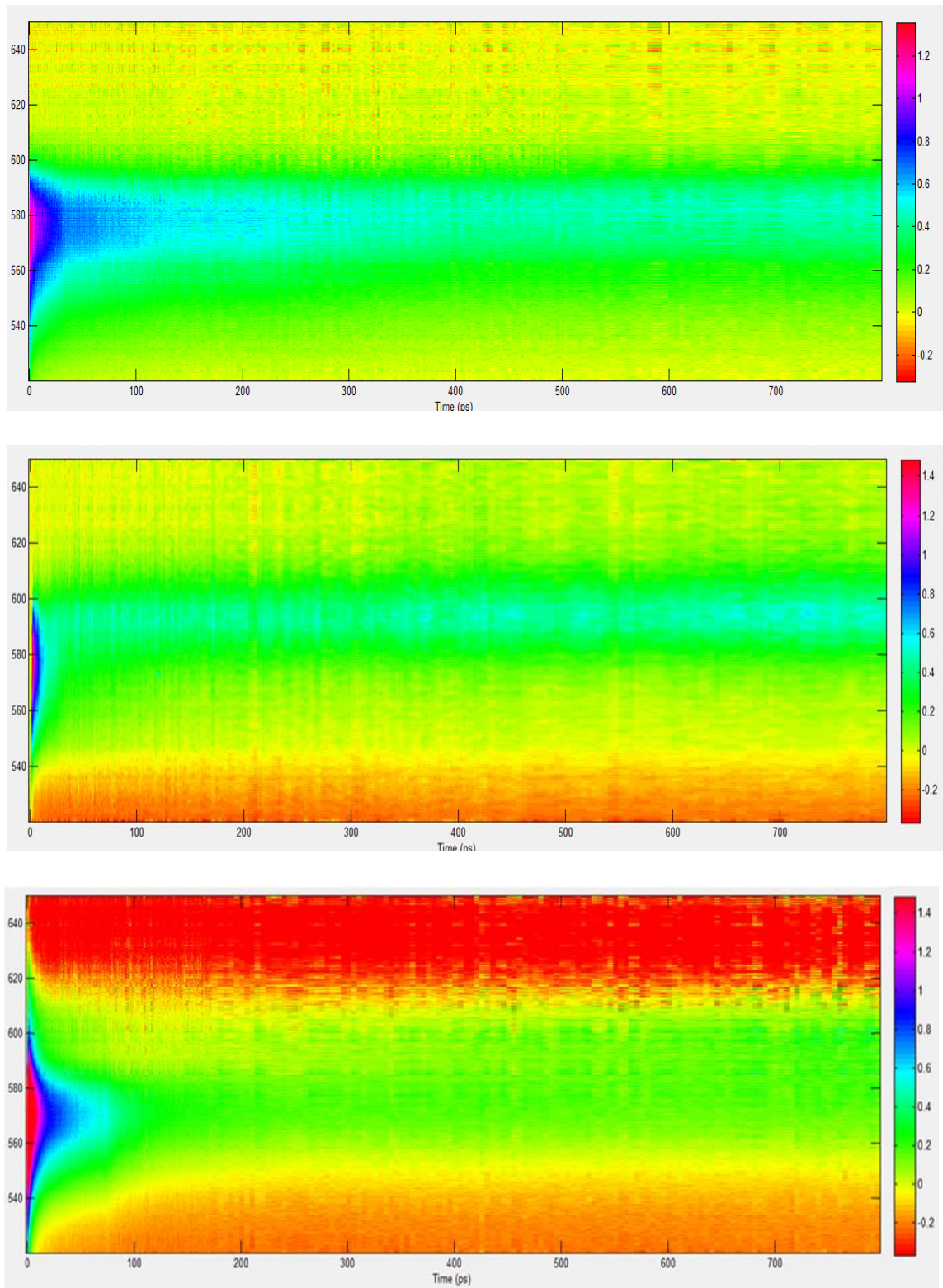
Figure 5.13 Transient transmission spectra obtained for the QDs on the glass microscope slide (top), on top of a graphene monolayer (middle) and on the MoS2 monolayer (bottom). Vertical axis presents the wavelength (520 to 650 nm); Color-bar scale: $\Delta T*10^{-3}$.
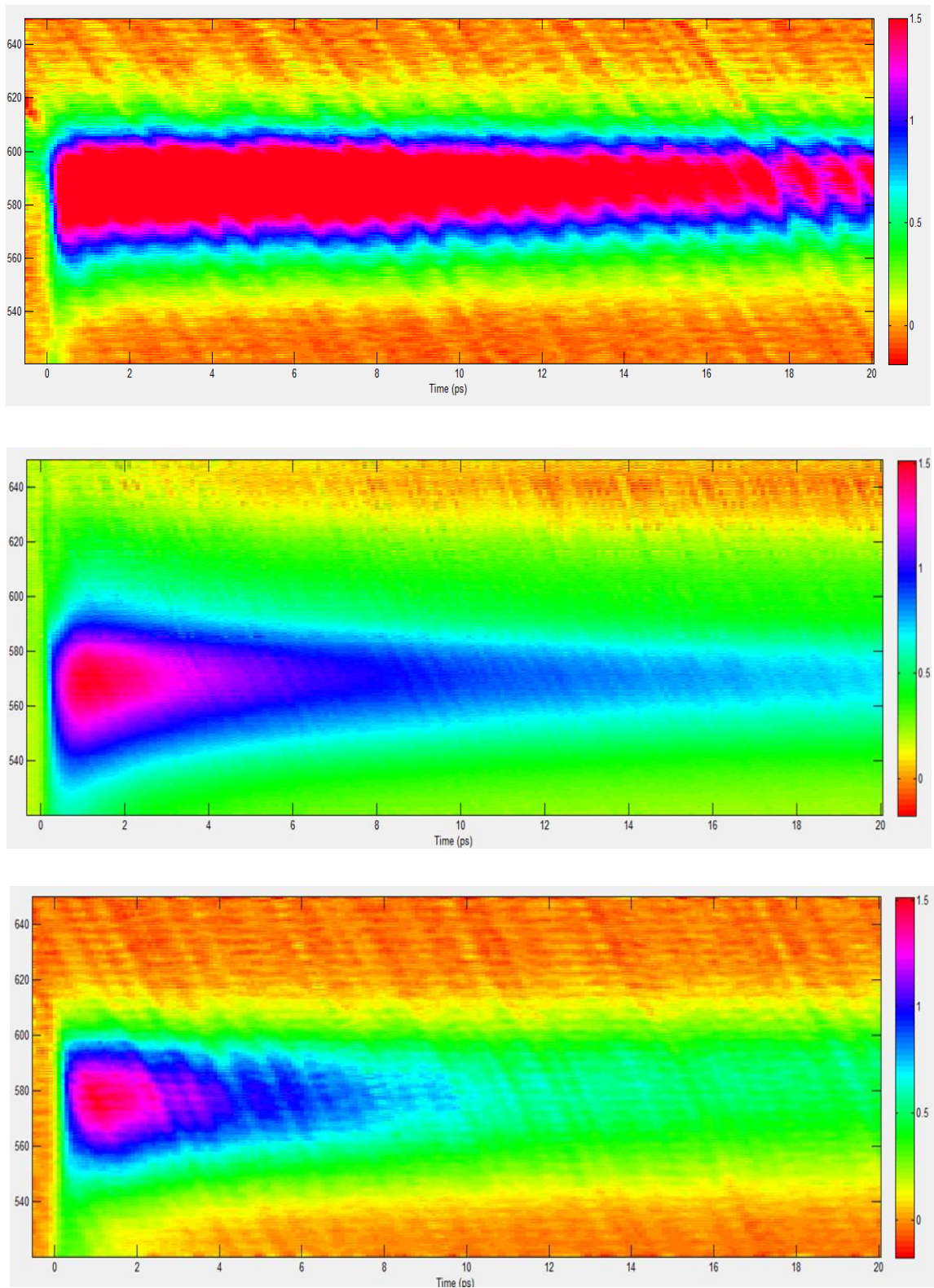
Figure 5.14 Transient transmission spectra for the QDs on the glass microscope slide (top), on graphene (middle) and on the MoS_2 monolayer (bottom). 20 ps time scale (bottom).). Vertical axis presents the wavelength (520 to 650 nm); Color-bar scale: $\Delta T * 10^{-3}$.

The most obvious difference is the greater temporal persistence of bleaching near the excitonic absorption band after initial excitation for the QDs on the glass substrate which is consistent with the TCSPC measurements. Also, the initial bleaching centered on the excitonic absorption has a considerably shorter duration for the QDs-graphene sample compared to the other two. A more subtle difference is the slight apparent shift of the initial bleaching to longer wavelengths in the QDs-graphene sample. Analyzing a more restricted time scale shown in Fig. 5.14 highlights these differences.

The initial bleach signal centered near 580 nm is depleted faster for QDs coupled to the monolayers, indicating strong coupling between the QD excitons and the monolayers. Graphene is more efficient than MoS_2 in this respect. The bleaching center of gravity appears shifted towards higher energies in the QD/MoS_2 system.

Plotting the change in absorbance as a function of the wavelength for various time delays, Figure 5.15, it becomes clear that both the QDs on glass and the QD-graphene system peak bleaching wavelengths relaxes to the red. For the QD-graphene sample, this shift is nearly 11 nm,
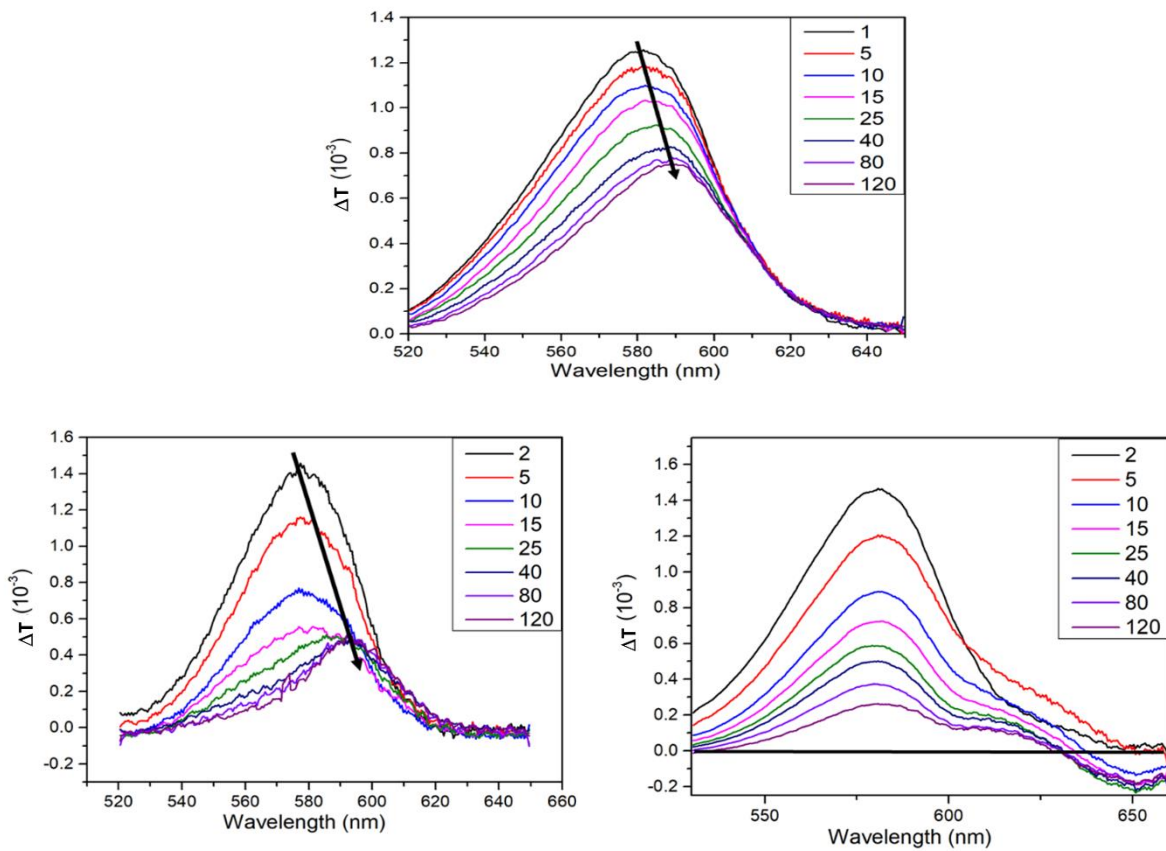
Figure 5.15 Pump-induced transmission change obtained for the QDs on a glass microscope slide (upper panel), coupled to the graphene (lower left) and MoS_2 monolayer (lower right) at various delay times (2, 5, 10, 15, 25, 40, 80, and 120 ps) after excitation.

corresponding to an energy shift of nearly 40 meV, while for the QDs on the glass substrate it is 8 nm or 29 meV. In contrast, the peak of the QD/MoS$_2$ systems moves only 2 nm (7 meV). This being a possible indication of the presence of homo-FRET in these systems.

For the sample with graphene, the initial changes in the bleaching spectra are faster, but after 40 ps the spectra seem to stabilize. In MoS$_2$ coupled QDs at 15 ps, it is possible to notice a feature signal from the B-exciton convoluted with the bleaching of the QDs. Due to this convolution, it was not possible to see the rise of this fingerprint. But since it is not present during the initial delay times, its appearance must be related to the QDs evolution and rather than some being associated with some feature of the incident light. Around 650 nm (1.91 eV), a photo-excited induced absorption feature appears between 5 and 10 ps after excitation, which seems to stabilize after 15 ps.

The differential transmission bleaching decays were monitored at 580 nm, Figure 5.16, and fit to a bi-exponential function.
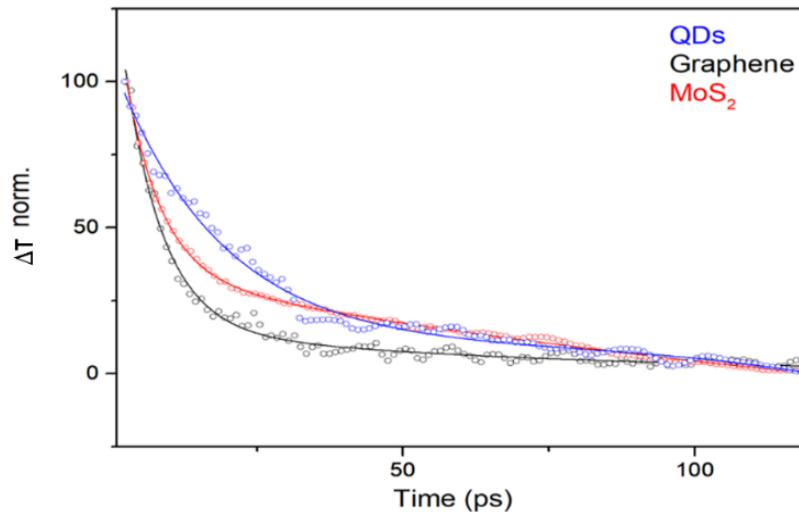
Figure 5.16 Normalized bleach recovery kinetics at 580 nm.

The resulting decay lifetimes and the average lifetimes are presented in Table 5.2.

Table 5.2 Kinetic parameters from bi-exponential fits to the measured transient decay for the first 125 ps after excitation.

	Multiexp(ps)					τ_{avg}
	A1	τ_1	A2	τ_2		τ_{avg}
QDGR	17%	72.109	83%	6.367		17.24
QDMOS	40%	79.164	60%	6.388		35.39
QDTF	33%	167.101	67%	15.484		66.18

Different time scales are observed. First, upon photoexcitation by the pump pulse, the bleaching quickly reaches a maximum value on a fast sub-picosecond time scale. A fast initial recovery then occurs within a few picoseconds followed by a slower recovery. Possible thermal diffusion of hot photoexcited carriers out of the pump or probe focus spots was ruled out as a contributing factor to the observed transients by changing the focus spot size in measurements. Carrier generation by the pump pulse and subsequent hot carrier intraband relaxation can contribute to the observed transients in the first picosecond but our measurement was limited by the temporal resolution of the setup and it was not possible to get a practical deconvolution, so we will only address the recovery.

The ground state exciton bleach recovery dynamics of the QDs in the presence of the 2D materials is faster compared with QDs supported only by the glass microscope slide with similar decays fit for the graphene and MoS_2 samples. However, the fast component of the graphene coupled sample amplitude is significantly larger than that of the MoS_2 sample.

The multi-exponential nature implies that more than one relaxation process is involved. The fast decay was rapid and did not exhibit a strong dependence on pump fluence, therefore, we can rule out exciton annihilation. For the longer time constant, τ_1, in the QD thin film seem to arise from the non-radiative recombination mediated by a thermal escape of the photocarriers out of QDs. When in the presence of the 2D materials, this longer decay time constant shortens.

5.4. Summary

In summary, it has been possible to couple the QDs to CVD and exfoliated graphene, and the emission quenching effect of the latter was demonstrated. It was found that the CVD graphene was not so effective a quencher as the exfoliated graphene, probably due to the method of fabrication and transfer that could introduce impurities,. The experimental data have been compared to the theoretical prediction based on a Förster-type energy transfer scaling law with distance from the emitter to the graphene monolayer, $k_{ET} \propto d^{-4}$. Even though a reasonable fit could be obtained for the case of exfoliated graphene by making a finite-size correction to the QD (semiconductor core + organic shell) for longer distances, the dependence of the non-radiative decay rate on the distance is weaker than expected, even though the investigated regimes are all within the near-field zone (the effect of graphene vanishes at a distance of roughly $\lambda_{em}/15$).

Coupling the QDs to MoS_2, with approximate energy matching to the B-exciton of the latter also led to a considerable quenching of the QD emission. Surprisingly in the framework of the Förster theory, this quenching was found weaker than in the case of graphene (the distance was the same in both cases). This suggests that the Förster theory is not valid in this case, possibly indicating that exciton energy transfer between QDs and MoS_2 may be reversible.

Further time-resolved studies of the 0D-2D systems have been performed using the pump-probe scheme and measuring the differential transmission. This allowed us to follow the evolution of the ground-state bleaching (GSB) of the QDs and correlate it with the influence of the neighboring 2D materials. The multi-exponential nature of the temporal evolution of the GSB implies that more than one relaxation process was involved. The fastest components which dominate the bi-exponential fit (Table 5.2) are all below the width of the FLIM instrument response, thus, the use of FLIM to quantify the energy transfer rates in these systems may be insufficient.

5.5.   References

[1]   A. Rogach, Ed., *Semiconductor Nanocrystal Quantum Dots: Synthesis, Assembly, Spectroscopy and Applications*. Wien: Springer-Verlag, 2008.

[2]   J. Wu and Z. M. Wang, Eds., *Quantum Dot Solar Cells*. New York: Springer-Verlag, 2014.

[3]   "2D Materials for Nanoelectronics," *CRC Press*. https://www.crcpress.com/2D-Materials-for-Nanoelectronics/Houssa-Dimoulas-Molle/p/book/9781498704175 (accessed Nov. 13, 2019).

[4]   E. Cao, W. Lin, M. Sun, W. Liang, and Y. Song, "Exciton-plasmon coupling interactions: from principle to applications," *Nanophotonics*, vol. 7, no. 1, pp. 145–167, 2018, doi: 10.1515/nanoph-2017-0059.

[5]   S. Roy *et al.*, "Observation of Charge Transfer in Heterostructures Composed of MoSe2 Quantum Dots and a Monolayer of MoS2 or WSe2," *J. Phys. Chem. C*, vol. 121, no. 3, pp. 1997–2004, Jan. 2017, doi: 10.1021/acs.jpcc.6b11778.

[6]   O. Salihoglu, N. Kakenov, O. Balci, S. Balci, and C. Kocabas, "Graphene as a Reversible and Spectrally Selective Fluorescence Quencher," *Sci. Rep.*, vol. 6, p. 33911, Sep. 2016, doi: 10.1038/srep33911.

[7]   D. Prasai *et al.*, "Electrical Control of near-Field Energy Transfer between Quantum Dots and Two-Dimensional Semiconductors," *Nano Lett.*, vol. 15, no. 7, pp. 4374–4380, Jul. 2015, doi: 10.1021/acs.nanolett.5b00514.

[8]   A. Raja *et al.*, "Energy Transfer from Quantum Dots to Graphene and MoS2: The Role of Absorption and Screening in Two-Dimensional Materials," *Nano Lett.*, vol. 16, no. 4, pp. 2328–2333, Apr. 2016, doi: 10.1021/acs.nanolett.5b05012.

[9]   F. Prins, A. J. Goodman, and W. A. Tisdale, "Reduced Dielectric Screening and Enhanced Energy Transfer in Single- and Few-Layer MoS2," *Nano Lett.*, vol. 14, no. 11, pp. 6087–6091, Nov. 2014, doi: 10.1021/nl5019386.

[10] B. Chakraborty, H. S. S. R. Matte, A. K. Sood, and C. N. R. Rao, "Layer-dependent resonant Raman scattering of a few layer MoS2," *J. Raman Spectrosc.*, vol. 44, no. 1, pp. 92–96, 2013, doi: 10.1002/jrs.4147.

[11] E. Mercado, A. Goodyear, J. Moffat, M. Cooke, and R. S. Sundaram, "A Raman metrology approach to quality control of 2D MoS2film fabrication," *J. Phys. Appl. Phys.*, vol. 50, no. 18, p. 184005, Apr. 2017, doi: 10.1088/1361-6463/aa6786.

[12] H. Gonçalves, M. Belsley, C. Moura, T. Stauber, and P. Schellenberg, "Enhancing visibility of graphene on arbitrary substrates by microdroplet condensation," *Appl. Phys. Lett.*, vol. 97, no. 23, p. 231905, Dec. 2010, doi: 10.1063/1.3527081.

[13] H. Gonçalves, L. Alves, C. Moura, M. Belsley, T. Stauber, and P. Schellenberg, "Enhancement of graphene visibility on transparent substrates by refractive index optimization," *Opt. Express*, vol. 21, no. 10, pp. 12934–12941, May 2013, doi: 10.1364/OE.21.012934.

[14] L. M. Malard, M. A. Pimenta, G. Dresselhaus, and M. S. Dresselhaus, "Raman spectroscopy in graphene," *Phys. Rep.*, vol. 473, no. 5, pp. 51–87, Apr. 2009, doi: 10.1016/j.physrep.2009.02.003.

[15] D. Yoon and H. Cheong, "Raman Spectroscopy for Characterization of Graphene," in *Raman Spectroscopy for Nanomaterials Characterization*, C. S. S. R. Kumar, Ed. Berlin, Heidelberg: Springer, 2012, pp. 191–214.

[16] W. Becker, *Advanced time-correlated single photon counting techniques*. Berlin: Springer, 2010.

[17] J. Demas, *Excited State Lifetime Measurements*. Saint Louis: Academic Press, 2014.

[18] A. J. M. Garrett, "Maximum Entropy with Nonlinear Constraints: Physical Examples," in *Maximum Entropy and Bayesian Methods*, P. F. Fougère, Ed. Dordrecht: Springer Netherlands, 1990, pp. 243–249.

[19] H. Gonçalves *et al.*, "Long range energy transfer in graphene hybrid structures," *J. Phys. Appl. Phys.*, vol. 49, no. 31, p. 315102, Jul. 2016, doi: 10.1088/0022-3727/49/31/315102.

[20] Thomas. Jue, "Biomedical applications of biophysics. Volume 3 Volume 3," 2010. https://doi.org/10.1007/978-1-60327-233-9.

[21] L. Gaudreau, K. J. Tielrooij, G. E. D. K. Prawiroatmodjo, J. Osmond, F. J. G. de Abajo, and F. H. L. Koppens, "Universal Distance-Scaling of Nonradiative Energy Transfer to Graphene," *Nano Lett.*, vol. 13, no. 5, pp. 2030–2035, May 2013, doi: 10.1021/nl400176b.

[22] L. Novotny and B. Hecht, *Principles of nano-optics*. Cambridge: Cambridge University Press, 2006.

[23] D. L. Dexter, "A Theory of Sensitized Luminescence in Solids," *J. Chem. Phys.*, vol. 21, no. 5, pp. 836–850, May 1953, doi: 10.1063/1.1699044.

[24] G. Gómez-Santos and T. Stauber, "Fluorescence quenching in graphene: A fundamental ruler and evidence for transverse plasmons," *Phys. Rev. B*, vol. 84, no. 16, p. 165438, Oct. 2011, doi: 10.1103/PhysRevB.84.165438.

[25] R. R. Nair *et al.*, "Fine structure constant defines visual transparency of graphene," *Science*, vol. 320, no. 5881, p. 1308, Jun. 2008, doi: 10.1126/science.1156965.

[26] J. M. Gordon and Y. N. Gartstein, "Local field effects for spherical quantum dot emitters in the proximity of a planar dielectric interface," *JOSA B*, vol. 31, no. 9, pp. 2029–2035, Sep. 2014, doi: 10.1364/JOSAB.31.002029.

[27] M. H. Hatzopoulos, C. James, S. Rogers, I. Grillo, P. J. Dowding, and J. Eastoe, "Effects of small ionic amphiphilic additives on reverse microemulsion morphology," *J. Colloid Interface Sci.*, vol. 421, pp. 56–63, May 2014, doi: 10.1016/j.jcis.2014.01.024.

[28] G. Mazzamuto *et al.*, "Single-molecule study for a graphene-based nano-position sensor," *New J. Phys.*, vol. 16, no. 11, p. 113007, Nov. 2014, doi: 10.1088/1367-2630/16/11/113007.

[29] M. Mohseni, *Quantum effects in biology*. Cambridge: Cambridge University Press, 2015.

PART III

CHAPTER 6

GAIN OF SECOND-ORDER NONLINEAR-OPTICAL SIGNAL BY OPTICAL STIMULATION

Contents

6.1.   Introduction

Second harmonic generation (2HG) is a non-linear optical process that occurs when high intensity light interacts with non-centrosymmetric materials or at surfaces, interfaces, or regions where centro-symmetry is broken.

The result of the interaction of an incident intense electric field, E, with a specific medium with nonlinear polarizability produces optical second harmonic generation. This incident electrical field, E, induces a macroscopic polarization, P, which contains new frequency components that depend on higher orders of the field and was given in Eq. (1.19), repeated here for convenience.

$$P_i = \varepsilon_0 \left(\sum_j \chi_{ij}^{(1)} E_j + \sum_{jk} \chi_{ijk}^{(2)} E_j E_k + \sum_{jkl} \chi_{ijkl}^{(3)} E_j E_k E_l \right). \qquad (6.1)$$

Where a Taylor expansion of the susceptibility in order of the applied electric field is carried out. The first term, $\chi^{(1)}$ is the linear susceptibility, while $\chi^{(2)}$ and $\chi^{(3)}$ are higher order nonlinearities that occur in the dielectric response. The first term, $\chi^{(1)}$, describes linear effects, associated with the conventional refractive index, birefringence, and optical activity. The second term, $\chi^{(2)}$, describes the second order optical effects, like frequency sum and difference processes used in up- and down-conversion processes. The third term, $\chi^{(3)}$, describes third-order optical effects, such as Four-Wave Mixing (FWM), third harmonic generation (3HG), self-phase modulation (optical-Kerr effect), cross-phase modulation (optical cross-Kerr effect), two-photon absorption (2PA), and Raman processes.[1]

Second-order optical processes involve 3 electric fields in total. In the case of second harmonic generation, two incident electric fields with the same fundamental frequency are combined to produce a coherent electrical field output at twice the fundamental frequency, i.e. the second harmonic (2HG) signal field.

Taking into account the vector nature of the fields, the nonlinear susceptibility describing 2HG becomes a third rank tensor that depends on the incident frequency, ω, and photon wave vector, q. Since q is usually small compared to the length scale for variation in the susceptibility, a second Taylor expansion is often used to obtain:

$$\chi_{ijk}^{(2)}(2\omega;\omega,\omega,q) = \chi_{D}^{(2)}{}_{ijk}(2\omega;\omega,\omega) + i\tilde{\chi}_{Q}^{(2)}{}_{ijkl}(2\omega;\omega,\omega)q_l + O(q^2)$$

(6.2)

Where $\chi_{D}^{(2)}(\omega)$ is the electric dipole term, and $\tilde{\chi}_{Q}^{(2)}(\omega)$ is the electric quadrupole/magnetic dipole.[2]

For frequencies far from material resonances, the 2HG response varies quadratically with the incident electric field. However, when resonances are involved, the occupation of the ground and excited states can be significantly altered by the incident light, leading to a non-quadratic behaviour. Because of its sensitivity to the material symmetry, second harmonic generation is frequently used to investigate thin films, surfaces, interfaces, and multilayers,[3–6] second harmonic generation is often employed as a sensitive probe of symmetry governed phenomena such as ferroelectricity [7], valley spin [8], and phase transitions [9]. If we explore it in a pump-probe design, for example using energies near the intra-band transition, we can access the electron dynamics in the materials with femtosecond time resolution.[10–12] A second possibility is to use second harmonic generation to study the ultrafast dynamics of charge transfer at donor-acceptor interfaces.[13–15]

MoS_2 is an especially attractive 2D material for 2HG studies since its inversion symmetry is broken in a monolayer, which has D_{3h} symmetry, giving rise to a dipole allowed 2HG.[16] This raises the possibility of probing the dynamics of our hybrid structures using 2HG.

However, given that the nonlinear medium is only a monolayer thick, the overall 2HG signal is extremely weak. Unfortunately, due to multiphoton ionization processes leading to irreversible photo-damage, one cannot arbitrarily increase the intensity of the incident fundamental field to increase the 2HG signal. Consequently, the 2HG count rates from MoS_2 are often quite low. Typically the experimental signal to noise ratio is limited by shot noise, leading to adverse statistics at low counting rates.[17]

Direct detection in a photon counting system using an avalanche photodiode is usually a logical option to acquire low-intensity signals [18], but these detectors are also sensitive to detecting the fundamental photons whose number is many orders of magnitude greater and which are therefore difficult to adequately filter.[19]

One possible way to increase sensitivity is by designing a 2HG pump-probe experiment with a modified detection scheme that takes advantage of a local oscillator (LOS) and coherent detection that is sensitive to the amplitude rather than the intensity of the signal's electric field.[20,21] These types of detection schemes are especially common in the field of radio waves and microwaves and have been successfully applied to detect weak optical signals in such diverse fields as spectroscopy [22], optical coherence tomography [23], Lidar systems [24], atmospheric and astrophysical studies [25].

Two general classes of detection schemes are used depending on whether the carrier frequencies of the signal and local oscillator fields are the same, homodyne[26], or different heterodyne[27].

In a heterodyne technique, small-signal measurements are generally performed by interfering a relatively strong coherent LOS field with the signal field using a beam splitter to combine the two fields collinearly. Superimposing the signal field with the local oscillator on a square-law detector results in a detected intensity given by:

$$I = \left| E_{LOS} \right|^2 + \left| E_s(t) \right|^2 + 2Re\left[E_{LOS}^* E_s(t) e^{i(\omega_{LOS} - \omega_s)t} \right]. \qquad (6.3)$$

Where E_s and E_{LOS} are the complex amplitudes of the signal and local oscillator fields respectively, while ω_s and ω_{LOS} are the associated carrier frequencies. For the best sensitivity, it is important to match the spatial modes of the signal and local isolator so that the interference term is maximized. The resulting interference generates a signal at the beat frequency between the signal and local

oscillator that can be isolated with a narrow band electronic filter to avoid thermal and electrical noise that often dominates a detection system at lower frequencies. Furthermore, the beat signal is proportional to the product of the amplitudes of the signal field and the local oscillator, providing a built-in gain when compared to direct detection which scales as the amplitude squared (i.e. intensity) of the signal field.

Using heterodyne techniques it is possible to acquire both amplitude and the phase information of the optical signal.[28] In principle this allows one to characterize both the real and imaginary components of the nonlinear response.

In general, the gain in signal to noise obtainable in a heterodyne experiment is limited by the amplitude noise of the local oscillator. It is possible to minimize the effect of local oscillator noise by employing a detection scheme that uses dual detectors to form a balanced configuration[28]. The local oscillator noise will be common to both detectors while the respective beat signals can be made to be 180 degrees out of phase to each other. Subtracting the balanced detector's signals cancels the common noise although at the cost of greater readout noise.

Heterodyne detection works especially well for continuous or quasi-continuous signals when it is possible to use frequency filters or lock-in detection techniques to isolate the beat frequency. For ultrafast pulses, the limited temporal width precludes using electronic frequency filters to isolate the interference term. However, techniques such as spectral interferometry can be used to isolate the contribution of the interference term, although the single-shot gain in this case is limited by the need to maintain reasonable fringe contrast.

The other possibility, the homodyne detection scheme, allows us to use the same source as the local oscillator but is difficult to implement in practice, as it requires the local oscillator frequency matches the carrier frequency exactly and is phase-locked to the incoming signal.[27,29] Some approaches minimize the phase difference between the received and local oscillator signals, one of them being the phase diversity design.[30] In this design, the generated optical field is divided by a 50/50 beam splitter. One half of the signal is mixed with the local oscillator signal, while the other half is mixed with a local oscillator signal that has been phase-shifted by 90° effectively measuring the two different quadratures of the homodyne signal. Although this method effectively allows for a signal with an arbitrary phase to be detected, the use of the beam splitter decreases the final signal to noise ratio doubling the number of signal photons that are required for this detection method. It's also possible to use a phase tracking system with an electronic feedback loop set to compensate for any phase variation. This avoids the adjustment of some of the optical path changes that are

introduced by the phase diversity design which requires an extra beam splitter and more detectors, but there's the requirement that the feedback loop must be faster than the phase drift.[31]

So there are obvious advantages and drawbacks for both of these types of coherent detection schemes, their main common characteristics/advantage being an increase in the signal to noise ratio. However, we have found that the need for optimized spatial mode and wave-front matching between the signal and local oscillator beams in a normal heterodyne experiment is especially difficult when the signal beam generated consists of only a few photons per pulse. An alternative approach that we take in this chapter is to embed the heterodyne detection scheme within the nonlinear optical process of second harmonic generation to effectively amplify the signal generated to levels where the signal to noise is acceptable.

For that, we present a detection scheme that uses optical stimulation of second harmonic generation to enhance our weak signal field generated by the material. To achieve this, the light of the signal field is coincident on a BBO crystal together with an external pump, seeding the nonlinear conversion of the pump into an enhanced 2H signal field. This approach has already proven to be successful in Raman scattering [32] and X-ray scattering [33] measurement schemes. Recently it's been also used in the stimulated enhancement of 2HG and difference frequency generation (DFG).[34]
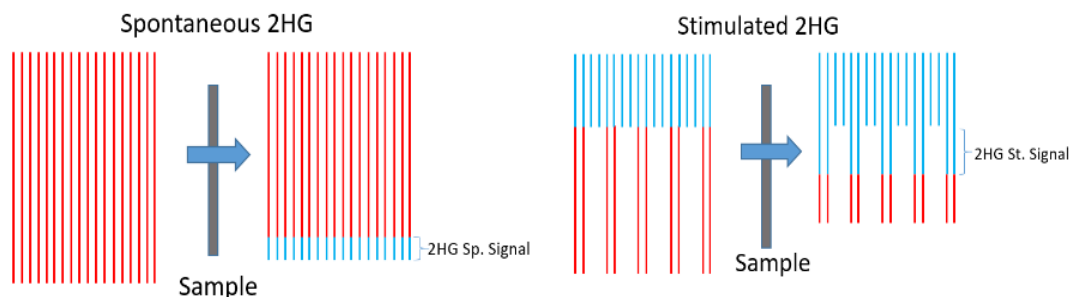
Figure 6.1 Conception of the signal modulation scheme used to differentiate the stimulated 2HG field signal stimulated from the stimulating photons as depicted in Goodman et al.[35]. Here red represents the fundamental field while blue is the second harmonic

This approach, employed by Goodman et al. [35], uses a strong second harmonic signal incident on the sample together with the pump to "stimulate" an enhanced second harmonic signal from the sample.

The amplification of the 2HG field signal follows the arguments given in the seminal work of Armstrong et al.[35]. Essentially, in a nonlinear medium amplitudes of the fundamental field and the

2HG field become coupled by the nonlinear susceptibility, making an exchange of energy possible and allowing amplification of one of the fields and a corresponding depletion of the other.

To use this approach, Goodman et al. [35], express the phase difference between the field as written in Eq. (6.4), while the amplitudes of the fields are normalized so that their sum corresponds to the total intensity,

$$\theta = 2\phi_\omega - \phi_{2\omega} \text{ and } A_\omega^2 + A_{2\omega}^2 = I_{total}. \tag{6.4}$$

Within the slowly varying envelope approximation to the nonlinear wave equation, the exchange of energy between the fundamental and second harmonic fields can be described by the following coupled equations:

$$\frac{\partial A_\omega}{\partial_\zeta} = A_\omega A_{2\omega} \, sin(\theta),$$

$$\frac{\partial A_{2\omega}}{\partial_\zeta} = -A_\omega^2 \, sin(\theta), \tag{6.5}$$

$$\frac{\partial \theta}{\partial_\zeta} = \frac{cos\,\theta}{sin\,\theta} \frac{d}{d_\zeta}(ln\,A_\omega^2 A_{2\omega}).$$

where ζ is the normalized propagation distance given by $\zeta = z/\mathrm{L}$, with L being the characteristic length associated with energy exchange between the fundamental and second harmonic fields:

$$L^{-1} = 2\omega^2 \left(\frac{2\pi d_{eff}}{c^2}\right) \frac{\sqrt{I_{total}}}{k_\omega}. \tag{6.6}$$

Here k_ω is the propagation vector of the fundamental wave and d_{eff} is the effective second-order susceptibility of the medium. Figure 6.2 presents the growth of the stimulated 2HG with distance propagated in the crystal using a coupled-wave formalism illustrating the solution of the coupled Eq. (6.5) and assuming ideal experimental conditions, ignoring diffraction, dispersion, etc. during the beam's propagation in the crystal. Note that the derivative of the second harmonic intensity represents the rate of growth of the second harmonic field intensity.

In their work, Goodman et al. [35], found that degree of signal amplification scales inversely with the sample's nonlinear susceptibility $\chi^{(2)}$ and with the distance over which the stimulating and fundamental fields interact, meaning that optical stimulation is of greater interest in systems with the weakest initial signals, this being our main point of interest. On the other hand, the difficulty of discriminating this amplified signal from that of the background local oscillator becomes increasingly difficult for these weaker signals.
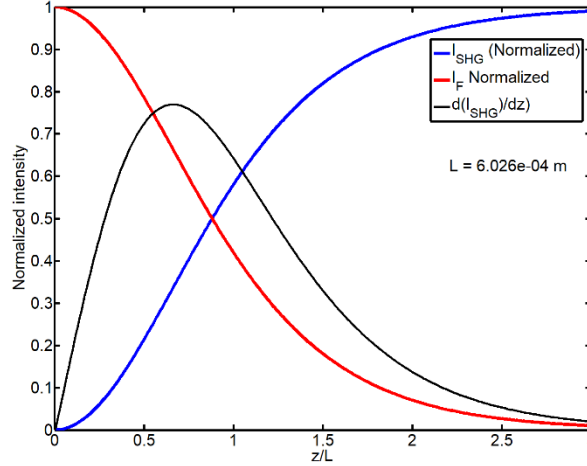
Figure 6.2 Solution of the coupled Eq. (6.5).

However, as our objective is to explore the possible transfer of charge from excited quantum dots (QDs) to a MoS_2 monolayer substrate, and probe the subsequent monolayers response using second harmonic generation we can't use the same scheme, as the incident second harmonic light used for the amplification would also excite the QDs. Hence we had to devise an alternate excitation scheme compatible with our pump-probe configuration.

6.2. Experimental Methods

6.2.1. Instrumental Design

The experiments were performed at a repetition rate of 76 MHz using a commercial Kerr mode-locked oscillator (Coherent Mira). This was pumped by a diode-pumped solid-state laser (Verdi 5v). This oscillator generated pulses with a 12 nm bandwidth centered at 794 nm, having an average power of 730 mW, with 100 fs pulse width (FWHM) and 5mm diameter size.

The beam was split using a half-wave plate and a Glan laser polarizer. About 70 mW was injected into an 80 cm nonlinear photonic crystal fiber using a 20x microscope objective with a 9 mm focal length and a 0.4 numerical aperture. The fiber was placed slightly behind the focal plane of the

objective so that the cross-section of the fiber end was fully illuminated. Due to self-phase modulation, a broadband continuum was generated as the beam propagated within the photonic fiber. The light exiting the fiber was collected by a second 20x microscope objective and collimated. Subsequently, it was directed to a diffraction grating and then passed through an iris to select a narrow-band of the polychromatic light. Rotating the grating, the center of the selected band could be chosen to coincide with the absorption spectrum of the QDs. This narrowband field served as the pump beam and its intensity was controlled via a broadband half-wave plate and a polarizer before it was merged collinearly with the 2HG pump pulse.

The other output from the polarizer, around 650 mW, was directed down an optical delay stage (DS) and was then split with a second half-wave plate & glans laser polarizer pair. One of the split beams, the probe, was merged collinearly with the narrowband pump and was used to generate the 2HG field in the sample. To optimize the 2HG field generation in the TMDC, its polarization was controlled via a half-wave plate.

Usually, 2HG pump-probe setup designs follow similar lines with small modifications, and the resulting 2HG field is detected via photon counting or a coherent detection method. Instead, we employ an alternate method illustrated inside the blue rectangle in Figure 6.3, using a portion of the leftover fundamental beam.

This second fundamental beam passes through a second delay line with a piezo adjustment for manipulating the phase and temporal overlap with the 2HG beam generated in the sample. After the delay line, this beam is divided by a beam splitter and one of the outputs is directed to a balanced photodiode to compensate for fluctuations in the fundamental beam intensity.

The second output is combined with the weak 2HG field using a dichroic mirror. The temporal overlap between the 2HG signal and this second fundamental beam is adjusted by the second delay line, Note that changing the optical path via the first delay line does not affect this overlap.

Both the second fundamental beam and the 2HG generated by the sample are focused onto a Beta Barium Borate (BBO) nonlinear crystal in a collinear geometry using a microscope objective. The BBO crystal is cut for type I phase matching at 800nm which requires the fundamental and 2H fields to have orthogonal polarizations, allowing for the crystal birefringence to compensate for dispersion.
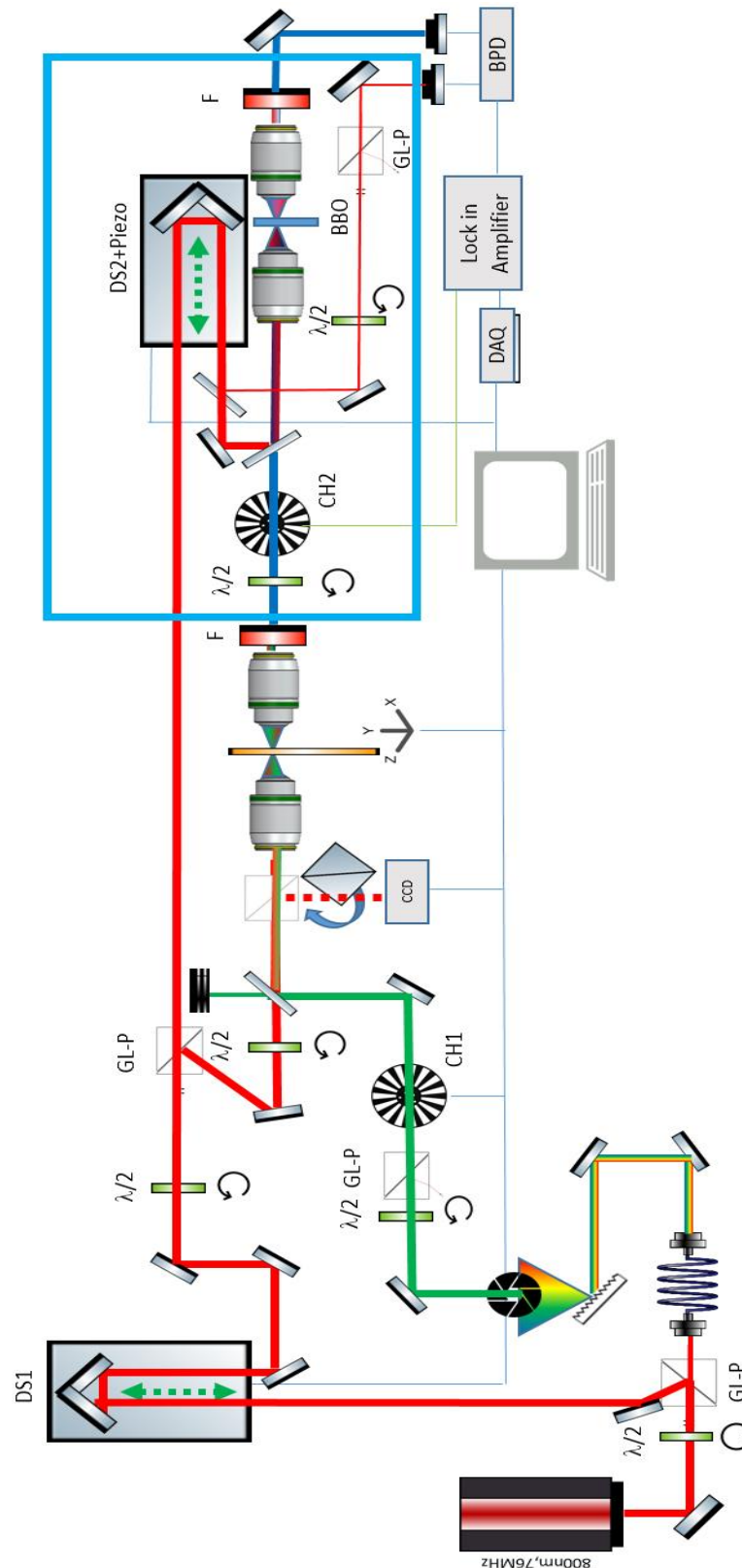
Figure 6.3 Diagram for optical 2HG amplification experiments implemented in our laboratory. The experiment is controlled through a LabVIEW program. $\lambda/2$-half wave-plate; GL-P- Glan-Laser Calcite Polarizer; F-Filter; P-Polarizer; BS Beam splitter, BPD-Balanced photodiode, CH-chopper, DS-Delay line, BBO- Beta Barium Borate crystal.

Provided the weak 2H field and the fundamental beam are co-propagating and overlapped in space and time, the weak 2HG field will effectively serve as a seed that will be amplified. However, this amplified 2HG will be superposed with a large background of spontaneous 2HG field generated by the fundamental field in the BBO crystal. This is analogous to heterodyne detection with the strong spontaneous second harmonic background playing the same role as the local oscillator intensity. Subsequently, the residual fundamental beam and initial narrowband pump are filtered out and the total second harmonic field is directed towards the second arm of the balanced photodiode.

Two optical choppers are used to discriminate the desired signals. The first chopper, modulates the pump beam at a frequency of 500Hz, allowing us to separate the signal generated in the presence of the pump beam from that occurring in its absence. To differentiate the enhanced 2H signal from the large 2HG background generated in the BBO crystal a second chopper operating at 3 kHz was placed between the sample and the BBO crystal. This chopper was used to trigger a phase-sensitive lock-in amplifier connected to the balanced photodiode allowing us to detect the small increase in 2HG due to stimulation by the second harmonic light generated in the sample.

There are two alternative positions for this second chopper. The above described placement is shown in Figure 6.4 (left) and modulates the sample's 2HG field before it is combined with the second fundamental beam at the dichroic mirror. Alternatively, the chopper could have been placed in the path of the fundamental beam before the coupling, corresponding to the situation in Figure 6.4 (right).
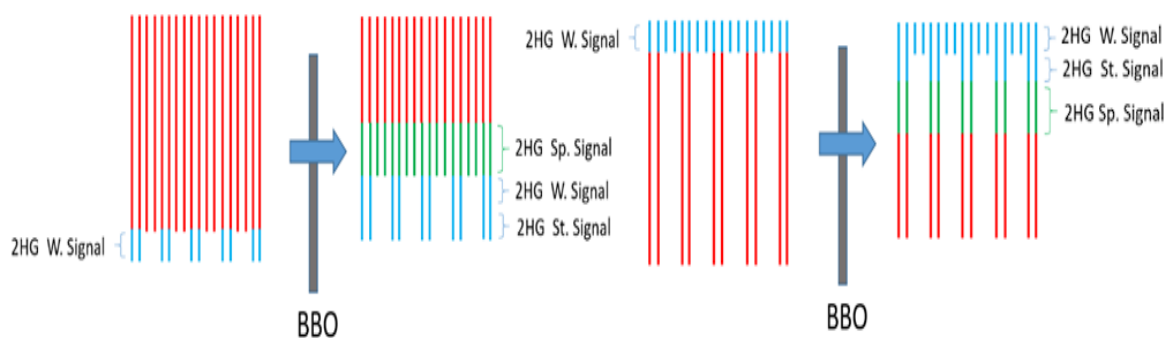
Figure 6.4 Two alternative signal modulation schemes that can be used to differentiate the 2HG signal field measured from the various other signal fields.The spontaneous 2HG signal is shown in green, the weak initial singal 2HG and stimulated 2HG are shown in blue, with the fundamental eam in red.

The first possibility allows one to separate the 2HG signal that originates from the sample and is amplified by the BBO crystal from that generated spontaneously in the BBO crystal by the incident fundamental light. The signal detected using the alternative placement is the superposition of the

spontaneous signal generated by the second fundamental in the BBO crystal together with the amplified component of the 2HG signal generated by the sample.

One can then separate the two contributions by scanning the fundamental beam in time – the amplified component only appears when the initial 2HG signal and the fundamental beam are overlapped, allowing us to estimate the amplification due to the stimulated 2HG component.

6.2.2. Samples

For the experiments described in this chapter CVD graphene and exfoliated MoS2 was used and coupled with QDs to obtain hybrid systems of QDs/MoS2 and QDs/graphene. They were produced as described in chapter 2 section6.

6.3.   Results and Discussion

Using another BBO crystal as a model system, to produce the first 2HG weak field signal instead of the sample to be probed, allows us to optimize the experimental setup and characterize the amplification generated when the weak 2HG field signal is overlapped in time with the fundamental field in the second crystal.

The two modulation schemes give similar trends in the output, modulating the fundamental field (right scheme of Fig. 6.4) a constant baseline is generated when the beams do not temporally overlap.
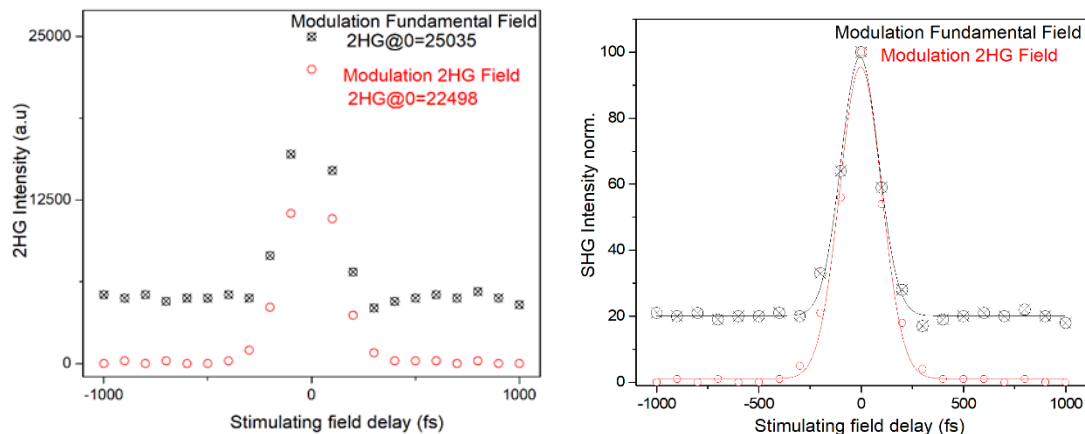
Figure 6.5 Demodulated 2HG signal field measured (left). Normalization of the demodulated 2HG signal field measured (right). The red curve denotes the signal obtained using the modulation scheme of the left side in Figure.4.4, while the black curve denotes the right one.

When the initial (weak) 2HG field signal is modulated (left scheme of Fig.6.4) the lock-in demodulates both the initial (weak) 2HG and the 2HG stimulated field signals, so we measure the original signal plus the amplification. When the fundamental field incident on the second crystal is modulated, as mentioned above, the signal obtained is the amplified 2HG field (which requires temporal superposition) and a constant 2HG, the spontaneous 2HG field generated by the fundamental in the second crystal.

The final practical result is that modulating the weak 2HG field signal leads to a cleaner output with almost no background. Although the peak signal, in this case, is roughly 20% lower this in effect corresponds to the background of the constant (spontaneous) signal generated in the second crystal. By combining information from these two different modulation schemes we can estimate the amplification factor achieved for the weak 2HG signal. First, using the background of the curve obtained when modulating the fundamental field, we can estimate the spontaneous 2HG field intensity is roughly two-tenths of the maximum signal obtained at temporal overlap corresponding to a magnitude of roughly 5×10^3 (units). The peak of the curve obtained when modulating the fundamental field (the black curve in Fig. 6.5) should correspond to this background plus the 2HG signal stimulated by the weak 2HG field, allowing us to estimate the latter as having a magnitude of roughly 2.0×10^4. Next, given that the peak signal obtained when modulating the weak 2HG signal field (the red curve in Fig. 6.5) is the superposition of the weak 2HG signal and the stimulated 2HG signal, we estimate that the weak signal 2HG intensity is approximately 2.5×10^3.

Altogether then, the amplification obtained, being the ratio of the peak of the red curve to the initial weak 2HG signal magnitude is roughly $2.25 \times 10^4 / 2.5 \times 10^3$ or a factor of 9. If instead of the peak magnitudes of Figure 6.5, we use the spectrally integrated signals at the maximum temporal overlap (see the curve of Fig 6.6) we obtain a slightly lower amplification factor of 8.8.
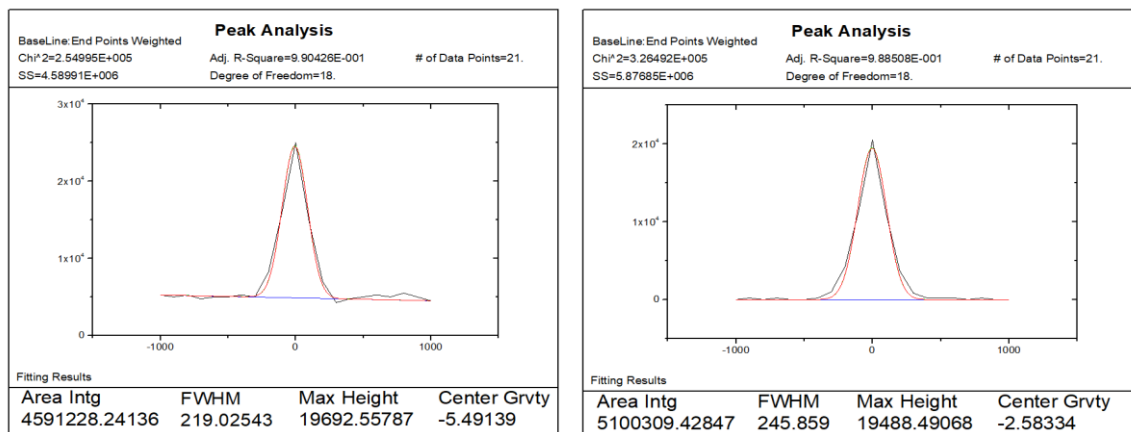
Figure 6.6 Gaussian fit to the 2HG signal field measured. For the modulation of the stimulating field (left) and for the modulation of the weak field (right).

The gain we managed to obtain is far below that reported by Goodman et al.[34], were they predict gains of several hundred or more for a sample with a thickness well below the scale length L and an optimized ratio of incident fundamental beam intensity to that of the stimulating second harmonic beam. However, it should be kept in mind that the estimates of Goodman et al neglect spatial propagation effects such as diffraction and birefringent walk-off of the extraordinary ray and a mismatch in group velocities between the fundamental and second harmonic waves. To assess the impact of these effects we developed the following numerical simulation.

Within the slowly varying envelope approximation, assuming that the second harmonic wave is polarized along the x-direction with propagation along the z-direction, the coupled-wave Eq. (6.5) take the following form:

$$\frac{\partial A_\omega}{\partial z} = i\left[\frac{1}{2k_\omega}\nabla_T^2 - i\,tan\,\rho_\omega\,\frac{\partial}{\partial x}\right]A_\omega + \left[\frac{-1}{v_{g,\omega}}\frac{\partial}{\partial t} + i\beta_\omega^{(2)}\frac{\partial^2}{\partial t^2}\right]A_\omega$$

$$+ \frac{i\mu_0\omega^2}{2k_\omega}2\varepsilon_0 d_{eff}A_{2\omega}A_\omega^* e^{i(k_{2\omega}-2k_\omega)z},$$

$$\frac{\partial A_{2\omega}}{\partial z} = i\left[\frac{1}{2k_{2\omega}}\nabla_T^2 - i\,tan\,\rho_{2\omega}\,\frac{\partial}{\partial x}\right]A_{2\omega} + \left[\frac{-1}{v_{g,2\omega}}\frac{\partial}{\partial t} + i\beta_{2\omega}^{(2)}\frac{\partial^2}{\partial t^2}\right]A_{2\omega}$$

$$+ \frac{i\mu_0(2\omega)^2}{2k_{2\omega}}\varepsilon_0 d_{eff}A_\omega^2 e^{i(k_{2\omega}-2k_\omega)z}$$

(6.7)

Here A_ω and $A_{2\omega}$ are the electric field envelope amplitudes for the fundamental and second harmonic waves respectively. On the right-hand side of the Eq. (6.7), the first group of terms represents diffraction and birefringent walk-off, the second group the dispersion, and the last group the nonlinear interaction. The $\beta^{(2)}$ factors represent the group delay dispersion.

Assuming perfect phase matching, $\Delta k = k_{2\omega} - 2k_\omega = 0$, we have that for the negative uniaxial crystal BBO at 800nm, the type I phase matching can occur for the polarizations $o + o \rightarrow e$ (o-ordinary polarization; e-extraordinary polarization) with a walk-off angle of $\rho = 68.04\,mrad$ for the second harmonic beam at 300 Kelvin.

According to the software, SNLO, developed by Dr. Arlee Smith [36], under these conditions, the refractive index is $n_\omega = n_{2\omega} = 1.660$ while the group indices are given by $n_{g,\omega} = 1.684$ and

$n_{g,2\omega} = 1.742$. The respective group delay dispersions are, GDD, $\beta_\omega^{(2)} = 75.1\,fs^2/mm$ and

$\beta_{2\omega}^{(2)} = 195.9\,fs^2/mm$; while the effective second-order susceptibility of the BBO is

$d_{eff} = 2.0\,pm/V$.

Using these parameters for a pulse with a FWHM of around 100fs, the lengths associated with the group velocity dispersion can then be estimated as:

$$L_{GVD,\omega} = \tau^2/\beta_\omega^{(2)} \approx 130\,mm \quad ; \quad L_{GVD,2\omega} = \tau^2/\beta_{2\omega}^{(2)} \approx 50\,mm, \quad (6.8)$$

while the "quasi-static" interaction length due to group velocity mismatch is:

$$L_{qs} = \tau * c / \left| n_{g,2\omega} - n_{g,\omega} \right| \approx 520\,\mu m. \quad (6.9)$$

The confocal length, or diffraction length, is equal two times the Rayleigh length, assuming a 5 micron beam waist:

$$L_{cf} = 2\frac{\pi w_0^{\,2}}{\lambda} = k(w_0)^2 \approx 200\,\mu m, \quad (6.10)$$

and the walk-off length of the extraordinary beam assuming again a beam waist of around 5-micron for the second harmonic field is

$$L_{wo} = 2w_0/\rho \approx 150\,\mu m. \quad (6.11)$$

Given the above estimates, the group velocity dispersion can be safely neglected and group velocity mismatch will probably only have a minor effect.

If we transfer to a frame moving with the group velocity of the fundamental beam, the faster beam, to keep the temporal grid more or less centered, the previous coupled equations become:

$$\frac{\partial A_{\omega}}{\partial z} = i\left[\frac{1}{2k_{\omega}}\left(\frac{\partial^2}{\partial x^2}+\frac{\partial^2}{\partial y^2}\right)\right]A_{\omega} + i\beta_{\omega}^{(2)}\frac{\partial^2}{\partial t^2}A + \frac{i\omega}{nc}d_{eff}A_{2\omega}A_{\omega}^{*}e^{i(k_{2\omega}-2k_{\omega})z}$$

$$\frac{\partial A_{2\omega}}{\partial z} = i\left[\frac{1}{2k_{2\omega}}\left(\frac{\partial^2}{\partial x^2}+\frac{\partial^2}{\partial y^2}\right) - i\,tan\,\rho_{2\omega}\frac{\partial}{\partial x}\right]A_{2\omega}$$

$$+ \left[\left(\frac{n_{g,\omega}-n_{g,2\omega}}{c}\right)\frac{\partial}{\partial t} + i\beta_{2\omega}^{(2)}\frac{\partial^2}{\partial t^2}\right]A_{2\omega}$$

$$+ \frac{i\omega}{nc}d_{eff}A_{\omega}^{2}e^{i(k_{2\omega}-2k_{\omega})z}$$

(6.12)

The effect of these equations can be simulated by using a discrete rectangular x-y-t grid (3D) and propagating the fields using a split-step Fourier method. This allows us to treat the linear terms: dispersion, diffraction, and beam walk-off, in Fourier space and the nonlinear interaction in real space. This method relies on computing the solution in small steps and treating the linear and the nonlinear steps separately. This is advantageous as the linear propagators are simple exponential factors in Fourier Space, while the nonlinear interaction which involves the superposition of the two waves is easiest to compute in real space, so we have to Fourier transform back and forth.

To efficiently integrate the nonlinear part in real space it is helpful to scale the fields. We decided to use the overall energy of the beams as the inherent scale. Analytically one can show that a Gaussian beam propagates under dispersion and diffraction according to the following expression [37]:

$$A\left(x,y,z,t\right) = \frac{1}{\sqrt{\left(1+Cz/z_D\right)-iz/z_D}}\frac{A_0}{\left(1-z/f\right)+iz/z_R}$$

$$exp\left[\frac{-\left(x^2+y^2\right)\left(1+iz_R/f\right)}{w_0^2\left[\left(1-z/f\right)+iz/z_R\right]} - \frac{-t^2\left(1+iC\right)}{\tau^2\left[\left(1+Cz/z_D\right)-iz/z_D\right]}\right],$$ (6.13)

with z_R the Rayleigh length ($\pi n w_0^2/\lambda$) and z_D the dispersion length ($L_{GVD}/2$), the pulse energy for such beam is given by

$$U = \int\limits_{-\infty}^{\infty} dt \int\limits_{-\infty}^{\infty} dxdy \, \tfrac{1}{2}\varepsilon_0 c \left| A(x,y,z,t) \right|^2 = \tfrac{1}{2}\varepsilon_0 c \left| A_0 \right|^2 \left(\frac{\pi}{2} \right)^{3/2} w_0^2 \tau . \quad (6.14)$$

This leads to

$$\left| A_0 \right| = \left(\frac{2}{\pi} \right)^{3/4} \sqrt{\frac{2U}{w_0^2 \tau \varepsilon_0 c}} . \quad (6.15)$$

Now under perfect phase-matching $\left(k_{2\omega} = 2k_{\omega} \right)$ the nonlinear parts of Eq. (6.12),

$$\frac{\partial A_\omega}{\partial z} = \frac{i\omega}{nc} d_{eff} A_{2\omega} A_\omega^*$$

$$\frac{\partial A_{2\omega}}{\partial z} = +\frac{i\omega}{nc} d_{eff} A_\omega^2 \quad , \quad (6.16)$$

can be rewritten by expressing the complex beam amplitudes as a real magnitude and a phase, $A_\omega = \mathrm{A}_\omega\, e^{i\phi_\omega}$ with a similar expression for $A_{2\omega}$. Then separating the real and imaginary parts, as in Armstrong et al [35], gives us:

$$\frac{\partial A_\omega}{\partial z} = -\frac{\omega}{nc} d_{eff} A_{2\omega} A_\omega \, sin\left(\phi_{2\omega} - 2\phi_\omega \right)$$

$$\frac{\partial A_{2\omega}}{\partial z} = \frac{\omega}{nc} d_{eff} A_\omega^2 \, sin\left(\phi_{2\omega} - 2\phi_\omega \right)$$

$$\frac{\partial \left(\phi_{2\omega} - 2\phi_\omega \right)}{\partial z} = \frac{\omega}{nc} d_{eff} \left(\frac{A_\omega^2}{A_{2\omega}} - 2A_{2\omega} \right) cos\left(\phi_{2\omega} - 2\phi_\omega \right) \quad . \quad (6.17)$$

Note that if one multiplies the first equation by A_ω and the second equation by $\mathrm{A}_{2\omega}$ and adds them together we obtain:

$$\frac{1}{2} \frac{\partial}{\partial z} \left(A_\omega^2 + A_{2\omega}^2 \right) = 0 . \quad (6.18)$$

Implying that the total intensity remains constant, which is essentially an expression of energy conservation. This suggests that we can use the total intensity $I_{Tot} = I_\omega + I_{2\omega}$ to scale the complex beam amplitudes in terms of the peak intensities at x = y = z =t = 0,

$$I_\omega = \left(\frac{2}{\pi}\right)^{3/2} \frac{U_\omega}{w_{\omega,0}^2 \tau_\omega} \quad , I_{2\omega} = \left(\frac{2}{\pi}\right)^{3/2} \frac{U_{2\omega}}{w_{2\omega,0}^2 \tau_{2\omega}}$$

(6.19)

as

$$A_\omega(\vec{r},t) = \sqrt{\frac{2I_{Tot}}{\varepsilon_0 c}} a_\omega(\vec{r},t) \quad , A_{2\omega}(\vec{r},t) = \sqrt{\frac{2I_{Tot}}{\varepsilon_0 c}} a_{2\omega}(\vec{r},t) .$$

(6.20)

Then the non-linear Eq. (6.16) becomes:

$$\frac{\partial a_\omega}{\partial z} = i\kappa a_{2\omega} a_\omega^*$$

$$\frac{\partial a_{2\omega}}{\partial z} = i\kappa \left(a_\omega\right)^{2'}$$

(6.21)

where a coupling constant has been defined as:

$$\kappa = \frac{\omega}{nc} d_{eff} \sqrt{\frac{2I_{Tot}}{\varepsilon_0 c}} .$$

(6.22)

These coupled equations can be then numerically solved for an arbitrary phase difference between the beams using a fourth-order Runge-Kutta algorithm. Furthermore, energy conservation implies that $\int dx dy \left(|a_\omega|^2 + |a_{2\omega}|^2\right) = 1$. This constraint can be used to control the step size in the Runge Kutta algorithm.
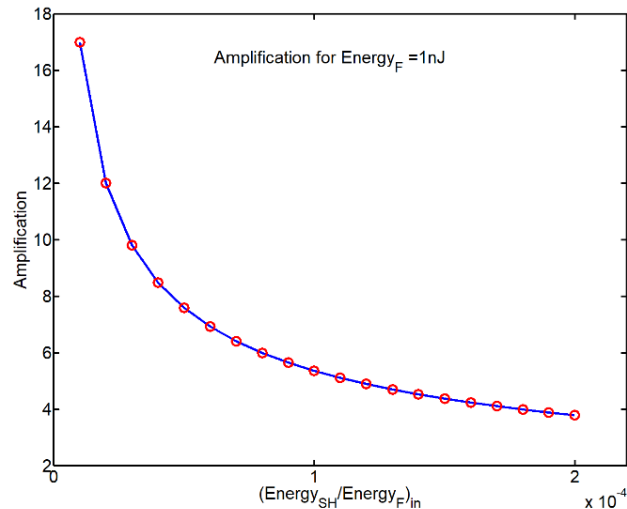
Figure 6.7 Estimative for the signal amplification using our experimental conditions.

With this method and under the aforementioned conditions, the dependence of the signal amplification on the incident energy of the 2HG weak signal for an amplification field can be estimated, as depicted in Figure 6.7.

Here, as in the experiment, the BBO crystal length was taken to be 1 mm. The initial wave-front of the fundamental beam was adjusted to produce a beam waist of 5 microns at the center of the crystal. This corresponds to the beam waist expected for a 1mm diameter incident beam focused by a 10x microscope objective with an effective focal length of 16.5 mm. The incident weak field second harmonic was taken to be mode matched with the fundamental, i.e. to possess the same Rayleigh range within the crystal (beam waist of $5/\sqrt{2}$ microns).

So in the experimental conditions we used are definitely in a lower regime of amplification than what had been originally anticipated, and in the vicinity of what was obtained experimentally. Nevertheless, the simulation suggests that it might be possible to slightly adjust the signal ratio to obtain a more efficient amplification than was obtained.

Probing the steady-state 2HG signal field of a MoS_2 monolayer it was possible to see a signal increase detected by the lock-in amplifier when the fundamental field was incident on the second crystal, corroborating the expected amplification of the 2HG field. Using a calibration curve the amplification as estimated to be roughly 9 times higher than the weak 2HG initial signal. So this was found to be in the same ballpark of the tested initially for the BBO model experiment. Controlling and decreasing the energy of both fields allowed us to improve the amplification, but decreased the overall signal obtained. This made it necessary for there to be a compromise to have enough sensitivity.

Using the pump and probe geometry a MoS_2 monolayer and hybrid sample of QDs and MoS_2, prepared as described in chapter 2, where probed to explore the charge carrier dynamics at the interface by monitoring the intensity of the 2HG signal with a temporal resolution of roughly 200 fs. To accomplish this a pump beam with a wavelength centered at 580 nm was produced in the photonic fiber and selected with the grating/iris pair to optically excite the sample. A portion of the fundamental beam (800 nm), was used as the probe pulse and its polarization was adjusted to generate as high a 2HG signal field as possible. The relative delay between the pump and probe pulses was controlled using a hollow retroreflector on a motorized delay stage. The two beams were collinearly combined with an ultrafast dichroic mirror and interacted with the sample after being focused by a 100x microscope objective. The intensities of the fields (pump and probe) were controlled to avoid laser-induced Auger recombination, multi exciton generation (MEG), and possible photo-damage in the samples being studied. After the interaction with the sample all fields were collected by a 10x objective microscope, and using a narrow band-pass filter centered at 400nm only the 2HG signal field was allowed to propagate to the amplification/detection arm containing a BBO crystal as previously described.

The lock-in amplifier signal output was acquired via a NIdaqmx with the software "P&P2HGamp", programed in LabView, which controlled the experiment.

The acquisition of the signal was synchronized with the chopper at 500 Hz in the pump beam and registered as I_{pump}. This is for when both the pump, the excitation of the system, at 580nm, and the probe, the fundamental beam, were present. The signal I_{2HGSS} acquired when only the probe was incident. The normalized difference:

$$I_{PP} = \frac{I_{pump} - I_{2HGSS}}{I_{2HGSS}},$$

(6.23)

is a measure of the effect of the pump induced optical excitation on the second harmonic response of the MoS_2. When I_{PP} is zero, there's no perturbation, while a positive value indicates an increase in the 2HG signal field when perturbed and vice versa.

In the MoS_2 monolayer sample, a fast pump induced decrease of the 2HG field signal response was observed, as expected by the depopulation of the valence band, and whose decay can be fit by a bi-exponential, in Figure 6.8, as suggested in the literature [38] for analyzing TMD monolayers.

And to be truthful adding a third exponential term didn't improve the fitting. The averaged time-constants obtained from the corresponding fits over the first 50 ps after excitation were 1.05 ± 0.03 ps and 81.5 ± 0.9 ps, as in Figure 6.8.
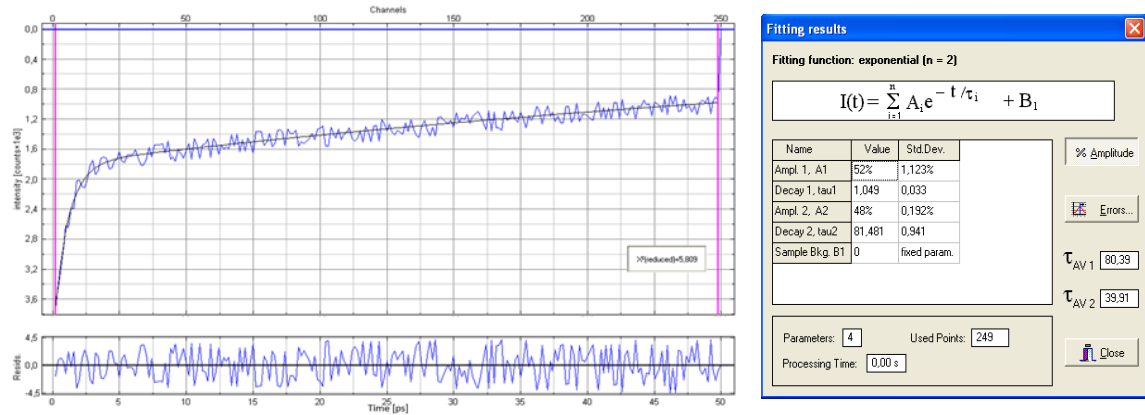
Figure 6.8 I_{PP} profile decay and corresponding fit for the second harmonic generated by a MoS$_2$ monolayer (left), Fit results for the decay (right).

The first, fast component of the 2HG response might be associated with a pump induced depopulation of the valence band via the creation of excitons in the MoS$_2$. The slower component would then reflect exciton relaxation within the monolayer material. These assignments are corroborated by similar trends found in the transient absorption measurements. In our case, using the same approach used in chapter 5.3.2, analyzing the bleach signal of the MoS$_2$, Figure 6.9, the equivalent time constants for the MoS$_2$ were found to be 1.751 ps and 95.478 ps.
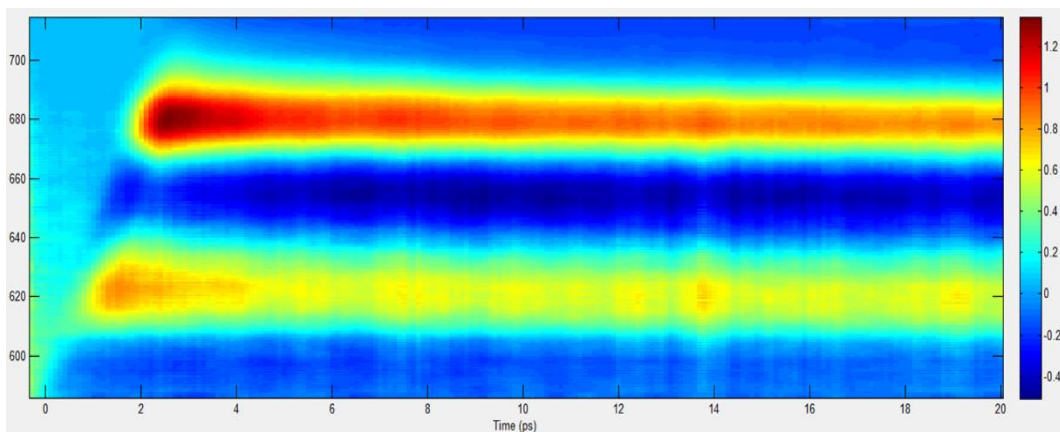
Figure 6.9 Transient spectra obtained for the MoS$_2$ on the glass microscope slide with 20 ps time scale, ranging from 580 to 720 nm and with an $-\Delta T*10^3$.

This slight difference might be due to the use of different pump and probe wavelengths and/or intensities used. There are studies where these values vary over a wide range: from 500 fs up to 100 ps for the fast time decay constant and from 15 ps up to 500 ps for the slow component in

TMD monolayers, [39–43], presumably depending on the temperature, excitation wavelength, and incident fluence. Occasionally, tri-exponential behavior has also been reported.[44] Taking into account the different substrates, temperatures, pump and probe intensities, wavelengths used as well as varying sample quality in terms of the nature of defects and defect density, these different behaviors are perhaps not too surprising. Given the wide range of values, the sensible approach when correlating the 2HG field signals and the transient absorption signals is to focus on comparing only the main trends.

The same experiment was then repeated for the hybrid structures composed of QDs on a MoS_2 monolayer, and this time the 2HG signal increased rather than decreased, Figure 6.10.

 A possible explanation for this increase is that charges generated by the excitation of the QDs might have migrated to the surface, producing a separation of electrons and holes across the interface, generating an electric field oriented at the surface and enhancing the second harmonic generation.
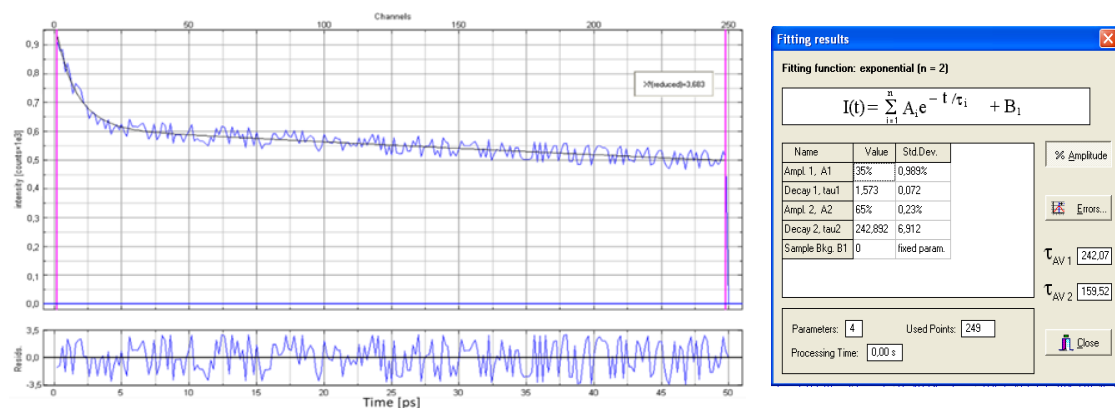
Figure 6.10 I_{PP} profile decay and corresponding fitting for the of the hybrid structure of QDs and MoS_2 monolayer (left). Fitting results for the previous decay (right).

The same trend with a fast initial decrease followed by a slower decay was verified by the fitting, Figure 6.10. However, one important difference is that both time decay constants are longer in the hybrid structure than for the MoS_2 monolayer. The faster one increased by ˜50 % to 1.563±0.072 ps and the slow by almost 300% to 242.9±6.9 ps. This could indicate the presence of delocalized indirect excitons that have a longer lifetime, slower recombination rate, due to the spatial separation of electron and hole wave functions, or possibly transit time effects associated with the migration of charge from the QDs to the MoS_2 interface.

An attempt was also made to acquire similar data for 2HG signals from graphene and the hybrid QDS/graphene coupled system. Due to the inherent centro-symmetry in graphene, the 2HG signal

from these systems is much reduced. To increase the signal, measurements were acquired at an oblique incidence of 45°. In this case, the 2HG signal arises in part from the inversion symmetry breaking by the underlying substrate surface but also has a contribution of the electric quadrupole response introduced by the in-plane component of the incident photon wave vector. Using this angle effectively breaks the overall symmetry of the system.

However, the 2HG signal under these conditions even with the amplification had an insufficient signal to noise ratio and no meaningful variation could be detected.

6.4. Summary

In conclusion, it was possible to amplify the 2HG signal by the proposed method roughly 10 times to have an improved signal to noise ratio. This allowed us to extract the time-resolved data from the MoS_2 and its hybrid structure conjugated with QDs. It was found that in the presence of the QDs the 2HG is increased. This probably was due to the presence of delocalized indirect excitons whose extended fields might enhance the generation of second harmonic light by the MoS_2.

6.5. References

[1] R. W. Boyd, *Nonlinear Optics, Third Edition*, 3rd ed. Orlando, FL, USA: Academic Press, Inc., 2008.

[2] P. N. Butcher and D. Cotter, *The Elements of Nonlinear Optics*. Cambridge: Cambridge University Press, 1990.

[3] A. Hermans *et al.*, "On the determination of $\chi^{(2)}$ in thin films: a comparison of one-beam second-harmonic generation measurement methodologies," *Sci. Rep.*, vol. 7, p. 44581, Mar. 2017, doi: 10.1038/srep44581.

[4] J. J. H. Gielis, P. M. Gevers, I. M. P. Aarts, M. C. M. van de Sanden, and W. M. M. Kessels, "Optical second-harmonic generation in thin film systems," *J. Vac. Sci. Technol. A*, vol. 26, no. 6, pp. 1519–1537, Nov. 2008, doi: 10.1116/1.2990854.

[5] Y. R. Shen, "Optical Second Harmonic Generation at Interfaces," *Annu. Rev. Phys. Chem.*, vol. 40, no. 1, pp. 327–350, 1989, doi: 10.1146/annurev.pc.40.100189.001551.

[6] G. Lüpke, "Characterization of semiconductor interfaces by second-harmonic generation," *Surf. Sci. Rep.*, vol. 35, no. 3, pp. 75–161, Nov. 1999, doi: 10.1016/S0167-5729(99)00007-2.

[7] S. A. Denev, T. T. A. Lummen, E. Barnes, A. Kumar, and V. Gopalan, "Probing Ferroelectrics Using Optical Second Harmonic Generation," *J. Am. Ceram. Soc.*, vol. 94, no. 9, pp. 2699–2727, 2011, doi: 10.1111/j.1551-2916.2011.04740.x.

[8] F. Hipolito and V. M. Pereira, "Second harmonic spectroscopy to optically detect valley polarization in 2D materials," *2D Mater.*, vol. 4, no. 2, p. 021027, May 2017, doi: 10.1088/2053-1583/aa6f4d.

[9] S. Achilli *et al.*, "Influence of phase transitions on the second harmonic generation in metal nanoparticles," *Eur. Phys. J. - At. Mol. Opt. Plasma Phys.*, vol. 24, no. 1, pp. 223–226, Jun. 2003, doi: 10.1140/epjd/e2003-00192-7.

[10] J. Hohlfeld, U. Conrad, and E. Matthias, "Does femtosecond time-resolved second-harmonic generation probe electron temperatures at surfaces?," *Appl. Phys. B*, vol. 63, no. 5, pp. 541–544, Nov. 1996, doi: 10.1007/BF01828954.

[11] C. Guo, G. Rodriguez, and A. J. Taylor, "Ultrafast Dynamics of Electron Thermalization in Gold," *Phys. Rev. Lett.*, vol. 86, no. 8, pp. 1638–1641, Feb. 2001, doi: 10.1103/PhysRevLett.86.1638.

[12] W. A. Tisdale, K. J. Williams, B. A. Timp, D. J. Norris, E. S. Aydil, and X.-Y. Zhu, "Hot-Electron Transfer from Semiconductor Nanocrystals," *Science*, vol. 328, no. 5985, pp. 1543–1547, 2010.

[13] A. J. Goodman, N. S. Dahod, and W. A. Tisdale, "Ultrafast Charge Transfer at a Quantum Dot/2D Materials Interface Probed by Second Harmonic Generation," *J. Phys. Chem. Lett.*, vol. 9, no. 15, pp. 4227–4232, Aug. 2018, doi: 10.1021/acs.jpclett.8b01606.

[14] D. E. Wilcox, M. E. Sykes, A. Niedringhaus, M. Shtein, and J. P. Ogilvie, "Heterodyne-detected and ultrafast time-resolved second-harmonic generation for sensitive measurements of charge transfer," *Opt. Lett.*, vol. 39, no. 14, pp. 4274–4277, Jul. 2014, doi: 10.1364/OL.39.004274.

[15] C. A. Nelson, J. Luo, A. K.-Y. Jen, R. B. Laghumavarapu, D. L. Huffaker, and X.-Y. Zhu, "Time-, Energy-, and Phase-Resolved Second-Harmonic Generation at Semiconductor Interfaces," *J. Phys. Chem. C*, vol. 118, no. 48, pp. 27981–27988, Dec. 2014, doi: 10.1021/jp5094614.

[16] N. Kumar *et al.*, "Second harmonic microscopy of monolayer MoS${}_{2}$," *Phys. Rev. B*, vol. 87, no. 16, p. 161403, Apr. 2013, doi: 10.1103/PhysRevB.87.161403.

[17] "Confocal Microscopy - Electronic Light Detectors: Photomultipliers | Olympus Life Science." https://www.olympus-lifescience.com/en/microscope-resource/primer/techniques/confocal/pmtintro/ (accessed Nov. 13, 2019).

[18] X. Sun and F. M. Davidson, "Photon counting with silicon avalanche photodiodes," *J. Light. Technol.*, vol. 10, no. 8, pp. 1023–1032, Aug. 1992, doi: 10.1109/50.156841.

[19] G. E. Stillman and C. M. Wolfe, "Chapter 5 Avalanche Photodiodes**This work was sponsored by the Defense Advanced Research Projects Agency and by the Department of the Air Force.," in *Semiconductors and Semimetals*, vol. 12, R. K. Willardson and A. C. Beer, Eds. Elsevier, 1977, pp. 291–393.

[20] H. P. Yuen and V. W. S. Chan, "Noise in homodyne and heterodyne detection," *Opt. Lett.*, vol. 8, no. 3, pp. 177–179, Mar. 1983, doi: 10.1364/OL.8.000177.

[21] R. M. Gagliardi and S. Karp, *Optical Communications*. Wiley, 1995.

[22] E. Matsuyama, T. Kondo, H. Oigawa, D. Guo, S. Nemoto, and J. Nakamura, "Principles and Application of Heterodyne Scanning Tunnelling Spectroscopy," *Sci. Rep.*, vol. 4, p. 6711, Oct. 2014, doi: 10.1038/srep06711.

[23] M. Akiba, K. P. Chan, and N. Tanno, "Full-field optical coherence tomography by two-dimensional heterodyne detection with a pair of CCD cameras," *Opt. Lett.*, vol. 28, no. 10, pp. 816–818, May 2003, doi: 10.1364/OL.28.000816.

[24] P. Adany, C. Allen, and R. Hui, "Chirped Lidar Using Simplified Homodyne Detection," *J. Light. Technol.*, vol. 27, no. 16, pp. 3351–3357, Aug. 2009, doi: 10.1109/JLT.2009.2016220.

[25] F. Schmülling, B. Klumb, R. Schieder, and G. Winnewisser, "An infrared heterodyne spectrometer with a tunable diode laser as local oscillator," 1997, Accessed: Nov. 13, 2019. [Online]. Available: https://kb.osu.edu/handle/1811/14146.

[26] R. H. Kingston, "Coherent or Heterodyne Detection," in *Detection of Optical and Infrared Radiation*, R. H. Kingston, Ed. Berlin, Heidelberg: Springer, 1978, pp. 24–38.

[27] E. Jakeman, C. J. Oliver, and E. R. Pike, "Optical homodyne detection," *Adv. Phys.*, vol. 24, no. 3, pp. 349–405, May 1975, doi: 10.1080/00018737500101421.

[28] K.-C. Lang and H.-K. Teng, "Optical balanced detection in heterodyne interferometric ellipsometry," *Appl. Opt.*, vol. 54, no. 27, pp. 8108–8115, Sep. 2015, doi: 10.1364/AO.54.008108.

[29] K. McKenzie, M. B. Gray, P. K. Lam, and D. E. McClelland, "Technical limitations to homodyne detection at audio frequencies," *Appl. Opt.*, vol. 46, no. 17, pp. 3389–3395, Jun. 2007, doi: 10.1364/AO.46.003389.

[30] K. Kikuchi, "Phase-diversity homodyne detection of multilevel optical modulation with digital carrier phase estimation," *IEEE J. Sel. Top. Quantum Electron.*, vol. 12, no. 4, pp. 563–570, Jul. 2006, doi: 10.1109/JSTQE.2006.876307.

[31] Q. Xu, A. Arvizu Mondragon, P. Gallion, and F. J. Mendieta, "Homodyne In-Phase and Quadrature Detection of Weak Coherent States With Carrier Phase Tracking," *IEEE J. Sel. Top. Quantum Electron.*, vol. 15, no. 6, pp. 1581–1590, Nov. 2009, doi: 10.1109/JSTQE.2009.2023803.

[32] G. Eckhardt, R. W. Hellwarth, F. J. McClung, S. E. Schwarz, D. Weiner, and E. J. Woodbury, "Stimulated Raman Scattering From Organic Liquids," *Phys. Rev. Lett.*, vol. 9, no. 11, pp. 455–457, Dec. 1962, doi: 10.1103/PhysRevLett.9.455.

[33] M. Beye *et al.*, "Stimulated X-ray emission for materials science," *Nature*, vol. 501, no. 7466, pp. 191–194, Sep. 2013, doi: 10.1038/nature12449.

[34] A. J. Goodman and W. A. Tisdale, "Enhancement of Second-Order Nonlinear-Optical Signals by Optical Stimulation," *Phys. Rev. Lett.*, vol. 114, no. 18, p. 183902, May 2015, doi: 10.1103/PhysRevLett.114.183902.

[35] J. A. Armstrong, N. Bloembergen, J. Ducuing, and P. S. Pershan, "Interactions between Light Waves in a Nonlinear Dielectric," *Phys. Rev.*, vol. 127, no. 6, pp. 1918–1939, Sep. 1962, doi: 10.1103/PhysRev.127.1918.

[36] A. V. Smith, *Crystal nonlinear optics : with SNLO examples*. 2018.

[37] A. E. Siegman, *Lasers*. Mill Valley, Calif.: University Science Books, 1986.

[38] J. E. Zimmermann, G. Mette, and U. Höfer, "Second-harmonic imaging microscopy for time-resolved investigations on transition metal dichalcogenides," *ArXiv160803434 Cond-Mat*, Sep. 2016, Accessed: Nov. 13, 2019. [Online]. Available: http://arxiv.org/abs/1608.03434.

[39] D. Sun *et al.*, "Observation of Rapid Exciton–Exciton Annihilation in Monolayer Molybdenum Disulfide," *Nano Lett.*, vol. 14, no. 10, pp. 5625–5629, Oct. 2014, doi: 10.1021/nl5021975.

[40] S. Cha *et al.*, "1 s -intraexcitonic dynamics in monolayer MoS 2 probed by ultrafast mid-infrared spectroscopy," *Nat. Commun.*, vol. 7, no. 1, pp. 1–7, Feb. 2016, doi: 10.1038/ncomms10768.

[41] X. Liu *et al.*, "Low temperature carrier transport study of monolayer MoS2 field effect transistors prepared by chemical vapor deposition under an atmospheric pressure," *J. Appl. Phys.*, vol. 118, no. 12, p. 124506, Sep. 2015, doi: 10.1063/1.4931617.

[42] R. Wang, B. A. Ruzicka, N. Kumar, M. Z. Bellus, H.-Y. Chiu, and H. Zhao, "Ultrafast and spatially resolved studies of charge carriers in atomically thin molybdenum disulfide," *Phys. Rev. B*, vol. 86, no. 4, p. 045406, Jul. 2012, doi: 10.1103/PhysRevB.86.045406.

[43] H. Wang, C. Zhang, and F. Rana, "Ultrafast Dynamics of Defect-Assisted Electron–Hole Recombination in Monolayer MoS2," *Nano Lett.*, vol. 15, no. 1, pp. 339–345, Jan. 2015, doi: 10.1021/nl503636c.

[44] H. Shi *et al.*, "Exciton Dynamics in Suspended Monolayer and Few-Layer MoS2 2D Crystals," *ACS Nano*, vol. 7, no. 2, pp. 1072–1080, Feb. 2013, doi: 10.1021/nn303973r.

PART III

<div style="text-align: right">

CHAPTER 7

</div>

KERR NON-LINEARITY OF GRAPHENE AS SEEN VIA CROSS-PHASE MODULATION

Contents

7.1. Introduction

The experimental discovery of graphene in 2004 [1] has stimulated increasing scientific interest in this remarkable two-dimensional material. Since its isolation, graphene, a single sheet of carbon atoms in a honeycomb lattice, has attracted the attention of many researchers due to its unique properties [2] and its potential use in many applications [3]. As a versatile experimental method, spectroscopy has been widely used to investigate the optical conductivity [4], electronic structure [5], and charge dynamics of graphene [6]. Graphene displays extraordinary broadband optical characteristics [7] and strong third-order nonlinear optical properties [8] that allowed the development of an active field of research in recent years.

Due to the high mobility and linear energy dispersion of graphene's charge carriers, it shows a strong third-order nonlinear electrodynamic response.[9] This opens up the possibility of using nonlinear

optical processes in graphene to modulate the frequency of incident optical fields or to create optical switches in ways similar to the use of nonlinear electronic elements in electronic circuits. The phenomena have already been demonstrated in several experiments and applications including third and higher harmonics generation, four-wave mixing, saturable absorption, and the Kerr effect.[10] Due to the centrosymmetric crystalline structure of graphene, even-order nonlinearities are forbidden at the level of the dipole approximation, so that the dominant nonlinear contribution is third order in the applied fields. In particular, the Kerr effect nonlinearity leads to both exceptionally strong self-focusing and rapid saturable absorption in graphene. Both these effects have been used to initiate mode-locking in short-pulsed lasers.

The optical Kerr effect is a nonlinear phenomenon related to a change in the refractive index of materials when they interact with the field of a strong electromagnetic wave,

$$n = \sqrt{\varepsilon} = n_0 + n_2 I \qquad (7.1)$$

here ε is the dielectric function of the material and I is the intensity of the incident electromagnetic field. The nonlinear refractive index n_2 at a single frequency is related to the third-order electric susceptibility $\chi^{(3)}(\omega, \omega, -\omega)$ of the medium. Several different experimental techniques have been used to determine the nonlinear refractive index of graphene, including Z-scan [11], four-wave mixing experiments [12], and OHD-OKE [13] (optical heterodyne detection of optical Kerr effect). The reported results for n_2 in graphene vary widely, spanning several orders of magnitudes, including disagreement about the sign of the effect. Opposite signs have even been reported when using the same basic experimental technique in some cases.[11,13–15] This indicates that the measured n_2 values are sensitive to a wide variety of experimental parameters including the wavelength, pulse duration, and the incident beam's transverse spatial profile. The influence of different sample preparation techniques is also likely the cause of at least part of this disagreement, as well as the presence of impurities (defects and doping) and the substrate material.[14,16]

To perform these experimental measurements it is necessary to employ intense incident fields which may give rise to several unwanted side effects such as multiphoton absorption or stimulated Raman scattering. Among these side effects, there is one interesting phenomenon that can occur when a high-intensity optical pulse propagates in a nonlinear responding medium, that of self-phase modulation that can be used to our advantage. The phenomenon now known as Self Phase Modulation (SPM) was first observed in the context of the transient self-focusing of optical pulses propagating in a cell filled with a solution of a carbon disulfide. The first observation of SPM in solids

and glasses was carried out by Alfano and Shapiro [17] using picosecond pulses. Subsequently, this effect was also observed in optical fibers, with the initial experiments making use of fibers whose core was filled also with a carbon disulfide solution.[18]

Self Phase modulation is a process in which an ultrashort optical pulse locally changes the index of refraction of the medium in which it is propagating. This change, in turn, introduces a phase modulation on the propagating optical pulse. If for simplicity, one ignores propagations effects, the optical phase acquired by a beam with intensity I and propagation vector $k_0 = \omega_0 / c$ after passing through a Kerr medium of thickness L is given by

$$\delta\phi = \bar{n}k_0 L = (n + n_2 I)k_0 L \tag{7.2}$$

Since the instantaneous optical frequency of a pulse is given by minus one times the temporal derivative of the pulse's spectral phase this can lead to the appearance of new frequencies and significant spectral broadening and chirping.

$$\omega_{\text{instantaneous}} = -\frac{\partial\varphi}{\partial t} \approx \omega_0 - \frac{n\omega_0}{c}n_2\frac{\partial I}{\partial t} \tag{7.3}$$

Normally the Kerr coefficient, n_2, is positive which causes the frequencies of the leading edge of the pulse to decrease (are red-shifted) while the frequencies at the trailing edge of the pulse increase or (are blue-shifted).

Generalizing the situation to the case of two incident beams, the modulation in the refractive index provoked by one of the pulses can be felt by the other, leading to an all-optical form of "crosstalk". This effect has come to be known as Cross Phase Modulation (XPM). and can result in several interesting phenomena. For example in optical fibers, the temporal intensity variation of one optical field can modulate the temporal phase of other copropagating optical signals in the same fiber and can be used for optical switching and signal processing.

To understand this more fully consider the superposition of two optical fields with carrier frequencies, ω_1 and ω_2,

$$E = E1 + E2 = \text{Re}[\text{E}(\omega_1,t)e^{j\omega_1 t} + \text{E}(\omega_2,t)e^{j\omega_2 t}] \tag{7.4}$$

These fields can induce a nonlinear polarization in the medium P, of the material due to the applied field, E, $P^{\text{XPM}} = \chi^{(3)}\text{E}^3$. Assuming Kleinmann symmetry and neglecting dispersion in the nonlinear susceptibility the contribution that oscillates at the frequency ω_1 is:

$$P^{(3)}\left(\omega_1,t\right)=\tfrac{3}{4}\,\chi^{(3)}\left[\left|E\left(\omega_1,t\right)\right|^2+2\left|E\left(\omega_2,t\right)\right|^2\right]E\left(\omega_1,t\right)e^{j\omega_1 t} \quad (7.5)$$

The first term represents the contribution of SPM while the second is the XPM component. This variation in polarization can be probed using, for example, the OKE method. For that, we have a strong pump beam and a weak probe superimposed in the sample. The probe signal power must be relatively weak, so that the phase shift/modulation in the sample is dominated by the strong pump light through XPM, allowing us to neglect the effect of SPM on the probe. Due to the temporal profile of the strong pump, the phase of the weak probe field is modulated through XPM. Detecting the new frequency components induced by the phase modulation allows one to determine $\chi^{(3)}$ or equivalently n_2.

More sensitive measurements can be made by taking advantage of the high polarization discrimination afforded by calcite polarizers. When both the pump and probe beams illuminate the sample, in the presence of nonlinearity, the pump induced birefringence or dichroism of the sample can alter the probe polarization. If the polarizer is crossed with the unmodulated probe beam, any Kerr induced polarization change will lead to a small part of the probe being transmitted and detected. Induced birefringence corresponds to the real part of the complex nonlinear refractive index, while induced dichroism corresponds to the imaginary part. To obtain time-resolved data, which reveals the temporal dynamics of the nonlinearity, a delay-line is used to control the temporal superposition between the pump and the probe pulse.

The sensitivity of this method can be further improved by employing optical heterodyne detection, OHD-OKE, using a local oscillator, to amplify the weak probe signal that passes through the polarizer. The resulting improvement in the signal-to-noise ratio is often sufficient in practical cases to distinguish between induced birefringence and dichroism or equivalently the real and imaginary parts of the Kerr coefficient. This method has been used to characterize the nonlinear susceptibilities of chalcogenides thin films [19], transition metal dichalcogenides [20], and also of graphene [13].

The quadratic dependence of the OHD-OKE signal on the material response makes the interpretation of the time-resolved signal, as well as the estimation of the relaxation dynamics difficult. Furthermore, the experiment is so sensitive that it can be affected by such normally neglected phenomena such as strain birefringence from the lenses.

Here we propose an alternative method to characterize n_2 detecting changes in the frequency spectrum of the probe rather than its polarization. This opens the possibility of spectrally resolving the nonlinear response. The experimental procedure we are developing to measure the nonlinear

refractive index, n_2, of graphene is a simple and effective technique based on the XPM effect using the OKE approach/geometry where we used a white-light continuum (WLC) as a probe and analyze the frequency modulation rather than polarization changes. To accomplish this we take advantage of the strong frequency chirp present in our WLC.
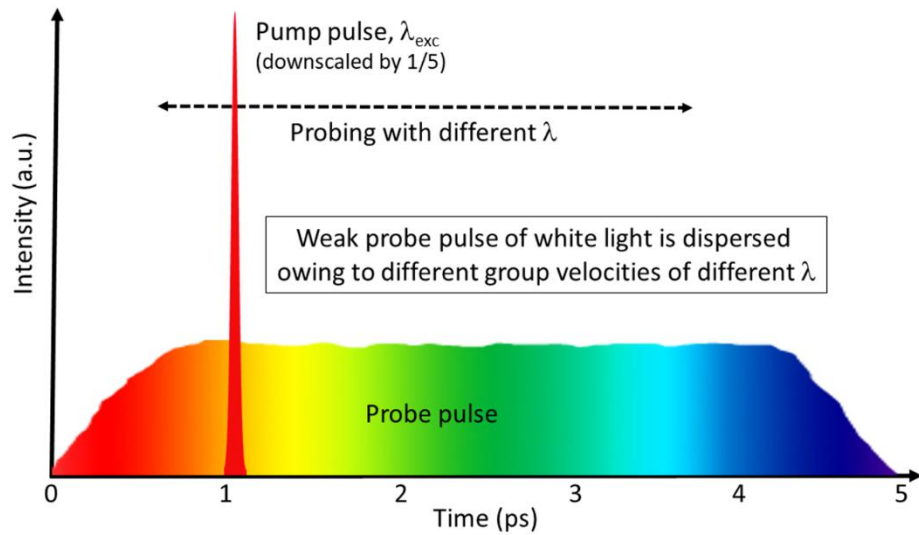
Figure 7.1 Diagram depicting the experimental method.

If the pump and probe pulses overlap in time, i.e., around the zero time delay point, the time-dependent change of the refractive index provokes a time-dependent modulation of its phase. This, in turn, creates a spectral change, which can be detected if the probe is dispersed after the sample. This spectral resolution is important since the mechanism involves no net energy transfer either away from or into the probe. In other words, the total energy of the probe remains constant but is only redistributed over different frequencies. It is important to notice that XPM occurs even when the medium is completely transparent to both the pump and the probe pulses. Because the WLC probe is highly chirped only a narrow band of its frequencies will overlap with the pump field at any given pump-probe delay. Varying the delay allows us to shift the spectral region affected, providing a convenient means to study the dispersion of the nonlinear Kerr effect.

7.2. Experimental Methods
7.2.1. Samples

The graphene sample used in the work reported in this chapter was CVD graphene, produced as explained in Chapter 2.6.

7.2.2. Setup

The details of the laser system and broadband ultrafast pump and probe apparatus and software have been previously described in Chapter 2.2 and 2.4.

Briefly, and as depicted in Figure 7.2, for the XPM experiment, a portion (500 µJ/pulse) of the output of the chirped pulse regenerative amplifier (110 fs FWHM pulses at 800 nm, at 1 kHz repetition rate) is used to pump the parametric amplifier which generates the final pump pulses with energies of around 100 µJ for the wavelengths used in this the experiment. Before reaching the sample, the pump beam is attenuated to around 100 nJ and then optically chopped to provide a reference signal. The chopper was synchronized with the regenerative amplifier and worked at half of its repetition rate.

The residual fundamental beam of the output of the chirped pulse regenerative amplifier was conducted down a variable delay line that determines the relative delay between the pump and probe pulses. After the delay line, a single filament WLC is generated in a sapphire window to create the probe pulse. An iris was inserted in front of the focusing lens before the sapphire window to adjust the beam diameter for optimal white light generation. The WLC pulse generated here has normal dispersion, meaning that the red wavelengths travel faster than the blue ones. Spectrally, the window of the WLC pulse used extends from 450 to 750 nm.

The pump and probe beams are focused onto the sample in a collinear geometry using a microscope objective. The probe intensity was always less than the pump intensity, and the probe spot size was chosen to be smaller than the pump spot size at the focus to ensure homogeneous interaction within the probed area. The light was then collected by an identical objective lens in a trans-illumination configuration and transmitted through a short pass dichroic filter or a notch filter to diminish the spectral intensity of the pump and avoid interference in the acquisition.

The XPM signals were collected using an Andor Shamrock SR-303i spectrograph which is synchronically triggered externally, at 1kHz, twice the frequency of the pump beam modulation. For normalization, the intensity of a small portion of the probe beam was registered by a fast photodiode and integrated by a Stanford Research boxcar integrator (SRS SR250) whose output was subsequently sampled via a NI-Daqmx.

Figure 7.2 Diagram for the XMP experiments implemented in our laboratory. The experiment is controlled through a LabVIEW program. $\lambda/2$-half wave-plate; GL-P- Glan-Laser Calcite polarizer; F-Filter; P-Polarizer; BS Beam splitter, PD-Photodiode.

The temporal resolution depends primarily on the degree of the WLC chirp, and the spectral resolution of the monochromator. The temporal resolution was around 12 fs, and was experimentally determined by analyzing the data from the XPM measured on a glass microscope slide to extract the chirp and the IRF.

7.2.3. Data Collection & Analysis

The XPM data, ΔT, was collected as a function of the delay between the pump and probe pulses, using the "TASpectra" program, rooted in the flowchart of "PPSystem" as in chapter 2.5.2, that controlled the setup and sequentially measured the WLC transmitted through the sample with the pump on (the disturbed signal), S_{pumped}, and with the pump blocked (the reference signal), S at each Δt.

The spectra were acquired at 1024 wavelength values over a 120 nm range and collected over delays ranging from -250 fs to 10 ps. For each acquisition, the spectrum was normalized using the synchronized information from the generated WLC intensity.

The differential transmission spectra were then compiled as:

$$\Delta T\left(\lambda,\Delta t\right)=\frac{S_{pumped}\left(\lambda,\Delta t\right)-S\left(\lambda\right)}{S\left(\lambda\right)}. \tag{7.6}$$

Each delay time step represents the acquired spectral region indicating the modifications in the spectrum for a particular delay between the pump and probe beams. The spectra were averaged at each delay until the desired signal-to-noise ratio was achieved (SNR~10); typically 10000 repetitions were required at each delay.

7.3. Results

Using a pump beam at 800nm and ensuring that the focused area of the probe is smaller than that of the pump, to ensure that "all" the probe is perturbed, we proceeded to obtain the change in the white-light spectrum due to the XPM. We analyzed several areas on the graphene samples deposited on the 1.1 mm thick microscope glass/slide and then areas only with the glass substrate to allow us to have a signal like an instrumental response function (IRF) to calibrate the set-up, Figure 7.3
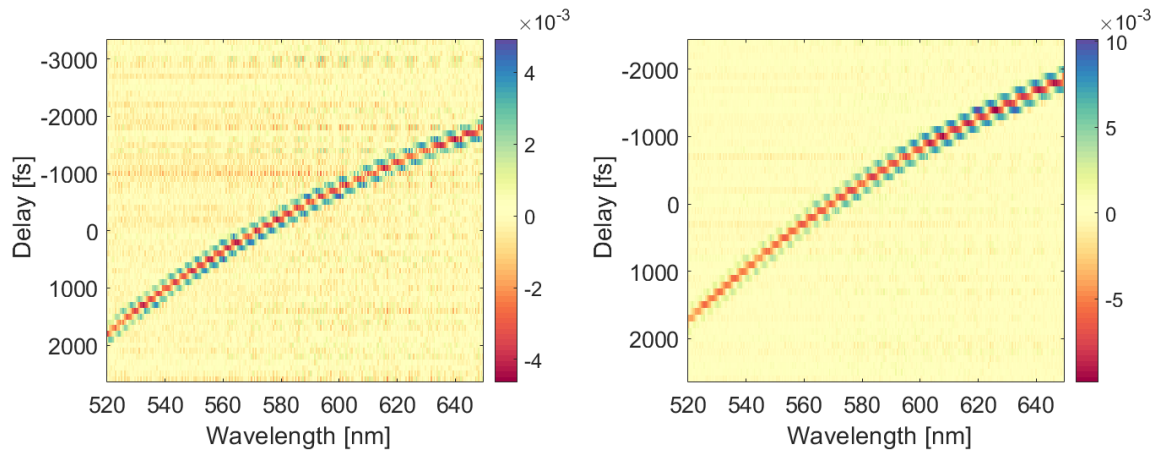
Figure 7.3 Experimental XMP signal obtained for the substrate only (left) and the graphene plus substrate (right) with the strong pump field at 800nm, longer wavelength than the sampled probe spectrum. The color-bar indicates the variation in ΔT.

Ideally, the experiment would be carried out on a single freestanding monolayer graphene flake, but this was not possible to obtain. Figure 7.3 (left) presents the XPM signal recorded from the microscope slide used as reference/IRF and physical support for the graphene, as a function of wavelength and time delay between pump and probe pulses. The same process was then repeated on parts of the substrate covered with the monolayer of graphene and is represented in Figure 7.3-right. In this experiment, the pump pulse was centered at 800 nm.

The variation in the wavelength of the central modulation as a function of delay allows us to characterize the frequency chirp of the white light probe (see Figure 7.8 below). It is dominated by a quadratic component (group velocity dispersion) but also contains a non-negligible third-order term.

The pump induced change in transmission as a function of wavelength for three distinct probe-pump delays, for both the microscope slide only and graphene plus microscope slide systems, is shown in Figure 7.4. As the pump-probe delay is decreased, the pump interacts with increasingly earlier parts of the probe pulse, with spectra more to the red. It should be noted that the zero value for the delay is somewhat arbitrary being related to the physical position of the delay stage.
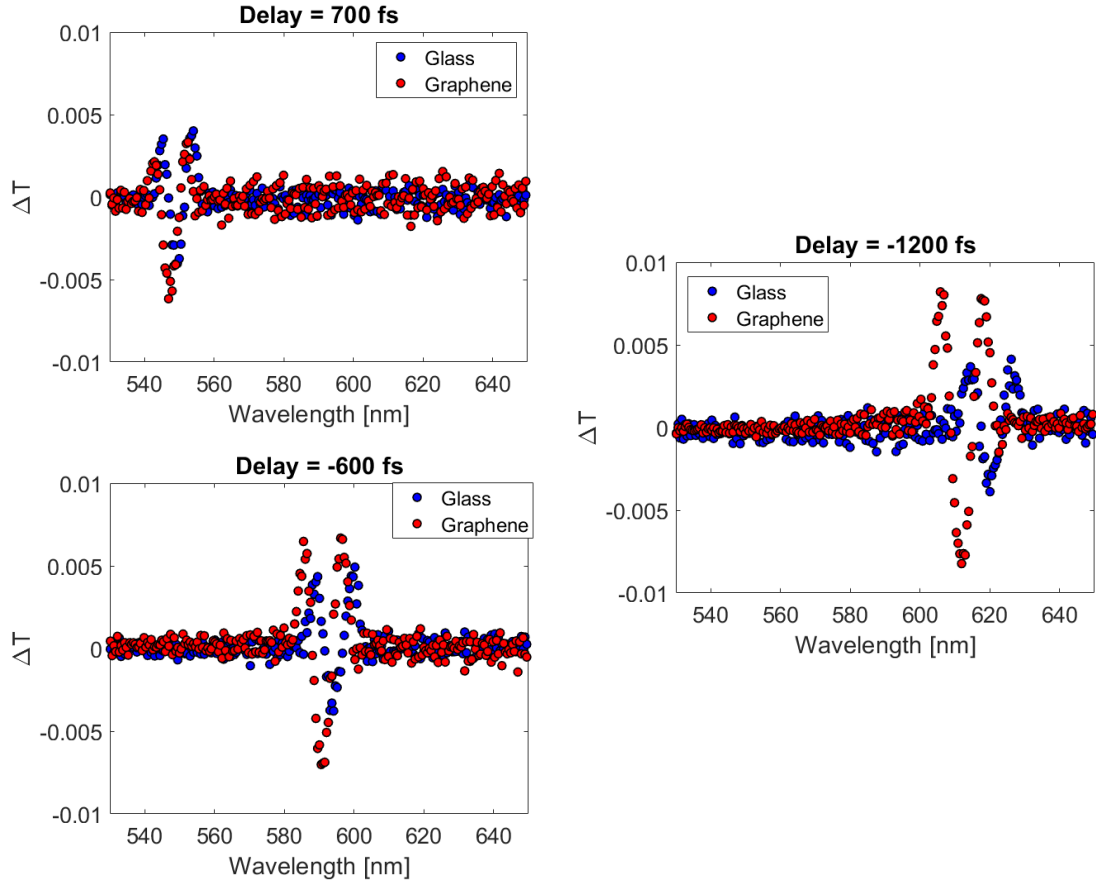
Figure 7.4 Experimental XMP signal, obtained from the microscope glass (blue) and the graphene plus microscope slide (red) as a function of wavelength for three representative pump-probe delays 700, -600 and -1200 fs respectively.

In general, the XPM leads to symmetrically shaped signals, with a magnitude comparable to those obtained in a normal transient absorption pump-probe experiment. To intuitively understand the general form of the signals, consider the effect of the phase modulation in the instantaneous frequency as described in Eq. (7.2) and (7.3) repeated here for convenience:

$$\delta\phi = \bar{n}k_0 L = (n + n_2 I)k_0 L, \tag{7.2}$$

$$\omega_{\text{instantaneous}} = -\frac{\partial \varphi}{\partial t} \approx \omega_0 - \frac{n\omega_0}{c} n_2 \frac{\partial I}{\partial t}. \tag{7.3}$$

Because the leading edge of the pump pulse has a positive derivative, the leading frequencies of the portion of the white light beam that overlaps with the pump will be downshifted in frequency, while the one superposed with the trailing edge of the pump are upshifted. This produces a modulation with a depletion in the center of the probed frequencies and a slight increase in the amplitudes of the

frequencies at the edges of the portion of the probe pulse simultaneous with the pump, as diagrammed schematically in Figure 7.5.
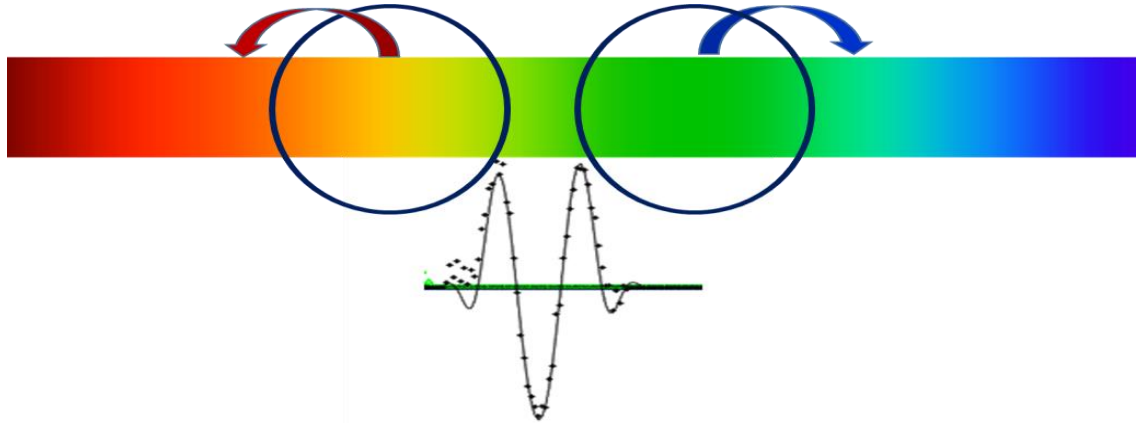
Figure 7.5 Depiction of the frequency redistribution due to the XMP provoked by the Kerr effect.

For the glass microscope slide, the signals have e roughly the same magnitude for the different time delays indicating a flat spectral response for the glass. For the signals from the graphene/substrate combination, it is clear that the central modulation magnitude increases for longer wavelengths. The variation of the magnitude of the modulation with the pump delay relative to the center of the probe spectrum as shown in Figure 7.6. Due to the positive chirp of the white light beam, negative times correspond to longer wavelengths (lower frequencies).
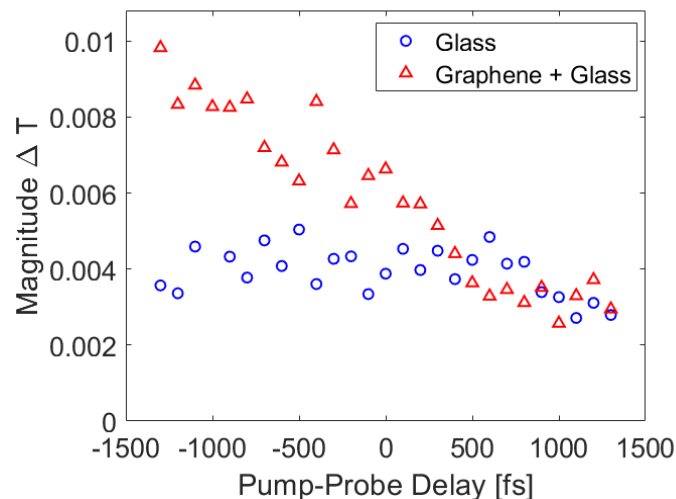
Figure 7.6 Variation of the magnitude of the XPM induced change in the spectrum with the pump-probe time delay for both the glass(blue) and the graphene plus glass (red) systems. Here the magnitude of ΔT corresponds to the depth of the central valley in the modulated spectra. The zero time delay has been set to the center of the delays probed.

It is also feasible to employ pump pulses at blue wavelengths, i.e. higher energies than those contained in the white light. In this case, we observed, as expected, a white light chirp similar to that previously extracted.
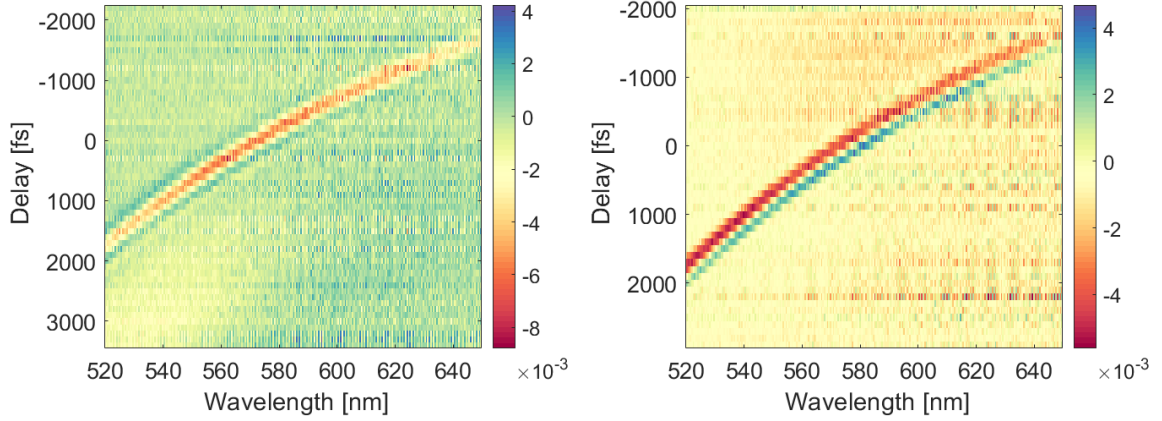

Figure 7.7 Experimental XMP signal obtained for the substrate only (left) image and the graphene (right) image with the strong field (pump=400nm), higher energies than the probe. The color-bar indicates the variation in ΔT .

There is significantly more noise in this data. The focusing of a pump beam centered at 400nm is different from that at 800nm due to diffraction and chromatic aberrations. This makes the experiment harder to carry out; in particular, at the beam waists, the pump is no longer much larger than the white light probe. One can therefore expect small variations in the overall signal magnitudes compared to the data shown in Figure 7.3 The depths of the glass valleys are somewhat deeper than was the case for the microscope glass only data of Figure 7.3. In contrast, the graphene plus microscope slide data pump at 400nm has a modulation depth rather less than the modulation when pumped at 800nm. Furthermore, the 400nm pump data is asymmetric with the peak on the blue side largely missing. However, the modulation depth does increase as the modulation wavelengths become closer to the wavelength of the pump; this time they increase towards the blue. This suggests that the third-order nonlinear response of the monolayer graphene shows considerable dispersion with a resonant enhancement as the probe wavelengths approximate those of the pump field.

7.4.   Analysis

Due to the difficulties in the experiment using the pump at 400nm, we will focus our attention on the data acquired with the pump center at 800nm. A first step in the analysis of the results is to

characterize the dispersion curve of the white light probe. Given the symmetric form of the spectral modulation, (see for example Figure 7.4) we assume that the center of the pump pulse at each delay is superimposed on the frequency component of the white light probe that suffers the most intense modulation. Fitting the variation of the frequencies at which the maximum modulation occurs with the pump-probe delay, we find that a third-order spline accurately reproduces the data.

Figure 7.8 displays the results. The obtained chirp is positive as expected and nearly linear, with a very slight negative third-order component.

One interesting observation to make is that due to this rather high chirp, the effective temporal resolution of the experiment is limited by the spectral resolution of the monochromator and not the 100 fs step size in the probe optical delay line or the temporal width of the pump pulse. For example, sampling the probe spectrum near 620 nm the fit value of the second-order chirp is roughly $C_2 \approx 15\,GHz\,/\,fs$. As the spectrometer samples the spectrum with a resolution close to 0.5nm, at 620nm this corresponds to a frequency resolution of approximately $\Delta f \approx 390\,GHz$ leading to an effective temporal resolution, $\Delta t \approx \Delta f\,/\,2C_2 \approx 12.9\,fs$ an order of magnitude better than the FWHM of the pump pulse.
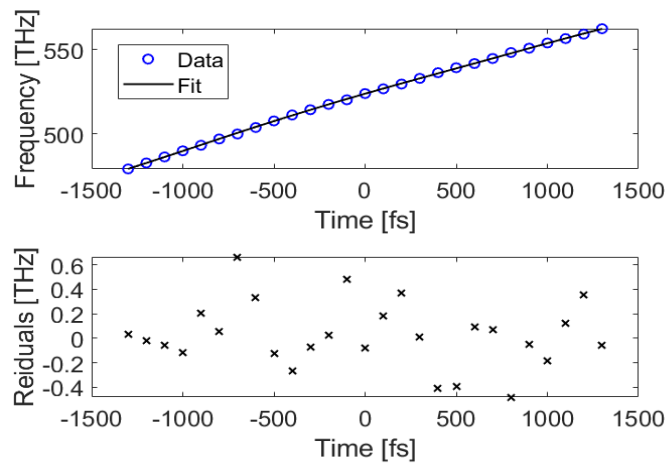
Figure 7.8 Spline fit to the variation in the peak modulation frequency due to XPM in a 1mm glass slide as a function of the relative delay between the pump and white light fields. The largest residuals are less than 0.1% of the peak frequency.

A second point to make is that the overall phase change induced in the probe beam by the pump is rather small. One can readily see this by considering an ideal situation in which the nonlinear media is so thin that the Kerr induced change in the refractive index is constant through the medium, allowing one to ignore any propagation effects within the media. If one further assumes that the white-light probe field is a linearly chirped Gaussian beam of the form:

$$E_{\mathrm{WL}}(t) = A_{\mathrm{WL}} \exp\left[-\left(\tfrac{t}{\tau_{WL}}\right)^2 - iC_2 t^2 \right], \qquad (7.7)$$

while the pump takes the form of an unchirped Gaussian with a $1/e2$ intensity half-width of τ_P, then it is a simple matter to calculate the change in the white-light prob spectrum induced by the pump. Under these conditions, the nonlinear phase will take the form

$$\Delta\Phi_{NL}(t) = \Delta\Phi_0 \exp\left[-\frac{2t^2}{\tau_P^2} \right]. \qquad (7.8)$$

The un-modulated spectrum is given by the Fourier transform of Eq. (7.7)

$$S(\omega) = \left| \int_{-\infty}^{\infty} dt\, e^{i\omega t} A_{\mathrm{WL}} \exp\left[-\left(\tfrac{t}{\tau_{WL}}\right)^2 - iC_2 t^2 \right] \right|^2$$

$$= \frac{\pi \tau_{WL}^2 |A_{\mathrm{WL}}|^2}{\sqrt{1 + \left(C_2 \tau_{WL}^2\right)^2}} \exp\left[\frac{-\omega^2 \tau_{WL}^2}{2\left(1 + \left(C_2 \tau_{WL}^2\right)^2\right)} \right], \qquad (7.9)$$

while the modulated spectrum is

$$S_{\mathrm{Pumped}}(\omega) = \left| \int_{-\infty}^{\infty} dt\, e^{i\omega t} A_{\mathrm{WL}} \Delta\Phi(t - t_d) \exp\left[-\left(\tfrac{t}{\tau_{WL}}\right)^2 - iC_2 t^2 \right] \right|^2. \quad (7.10)$$

Figure 7.9 shows how the modulation varies with the amplitude of the nonlinear phase, $\Delta\Phi_0$, when the duration fo the pump $\tau_P = 120\,fs$, that of the white-light probe $\tau_{WL} = 2.5\,ps$ and the linear chirp parameter $C_2 = 15\,GHz/fs$.

The right-hand portion of Figure 7.9 confirms that under these conditions the modulation depth scales linearly with the peak nonlinear phase; the slope for the chosen parameters is roughly $|\Delta T|_{\max} / \Delta\Phi_0 \approx 0.7 / \mathrm{radian}$. From Figure 7.3, one can confirm that the maximum observed modulation depth in ΔT never exceeds 0.01.
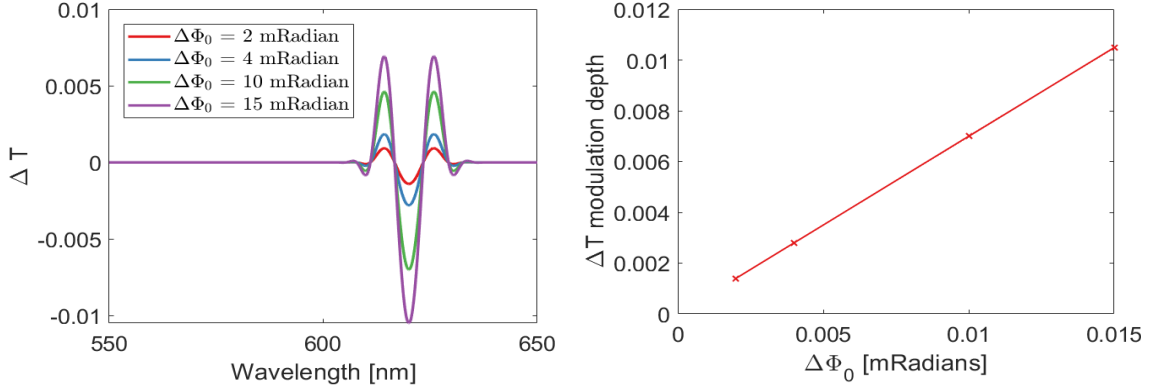
Figure 7.9 One dimensional simulation of the effects of XPM as a function of the peak nonlinear phase modulation(left). Here the pulse widths of the pump and white light probe were taken to be 120 fs and 2.5ps respectively. Propagation effects were ignored. The modulation depth is linearly proportional to the peak nonlinear phase.

The above simulation then implies that the peak nonlinear phase, $\Delta\Phi_0$, is less than 15 mrad. In this one-dimensional model, $\Delta\Phi_0$, effectively corresponds to twice the value of the B integral for the pump beam:

$$\Delta\Phi_0 = 2B = \frac{4\pi}{\lambda}\int_0^L dz\, n_2 I_{Pump}\left(z, t = 0\right).$$
(7.11)

The factor of two arises because XPM is twice as effective as self-phase modulation. The B integral is frequently used in the design of nonlinear linear amplifiers. When B =3, the integrated on-axis phase change due to the nonlinear change in the refractive index corresponds to a phase change of nearly half a cycle, which is a rough threshold for when catastrophic self-focusing might occur. Under our conditions, the effective B integral for the pump is less than one-hundredth, meaning the phase front of the pump beam is only slightly affected. We note that research-grade front surface mirrors often have a surface quality specified to a level of $\lambda/10$ an order of magnitude greater than the on-axis pump B integral due to the Kerr effect. This implies that in a first approximation, the nonlinear modifications in the propagation of the pump beam, due to self-phase modulation can be safely ignored.

Concentrating on the WLC, the two main linear effects affecting the propagation fo the beams within a medium are diffraction and dispersion. Usually, in the description of ultrafast laser beam propagation, linear dispersion effects are expanded in a power series about the carrier frequency,

$$k(\omega) \approx k(\omega_0) + \frac{\partial k}{\partial \omega}\bigg|_{\omega_0}(\omega - \omega_0) + \frac{1}{2}\frac{\partial^2 k}{\partial \omega^2}\bigg|_{\omega_0}(\omega - \omega_0)^2 + \cdots \quad (7.12)$$

The zero-order (first) represents the usual phase accumulation due to propagation in a linear medium and is a global constant for the entire beam. The first-order term is proportional to the inverse of the group velocity at the carrier frequency, $1/v_{Group} = \partial k / \partial \omega$. For a single beam, within the slowly varying envelope approximation, this term can be eliminated by transferring to a reference frame that travels with the group velocity $z' = z - v_{Group}t$, $t' = t$. Therefore, it describes the overall delay of a pulse traveling at the group velocity and will not lead to any distortion of the overall pulse shape. The derivative in the second-order term is the group delay dispersion, $\beta_2 = \partial^2 k / \partial \omega^2$, i.e. the variation in the inverse group velocity with frequency. Under normal dispersion, corresponding to a positive value of the second derivative, the lower frequency components tend to travel faster (they see a lower effective refraction index) while the higher frequencies travel more slowly. This effect tends to spread out the pulses, effectively creating a frequency chirp. For a pulse with a Gaussian temporal shape of duration τ, the characteristic length scale over which group velocity dispersion becomes an important effect is the dispersion length (analogous to the Rayleigh length for diffraction), $L_{\text{disp}} = \tau^2 / 2\beta_2$. Taking the example of BK7 glass in the visible, the group velocity dispersion, β_2, is less than 100 fs2/mm which leads to a dispersion length L_{disp} greater than 50 mm for a 100fs pulse. As the glass slide used in the XPM experiments is only 1.1 mm thick, group velocity dispersion will make a very minor contribution to the pump and can be safely ignored for the white-light probe.

Given the above considerations, the propagation of the white-light probe beam can be well-described, within the slowly varying envelope approximation, e.g. in [21], by the following differential equation,

$$\frac{\partial A_{WL}(\vec{r},t)}{\partial z} = \left\{ \begin{array}{l} \dfrac{i}{2k_{WL}}\nabla_T^2 + \left(\dfrac{1}{v_{g,Pump}} - \dfrac{1}{v_{g,WL}}\right)\dfrac{\partial}{\partial t} + \\[2ex] 2i\dfrac{\omega_0}{c}n_2 I_{Pump}(\vec{r},t) \end{array} \right\} A_{WL}(\vec{r},t) \quad (7.13)$$

Here A_{WL} is the WLC electric field amplitude with the carrier frequency removed. On the right-hand side, the first term describes diffraction; the second describes the difference in the group velocities

between the pump and probe beams, and the last term describes the nonlinear interaction corresponding to the XPM. We have transferred to a reference frame traveling with the group velocity fo the pump beam. We will further assume that the pump beam with intensity $I_{Pump}(\vec{r},t)$ can be adequately modeled as an unchirped Gaussian beam propagating in a uniform linear medium. Since we measure the modulation as a relative change in the white light spectrum, we reasoned that the exact temporal form of the white light beam is not important, and for simplicity, we have assumed a Gaussian beam, both spatially and temporally, with a chirp imposed by the above-determined temporal phase (see Figure 7.8). To avoid aliasing when performing Fourier transforms, the temporal full-width at half maximum of the white light Gaussian beam was limited to be five times the width of the pump. We believe this is more than sufficient to model the XPM. The central (carrier) frequency of the simulated white light beam was varied to match that corresponding to the peak modulation (largest value of $|\Delta T|$) at each delay.

To calculate the modulated spectrum, Eq. (7.13) was integrated using a split-step Spectral method, e.g. in [21]. Under this method, operators on the right-hand side of Eq. (7.12) are written a symbolic representation as

$$\frac{\partial A_{WL}}{\partial z} = \left(\hat{L}_s + \hat{L}_t + \hat{N} \right) A_{WL} , \qquad (7.14)$$

where $\hat{L}_s$ is the linear operator describing diffraction, $\hat{L}_t$ is the linear operator describing the group velocity mismatch between the pump and probe beams and $\hat{N}$ is the nonlinear operator describing XPM. Formally integrating Eq. (7.14) over a small step size Δz along the propagation direction leads to

$$A_{WL}\left(z + \Delta z \right) = e^{\left(\hat{L}_s + \hat{L}_t + \hat{N} \right)\Delta z} A_{WL} . \qquad (7.15)$$

The key insight to the split-step formalism is to realize that to up to terms that are quadratic in the step size, Δz ,

$$e^{\left(\hat{L}_s + \hat{L}_t + \hat{N} \right)\Delta z} = e^{\left(\hat{L}_s + \hat{L}_t \right)\Delta z/2} e^{\hat{N}\Delta z} e^{\left(\hat{L}_s + \hat{L}_t \right)\Delta z/2} + Order(\Delta z^3). \qquad (7.16)$$

as can be readily confirmed by expanding the exponentials in power series. Note that the linear propagation steps are most easily carried out in the Fourier space. Consider for example the diffraction operator. When only this operator is present

$$\frac{\partial A_{WL}}{\partial z} = \frac{i}{2k_{WL}}\left(\frac{\partial^2}{\partial x^2}+\frac{\partial^2}{\partial y^2}\right)A_{WL}.$$
(7.17)

Using the Fourier transform relation

$$A_{WL}(x,y,z) = \int dk_x dk_y e^{i(k_x x + k_y y)}\tilde{A}_{WL}(k_x,k_y,z),$$
(7.18)

Eq. (7.17) becomes in Fourier space,

$$\frac{\partial \tilde{A}_{WL}}{\partial z} = -\frac{i}{2k_{WL}}\left(k_x^2+k_y^2\right)\tilde{A}_{WL},$$
(7.19)

which can be immediately integrated to give

$$\tilde{A}_{WL}(k_x,k_y,z+dz) = e^{-i(k_x^2+k_y^2)dz/2k_{WL}}\tilde{A}_{WL}(k_x,k_y,z).$$
(7.20)

Transforming this expression back into real space propagates the field by a distance dz under the action of the diffraction operator. A similar procedure can be carried out in the temporal domain for the group velocity mismatch operator. On the other hand, the action of the nonlinear operator is easiest to solve in real space,

$$\frac{\partial A_{WL}}{\partial z} = 2i\frac{\omega_0}{c}n_2 I_{Pump} A_{WL}$$
$$A_{WL}(z+dz) = e^{2i\frac{\omega_0}{c}n_2 I_{Pump}(z)dz}A_{WL}(z)$$
(7.21)

Here we have assumed that the slice thickness dz is sufficiently thin that the intensity profile of the pump beam is approximately constant. Putting the above steps together, one has all that is needed to propagate a numerical solution of the white light field amplitude forward by a single step of size dz. An adaptive routine with error estimation can be constructed by propagating the field forward by an entire step dz and then repeating the calculation by carrying out a finer mesh, propagating two successive steps of size $dz/2$ and comparing the results. If they agree to a specified tolerance the step is accepted, if they disagree the step size is reduced and the procedure is repeated. Sinkin et al. [22] show how one can combine the results of the coarse propagation (corresponding to a single step size of dz) and the fine propagation (corresponding to two successive steps each of size $dz/2$) to obtain an algorithm accurate to order dz^3.

To carry out this procedure we chose the size of the spatial grid (64 x64 points) and the windows to provide at least 5 sampling points across the beam width at any point during the propagation, both in real space and Fourier space. To achieve the required resolution in Fourier space the window size was set to be 12 times larger than the maximum pump-beam waist radius upon entering or leaving the sample. This limited our simulation to a pump-beam waist diameter at the focus of at least 10 microns. This corresponds to a Rayleigh range of just under 150 microns in the glass slide, meaning the effective beam diameter changes by nearly a factor of 3.5 when propagating through the glass. Increasing the number of spatial grid points would allow simulating tighter foci at the cost of higher runtime. In the temporal domain, we chose the window size to be 8 times the FWHM of the assumed white light temporal width, sufficient to provide a spectral resolution of 0.25 nm at a wavelength of 570nm improving slightly as the delay scan towards the red. We required 256 temporal points to avoid aliasing in the spectral region modified by the XPM.

As already mentioned, the simulations were carried out in the reference frame moving at the group velocity of the pump beam. To initialize the simulation, we shifted the temporal grid slightly so that the white light peak passed coincided with the temporal window center at the midpoint of its propagation through the glass slide. The exact temporal translation of the white light beam during propagation depends on the carrier frequency (set by the delay) and the glass slide material; typical values are of the order of 50-70 fs, a significant fraction of the pump beam's temporal width.

The simulation has the flexibility to vary the pump beam waist position to any point within the glass slide. Not having previously characterized the spacial dependence of the white light beam, we assume the most favorable situation: equal Rayleigh ranges and beam waist positions for the pump and white light beams. This means that the white light beams waist is only slightly smaller than that of the pump beam, their respective radii scale as the ratio in the central wavelengths fo the two beams. Admittedly this does not exactly correspond to the conditions under which the experiment was carried out. By using a CCD camera to image the beams incident on the sample we endeavored to make the white light beam several times smaller than the pump. However, it does represent a reasonable attempt to take into account spatial propagation effects. A better solution would have been to increase the beam sizes so that the Rayleigh length was at least as large as the glass slide thickness. We also ignore any chromatic aberration effects of the microscope objective used to focus the beams, which are probably significant for the WLC.

Our procedure for carrying out the simulations is as follows. First, we create a mask centered about the modulation and extending three times the width of the central prominence to either side of the

central valley in the differential transmission curves. This allows us to emphasize the main variations but also retain sufficient points to access the accuracy of the subtraction used to determine the differential transmission. We assume the pump beam focuses to a beam waist of 5 microns at the center of the glass slide. We have also assumed that the glass slide is fabricated from the Schott glass BK7 and have used the Sellmeier coefficients to calculate the group velocities for the different wavelengths probed as the pump-probe delay is varied. Having fixed the pump beam waist there are effectively two free parameters remaining need to characterize the pump beam: its energy and temporal width. Additionally, due to the effects of group velocity mismatch, there will be slight variations in the temporal shift between the pump and probe beams as the pump modulates different spectral components of the probe beam. Finally, we also allow for the possibility of a slight offset in the subtraction procedure used to calculate the differential transmission.
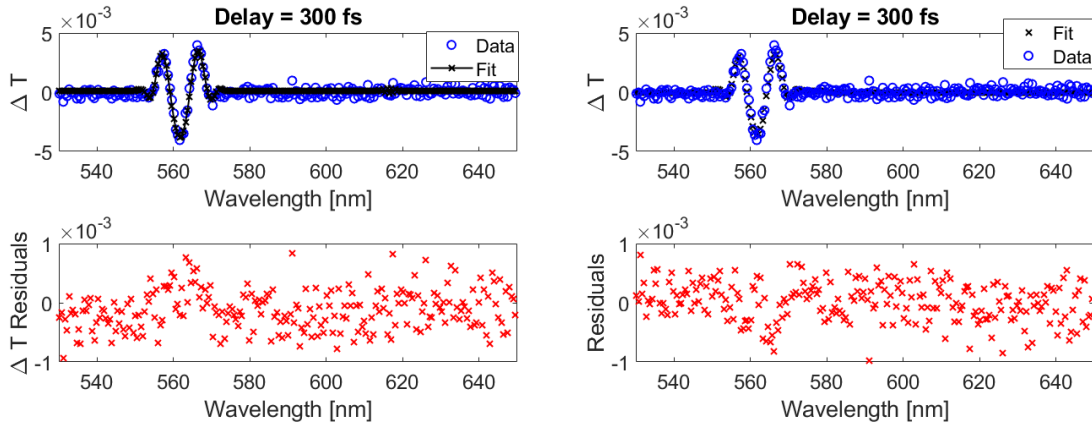

Figure 7.10 An example of the fit obtained for the glass slide data at a single delay glass slide. On the left the fit was for the individual delay and the resulting fit values are pump temporal FWHM = 120.6 ±3.8fs, pump energy = 1.20±0.06 pJ, baseline shift = (1.34±0.5)x10-4, probe temporal shift = 67.3±1.3 fs. On the right is the fit for the same delay when all 26 delays were globally fit to determine the pump temporal FWHM = 123.1 ±1.6 fs, pump energy = 1.15±0.02 pJ (The baseline shift and probe temporal delay were kept as given for the individual fit on the left).

All told then, individual fits of differential transmission to the experimental data points for each delay were performed by varying the four parameters: the incident pump-field temporal FWHM, energy, and small individual corrections to the baseline and temporal position of the simulated white light beam relative to the pump. The fitting procedure was performed using the nonlinear regression algorithm in MATLAB, "fitnlm" as a function. An example of the quality of the fit obtained for one of the delays is given in Figure 7.10 (left). We note that the pump beam energy values depend on the

assumed value of the glass slide's Kerr coefficient. We have used the literature value for the Kerr coefficient of fused silica glass at 800nm, $n_2 = 2.4x10^{-16} cm^2 / W$.

In the next step, we sought to globally fit the pump energy and pump temporal FWHM to all 26 delays, while applying the previously determined individual baseline and temporal shift values at each given delay. Because the noise varies somewhat amongst the various delays we decided to weigh each delay contribution to the global fit by the inverse of the variance of the baseline values. These baseline values are the measured differential transmission values far from the main modulation, i.e. spectral components in the WLC which have negligible overlap with the pump beam. Each delay contains 256 spectral points which we separate using a logical mask into a "signal portion" extending to 3 times the width of the main prominence to either side of the central modulation and a baseline. Typically, the signal portion contains around 50 spectral points. Plotted in Figure 7.11, the estimated noise in ΔT is simply the standard deviation of the baseline. For the glass data, the average noise value is $4.1x10^4$ while the average modulation depth over the 26 delays is $3.94x10^3$ leading to an average signal to noise ratio of just under 10.
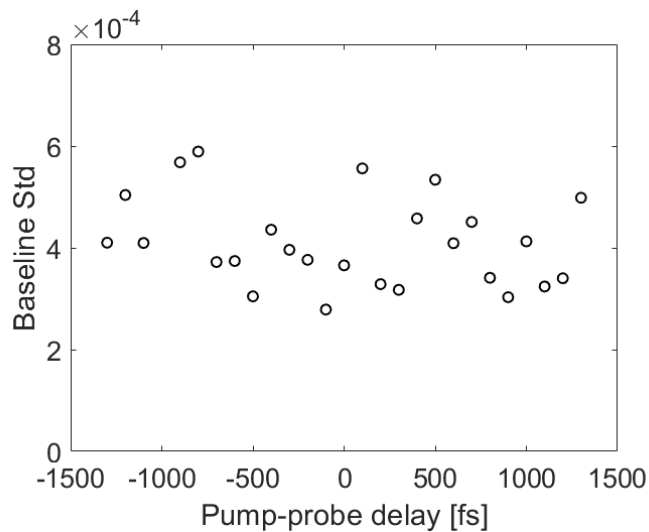
Figure 7.11 Estimated noise in the glass slide data obtained by calculating the standard deviation of the baseline (sections will-removed from the central modulation) in each trace.

Figure 7.12 displays the variation in the found best-fit values for the pump beam energy and pump beam temporal FWHM. There appears to be a slight systematic bias that leads to longer pulses and higher energies for the smaller delays, which correspond to the pump probing the redder portion of the white-light spectra. This might be an indication that the microscope slide employed was not fabricated from BK7 glass, and hence slightly wrong group velocity mismatch values. It could also reflect the effect of chromatic aberration in the focus of the white-light beam. We have assumed that

for all the delays the focus of the white light is precisely superimposed with that of the 800nm pump beam. Never the less, the global fit values seem to provide a reasonable estimate of the average values of the individual fits.
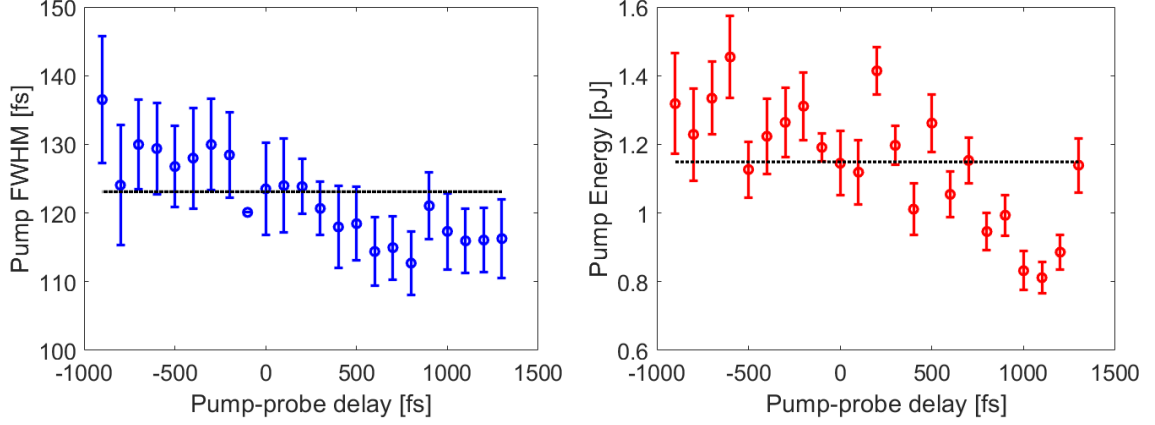

Figure 7.12 The best-fit parameter values for the individual fit of the glass slide data for the pump FWHM (left) and the pump beam energy (right). The dotted lines in each case represent the global fit parameter values corresponding to 123.1 ±1.6 fs and 1.15±0.02 pJ respectively. The error bars represent the standard error in the estimate as output by the Matlab non-linear regression algorithm.

These global values for the pump energy and temporal width serve as fixed inputs for the fit to the system composed of a monolayer of graphene on top of the glass slide. We model the graphene flake's effect as imposing a sharp initial nonlinear phase on the white light field according to the expression:

$$\Delta\Phi_{Graphene}\left(x,y,t\right)=\frac{2\omega_{WL}}{c}n_{2,Graphene}L_{Graphene}I_{pump}\left(x,y,t\right) \quad (7.22)$$

Here $L_{Graphene}$ is the thickness of a monolayer of graphene (0.354 nm)[23].

For these graphene plus glass fits, each delay was fit separately using only two fit parameters, the effective Kerr coefficient, $n_{2,Graphene}$ and the temporal shift. The focus of the pump and probe beams was changed to coincide with the graphene on the front surface of the microscope slide. Figure 7.13 displays an example of a typical fit obtained for an individual delay. In general, the quality of the obtained fits is somewhat worse than that for the glass slides with a slight underestimation of the main valley depth and shoulder heights.
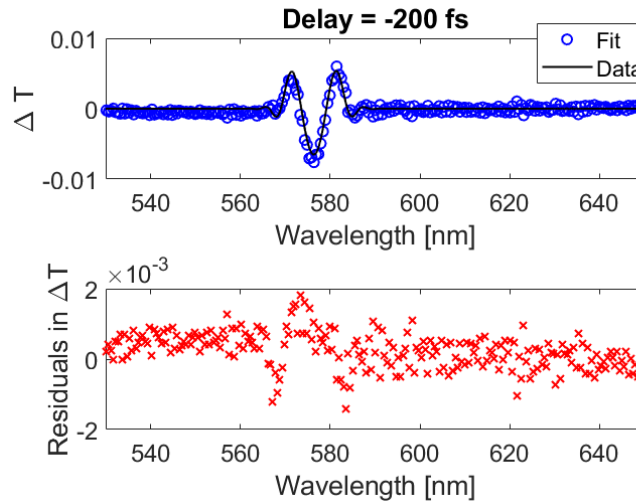
Figure 7.13 Individual fit for the graphene plus glass slide system at a pump.probe delay of -200 fs. The effective value for the graphene Kerr coefficient is n2 = (5.49±0.27)x10[-10] cm²/W.

Since the values used for the pump intensity depend on the Kerr coefficient of the glass slide, which we have not yet measured, we report the results scaled by the Kerr coefficient of the glass slide. Finally, we present the fitting of the combined graphene plus glass using the global fit of the glass data with the beams focused at the front surface of the glass slide, Figure 7.13.
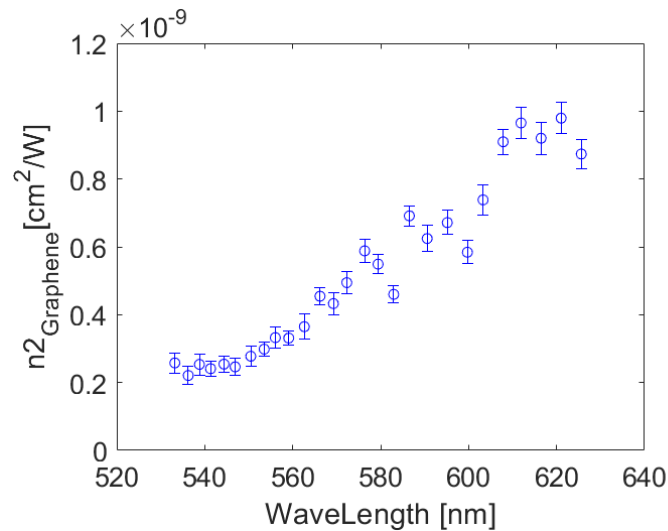
Figure 7.14 Results of fitting the combined graphene plus glass system using the global fit of the glass data with the beams focused on the graphene at the front surface of the glass slide. Error bars represent the standard error estimate output by the fitting algorithm.

Despite a fair amount of dispersion in our values, there is a clear increase in the relative signal as the modulated frequencies approach the frequency of the pump beam. Our data imply that the real part of the Kerr coefficient in Graphene is positive. We do not observe any convincing evidence of a significant imaginary part of the Kerr coefficient. We note that our estimates are based on assuming

that the Kerr coefficient for the glass slide of unknown material is approximately the same as that of fused silica at 800nm, $n_2 = 2.4x10^{-16} cm^2/W$ to estimate the energy of the pump pulse. To make a definite estimate we will need to carefully measure this value by for example carrying out a Z-scan experiment using the mode-locked femtosecond oscillator beam at 800nm.

Previous measurements using FWM with picosecond pulses in the red and near-infrared by Hendry et al.[12] had arrived at a value for graphene's third-order susceptibility of $\left|\chi^{(3)}\right| \approx 1.5x10^{-7} esu$, corresponding to a Kerr coefficient of approximately $n_2 = 2.6x10^{-10} cm^2/W$ which agrees with the lower limits of our estimates. Miao et al.[11], using the Z-scan technique at 1562nm deduced a much higher value of $n_2 = 1.64x10^{-7} cm^2/W$. However, Hendry et al. [12] predict that the third-order susceptibility scales as the wavelength to the fourth power, which amounts to roughly a factor of 50 enhancement for the response at 1562 nm compared to 600nm. Notice, that this is divergent to the Dremetsika et al.[13] endeavor using the OHD-OKE method, that obtained a negative Kerr coefficient, $n_2 = -1.1x10^{-9} cm^2/W$ at a wavelength of 1600nm, being this negative values and magnitudes also retrieved using the Z-scan technique by their group and also by Demetriou et al.[15].

7.5. Summary

In conclusion, it was possible to estimate the size of the third-order optical nonlinearity of graphene with the proposed XPM method. We believe this method is a promising tool for the characterization of the optical nonlinearity of graphene or other 2D materials, mainly because it is not sensitive to sample inhomogeneity's and thermal effects, and also because it provides a ready means of measuring the dispersion of the third-order susceptibility against the standard of the substrate. For it to be quantitatively successful, it will be necessary to adjust the beam diameters so that diffraction and chromatic aberration effects play a lesser role. Towards that aim, we plan to substitute the x10 microscope objective by slightly off-axis ultrafast silver spherical mirrors. Ideally, one should perform these measurements on a free-standing graphene sample, although this is difficult to arrange.

7.6. References

[1]   K. S. Novoselov *et al.*, "Electric Field Effect in Atomically Thin Carbon Films," *Science*, vol. 306, no. 5696, pp. 666–669, Oct. 2004, doi: 10.1126/science.1102896.

[2]   A. H. Castro Neto, F. Guinea, N. M. R. Peres, K. S. Novoselov, and A. K. Geim, "The electronic properties of graphene," *Rev. Mod. Phys.*, vol. 81, no. 1, pp. 109–162, Mar. 2009, doi: 10.1103/RevModPhys.81.109.

[3]   K. S. Novoselov, V. I. Fal'ko, L. Colombo, P. R. Gellert, M. G. Schwab, and K. Kim, "A roadmap for graphene," *Nature*, vol. 490, no. 7419, pp. 192–200, Oct. 2012, doi: 10.1038/nature11458.

[4]   K. F. Mak, M. Y. Sfeir, Y. Wu, C. H. Lui, J. A. Misewich, and T. F. Heinz, "Measurement of the Optical Conductivity of Graphene," *Phys. Rev. Lett.*, vol. 101, no. 19, p. 196405, Nov. 2008, doi: 10.1103/PhysRevLett.101.196405.

[5]   A. Bostwick, T. Ohta, T. Seyller, K. Horn, and E. Rotenberg, "Quasiparticle dynamics in graphene," *Nature Phys*, vol. 3, no. 1, pp. 36–40, Jan. 2007, doi: 10.1038/nphys477.

[6]   Z. Q. Li *et al.*, "Dirac charge dynamics in graphene by infrared spectroscopy," *Nature Phys*, vol. 4, no. 7, pp. 532–535, Jul. 2008, doi: 10.1038/nphys989.

[7]   Q. Bao and K. P. Loh, "Graphene Photonics, Plasmonics, and Broadband Optoelectronic Devices," *ACS Nano*, vol. 6, no. 5, pp. 3677–3694, May 2012, doi: 10.1021/nn300989g.

[8]   J. L. Cheng, N. Vermeulen, and J. E. Sipe, "Third order optical nonlinearity of graphene," *New J. Phys.*, vol. 16, no. 5, p. 053014, May 2014, doi: 10.1088/1367-2630/16/5/053014.

[9]   Y. S. Ang, Q. Chen, and C. Zhang, "Nonlinear optical response of graphene in terahertz and near-infrared frequency regime," *Front. Optoelectron.*, vol. 8, no. 1, pp. 3–26, Mar. 2015, doi: 10.1007/s12200-014-0428-0.

[10] P. Minzioni *et al.*, "Roadmap on all-optical processing," *J. Opt.*, vol. 21, no. 6, p. 063001, Jun. 2019, doi: 10.1088/2040-8986/ab0e66.

[11] L. Miao *et al.*, "Broadband ultrafast nonlinear optical response of few-layers graphene: toward the mid-infrared regime," *Photon. Res., PRJ*, vol. 3, no. 5, pp. 214–219, Oct. 2015, doi: 10.1364/PRJ.3.000214.

[12] E. Hendry, P. J. Hale, J. Moger, A. Savchenko, and S. A. Mikhailov, "Coherent nonlinear optical response of graphene.," *Physical review letters*, vol. 105, no. 9, p. 097401, 2010, doi: 10.1103/PhysRevLett.105.097401.

[13] E. Dremetsika *et al.*, "Measuring the nonlinear refractive index of graphene using the optical Kerr effect method," *Opt. Lett., OL*, vol. 41, no. 14, pp. 3281–3284, Jul. 2016, doi: 10.1364/OL.41.003281.

[14] S. Thakur, B. Semnani, S. Safavi-Naeini, and A. H. Majedi, "Experimental Characterization of the Ultrafast, Tunable and Broadband Optical Kerr Nonlinearity in Graphene," *Sci Rep*, vol. 9, no. 1, pp. 1–10, Jul. 2019, doi: 10.1038/s41598-019-46710-x.

[15] G. Demetriou *et al.*, "Nonlinear optical properties of multilayer graphene in the infrared," *Opt. Express, OE*, vol. 24, no. 12, pp. 13033–13043, Jun. 2016, doi: 10.1364/OE.24.013033.

[16] D. Castelló-Lurbe, H. Thienpont, and N. Vermeulen, "Predicting Graphene's Nonlinear-Optical Refractive Response for Propagating Pulses," *Laser & Photonics Reviews*, p. 1900402, May 2020, doi: 10.1002/lpor.201900402.

[17] R. R. Alfano and S. L. Shapiro, "Observation of Self-Phase Modulation and Small-Scale Filaments in Crystals and Glasses," *Phys. Rev. Lett.*, vol. 24, no. 11, pp. 592–594, Mar. 1970, doi: 10.1103/PhysRevLett.24.592.

[18] E. P. Ippen, C. V. Shank, and T. K. Gustafson, "Self-phase modulation of picosecond pulses in optical fibers," *Appl. Phys. Lett.*, vol. 24, no. 4, pp. 190–192, Feb. 1974, doi: 10.1063/1.1655148.

[19] Q. Liu, B. Lu, X. Zhao, F. Gan, J. Mi, and S. Qian, "Ultrafast non-linear optical properties of Ge20As25Se55 chalcogenide films," *Optics Communications*, vol. 258, no. 1, pp. 72–77, Feb. 2006, doi: 10.1016/j.optcom.2005.07.045.

[20] F. Liu, X. Zhao, X.-Q. Yan, X. Xin, Z.-B. Liu, and J.-G. Tian, "Measuring third-order susceptibility tensor elements of monolayer MoS2 using the optical Kerr effect method," *Appl. Phys. Lett.*, vol. 113, no. 5, p. 051901, Jul. 2018, doi: 10.1063/1.5034079.

[21] P. E. Powers and J. W. Haus, *Fundamentals of Nonlinear Optics, Second Edition.* Boca Ratón, Florida: Milton : CRC Press, 2017.

[22] O. V. Sinkin, R. Holzlohner, J. Zweck, and C. R. Menyuk, "Optimization of the split-step Fourier method in modeling optical-fiber communications systems," *Journal of Lightwave Technology*, vol. 21, no. 1, pp. 61–68, Jan. 2003, doi: 10.1109/JLT.2003.808628.

[23] C. J. Shearer, A. D. Slattery, A. J. Stapleton, J. G. Shapter, and C. T. Gibson, "Accurate thickness measurement of graphene," *Nanotechnology*, vol. 27, no. 12, p. 125704, Feb. 2016, doi: 10.1088/0957-4484/27/12/125704.

CHAPTER 8

SUMMARY

Contents

8.1.   What has been done

To recap, it was possible to gain some insights of the linear and non-linear optical properties arising from interactions of elementary excitations in several nanostructures.

We started for obtaining a rather clear indication that the graphene environment does indeed influences the RRS signal coming from either QDs or NPLs. With the former, there are two effects observed: (i) QDs deposited on graphene show a much smaller shift of the LO-phonon peak with respect to the bulk CdSe value than dots deposited on glass, and (ii) the magnitude of the Raman peak depends considerably on the gate voltage applied to graphene. Both effects may be related to electron transfer between graphene and QDs of certain sizes, which can suppress (or enhance) Raman scattering for that QD population. This explanation, however, would not work for nanoplatelets because, in contrast with QDs, they have a very limited dispersion of thickness. Therefore, the hybrid nature of the NPLs' Raman mode, with the frequency varying remains a plausible explanation. Yet, further experiments are required to fully prove the theoretical concept proposed.

In order to obtain enhanced 2HG biomaterials it was possible to show that polymer nanofibers embedded with optically nonlinear organic compounds give rise to a strong anisotropic response of the second-harmonic generation as a function of the polarization direction of the incident light. The

macroscopic orientation of small nonlinear active molecules in conjugation with an appropriate biopolymer host can improve the optical properties of the materials, exceeding the properties of the bulk crystals. The values obtained for the hosted nanofibers encourage us to look forward to developing promising and low cost bioorganic optical devices, with a number of potential applications.

Fast forward to the time resolved experiments it was possible to couple the QDs to CVD and exfoliated graphene, in order to verify their possible viability as a molecular ruler. It was found, probably due to the method of fabrication and transfer as a chance of introducing some impurities the CVD graphene, was not so effective a quencher as the exfoliated.

For the exfoliated graphene an ET transfer model with a dimensionality of 4 and using a parameter that contains the geometric factor and the coupling coefficients seemed to be appropriated.

Coupling the QDS with the B exciton of the MoS_2 and also with graphene without a spacer was also possible, and with a side effect of also increasing the efficiency of ET to graphene. Still, the ET rates estimated where no compatible with the models used. In expectation to obtain an elucidative answer for this mismatch transient absorption was used. This allowed to follow the evolution of GSB of the QDs in the monolayers and correlate it with when is without 2D neighbors. The multi-exponential nature of the evolution of the GSB implies that more than one relaxation process was involved.

In other to further evaluate the previous systems it was proposed a time resolved 2HG experiment, but since the 2HG arising from monolayers is of low magnitude it was devised a setup to improve their noise signal ratio.

In that frame, the amplification of the 2HG signal by the proposed experimental method achieved and was roughly about 10 times in order of the initial signal. This allowed us to extract the time resolved data from the MoS_2 and from its hybrid structure conjugated with QDs and resolve it time. It was found that in the presence of the QDs the 2HG is increased. This was probably due to the presence of delocalized indirect excitons allowing for a possible enhanced emitter system of second harmonic light.

Lastly it was possible to characterize the signal of the third-order optical nonlinearity of graphene with the proposed XPM method. We suggest that this method seems a promising tool for the

characterization of the optical nonlinearity of graphene or other 2D materials, mainly because it is not sensitive to sample inhomogeneity's and thermal effects.

8.2.   What is left to do

Despite the knowledge and the experience gained from the experiments done in the framework of this thesis, further research is welcomed in order to:

A) Achieve an unambiguous demonstration of phonon-surface plasmon polariton coupling in the NPLs/graphene system, or if possible develop an alternative explanation for the observed deviation;

B) Explore the existence of some additional energy transfer channel in the case of PL quenching in the QDs/graphene system and the possibility of reversibility of this process in the several hybrid systems;

C) Obtain a consistent description of the role of graphene in the Kerr effect in the graphene/glass-like system, since the description of graphene (a 2D material) in terms of refractive index is quite imperfect and even more imperfect is to prescribe an effective refractive index to the joint graphene/substrate system.